MEASUREMENTS OF ULTRASHORT INTENSE LASER-INDUCED FRAGMENTATION OF SIMPLE MOLECULAR IONS

by

A. MAX SAYLER

B.S., Kansas State University, 2002

AN ABSTRACT OF A DISSERTATION

submitted in partial fulfillment of the
requirements for the degree

DOCTOR OF PHILOSOPHY

Department of Physics
College of Arts and Sciences

KANSAS STATE UNIVERSITY
Manhattan, Kansas
2008

Abstract

Present laser technology allows for the production of ultrashort ($\gtrsim$7 fs) intense ($\lesssim 10^{16}$ W/cm^2) pulses, which are comparable in duration and interaction strength to the vibrational period and the interaction that binds the electron in molecules, respectively. In this intense-field ultrashort-pulse regime one can both measure and manipulate dynamics on the femtosecond timescale. To probe the dynamics of laser-matter interactions in this regime, we have chosen to start from the simplest possible molecule — H_2^+, which can either dissociate into $H + p$ or ionize into $p + p + e$. We have designed and employ a coincidence three-dimensional momentum imaging technique which allows us to measure ionization and dissociation of a molecular ion beam target simultaneously, while completely separating the two channels from each other. By varying the laser intensity and the pulse duration, we measure the intensity and pulse length dependent momentum distributions for laser-induced fragmentation of H_2^+ at 790 nm. These dissociation measurements are in agreement with the phenomena predicted using the adiabatic Floquet picture, e.g. bond softening, in addition to more sophisticated calculations done by solving the time-dependent Schrödinger equation in the Born-Oppenheimer representation. Furthermore, the structure seen in ionization in our measurements and soon after by others is explained via a unified diabatic Floquet picture, which includes both ionization and dissociation in a single intensity and wavelength dependent picture that includes nuclear motion. Additionally, we use the same experimental techniques and apparatus to probe the laser-induced dynamics of multi-electron diatomic molecules, e.g. O_2^+, N_2^+, and ND^+. The most probable dissociation and ionization pathways producing the features seen in these measurements are discerned using the angular and kinetic-energy-release distributions in conjunction with the diabatic Floquet picture. Finally, we extend these experimental techniques and interpretive models to the simplest polyatomic molecule — H_3^+, whose fragmentation presents challenges both in our first-of-their-kind experiments and in physical interpretation.

MEASUREMENTS OF ULTRASHORT INTENSE LASER-INDUCED FRAGMENTATION OF SIMPLE MOLECULAR IONS

by

A. MAX SAYLER

B.S., Kansas State University, 2002

A DISSERTATION

submitted in partial fulfillment of the
requirements for the degree

DOCTOR OF PHILOSOPHY

Department of Physics
College of Arts and Sciences

KANSAS STATE UNIVERSITY
Manhattan, Kansas
2008

Approved by:

Major Professor
Professor Itzik Ben-Itzhak

Copyright

This document is prepared using LaTeX.

Abstract

Present laser technology allows for the production of ultrashort ($\gtrsim$7 fs) intense ($\lesssim 10^{16}$ W/cm^2) pulses, which are comparable in duration and interaction strength to the vibrational period and the interaction that binds the electron in molecules, respectively. In this intense-field ultrashort-pulse regime one can both measure and manipulate dynamics on the femtosecond timescale. To probe the dynamics of laser-matter interactions in this regime, we have chosen to start from the simplest possible molecule — H_2^+, which can either dissociate into $H + p$ or ionize into $p + p + e$. We have designed and employ a coincidence three-dimensional momentum imaging technique which allows us to measure ionization and dissociation of a molecular ion beam target simultaneously, while completely separating the two channels from each other. By varying the laser intensity and the pulse duration, we measure the intensity and pulse length dependent momentum distributions for laser-induced fragmentation of H_2^+ at 790 nm. These dissociation measurements are in agreement with the phenomena predicted using the adiabatic Floquet picture, e.g. bond softening, in addition to more sophisticated calculations done by solving the time-dependent Schrödinger equation in the Born-Oppenheimer representation. Furthermore, the structure seen in ionization in our measurements and soon after by others is explained via a unified diabatic Floquet picture, which includes both ionization and dissociation in a single intensity and wavelength dependent picture that includes nuclear motion. Additionally, we use the same experimental techniques and apparatus to probe the laser-induced dynamics of multi-electron diatomic molecules, e.g. O_2^+, N_2^+, and ND^+. The most probable dissociation and ionization pathways producing the features seen in these measurements are discerned using the angular and kinetic-energy-release distributions in conjunction with the diabatic Floquet picture. Finally, we extend these experimental techniques and interpretive models to the simplest polyatomic molecule — H_3^+, whose fragmentation presents challenges both in our first-of-their-kind experiments and in physical interpretation.

Contents

List of Figures

List of Tables

Acknowledgments

Though the following dissertation is an individual work, I could never have accomplished this work without the help, support, guidance and efforts of a lot of people. First, I would like to thank my advisor and mentor Dr. Itzik Ben-Itzhak as his kindness, unlimited enthusiasm, and love of a good argument have been the major driving forces through my graduate career at the Kansas State University. I am also grateful to have worked with post-doctoral researchers, i.e. Dr. Jarlath McKenna and Dr. Pengqian Wang, of the highest quality in both ability and character. Additionally, I would like to thank Dr. Brett Esry and Dr. C. Lew Cocke for always pushing me (often not too gently) to be a better physicist. Thanks also go to Dr. Kevin Carnes for always keeping me honest in my work along with all the J.R. Macdonald Laboratory technical staff (especially Mike Wells) for all of their thankless work which facilitated my measurements. I also acknowledge that I am very fortunate to work with excellent graduate and undergraduate students, i.e. Nora G. Johnson, Bishwanath Gaire, Mat Leonard, and Eli Parke, who keep my day-to-day work enjoyable. Finally, I wish to thank Professor Z. Chang's group (especially Dr. Hiroki Mashiko, Dr. Chengquan Li, Eric Moon, and Chris Nakamura) for contributing the vast majority of the work and expertise needed to produce the laser beam and Dr. C. Fehrenbach for his help with the ion beam.

On a more personal note, I wish to thank my father — Arthur M. Sayler III, who embodies much of what I am proud of being today and everything that I aspire to be in the future. His infinite patience, unwavering support, and genuine kindness have shaped me to be the person I am today. My thanks also go out to my late grandfathers — Arthur M. Sayler II and Benny Deckert who showed me the strength of optimism and joy of family. I would also like to thank my sister and mother — Andrea and Esther, for their love and support (not to mention all the food and proof reading that made this dissertation possible).

This work was supported by the Chemical Sciences, Geosciences, and Biosciences Division, Office of Basic Energy Sciences, Office of Science, U.S. Department of Energy.

Chapter 1

Introduction

1.1 Intense ultrafast laser matter interactions

Unlike relatively weak laser fields which do not significantly distort the structure of the matter they are incident upon, intense lasers can be used to induce non-linear effects. Understanding and controlling matter via this manipulation holds a great deal of promise in many fields. For example, when the laser-electron interaction is sizable in comparison to the Coulomb potential binding the electron in atoms,[1] i.e. $\gtrsim 10^{13}$ W/cm^2, an electron can be ionized and then driven back into the atomic potential by the laser field producing high energy photons, i.e. high-harmonic generation (HHG) [1–5]. This process has been used to produce XUV attosecond[2] laser pulses, which hold the promise of being able to image the structure of a single atom or molecule and potentially also follow electron motion [6, 7]. In addition to probing structures on the atomic scale, intense ultrafast laser pulses have large scale practical applications, e.g. laser surgery and precision fabrication, which involve solid state materials [8].

However, to gain the basic understanding of laser matter interactions necessary for fine control of intense laser phenomena, it is more effective to begin with simple matter. This has prompted many experimental and theoretical studies of atoms in intense fields, which have led to our current understanding of many laser-induced non-linear effects including the aforementioned HHG. Further-

[1] For a hydrogen atom the Coulomb attraction binding an electron in the first Bohr orbital is equal to the force exerted on an electron by a laser field of intensity 3.51×10^{16}W/cm^2.

[2] An attosecond, a femtosecond, and an atomic unit of time are defined as 10^{-18}, 10^{-15}, and 2.4×10^{-17} seconds, respectively.

more, the discovery and understanding of interesting physical processes in atoms exposed to intense laser fields have spawned interest in molecular dynamics in intense and ultrashort laser pulses. The resulting theoretical and experimental work have uncovered many interesting phenomena

1.2 Our focus

In particular, as we are trying to understand the dynamics of molecules in intense ultrashort laser fields, we have chosen to begin by focusing on the *simplest* molecule, i.e. the one with the fewest constituents. This is the hydrogen molecular ion, H_2^+. As the simplest molecule in nature, H_2^+ plays a fundamental role in theoretical and experimental investigation of the interaction between intense laser fields and molecules, e.g. see references [1, 9–32] as well as several excellent reviews [8, 33]. To that end, we have developed a coincidence time-of-flight experimental method that enables kinematically complete measurements of the laser-induced fragmentation of H_2^+. These state-of-the-art intensity and pulse-width dependent measurements have given us a great deal of insight into the ultrashort pulse laser-induced dynamics of H_2^+ in terms of the unified Floquet picture.

Furthermore, we have used the insight and experimental expertise gained from our studies of H_2^+ to measure and interpret the laser-induced fragmentation of multi-electron diatomic molecules. Interpretation of the experimental results for multi-electron molecules has been crude compared to the extensive theoretical and experimental studies of H_2^+ and H_2-laser interactions mainly due to the more complex electronic structure of multi-electron diatomic molecules. However, we have combined all the information given by the unified Floquet picture with a complete intensity-dependent 3D momentum imaging technique to create a method to determine the laser-induced dissociation pathways of a multi-electron diatomic molecule, e.g. O_2^+, N_2^+, and ND^+.

Finally, with the successful studies of laser-induced fragmentation of diatomic molecular ions, we have recently begun to examine laser-induced fragmentation of H_3^+. The H_3^+ molecular ion is an important benchmark in the understanding of laser-matter interactions because its status as the simplest polyatomic molecule places H_3^+ at the threshold between the relatively well understood

diatomic molecule-laser interactions and the increasing complexity of polyatomic molecule-laser interactions. Thus, we envision H_3^+ playing the same fundamental role in the understanding of polyatomic systems in intense laser fields as H_2^+ has played for diatomic molecules.

1.3 Document structure

As is apparent from the extensive table of contents, the structure of this dissertation is slightly unusual in two ways. First, the appendices comprise a significant portion of the document. This has been done intentionally so (i) the body of the text is easier to read for a broad audience and (ii) the appendices can serve as self-contained documents on each topic. Second, the document has been segmented into many sections so that it is easier to use as a quick reference on multiple topics. Furthermore, in this way the associations with our existing publications are also readily apparent.

In the remainder of this chapter, the theoretical groundwork used in interpretation and discussion to follow will be laid. This is followed by a chapter describing the experimental method we use to perform the measurements discussed within this dissertation.[3] Next, the body of this work, i.e. the experimental results and discussion of intense ultrashort laser-induced fragmentation of molecular ions, is broken into three chapters. The first, chapter 3, covers laser-induced fragmentation of the simplest molecule — H_2^+. The understanding of laser-molecule interactions gained from this study are then extended to multi-electron diatomic molecular ions, i.e. O_2^+, N_2^+, and ND^+, in chapter 4. Finally, the experimental complexities and some results of our ongoing benchmark study of the prototypically polyatomic molecular ion, H_3^+, will be discussed. To conclude, there is a brief summary and a discussion of the future direction of our experimental group.

1.4 Floquet or dressed potential picture

1.4.1 Introduction

In both experimental and theoretical work with intense laser-molecule interactions the use of Floquet theory is common place. Frequently, especially in qualitative interpretations of dissociation

[3] Many of the nonessential highly technical details have been excluded from chapter 2 and placed in the appendices for readability.

and ionization mechanisms of diatomic molecules [8–18, 33–52], results are compared with what the Floquet theory predicts. Therefore, to familiarize the reader with concepts that will be used throughout this dissertation and predicate the discussion and interpretation that follows, this section will briefly explain what the Floquet theory is, within the scope of laser-molecule interactions, and lists the approximations it entails. Furthermore, some of the popular jargon, e.g. bond softening, bond hardening, above-threshold dissociation, and zero photon dissociation, associated with the Floquet approximation for molecules in a laser field will be addressed.

1.4.2 Diabatic Floquet curves compared to the "vertical transition model"

The first, and perhaps most important, property to notice about the Diabatic Floquet potential energy curves (PECs) is that they are completely interchangeable with the drawing of vertical arrows on the PECs to represent photons, which will be referred to as the vertical-transition (VT) model, see figure 1.1. In the VT model one draws photon absorption/emission as vertical transition(s) with energy equal to n-photons, i.e. $E = \pm nE_{photon}$, on top of the established Born-Oppenheimer PECs. In the Diabatic Floquet picture, one draws the "dressed" PECs shifted by $E = \pm nE_{photon}$ intervals and allowed transitions can take place at the curve crossings. Furthermore, in both pictures one can include a plot of the transition probability (a.k.a. the coupling between PECs) as a function of R, as shown in figure 1.1(c). In the example shown in figure 1.1 the 1-photon transition probability is both larger and wider than that of the 3-photon transition. This is what one would expect for moderate laser intensities as transitions are confined to a small region around the resonant position, i.e. where the PECs are separated by exactly the energy of n photons, and the transition probability and resonance width decrease with an increase in the number of photons required to make the transition. Although both pictures now include the PECs needed to determine the radial nuclear motion and the transition probability needed to transfer the nuclear wavepacket from one PEC to another, it is often more convenient to incorporate the coupling into "new" PECs so that as much information as possible is contained in the PECs alone. This procedure of incorporating the laser-induces coupling into new PECs is exactly what the will be discussed in the adiabatic Floquet section.

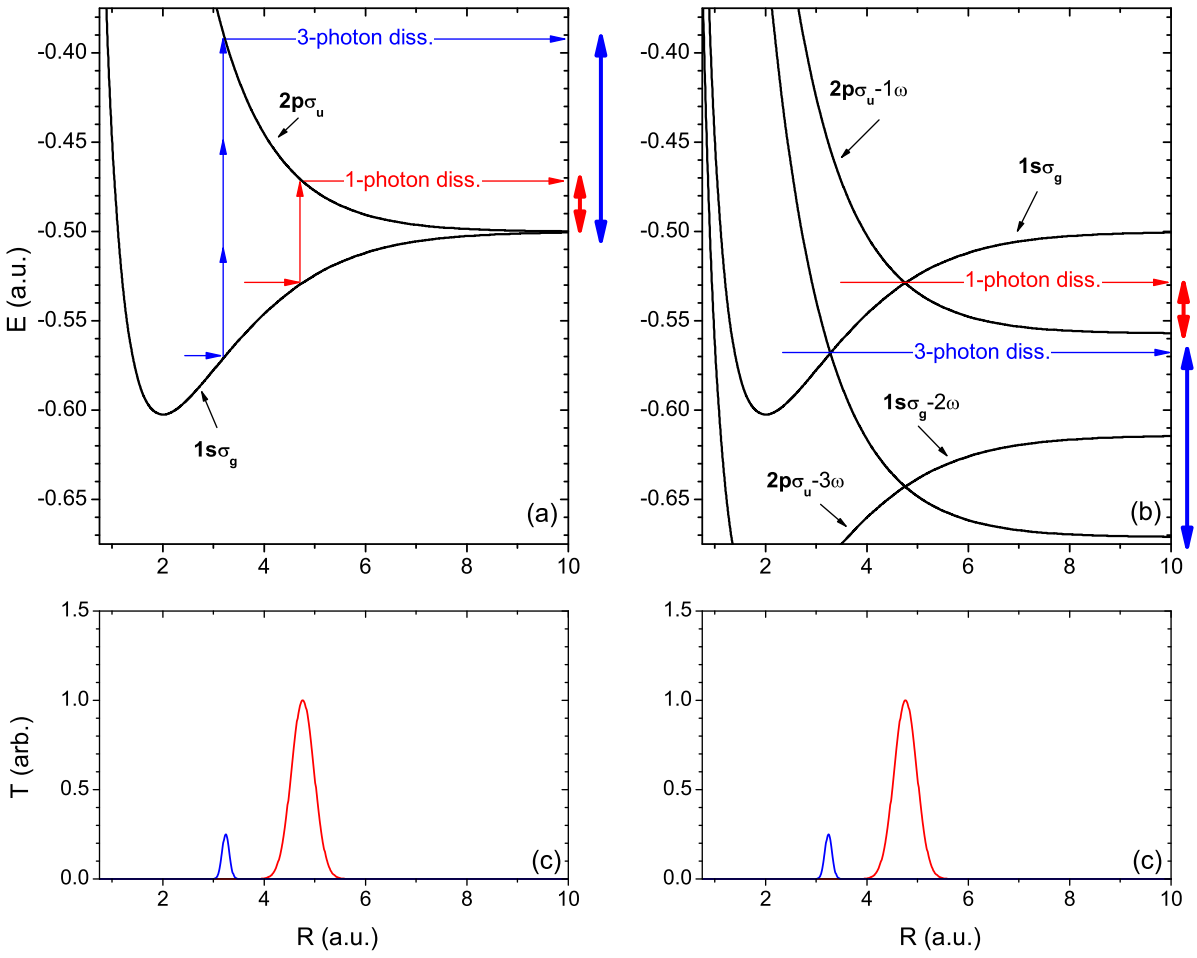

Figure 1.1: Diabatic Floquet curves compared to the vertical transition model. (a) Photon transitions are represented as vertical arrows of length $E = |\hbar\omega| = |E_{photon}|$. (b) In the Diabatic Floquet picture, potential energy curves are duplicated at $E = \pm nE_{photon}$ intervals to represent $\pm n$-photon transitions. The processes of a 1- and 3-photon transitions from the $H_2^+(1s\sigma_g)$ potential to the $H_2^+(2p\sigma_u)$ potential via 790 nm light are shown in both figures. Bold arrows to the right of figures represents the kinetic energy release from the respective processes. (c) A schematic transition probability, T, for the 1- and 3-photon crossings, shown in red and blue, respectively. Note that this figure is identical for diabatic Floquet and vertical transition models.

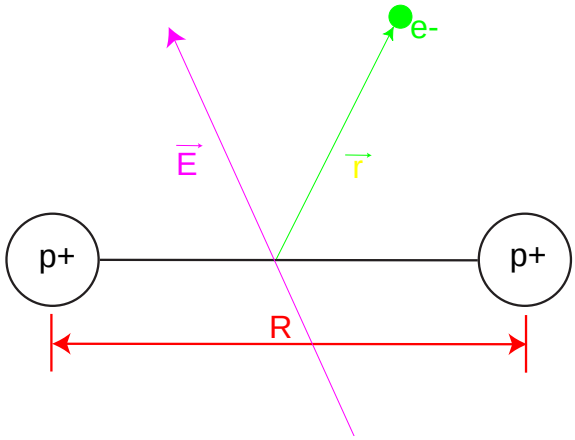

Figure 1.2: Coordinate system used for the H_2^+ Floquet derivation. R is the internuclear separation, $\overrightarrow{r}$ is the electron position relative to the midpoint of the internuclear axis, and $\overrightarrow{E}$ is the electric field vector.

1.4.3 Adiabatic molecular Floquet potential energy curves for H_2^+

Before the features of the Floquet picture in either adiabatic or diabatic form are discussed in detail, it may behoove the reader to review the basic formulation of the Floquet picture. Thus, a brief discussion of how one can incorporate some of the effects of a periodic light field into molecular potential energy curves is in order and will be addressed in this subsection. As always, a good place to start is with the complete Hamiltonian for the situation at hand. In this case the Hamiltonian $\mathbf{H}$ can be written as

$$\mathbf{H} = \mathbf{T}_N + V_{field} + \mathbf{H}_{ad} = -\frac{1}{2\mu}\nabla_R^2 - \overrightarrow{E} \cdot \overrightarrow{d} + \mathbf{H}_{ad} \ , \tag{1.1}$$

where R is the internuclear distance, $\overrightarrow{E}$ is the electric field due to the laser, μ is the molecular reduced mass, $\overrightarrow{d}$ is the dipole moment of the molecule, $\overrightarrow{r}$ is the position of the electron with respect to the midpoint of the internuclear axis, $\mathbf{T}_N = -\frac{1}{2\mu}\nabla_R^2$ is the nuclear kinetic energy, $V_{field} = -\overrightarrow{E} \cdot \overrightarrow{d}$ is the potential due to the laser field,[4] and $\mathbf{H}_{ad} = \mathbf{T}_e + V$ is the sum of the electronic kinetic energy and Coulomb interaction of all particles.[5] (See figure 1.2.) This is of course too difficult to solve exactly. Therefore, the common Born-Oppenheimer approximation will be made allowing one to

[4] This asserts the dipole approximation, which is valid for laser fields that will be discussed within this dissertation as $\lambda_{\text{laser}} \gg |\overrightarrow{r}|$.

[5] Note that boldface symbols, e.g. $\mathbf{H}_{ad}$, represent matrix operators and an arrow over a symbol, e.g. $\overrightarrow{E}$, represents a vector quantity. Furthermore, the derivation in this section is done in atomic units where $\hbar$ and the mass and charge of an electron have a value of 1.

solve for the field-free electronic wave functions $\Phi_\nu(R;\overrightarrow{r})$ and the electronic energies $U_\nu(R)$ given a fixed internuclear separation R.

$$\mathbf{H}_{ad}\Phi_\nu(R;\overrightarrow{r}) = U_\nu(R)\Phi_\nu(R;\overrightarrow{r}) \tag{1.2}$$

The electronic wavefunctions are subsequently used as the basis set onto which the total wave function Ψ is projected. In other words,

$$\Psi = \sum_{\nu=0}^{\infty} F_\nu(R,t)\Phi_\nu(R;\overrightarrow{r}_e) \ , \tag{1.3}$$

where $|F_\nu(R,t)|^2$ are the time and internuclear distance dependent probabilities for an electronic state ν. Using this total wavefunction, the time dependent Schrödinger equation, i.e. $\mathbf{H}\Psi = i\frac{\partial}{\partial t}\Psi$, takes the form

$$\mathbf{H}\Big(\sum_\nu F_\nu\Phi_\nu\Big) = i\frac{\partial}{\partial t}\Big(\sum_\nu F_\nu\Phi_\nu\Big) \ , \tag{1.4}$$

where $F_\nu(R,t)$ and $\Phi_\nu(R;\overrightarrow{r})$ are written as F_ν and Φ_ν, respectively, for simplicity. This equation can be expanded to,

$$\sum_\nu(\mathbf{T}_N + U_\nu - \overrightarrow{E}\cdot\overrightarrow{r})F_\nu\Phi_\nu = i\sum_\nu\frac{\partial F_\nu}{\partial t}\Phi_\nu \ . \tag{1.5}$$

To find equations for the unknowns, F_ν, both sides are projected onto Φ_λ. In other words,

$$\int d^3r_e\Big[\Phi_\lambda^*\sum_\nu(\mathbf{T}_N + U_\nu - \overrightarrow{E}\cdot\overrightarrow{r})F_\nu\Phi_\nu\Big] = \int d^3r\Big[\Phi_\lambda^* i\sum_\nu\frac{\partial F_\nu}{\partial t}\Phi_\nu\Big] \ . \tag{1.6}$$

Further, $\langle\Phi_\lambda|\Phi_\nu\rangle = \delta_{\lambda\nu}$, thus, the above equation can be simplified to

$$\mathbf{T}_N F_\lambda + U_\lambda F_\lambda - \sum_\nu\langle\Phi_\lambda|\overrightarrow{E}\cdot\overrightarrow{r}|\Phi_\nu\rangle F_\nu = i\frac{\partial F_\lambda}{\partial t} \ , \tag{1.7}$$

where $\overrightarrow{E} = \overrightarrow{E}_0\cos(\omega t)$ and $\overrightarrow{E}_0 = E_0\widehat{z}$. Note that $\overrightarrow{E}_0$ and ω are time independent in this equation. Therefore, *this derivaton does not allow for laser fields which are not monochromatic and of a constant intensity without modification* and thus should only be used as a rough guide when dealing

with ultrashort laser pulses.[6] Nevertheless, it is still a good qualitative tool and has been shown to even give quantitative agreement as long as the laser pulse is comprised of many cycles, i.e. $\tau_{\text{pulse}} \gg \tau_{\text{cycle}}$.[7] Continuing under these conditions yields

$$\left(-\frac{1}{2\mu}\nabla_R^2 + U_\lambda - i\frac{\partial}{\partial t}\right) F_\lambda - E_0 \cos(\omega t) \sum_\nu \langle \Phi_\lambda | \widehat{z} \cdot \overrightarrow{r} | \Phi_\nu \rangle F_\nu = 0 \ , \tag{1.8}$$

which can be written in matrix notation as

$$\left(-\frac{1}{2\mu}\nabla_R^2 + \mathbf{U} - E(t)\mathbf{D}\right) \overrightarrow{F} = i\frac{\partial}{\partial t}\overrightarrow{F} \ . \tag{1.9}$$

Assuming now for simplicity that there are only two effective states in the system in question, e.g. a simplified model of H_2^+ with only $1s\sigma_g$ and $2p\sigma_u$, $\overrightarrow{F}$, $\mathbf{U}$, and $\mathbf{D}$ would be written as

$$\overrightarrow{F}(R) = \begin{bmatrix} F_{1s\sigma}(R) \\ F_{2p\sigma}(R) \end{bmatrix} \tag{1.10}$$

$$\mathbf{U} = \begin{bmatrix} U_{1s\sigma}(R) & 0 \\ 0 & U_{2p\sigma}(R) \end{bmatrix} \tag{1.11}$$

$$\mathbf{D} = \begin{bmatrix} 0 & D_{1s\sigma\rightarrow 2p\sigma}(R) \\ D_{2p\sigma\rightarrow 1s\sigma}(R) & 0 \end{bmatrix} \tag{1.12}$$

$$D_{ij} = E_0 \cos(\omega t) \langle i | \widehat{z} \cdot \overrightarrow{r} | j \rangle \tag{1.13}$$

Finally, the Floquet Theorem will be used. This is applicable as

> "the total Hamiltonian is given by $\mathbf{H}(R,t) = \mathbf{H}_0(R) + V(R,t)$ with $V(R,t) = V(R,t+\tau)$. The unperturbed Hamiltonian $H_0(R)$ has a complete orthonormal set of eigenfunctions: $H_0(R)|\alpha(R)\rangle = E_\alpha^0 |\alpha(R)\rangle$. The wavefunction F, called a quasienergy-state (QES), can be written, according to Floquet theory, in the form $F(R,t) = \exp(-i\epsilon t)\Phi(R,t)$, where $\Phi(R,t)$ is periodic in time, i.e., $\Phi(R,t) = \Phi(R,t+\tau)$, and ϵ is a real parameter, which is unique up to multiples of $\frac{2\pi n}{\tau}$, called the Floquet characteristic exponent or the quasienergy" [55].

[6] Note that one can use the Floquet framework and include the frequency bandwidth and intensity time dependence in accurate quantitative models, e.g. a review by S. I. Chu and D. A. Telnov [53], a model including carrier-envelope phase effects in H_2^+ [54], and a quasi-stationary Floquet based model for H_2^+ [19].

[7] See, for example, the discussion in chapters 3 and 4 and references therein.

The Hamiltonian acting on the vibrational wavefunction is of the form $H(t+T) = H(t)$, discussed above. Therefore, Floquet theory allows for the removal of the periodic time dependance of the potential by copying the potential block $\mathbf{U}$ with offsets of the quasienergy $n\hbar\omega$ and dipole coupling block $\mathbf{D}$ along the diagonal and off-diagonal, respectively, of a new Floquet potential matrix $\mathbf{U}'$. Thus, the effect of an n-photon absorption or emission is taken into account by copying the aforementioned blocks up or down the diagonal of the Floquet matrix n spaces respectively. Note that one must include many blocks even if they are interested in 1-photon transitions.[8] Thus, the Floquet potential matrix $\mathbf{U}'$ takes the form

$$\mathbf{U}' = \begin{bmatrix} \dots & \dots & 0 & 0 & 0 \\ \mathbf{D} & \mathbf{U} - \hbar\omega & \mathbf{D} & 0 & 0 \\ 0 & \mathbf{D} & \mathbf{U} & \mathbf{D} & 0 \\ 0 & 0 & \mathbf{D} & \mathbf{U} + \hbar\omega & \mathbf{D} \\ 0 & 0 & 0 & \dots & \dots \end{bmatrix}, \tag{1.14}$$

which can be expanded to

$$\begin{bmatrix} \dots & \dots & 0 & 0 & 0 \\ \begin{bmatrix} 0 & D_{12} \\ D_{21} & 0 \end{bmatrix} & \begin{bmatrix} |1\rangle - \hbar\omega & 0 \\ 0 & |2\rangle - \hbar\omega \end{bmatrix} & \begin{bmatrix} 0 & D_{12} \\ D_{21} & 0 \end{bmatrix} & 0 & 0 \\ 0 & \begin{bmatrix} 0 & D_{12} \\ D_{21} & 0 \end{bmatrix} & \begin{bmatrix} |1\rangle & 0 \\ 0 & |2\rangle \end{bmatrix} & \begin{bmatrix} 0 & D_{12} \\ D_{21} & 0 \end{bmatrix} & 0 \\ 0 & 0 & \begin{bmatrix} 0 & D_{12} \\ D_{21} & 0 \end{bmatrix} & \begin{bmatrix} |1\rangle + \hbar\omega & 0 \\ 0 & |2\rangle + \hbar\omega \end{bmatrix} & \begin{bmatrix} 0 & D_{12} \\ D_{21} & 0 \end{bmatrix} \\ 0 & 0 & 0 & \dots & \dots \end{bmatrix} \tag{1.15}$$

with $|1\rangle \equiv F_{1s\sigma}(R)$ and $|2\rangle \equiv F_{2p\sigma}(R)$. Furthermore, as there is only odd photon coupling between the $1s\sigma_g$ and $2p\sigma_u$ states of H_2^+, e.g. $|1\rangle$ and $|1\rangle + \hbar\omega$ do not couple, this matrix has two sets of

[8] In general, the number of blocks included should be increased until the potential energy curves now longer change in the range of interest with the inclusion of additional blocks. We find that the inclusion of a few hundred blocks both above and below the shifted potentials typically provides the precision we desire.

equivalent non-interacting elements. Therefore the potential matrix can be simplify to

$$\mathbf{U}' = \begin{bmatrix} \ldots & \ldots & 0 & 0 & 0 & 0 \\ D_{21} & |2\rangle - \hbar\omega & D_{21} & 0 & 0 & 0 \\ 0 & D_{12} & |1\rangle & D_{12} & 0 & 0 \\ 0 & 0 & D_{21} & |2\rangle + \hbar\omega & D_{21} & 0 \\ 0 & 0 & 0 & D_{12} & |1\rangle + 2\hbar\omega & D_{12} \\ 0 & 0 & 0 & 0 & \ldots & \ldots \end{bmatrix}. \tag{1.16}$$

Finally, by diagonalizing the potential matrix, one obtains the adiabatic Floquet potentials.

$$\mathbf{\Gamma} \equiv \text{diagonalize}\left[\mathbf{U}'\right] = \begin{bmatrix} \ldots & 0 & 0 & 0 & 0 & \\ 0 & \beta_{-1} & 0 & 0 & 0 & 0 \\ 0 & 0 & \alpha_0 & 0 & 0 & 0 \\ 0 & 0 & 0 & \beta_{+1} & 0 & 0 \\ 0 & 0 & 0 & 0 & \alpha_{+2} & 0 \\ 0 & 0 & 0 & 0 & 0 & \ldots \end{bmatrix}. \tag{1.17}$$

Note that many Floquet coupling blocks must be included for a converged calculation as each of the diagonalized potentials of equation 1.17 is affected and modified from its original from by all the off-diagonal elements not just the adjacent ones. That is to say that when moving from $|1\rangle$ to α_0 one needs to include more than just the coupling to the adjacent $|2\rangle$ states.

1.4.4 Discussion

In general, it is worth noting several general features of the Floquet picture. (i) The diabatic Floquet picture is simply a representation of equation 1.16 without the off-diagonal coupling and is equivalent to the VT model. (ii) The adiabatic Floquet picture is a way of including the coupling of various electronic states due to a periodic electric field into the PECs. (iii) As the electric field strength diminishes the adiabatic Floquet picture reduces to the diabatic Floquet picture as shown in equations 1.16 and 1.17. In other words, as the off-diagonal, i.e. coupling, elements go to zero, the diagonalized matrix in equation 1.17 will become equivalent to the matrix in equation 1.16.

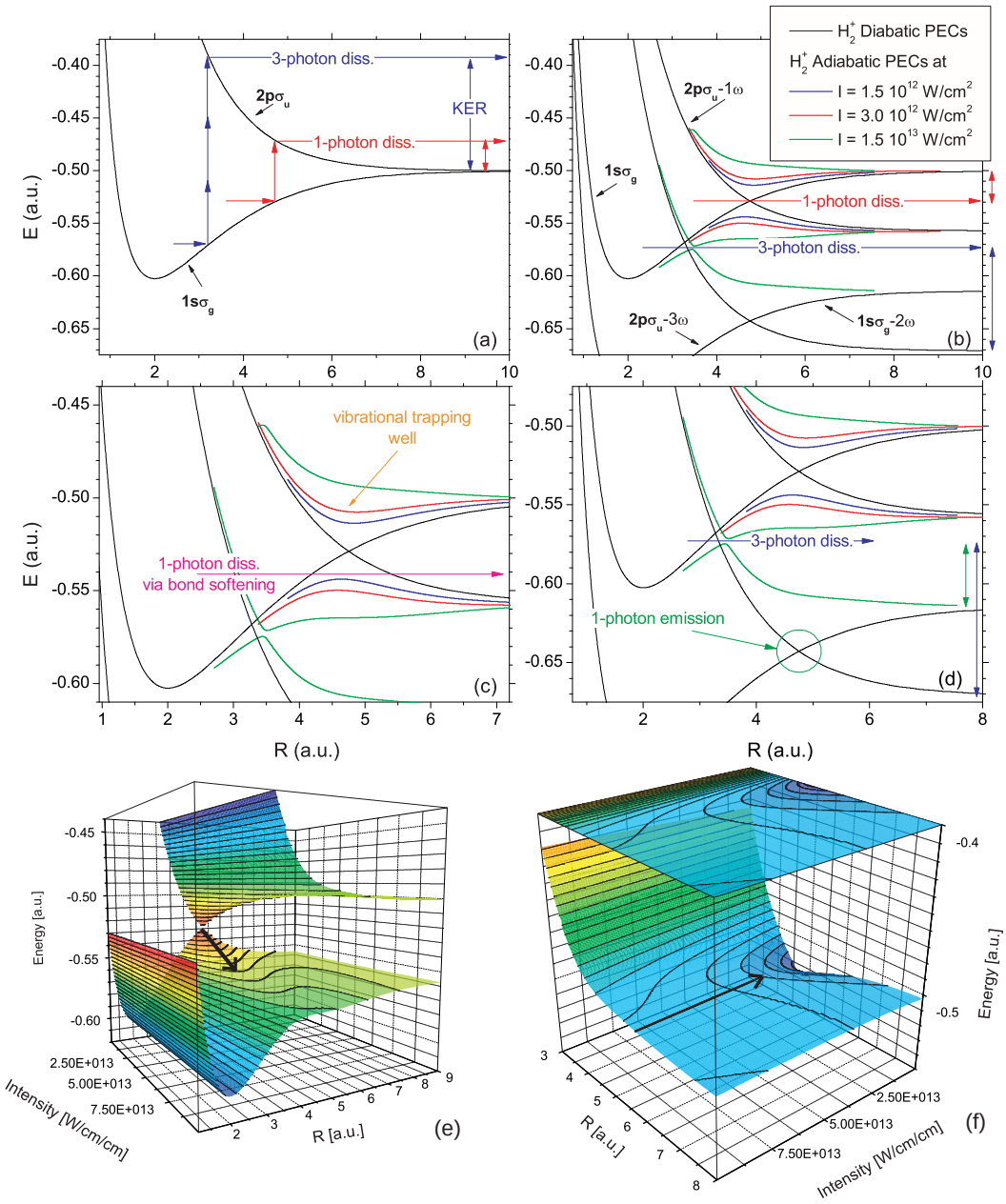

Figure 1.3: H_2^+ adiabatic and diabatic Floquet potential energy curves. (a) Using vertical arrows to represent photon absorption/emission. (b) Floquet picture with diabatic curves in black and adiabatic curves in color. (c) Adiabatic Floquet curves at the 1-photon crossing with bond softening and vibrational trapping marked. (d) Adiabatic curves a the 3-photon crossing with the 1-photon emission crossing circled. Note that the vertical arrows to the right of figures mark the expected kinetic energy release (KER) for the respective processes. (e) The upper and lower adiabatic Floquet PEC as a function of laser intensity. The path for laser induced alignment is marked with an arrow. (f) The upper adiabatic Floquet PEC. The path for laser induced anti-alignment is marked with an arrow. See text for details and discussion.

1.4.4.1 Distortion of potentials due to electric field

The result of the inclusion of coupling due to the electric field is a distortion of the potentials. As one can see in figure 1.3, the effect of the coupling between potentials is the formation of an avoided crossing which grows in separation with an increase in laser intensity. This avoided crossing formation has led to concepts, which have been confirmed by experimental evidence, that are not readily apparent in VT or diabatic Floquet pictures. These processes will be briefly outlined here and discussed in further detail when applicable to our experimental data.

Bond softening The most obvious of these processes — bond softening — is a result of the $|1s\sigma_g\rangle \rightarrow |2p\sigma_u - 1\omega\rangle$ avoided crossing on the dissociating nuclear wavepacket. At an intensity corresponding to a significant opening in the avoided crossing, as shown in figures 1.3(c) and (e), portions of the nuclear wavepacket with vibrational energy below the diabatic curve crossing can dissociate by passing over the barrier formed by the avoided crossing. Thus, dissociation events with kinetic energy release (KER) lower than expected from the vertical transition and diabatic Floquet pictures are predicted. Exactly this phenomenon has been seen in experimental measurements, e.g. see [10–12, 52].

Vibrational level shifting In addition to bond softening, one would expect the distortion of the $H_2^+(1s\sigma_g)$ potential energy well, i.e its broadening with increased intensity, to shift the vibrational levels downward with respect to the diabatic PECs. This means that as the intensity is increased the vibrational levels should shift to lower energies and a closer spacing. Again, this phenomenon has been seen in experimental measurements, see for example [12, 52]. This can be seen in the distortion of the PEC in figures 1.3(c) and (e) as one moves to higher laser intensities.

Vibrational trapping The avoided crossing between the $1s\sigma_g$ and $2p\sigma_u$ PECs also produces a "new" upper potential energy well, as denoted in figure 1.3(c), (e), and (f). The vibrational wavepacket can make a transition to this well from the $1s\sigma_g$ PEC and become trapped. This would lead one to predict that vibrational states lying above the bottom of this new well would have less

probability to dissociate than those lying below the bottom of this well. Thus, the internuclear bond is "hardened", i.e. softened less, for these states leading to the other name for this process — bond hardening. This is seen as a reduction in dissociation probability for high lying vibrational states, see for example [20].

1.4.4.2 Multiphoton processes

As shown in figure 1.3(d), multiphoton processes are also predicted in the Floquet picture. As one would expect, the larger the number of photons involved in a process, the higher the intensity before these phenomena become prevalent. For example the 3-photon dissociation avoided crossing shown for H_2^+ in figure 1.3 only begins to open after an increase in intensity of more than an order of magnitude from the intensities at which significant bond softening occurs. Nevertheless, when the intensity is great enough to facilitate these processes, the same effects discussed above can be seen [13, 21, 42, 56]. In general, one should notice that photon emission as well as photon absorption is taken into account in the adiabatic Floquet picture. In figure 1.3(d) for example, when the 3-photon avoided crossing begins to open, i.e. allowing dissociation through 3-photon absorption, the subsequent 1-photon avoided crossing is well open, thereby ushering the nuclear wavepacket along the $|1s\sigma_g - 2\omega\rangle$ PEC, i.e. the molecule undergoes stimulated emission of 1 photon. This will be discussed in detail in regards to our high intensity ultrashort pulse studies of H_2^+ in chapter 3.

1.4.4.3 Time/Intensity evolution in the Floquet picture

As stated above, the Floquet theory is, strictly speaking, applicable to laser fields with a constant intensity and wavelength. Nevertheless, for slowly evolving electric field intensities where the laser pulse is comprised of many cycles, i.e. $\tau_{\text{pulse}} \gg \tau_{\text{cycle}}$, this theory still serves as an excellent guideline for picturing laser-induced processes in molecules. In this time-dependent Floquet picture one would allow the PECs to change in time with respect to the intensity of the laser pulse as shown in figures 1.3(e) and (f). Note that even when the laser pulse is comprised of only a few cycles the Floquet theory can provide the basis for highly accurate calculations [19].

Zero photon dissociation One process which is easily envisioned on the time-dependent Floquet PECs is zero photon dissociation as shown in figures 1.3(c) and (f). This process begins in the same manner as vibrational trapping — with a transition from the lower potential curve to the upper PEC. However, once the radial wave packet is in the upper potential well, the time evolution of the upper potential can "lift" the wave packet up above the dissociation limit allowing very low energy dissociation without the net absorption or emission of any photons. Note that this process is not as well known or widely accepted as the bond softening or vibrational trapping processes and has been experimentally highlighted by Posthumus *et al.* [14]. The equivalent picture can also be used for the potential well formed by 3-photon avoided crossing, which can "push" the nuclear wavepacket out along the bond softening pathway even if it is initially below the barrier of the avoided crossing. This process is typically referred to as below-threshold dissociation, e.g. see [15, 57]. The temporal component of vibrational level shifting discussed above is also apparent in the picture. Additionally, the opening and closing of avoided crossings along the pathway taken by the dissociation nuclear wavepacket can be envisioned in this way as will be discussed in section 3.2.3.

1.4.4.4 Molecular alignment in the Floquet picture

Much in the same way that the effects of time dependent intensity can be described in the Floquet picture, one can interpret the angular alignment of molecules in a laser field [18, 22, 58, 59]. For example, if one assumes[9] that only the component of the electric field parallel to the molecular axis is important, then an effective intensity, I_{eff}, can be written with respect to the angle between the laser field and the molecular axis, θ, as $I_{\text{eff}} = I\cos^2\theta$. This would lead to two different alignments effects for the PECs shown in figures 1.3(e) and (f) and denoted with arrows. (i) For a given constant laser intensity, I, molecules that are nearly perpendicular to the laser field, i.e. with $\theta \sim 90°$ and $I_{\text{eff}} = I\cos^2\theta \sim 0$, on the lower adiabatic Floquet PEC will rotate to align themselves with the laser field. This is to say that the nuclear wavepacket would "roll down" the Floquet surface in figure 1.3(e) aligning itself with the laser field experiencing an increased I_{eff} (ii) For

[9]Note that this is a valid assumption when 1-photon transition between two states with the same angular momentum (Λ), i.e. weak field interactions between the $|1s\sigma_g\rangle$ and $|2p\sigma_u - 1\omega\rangle$ states in H_2^+, dominate the laser-molecule interaction.

a given constant laser intensity, I, molecules that are nearly parallel to the laser field, i.e. with $\theta \sim 0^\circ$ and $I_{\text{eff}} = I\cos^2\theta \sim I$, on the upper adiabatic Floquet PEC will rotate to an alignment perpendicular to the laser field. In other words, the nuclear wavepacket would "roll" into the well shown in figure 1.3(f). Therefore, molecules undergoing bond softening and vibrational trapping should align parallel and perpendicular to the laser field, respectively [23].

1.4.5 Conclusions

As discussed above, the Floquet picture allows one to envision the effects of the laser-induced adiabatic coupling of PECs, which are obscured in the Vertical Transition and diabatic Floquet pictures. Thus, the Floquet theory is a useful tool when dealing with laser-molecule interactions, which allows one to easily make qualitative predictions about the behavior of molecules in a laser field. Furthermore, this picture will be referred to in upcoming discussions of experimental results as a basis for expectations and results. However, one must remember the assumptions made in generating the Floquet potentials so that the theory is not over extended.

Chapter 2

Experimental Method

2.1 Introduction

This chapter will focus on the experimental techniques used, both by ourselves and others, to measure high-intensity short-pulse laser-molecule interactions. First, the differences between neutral and ionic molecular targets will be discussed. Second, a brief review of experimental techniques using ionic molecular targets will be undertaken. Third, double-pulse, i.e. pump-probe, measurements will be briefly touched upon to serve as a basis for discussion in subsequent chapters. Fourth, a detailed description of the experimental method used in in the measurements presented within this dissertation will be given. Fifth, there will be a discussion of the spatial and temporal properties of focused Gaussian laser beams and the methods we developed to obtain the spectrum from a limited intensity range.

2.2 Molecular ions vs. neutral molecules

The first distinction to make in high-intensity short-pulse laser-molecule interactions is whether the initial molecular target is neutral or charged. Although ultrashort laser-molecule interactions have been studied for over a decade by many researchers, molecular-ion studies are rather scarce, though their number has increased rapidly in the last few years. To compare and contrast neutral and ionic molecular target experiments, (i) H_2/H_2^+ will be used as it is the simplest diatomic molecule and will provide the general framework necessary for this discussion and (ii) the cold target recoil ion

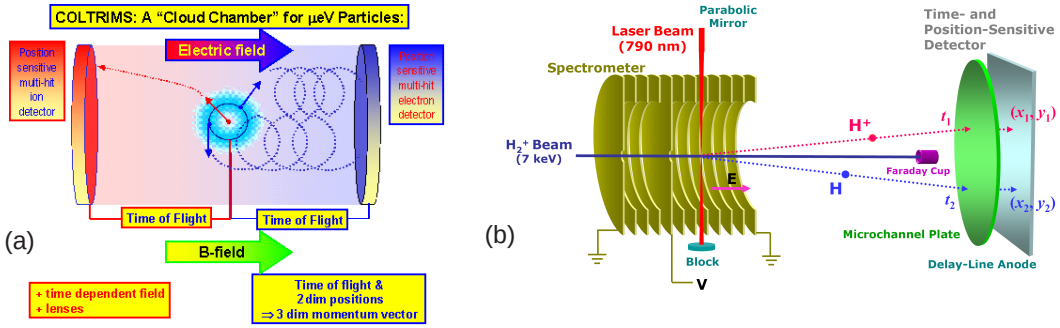

Figure 2.1: (a) Typical COLTRIMS setup. (Figure adapted from reference [62].) In this setup all charged particles are detected, but neutrals are not. (b) Typical molecular ion beam experiment [52]. In this example, both the p^+ and H are detected as the initial molecular ion beam energy is sufficient to detect the neutral H downstream.

momentum spectroscopy or COLTRIMS technique [2, 60, 61] shown in figure 2.1(a) will be used to exemplify neutral target measurements.

2.2.1 Detection of positive, negative, and neutral particles

In the COLTRIMS arrangement, shown in figure 2.1(a), the neutral target is produced via a supersonic cold jet, which typically makes a molecular target with a density of $\sim 10^{11}$ molecules/cm^3 and low kinetic energy spread. The target is also vibrationally and electronically cold, e.g. H_2 in the v=0 vibrational state of the ground $X\ ^1\Sigma_g^+$ electronic potential. After the target is subjected to the incident radiation, all charged fragments are collected via the electric and magnetic fields. The electric field accelerates positively charged ions towards one detector, the left side of figure 2.1(a), while electrons are accelerated towards the other side and are confined to a cyclotron path by the axial magnetic field. Finally, the time and position information detected for each particle is used along with first principles to reconstruct the initial "breakup" momentum components of each charged particle. Notice, however, that one can only measure the ions and electrons, e.g. p^+, e^-, and not H from the reaction $H_2 \rightarrow H_2^+ + e^- \rightarrow H + p^+ + e^-$.

In contrast, molecular beam experiments, e.g. using a few keV H_2^+ molecular ion beam as shown in figure 2.1(b), have the distinct disadvantages of (i) lower target densities and (ii) presently not including electron detection. Nevertheless, molecular beam experiments do have the advantage of

allowing for the detection of neutral particles. This is because the initial velocity of the molecular beam provides enough energy to the neutral fragments to be detected downstream. For example, in the process $H_2^+ \rightarrow H + p^+$ starting from a H_2^+ beam, all dissociation fragments (both H and p^+) are measured as shown in figure 2.1(b).

2.2.2 Initial state of the molecular ion

2.2.2.1 Coherence of nuclear wavepacket

Another distinct difference between molecular ion beams and neutral targets is in the behavior of the "intermediate" molecular ion. This behavior is dictated by the details of its creation. Typically, in experiments using neutral targets, e.g. H_2, the molecule is either (i) ionized with the same pulse that subsequently dissociates the molecule or (ii) is ionized with a "pump" pulse that arrives before a "probe" pulse which dissociated the molecule.[10] In both cases, when starting from H_2 in a laser field, the nuclear wavepacket (i) makes an electronic transition to the H_2^+ potential by releasing an electron and then (ii) the resulting coherent wavepacket will be launched on the H_2^+ potential. Subsequently, when the H_2^+ molecule is ionized/dissociated a short time later, i.e. attoseconds – picoseconds, the nuclear wavepacket will not be dephased and will still contain temporal information relating to the delay between the first step, e.g. $H_2 \rightarrow H_2^+ + e^-$, and the second step, e.g. $H_2^+ \rightarrow H + p^+$, of the process.

In contrast, molecular ion beams are typically formed through electron-impact ionization and then accelerated towards a laser-molecule interaction region. By the time the molecular ion reaches the interaction region, typically μs after its creation in the ion source and with a large spread in time-of-flight compared to the vibrational period, the vibrational population is an incoherent sum of the vibrational states populated in the ion source. Thus, the vibrational wavepacket for neutral and ion beam measurements should be treated as coherent and incoherent sums of the vibrational levels, respectively.

[10] See section 2.4 for a more detailed discussion of single and multiple pulse measurements.

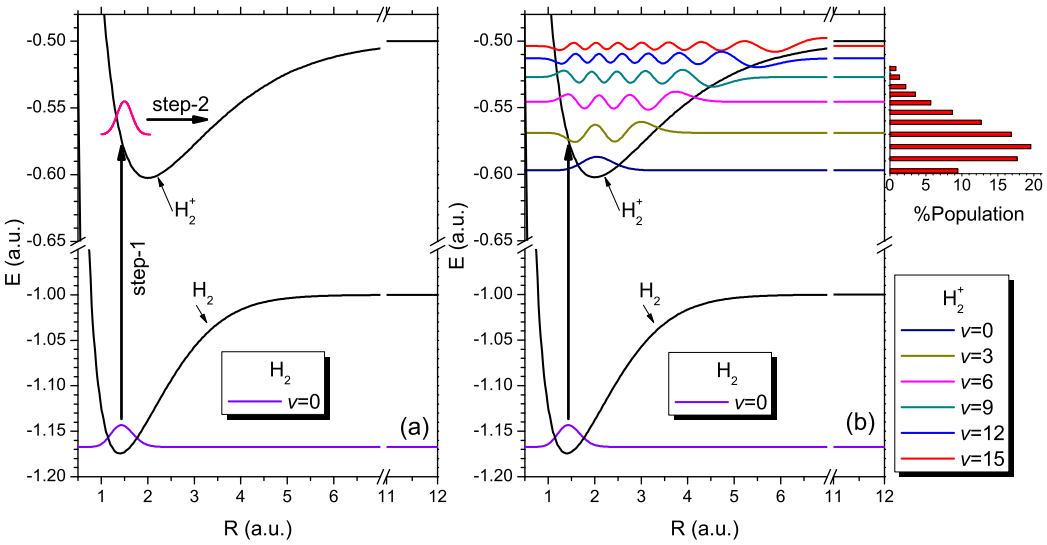

Figure 2.2: Illustration of the difference in H_2^+ when starting from a neutral (a) and an ionic (b) target. (a) When starting from H_2 in a laser field, the nuclear wavepacket (i) makes a vertical transition to the H_2^+ potential by releasing an electron and then (ii) the resulting coherent wavepacket will be launched on the H_2^+ potential. (b) Although the nuclear wavepacket makes an almost equivalent vertical transition in the ion source, the long time-of-flight to the interaction region (typically μs) means that the wavepacket is dephased and at the time of laser-molecule interaction the molecule occupies an incoherent sum of vibrational states. Additionally, the initial vibrational wavefunction of H_2 along with several of the lower vibrational wavefunctions for H_2^+ are displayed. The bar graph displays the populations of the H_2^+ vibrational states resulting from a vertical transition from the H_2 ground state.

2.2.2.2 Vibrational population

In addition to coherence, the vibrational state of neutral and ionic targets differ in population distribution. For neutral targets, the vibrational population of the molecular ion, e.g. H_2^+, is generally assumed to be determined by the Franck-Condon factors for a vertical transition from the ground state of the neutral, e.g. $H_2(X\,^1\Sigma_g^+, v = 0) \rightarrow H_2^+(1s\sigma_g)$ as shown in figure 2.2(a). However, the vibrational population of the intermediate H_2^+ has been shown to be dependent on the laser pulse parameters and is thus only approximated by the aforementioned Franck-Condon factors [63, 64]. Note that more recent calculations have taken some of these assumptions into account, e.g. [65]. Additionally, experimentalists have begun measuring the vibrational population dependence on laser parameters [63, 64].

For ionic molecular targets produced in an ion source using electron impact ionization, the initial ionization process, e.g. $H_2(X\,^1\Sigma_g^+, v = 0) \rightarrow H_2^+(1s\sigma_g)$, is well described by a vertical transition producing a Franck-Condon population in the resulting molecular ion, as shown in 2.2(b) and discussed in appendix A.2.1.1. This has been experimentally confirmed for H_2^+ by Z. Amitay et al. [66]. Furthermore, as electron impact ionization is a well-established technique, the resulting vibrational populations for many molecules have been measured, e.g. O_2^+ [67] and N_2^+ [68–70]. Thus, the initial vibrational population of the molecular ion target, e.g. H_2^+, is currently more well known and/or easily obtained than that of the intermediate molecular ion produced from a neutral target, e.g. $H_2 \rightarrow H_2^+$. Additionally, work is being done to control and measure the initial vibrational population of molecular ions [63–65] to tailor the vibrational population.

2.2.3 Minimum laser intensity

For neutral target studies of molecular ions, it is a requirement that the first and/or only laser pulse has enough intensity to ionize the target, e.g. $H_2 \rightarrow H_2^+ + e^-$. In the case of single Gaussian pulse measurements (e.g. [10, 20, 34]), which use the leading edge of the pulse to ionize the neutral target and the remainder of the pulse to dissociate and/or ionize the resulting molecular ion, one cannot study the effects of intensities lower than that required to ionize the neutral target. In other words, the prerequisite of ionizing the neutral target sets the lower bound of intensities that one can use to interact with the ion. Even for multiple laser pulse setups (e.g. pump-probe as discussed in section 2.4), which can use one pulse to ionize the neutral target and a second to ionize/dissociate the resulting ion, the intensity required to ionize the neutral target can also cause difficulties. This is due to the fact that ionization occurs over a distribution of intensities.[11] Thus, the time at which the nuclear wavepacket is promoted to the ionic surface is a distribution dictated by the ionization probability and laser pulse shape. Therefore, the wavepacket "launch" time has uncertainty, which can convolute temporal measurements, as discussed in section 2.4. In contrast, if one starts with

[11] In addition to the temporal intensity distribution, there is a spatial intensity distribution, as discussed in section 2.6. Furthermore, in the case of a prerequisite step, e.g. a pump, which requires a high intensity, the affected volume is limited to an area near the focal point. This spatial limitation can then serve as an advantage in limiting the intensity-volume effect for the second or probe pulse.

a molecular ion target, which is already in the charge state desired,[12] the minimum intensity for dissociation is not set by the lower limit required to ionize the corresponding neutral.

2.2.4 Target density

One of the major drawbacks of measurements using ionic beams is that the target density is limited by ion current from the source, beam divergence, and the space-charge effect. The yield expected from a given measurement per unit time is linearly proportional to the target density. Thus, high target density makes measurements easier and less time consuming. Experiments using a neutral gas cell target, e.g. see reference [71], typically achieve target densities of up to about 10^{17} molecules/cm^3, while experiments using cold supersonic jets achieve target densities of $\lesssim 10^{11}$ molecules/cm^3, e.g. see reference [2]. Both of these are much higher than is typically achieved in an ion beam experiment, i.e. $\lesssim 10^5$ molecules/cm^3. Therefore, detailed measurements of channels with small experimental yields is more difficult when starting from a ionic target.[13] The target density ρ for ion beams is given by

$$\rho = \frac{I}{A q_{\text{ion}}} \sqrt{\frac{m}{2E_{beam}}} \,, \tag{2.1}$$

where I is the ion current, A is the cross-sectional area of ion beam, q_{ion} is the charge of one ion, m is the mass of an ion, and E_{beam} is the ion beam energy. Thus, for a typical H_2^+ beam in our experiments with a cross-sectional area of $A \simeq 1 \times 1$ mm^2, a current of $I = 10$ nA, and a beam energy of 9 keV; $\rho \simeq 6 \times 10^4$ molecules/cm^3.

In addition to the target density limit imposed by the ion source in ion beam experiments, the ionic target density is limited by the space-charge effect. This is because the particles in an ionic target will experience a Coulomb repulsion from one another, which in turn adds an energy spread to the target particles. Assuming a cylindrical target of uniform density ρ and radius r comprised of particles of mass m and charge $q = q_e$, the acceleration of the outermost particles can

[12] Note that if one wishes to study the behavior of a multiply charged ion, e.g. CO^{++}, without a required minimum intensity, that charge state must be produced in the ion source. For example, studying CO^{++} starting with a beam of CO^+ would have the same problems mentioned above.

[13] Both the laser repetition rate and physical dimension of the target also play an important role in experimental yield. The influence of the former is obvious and the latter will be discussed in section 2.6.

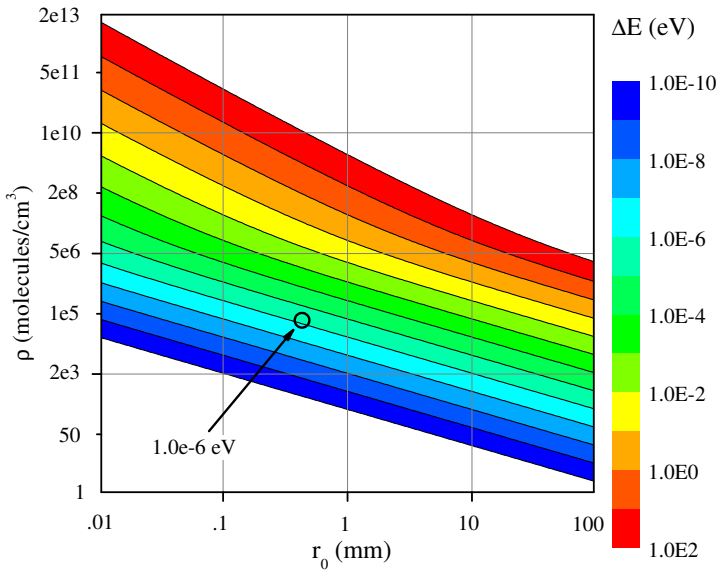

Figure 2.3: Energy gained due to the space-charge effect for a cylindrical target with uniform density ρ and initial radius r_0 after a 1 μs flight time. The circle marks the typical conditions under which our measurements are taken.

be approximated as

$$\ddot{r} \equiv a = \frac{F}{m} = 2k\frac{\lambda q_{\text{mol}}}{mr} = 2k\frac{\rho q_{\text{mol}}^2 \pi r_0^2}{mr} \tag{2.2}$$

where $k = 1/4\pi\epsilon_0 = 9\times10^9$ Nm^2/C^2, r_0 is the initial target radius, and λ is the linear charge density. As equation 2.2 is not easily solved for $r(t)$ analytically, we have chosen to solve the time evolution of this distribution numerically. By evolving the distribution over the time it takes to reach the detector from the interaction point, i.e. the time-of-flight, one can determine an approximate spread in energy due to space charge. This is done by calculating the velocity v and corresponding energy E, in the center-of-mass frame, after the time-of-flight for a particle starting at rest on the edge of the initial cylindrical target. The distribution shown in figure 2.3 has been calculated for a flight time of 1 μs as a function of the initial target radius r_0 and density ρ. For example, in a typical configuration for our setup using H_2^+ with r_0=1/2 mm and $\rho \simeq 10^5$ molecules/cm^3, the target can gain approximately 1 μeV of energy in the transverse direction in 1 μs. Furthermore, by using a numerical time evolution algorithm, one can create a plot analogous to figure 2.3 to determine the range of acceptable target parameters given the desired energy precision ΔE. Additionally, it is clear from figure 2.3 that the space-charge effect excludes ion beam measurement with target densities even close to those used in cold-jet measurement.

2.2.5 Rescattering

The final distinction between molecular ion beams and neutral targets that will be discussed is the possibility for rescattering. As compared to the molecular ion beam case, for neutral targets there is one additional electron present to affect the system. This means that if one wishes to study the dissociation process, $H_2^+ \rightarrow p^+ + H$, for the benchmark one-electron system H_2^+, the first step from a neutral H_2 is $H_2 \rightarrow H_2^+ + e^-$. The free electron ionized in this step can be subsequently driven by the laser field and recollide with the molecule producing effects not seen in the molecular ion beam target case.[14] In contrast, for many-electron molecules, both neutral and ionic targets will produce electrons that can rescatter off the molecule. It should be noted that the differences in characteristics between the two types of targets is not disparaging to either, rather it indicates unique and complementary knowledge that can be gained from each type of measurement. For example, rescattering has been used as a measurement tool with great success (e.g. [35, 80]).

2.3 Experimental techniques in laser-induced breakup of molecular-ion beams

2.3.1 Introduction

Despite the unique information that can be gained by using H_2^+ targets, these studies are rare due to the additional complexity of using an ion beam as a target. In recent years there are a few main groups that have emerged in this field, although new players have recently begun to surface (e.g. Paulus *et al.* at Texas A&M and Friedrich-Schiller-Universität Jena, Germany and Zajfman, Heber, Silberberg *et al.* at The Weizmann Institute of Science, Israel). The main groups that will be discussed here are (i) Figger, Hänsch, *et al.* at Max Planck Institut für Quantenoptik, who where the first to use a molecular ion target of Ar_2^+ [83]; (ii) Williams *et al.* at Rutherford Laboratory, who did the pioneering measurements of H_2^+ in parallel with the aforementioned group [82, 84];

[14] In general, dissociation of multi-electron molecules can be affected by rescattering in both neutral and ionic target experiments as the process of dissociative recombination (DR), e.g. $AB^+ \rightarrow AB^{++} + e^- \rightarrow (AB^+)^* \rightarrow A^+ + B$, can take place [72–79]. However, the probability for this process to happen is very small in comparison to the standard dissociation process, e.g. $AB^+ \rightarrow A^+ + B$. Thus, in most cases, the study of non-ionizing dissociation of molecular ions is affected much less by rescattering when starting from a molecular-ion target

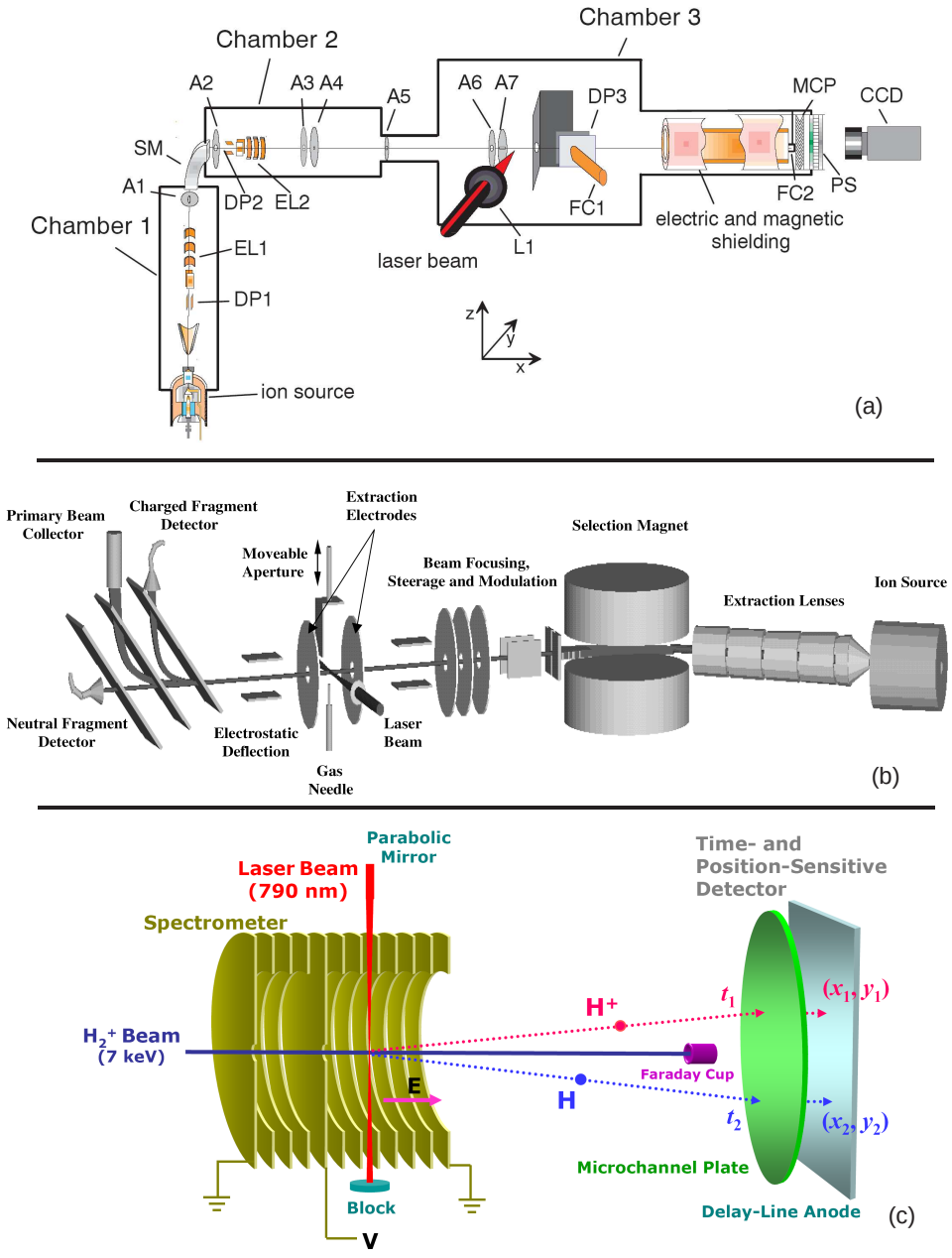

Figure 2.4: Experimental Setups used in laser induced breakup of molecular ion targets. (a) Schematic diagram of the ion beam apparatus used by Figger, Hänsch, *et al.* at Max Planck Institut für Quantenoptik, where DP is deflection plates, EL is Einzel lenses, SM is sector magnet, A is apertures, L1 is focusing lens, FC is Faraday cups, MCP is multichannel plate detector, PS is phosphor screen, and CCD is (charge-coupled device) camera. (Figure adapted from reference [81].) (b) Schematic diagram of the ion beam apparatus used by Williams *et al.* at Rutherford Laboratory. (Figure adapted from reference [82].) (c) Schematic diagram of the ion beam apparatus used by our group at J. R. Macdonald Laboratory. (Figure adapted from reference [36].) See appendix A for further detail.

and (iii) our group lead by Ben-Itzhak *et al.* at J. R. Macdonald Laboratory [36], which joined the field shortly after the other two groups. A rough schematic of each group's experimental setup is shown in figure 2.4 and some of the results of the first two groups will be discussed in comparison to our own in subsequent chapters.

2.3.2 Figger, Hänsch, *et al.* at Max Planck Institut für Quantenoptik

The group lead by Figger and Hänsch at Max Planck Institut für Quantenoptik [81, 83–88] used a 2D position sensitive detector to image one of the fragments. By using linear polarization aligned parallel to the detector plane (and defining the laser polarization to be along the k-axis in spherical coordinates) they use the inherent ϕ and $\pm k$ symmetry to enable an Abel transformation, which gives complete 3D momentum information [81], see figure 2.4(a). To eliminate the charge fragments and thereby measure only dissociation of H_2^+, Sändig et al. applied a transverse electric field [84]. Ionization of H_2^+ was also studied by measuring the charged particles and distinguishing ionization from dissociation by the larger kinetic energy release expected for this process [85, 87].[15]

2.3.3 Williams *et al.* at Rutherford Laboratory

Working at the Rutherford Laboratory, the second group led by Williams [24, 82, 89–91] uses the apparatus shown in figure 2.4(b) [82]. In this setup an energy analyzer is used in conjunction with time-of-flight information to determine the energy spectrum of the charged and neutral fragments, respectively. Distinction of ionization and dissociation events is achieved by normalizing the low energy peak of the two channels and subtracting dissociation from the total yield leaving only ionization.[16]

2.3.4 Ben-Itzhak *et al.* at J. R. Macdonald Laboratory

As shown in figure 2.4(c), our apparatus utilizes a spectrometer, detector, and Faraday cup that are collinear with the molecular ion beam [36–38, 52, 92–96]. This setup allows for the time- and

[15] Note that we have found that under certain conditions ionization and dissociation of H_2^+ overlap in KER and a coincidence measurement can be employed to distinguish the channels regardless of kinetic energy release (see chapter 3 for details).

[16] This will be discussed in further detail in chapter 3.

position-sensitive detection of both neutral and charged nuclear fragments, which are separated in time by the weak longitudinal electric field of a spectrometer. Furthermore, since both fragments are detected in coincidence, ionization and dissociation channels can be measured simultaneously and separated even if the two channels overlap in kinetic energy release. This apparatus will be discussed in detail in section 2.5.

2.4 Pump-probe measurements

All of our measurements discussed within this dissertation are performed using a single laser pulse, which distinguishes them from measurements involving multiple laser pulses. In this section, an analogue to our single pulse H_2^+ ionization using the pump-probe technique will be discussed. Typically, in the pump-probe configuration the first pulse, i.e. the pump, is used to put the target into a desired state and the second pulse, i.e. the probe, is used to probe the state of the target at a subsequent time. The time between the two pulses is then scanned over the desired time range yielding results as a function of pump-to-probe time delay. This information is then used to deduce the dynamics of the process under study. For example, one can (i) use a pump laser pulse to ionize $H_2(X\,^1\Sigma_g^+,\ v=0)$ and launch a nuclear wavepacket on the $H_2^+(1s\sigma_g)$ PEC, (ii) use a probe pulse to ionize and dissociate the molecule, i.e. $H_2^+ \rightarrow H_2^{++} \rightarrow p^+ + p^+ + e^-$, at a later time, (iii) measure the fragments, i.e. protons, kinetic energy, (iv) use the kinetic energy from the Coulomb repulsion, i.e. Coulomb explosion imaging, to determine an internuclear distance at the time of the probe, and (v) use the data obtained over a range of delays to determine the nuclear dynamics of a molecule after exposure to a laser pulse. For an example of such a measurement see reference [39, 40, 97]. In general, this technique is applicable to any process for which one wishes to map the time-dependent dynamics.[17]

The pump-probe technique has been proven to be a powerful experimental technique that has revealed many interesting phenomena, e.g. see references [40, 97]. Nevertheless, the assumptions being used in this type of interpretation must be recognized. For example in the process outlined

[17] In some experimental setups, e.g. COLTRIMS, the electron momentum can also be measured.

above, one must estimate the launch time and vibrational composition of the nuclear wavepacket put onto the molecular ion potential by the pump pulse. Typically, the wavepacket is assumed to be (i) unaffected in its initial ground state by the pump pulse, (ii) launched at a given instant during the pump pulse when the intensity is high enough to facilitate $H_2 \rightarrow H_2^+(1s\sigma_g)$ transitions but low enough to make $H_2 \rightarrow H_2^+(2p\sigma_u)$ and $H_2 \rightarrow H_2^{++}$ negligible, and (iii) comprised of the vibrational states expected from a vertical or Franck-Condon transition from the ground vibrational and electronic state to the excited electronic state, e.g. the H_2 $X\,{}^1\Sigma_g^+$ v=0 state to a Franck-Condon vibrational population of the H_2^+ $1s\sigma$ state as shown in figure 2.2.[18] Assumption (i) is approximate as electric fields which are strong enough to ionize the neutral target, e.g. $H_2 + n\hbar\omega_{\text{pump}} \rightarrow H_2^+ + e^-$, may also have enough strength to deform the initial ground state potential and wavefunction. Assumption (ii) is also approximate in that the pump pulse has a probability to ionize the target on the rising and falling edges as well as the peak. Additionally, the vibrational population of the intermediate H_2^+ has been shown to be dependent on the laser pulse parameters and is thus only approximated by assumption (iii) [63–65]. The assumptions discussed above and the degree of uncertainty they produce will vary for different measurements. Regardless, however, pump-probe measurements allow one to *directly* measure the temporal evolution of a molecule on a sub-femtosecond time scale, which distinguishes it from other techniques. Furthermore, we plan to preform these types of experiments when we can achieve the experimental yield necessary to make the measurement time reasonable.

2.5 Crossing a laser with a molecular-ion beam

2.5.1 Introduction

In this section, the experimental apparatus and techniques used in our measurements presented in this dissertation will be discussed. The goal of our measurements is to determine the dynamics of ultrafast laser interactions with molecular ions. To this end, we produce and characterize (i) a molecular-ion target and (ii) an ultrafast laser pulse, (iii) detect the fragments resulting from the

[18] More recent calculations have taken some of these assumptions into account, e.g. [63–65, 98]. However, this makes the interpretation more complex.

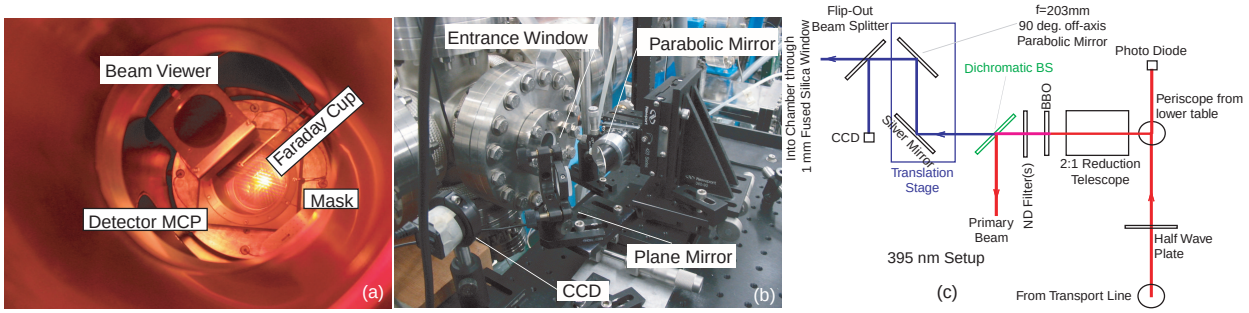

Figure 2.5: (a) A photograph of the inside of our detector chamber looking along the ion-beam path with major components marked. (b) A photograph of our 90° off-axis parabolic mirror setup with major components marked. (c) A schematic of the optics used after transport from the Kansas light source (KLS). See text and appendix A for details.

laser-molecule interaction, and (iv) use this information to reconstruct the dynamics of the laser-induced breakup. In addition to the brief discussion of these four topics in this section, a detailed and highly technical discussion has been relegated to appendices A, B, C, and D so that they are accessible to those who are interested and easily avoided by the more general audience. Additionally, this technique has been briefly outlined in several of our existing publications [36, 37, 52, 92–94, 96].

2.5.2 Molecular-ion beam

2.5.2.1 Production

All the measurements presented within this dissertation were performed using an electron cyclotron resonance (ECR) ion source,[19] which produces ions (both molecular and atomic) by electron impact ionization. This process involves a vertical transition and produces a Franck-Condon vibrational population[20] as shown in figure 2.2. The molecular ions are then accelerated by an electric field to an energy typically ranging from 5 – 11 keV in our measurements. The desired molecular species is then (i) magnetically selected, (ii) steered using electrostatics, and (iii) collimated using focusing ion optics and transverse confinement apertures (see appendix A.2 for details). Additionally, as the

[19]The detailed functionality of an ECR is beyond the scope of this dissertation and is described in multiple publications (see, for example, [99]), and thus will not be discussed here.

[20]Electron-impact ionization, such as that in an ECR source, can produce a vibrational population that slightly differs from the Franck-Condon population, especially for hot interaction conditions [100, 101]. Nevertheless, the population is generally very well approximated by the Franck-Condon factors.

ion beam is directed at the center of our detector, the beam is collected by a translatable 2 mm Faraday cup (FC) so that it is not incident upon the face of the position-sensitive detector. This is important as the ion beam would quickly damage the multi-channel plates of the detector and would also flood the electronics with counts obscuring the laser-induced molecular fragmentation.

This molecular-ion beam arrangement allows for the detection of all molecular fragments regardless of charge given that their transverse momentum is both (i) large enough to move them beyond the small 2 mm diameter translatable FC and (ii) small enough so that they do not fly beyond the outer edge of the 80 mm diameter detector. Neutral fragments are detectable in this setup because they retain the velocity of the molecular-ion beam after the laser-induced breakup and this velocity is sufficient to produce a signal on the detector. Furthermore, as both charged and neutral fragments are detected on the same detector, they are measured in the same absolute lab coordinate system. The technique used to transform these measured values into momentum components in the breakup frame will be discussed momentarily.

2.5.2.2 Characterization

To insure the ion beam is well collimated and collected by the FC, a removable "beam viewer"[21] is employed behind the FC and in front of the position-sensitive detector as shown in figure 2.5(a). This allows us to (i) image the intensity profile, i.e. transverse current density, of the molecular-ion beam when the FC is translated out of the ion beam's path and (ii) center the translatable FC along the ion beam's trajectory so as to minimize the number of scattered particles incident upon the beam viewer, thereby minimizing the scattered particle current on the position sensitive detector when the beam viewer is removed (see appendix A.2.3 for a detailed description of this procedure). During the actual collection of data, the FC is connected to a current meter so that measurements can be normalized to the target density, i.e. the beam current.

[21] What we call a beam viewer is a stack of two multi-channel plates in front of a phosphor screen, which is imaged by a CCD camera (see appendices A.2.2.4 and C.2.1 for details).

2.5.3 Ultrafast laser

2.5.3.1 Production

Now that the molecular-ion target has been produced, the ultrafast laser used to fragment the molecule is needed (see appendix A.3 for a detailed discussion). We use a Ti:Sapphire oscillator, stretcher, amplifier, and compressor (as detailed in recent publications [102–109]) housed inside the Kansas Light Source (KLS) facility within the J. R. Macdonald Laboratory (JRM) and operated by Prof. Zenghu Chang's research group. This laser produces 35 fs Fourier-Transform-Limited (FTL) pulses with a repetition rate of 1 kHz and $\leq$3 W of power at 790 nm.

The "basic" pulse is then either (i) transported via an evacuated transport line to the experiment or (ii) propagated through a gas-filled hollow-core fiber that can produce the frequency bandwidth necessary for $\lesssim$ 5 fs pulses and then transported in the same way. After transport to an optics table near the interaction point, the pulse can be further manipulated, e.g. temporal pulse width, polarization, frequency doubling, to produce the desired pulse in the interaction region as shown in figures 2.5(c) and A.7. If 395 nm light is desired the frequency is doubled using a non-linear second-harmonic generation crystal, namely a β-BaB_2O_4 (a.k.a. BBO) crystal. The polarization is controlled with half- and quarter-wave plates and chirp is compensated for with fused silica wedges or thin plates.

After the laser beam has been given the preferred polarization, frequency, and temporal profile, it needs to be focused on to the target molecular-ion beam to achieve the high intensities desired in our measurements, i.e. $I \lesssim 10^{16}$ W/cm^2. To do this we employ a 90° off-axis parabolic mirror with a focal length of 203 mm as shown in figure 2.5(b) and (c). The focusing mirror is positioned outside of the vacuum chamber to allow for easy adjustability.[22] Furthermore, this configuration allows us to easily *and directly* image our intensity distribution, as will be discussed in the next section. A disadvantage of this setup is that the focal length of the mirror must be greater than the vacuum chamber size, thereby restricting us to lower intensities than can be achieved utilizing

[22] In some of the measurements presented in this dissertation, i.e. those done before we began utilizing the parabolic mirror, we used a fused silica focusing lens, which introduces dispersion and aberrations to the pulse [110, 111]. Therefore, the reader will be informed when measurements were taken using the lens, which yields more uncertainty in pulse duration and intensity, especially for pulses where $\tau \lesssim 10$ fs.

a focusing mirror inside the vacuum. However, focusing mirrors placed inside the vacuum chamber are typically on-axis focusing mirrors, which require the unfocused laser beam to pass through the target before being focused onto the target, see for example reference [112]. This arrangement can cause problems if the unfocused laser beam is intense enough to significantly influence the state of the target. Additionally, in our setup, the laser must pass between rings of our spectrometer, which is discussed in appendix B.3, thus restricting the size and position of the incoming laser beam.

2.5.3.2 Characterization

The temporal and frequency profiles of 790 nm laser pulses are measured as a function of intensity using the frequency-resolved optical-gating (FROG) technique [113]; see figure A.8 for an example. In the case of the second-harmonic, one needs to determine the quantities using standard nonlinear optics [110, 111] as we do not have an apparatus to measure it directly.[23] The pulse duration of the second harmonic emerging from the BBO is

$$T_{2\omega} \simeq \frac{T_\omega}{\sqrt{2}}\sqrt{1+\frac{2\ln(2)}{3}\left(\frac{gL}{T_\omega}\right)^2}\,, \tag{2.3}$$

where $g \simeq 200$ fs/mm is the group velocity mismatch, T_ω is the pulse duration of the primary 790nm beam, and $L = 0.25$ mm is the thickness of the BBO crystal in our setup. Furthermore, the pulse duration of the second harmonic after dispersion is

$$T'_{2\omega} = T_{2\omega}\sqrt{1+\left(\frac{\alpha_{395}\ln(2)}{T_{2\omega}^2}\right)^2}\,, \tag{2.4}$$

where $T_{2\omega}$ is the Fourier-transform limited second-harmonic pulse directly out of the BBO, $\alpha_{395} = 49.6L_3$ is the second-order dispersion of the second harmonic after the BBO due to fused silica, and L_3 is the thickness of fused silica through which the second harmonic travels on its way to the interaction point in mm. This yields a minimum second-harmonic pulse duration of 47 fs in our setup.

The power of the laser (P) is measured with a power meter, the repetition rate (R) is measured

[23] The details of this calculation are shown in appendix A.3.3.2.

with a photodiode, and the temporal full width at half the maximum in intensity ($FWHM_I$) has been measured or calculated as discussed in a previous paragraph. Therefore, the final piece of information necessary to determine the spatiotemporal intensity profile of the laser pulse is the spatial focal profile. The spatial focal profile is measured with the same setup used to align the parabolic mirror, i.e. by using the beam splitter to create a path equivalent to the path to the molecular target, and imaging the focal profile with the CCD shown in figures 2.5(b), (c), A.9, and A.10.[24] Given this information and assuming that the laser pulse is well approximated by a Gaussian, the peak intensity is

$$I_0 \simeq 1.88 \frac{P/R}{\pi \omega_0^2 \tau} \ , \tag{2.5}$$

where P is the laser power, R is the repetition rate, ω_0 is the Gaussian beam waist (i.e. the radius using the $1/e^2$ criterion), and τ is the temporal FWHM in intensity (see appendix A.3.4.2 for a detailed calculation).

2.5.4 Beam overlap

Spatial Overlap Now that both the basic elements of, and the procedures used to tune and characterize, the laser and molecular-ion beams have been discussed, the last step needed is crossing the two beams. As shown in figure 2.6(a), the laser beam and molecular-ion beam should intersect at $\sim 90^\circ$ with the focus of the laser beam incident upon the center of the ion beam. This is done by measuring the laser-induced ionization and dissociation rates while manipulating the laser focal position by translating the 90° off-axis parabolic mirror perpendicular to the ion-beam in the vertical direction as detailed in appendix A.4. Additionally, the focal- or z-position is also determined by recording the laser-induced ionization and dissociation rates as a function of z-translation. The z-scan will create a symmetric distribution about the focal point, i.e. z=0, as the focal profile is roughly symmetric in z.

[24] Aligning the 90° off-axis parabolic mirror to create a Gaussian focal profile is a non-trivial and is detailed in appendix A.3.4.1.

Chirp In addition to overlapping the two beams, one needs to consider the temporal shape of the pulse at this point in space. For ultrashort pulses, i.e. $\lesssim 10$ fs, a small dispersion, i.e. an error in the balancing between positive chirp due to fused silica optics and negative chirp introduced by chirped mirrors, will produce a significant temporal broadening of the pulse. Thus, the frequency-resolved optical gating (FROG) [113] measurement taken before our evacuated transport line, as shown in figure A.8, may not be accurate for the laser pulse at the interaction point. Furthermore, due to the low counting rate of our experiment, which is typically less than 10 Hz, it is impractical to look at the effects of compensation fused silica for many points. Therefore, using the molecular-ion beam laser interaction as the measure for the fine chirp compensation is not practical. To determine the optimum amount of chirp compensation fused silica quickly and accurately, we use the above-threshold ionization (ATI) yield of the residual gas in the vacuum chamber. This yield is recorded as a function of chirp compensation and the strong dependence on peak intensity for ATI processes is well established (e.g. [114]). Thus, one can determine the amount of glass needed to produce the shortest pulse very accurately (typically to better than 0.2 mm of fused silica) and quickly.

2.5.5 Distinction and detection of particles

As detailed in appendix B, we use a longitudinal spectrometer, coincidence time- and position-detection of molecular fragments, and a molecular-dissociation imaging technique to enable our measurements [36–38, 52, 92–96]. These measurements are done in "event mode", which is to say that the measured quantities, i.e. the impact position and time of each particle hit on the detector, are gathered and recorded for each and every laser pulse and that the information gathered for any and all individual laser pulses can be distinguished from all others.[25] This is an important aspect of our measurements as it allows for the collection of information which is typically lost in "time integrated measurement", i.e. measurements in which the correlation between all signals of each event is not recorded.

Additionally, since the initial beam velocity allows us to detect both charged and neutral par-

[25] The event mode technique is enabled by the electronics discussed in appendix C and employed in all our measurements.

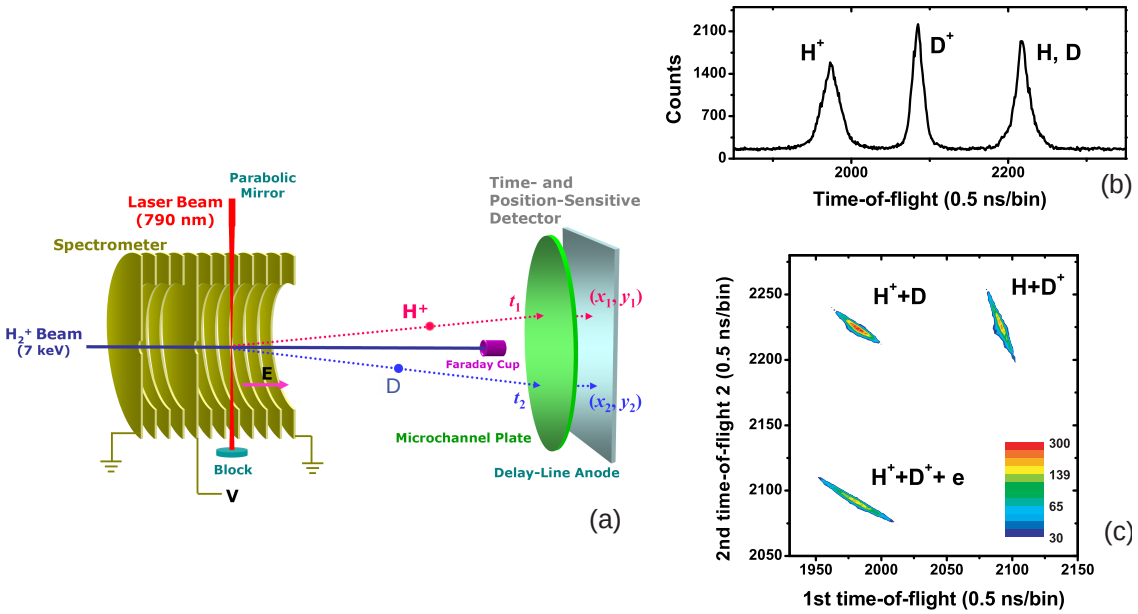

Figure 2.6: (a) Cross-section of laser-molecular ion beam interaction region in our setup. (Figure adapted from reference [36].) (b) Time-of-flight measurement for HD^+. (c) Coincidence time-of-flight measurement for HD^+ illustrating the detection and separation of various dissociation channels.

ticles, it is advantageous to separate particles with different charges and/or masses in time so that each particular fragmentation channel is easily distinguishable. For example, if an intense laser is incident upon HD^+, one expects and wants to separate the three fragmentation channels — (i) $H + d^+$, (ii) $p^+ + D$, or (iii) $p^+ + d^+$. This is achieved in our setup by the time-of-flight (TOF) spectrometer shown in 2.6(a), which creates an electric field parallel to the ion beam in the laser-molecule interaction region. This field provides different acceleration to particles with different mass-to-charge (m/q) ratios, thus separating different fragmentation channels in the coincidence TOF measurement (see for example a typical coincidence TOF spectrum for HD^+ in figure 2.6(b)). This setup allow us to measure all fragmentation channels from a single target at the same time, which gives us highly accurate information concerning the relative yield of each channel, as all channels are measured simultaneously.

2.5.6 Momentum imaging

At this point, the fragmentation channels are separated and the position and time information for all fragments resulting from each laser-molecular ion interaction are associated with the appropriate laser pulse.[26] However, we wish to know the three-dimensional momentum components of the fragments in the molecule center-of-mass frame. To this end, we use a momentum imaging technique to determine the molecular break-up conditions from the measured time and position information. As this method is described in great detailed in appendix B, it will suffice to say that, given our knowledge of the experimental geometry, the measured quantities contain enough information to determine the desired three-dimensional momentum image of each fragmentation event. In other words, the momentum vectors in the molecule center-of-mass frame can be written as functions of the measured values of positions and time.[27]

2.6 Focused Gaussian beam properties

When describing intense short pulse laser interactions, the laser pulse is typically described with three quantities — the peak intensity I_0, the pulse duration τ, and the central wavelength λ, e.g. a $I_0 = 10^{14}$ W/cm^2, $\tau = 35$ fs, $\lambda = 790$ nm Ti:Sapphire pulse. However, this does not tell the entire story. In fact, the results from a single measurement with a given set of the three parameters given above can be quite deceiving due to several effects. This section will focus on these effects in an effort to alert the reader to *hidden* effects which may be taking place and to explain what efforts we have taken to minimize these effects.

[26] Not all laser-molecular ion interactions are measured, as the probability to detect a particle hitting the delay-line detector is 30%. However, experimental conditions are tailored so that the detection probability for all fragments is roughly equal. Additionally, we have developed a method for using the measurement itself to address this insidious problem and determine the absolute detection efficiency for each particle as a function of position on the detector [93].

[27] The TOF for each fragment is measured with respect to a photodiode signal induced by the laser pulse. Thus, the *absolute* TOF, i.e. the time it takes the particle to reach the detector starting from the laser-molecule interaction instant, not just the *relative* TOF, i.e. difference in TOF between the break-up fragments, is measured. The details of this technique along with the electronics and experimental setup used to enable it are discussed in appendices A – C.

2.6.1 Intensity-volume effect

First, there will be a brief discussion of the intensity-volume effect, which is detailed in several of our previous publications, e.g. [37, 52, 94, 96], and references therein. An ideal focused Gaussian laser beam [110] has the intensity distribution

$$I(\rho, z) = \frac{I_0}{1 + z^2/z_r^2} \exp\left[-\frac{2\rho^2}{\omega_0^2(1 + z^2/z_r^2)}\right] \tag{2.6}$$

in cylindrical coordinates with $(\rho, z) = (0, 0)$ defined as the focal point, where I_0 is the peak intensity, z_r is the Rayleigh range, ω_0 is the beam waist at the focus, and the beam waist at z is

$$\omega(z) = \omega_0 \sqrt{1 + z^2/z_r^2} \ .$$

The techniques we use to measure these quantities are detailed in appendix A.3.2. The number of particles, N, subject to an intensity within the range (I_1 to I_2) can be expressed as

$$N = \int_{I_1}^{I_2} \xi d^3r = 2\pi\xi \int_{z_{min}}^{z_{max}} \int_{\rho(I_1,z)}^{\rho(I_2,z)} \rho \, d\rho \, dz \ ,$$

where ξ is the density of particles, which is assumed to be uniform. In addition, z_{min} and z_{max} are the minimum and maximum values of z at which the intensity range between I_1 and I_2 acts upon the target, respectively. Furthermore, these values can be assumed to be the extent or bounds of the target in z if the target thickness is very small compared to the focused laser's Rayleigh range. Thus, for all parts of the target-space, other than the point where $\rho = 0 = z$, the maximum intensity felt by the target will be less than I_0 and dependent upon ρ and z, as shown in figure 2.7(a). In other words, the focused laser beam will produce volumes with peak intensities from zero to I_0 and the intensity-volume effect must be taken into account to accurately determine the intensity dependence of a process.

2.6.1.1 Intensity-difference spectrum (IDS)

Due to the intensity-volume effect, it is difficult to compare experimental data, which have contributions from a range of intensities, to theoretical predictions without convoluting the calculations

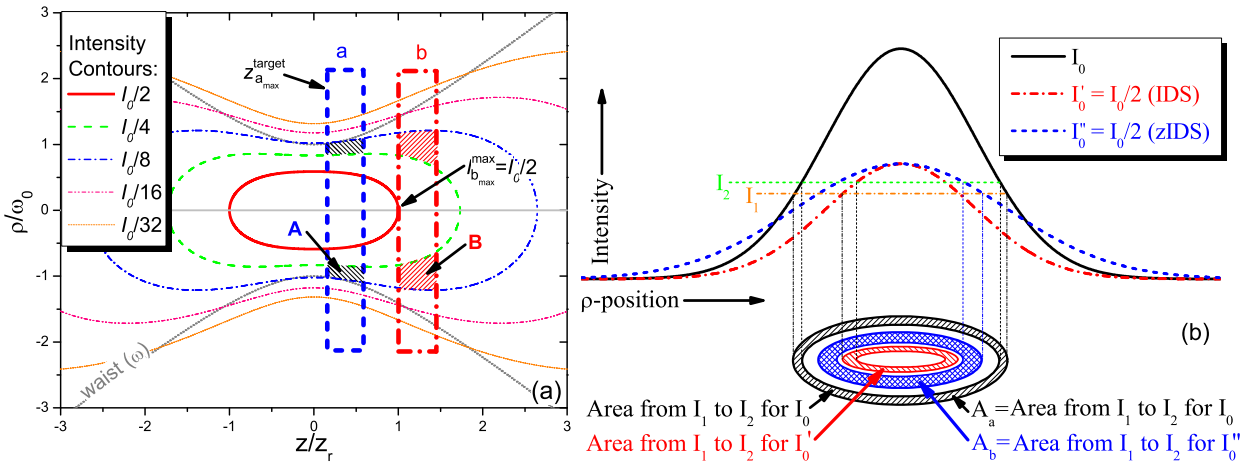

Figure 2.7: (a) Intensity profile of a focused Gaussian laser beam [110]. (b) A schematic illustrating IDS (left) and zIDS (right) subtraction. I_0 is the maximum intensity distribution and $I_0' = I_0/2$ for a 50% attenuated beam. I_0'' has a width $\sqrt{2}$ larger than I_0 and the same area under the curve as I_0, which one would expect from moving the focal point off the target in z by z_r. Note that the area between I_1 and I_2 (indicated by the hatched circles) is the same for both I_0 and I_0' and the area between I_1 and I_2 (indicated by the crosshatched circle) for I_0'' is twice as much. This is true for any and all intensity slices below the maximum value of I_0'' or I_0' as discussed in the text. (Figures adapted from references [94, 96].)

with the experimental intensity distribution [52, 115–117]. Experimentalists have also addressed the intensity volume effect in an effort to make experimental data more directly comparable with calculations by partially limiting the intensity volume. This is accomplished by either (i) making the target effectively one-dimensional (1D) with respect to the laser focus, e.g. by tightly collimating an ion-beam target [84, 87], (ii) reducing the interaction volume, e.g. in cold target recoil ion momentum spectroscopy (COLTRIMS) measurements [88, 118], such as those described in an excellent review by Ullrich *et al.* [119], or (iii) by selectively detecting a small part of a larger target with a pin-hole aperture, e.g. [120]. Combining this volume reduction with measurements at successive intensities, as is done in the intensity-selective scanning (ISS) method developed by Hansch and Van Woerkom [121], allows one to better discern intensity dependent trends. In the ISS method, an inversion algorithm is used to obtain the underlying intensity dependence [122, 123], for example, from a differential measurement of the focal volume.

We developed the intensity-difference spectrum (IDS) method [96] so that one could experi-

mentally determine the effects of a chosen intensity range by *eliminating all contributions from outside that range*. IDS is based upon the idea of taking the difference between two measurements, which are performed under identical conditions except using different peak intensities, and it has proved effective in short pulse laser experiments [37, 52]. In the IDS method [96], one does not vary the focal position with respect to the target. Rather, the intensity of the beam is changed by attenuating the laser beam. In cases where the target can be assumed to be infinitely thin and wide with respect to the laser beam, as is required in the IDS case, the number of target particles N exposed to a particular intensity range is simply proportional to the area within a ring bounded by the desired intensity limits of the two-dimensional Gaussian profile, as shown in figure 2.7(b). For a laser attenuated by β, the resulting laser profile, $I'(\rho, z)$, will be identical to the original, $I(\rho, z)$, with the inclusion of an attenuation factor, i.e. $I'(\rho, z) = \beta I(\rho, z)$. Therefore, the aforementioned areas for I and I' will be identical for all intensities below I'_{max}.

Thus, the total yields of two measurements, M_A and M_B, in which only the peak intensity is different, can be subtracted from one another to remove all contributions from intensities outside of the desired intensity range. In other words, only contributions from the intensities between the maximum intensities of the two measurements, I_A^{max} and I_B^{max}, will remain if the IDS technique is used. Explicitly, the measured contribution from intensities between I_A^{max} and I_B^{max}, where $I_A^{max} > I_B^{max}$, can be written as

$$M_{B\to A} = M_A - \alpha \cdot M_B \ , \tag{2.7}$$

where $\alpha = n_A \xi_A / n_B \xi_B$, n_X is the number of laser pulses, and ξ_X is the target density in measurement X. More explicitly, the IDS method allows one to determine the contributions from a particular intensity range when the target is (i) much thinner than the Rayleigh range in the laser z-dimension ($\Delta z_{target} \ll z_r$), (ii) much wider than the laser waist in the laser ρ-dimension ($\rho_{target} \gg \omega$), and (iii) the target density is uniform (ξ = constant).[28]

[28] It is important to note that the method is also applicable when the target density is not exactly uniform as long as the density gradient is small on the scale of the laser spot size. For example, the density of a super sonic jet with a 1 mm FWHM Gaussian density profile, which is typical in many setups, will change only slightly within a laser beam tightly focused to a waist of about 25 μm. The method is therefore applicable in many cases, at least approximately.

2.6.1.2 z-scanning intensity-difference spectrum

Now let us consider the case in which the laser intensity is changed by varying the focal position, z, with respect to the target instead of attenuating the laser beam. At this point it will be assumed, as was the case for IDS, that the uniform-density target is very thin, i.e. $\Delta z \ll z_r$. In this thin target case,

$$N = 2\pi\Delta z \int_{\rho(I_1,\overline{z})}^{\rho(I_2,\overline{z})} \xi\rho d\rho = \pi\xi\Delta z\rho^2\Big|_{\rho(I_1,\overline{z})}^{\rho(I_2,\overline{z})},$$

where $\overline{z}$ is the distance from the target mid-plane to the laser focus. Therefore, by evaluating the definition of $I(\rho, z)$ and inserting it into the above equation, the number of particles in the interaction region is determined to be

$$N_{\overline{z}} \equiv N(z=\overline{z}) = \pi\xi\Delta z\frac{\omega_0^2}{2}\left(1+\overline{z}^2/z_r^2\right)\ln\left[\frac{I_1}{I_2}\right],$$

for a target at a distance $\overline{z}$ from the focus. Thus, using the definition of the beam waist $\omega(z)$, the ratio of the number of particles subject to the intensity range in question at two different off-focus distances, denoted as $z=\overline{a}$ and $\overline{b}$, is found to be

$$R'_{ab} \equiv \frac{N_{\overline{a}}}{N_{\overline{b}}} = \frac{z_r^2+\overline{a}^2}{z_r^2+\overline{b}^2} = \frac{\omega_a^2}{\omega_b^2},$$

where $\omega_a \equiv \omega(z=\overline{a})$. This relation is also illustrated in figure 2.7(b) where the number of particles subject to a given intensity range, N, is proportional to the area, A, within the ring bound by that intensity range, i.e. $R'_{ab} = A_a/A_b = \omega_a^2/\omega_b^2$.

Integrating both measurements from zero up to the lower peak intensity, I_b^{max}, will yield the same number of counts from the same intensities if measurement b, M_b, is scaled by R'_{ab}. This is because R'_{ab} is independent of which intensity slice is being considered, i.e. independent of I_1 and I_2, and $N_{\overline{b}}R'_{ab} = N_{\overline{a}}$ by definition. The subtraction of the two measurements after proper scaling of the lower peak intensity measurement, thus eliminates all contributions from intensities below I_b^{max} and yields the desired intensity difference spectrum, i.e. counts originating only from

intensities between I_b^{max} and I_a^{max}. In other words,

$$M_{b\to a} = M_a - \alpha \cdot R'_{ab} \cdot M_b \ , \tag{2.8}$$

where α (defined following equation 2.7), which was dropped for simplicity, has been reintroduced here for generality. To reiterate, for thin targets with uniform density subject to a Gaussian laser beam, the contribution of measured events from a particular intensity slice can be determined by subtracting measurements at two different focal positions from one another using equation 2.8.

In practice, one would take a series of measurements at various z-positions. Then subtraction of any two measurements with the proper zIDS ratio will result in a yield that has no contribution from intensities below the maximum intensity of the lower intensity measurement or above the maximum intensity of the higher intensity measurement. Furthermore, the counts remaining after a subtraction will decrease with the width of the intensity slice. Thus, achieving fine intensity dependence by taking a series of thin slices requires increased statistics. Therefore, an important benefit of the zIDS method is an increase in count rate as compared to IDS measurements for all intensities below the maximum focal spot intensity. Additionally, the zIDS method also allows one to continuously vary the intensity range of interest while only intensities corresponding to one's laser attenuation optics can be achieved using IDS. This is because the z-position can be varied over a range and with a precision determined by one's micrometer. However, there will be a small additional uncertainty in determining the precise intensity range associated with the zIDS method due to the uncertainty in z-position.

The zIDS method is also easily applicable to ultrashort, e.g. < 10 fs, laser pulses since it does not require laser power attenuation. Decreasing the power with standard optics (e.g. a variable neutral density filter or a polarizer and half-wave plate pair) is difficult because (i) the optics used must support the large frequency range of the ultrashort pulse, (ii) the dispersion of the attenuation optics must be counteracted (e.g. negative-chirp mirrors employed to cancel out the chirp of fused silica), and (iii) the optics used must have a negligible change in dispersion over the attenuation

range.[29] Additionally, this method can also be extended to thick targets where $\Delta z_{target} \sim z_r$ as shown in figure 2.7(a). For a thick target, one finds that the weighting ratio changes slightly from the thin target case to

$$\mathcal{R}_{ab} = \frac{(\omega_{a_{min}^{target}})^2 + \omega_0^2(\frac{1}{3}\Delta z_{target}^2 + a_{min}^{target}\Delta z_{target})/z_r^2}{(\omega_{b_{min}^{target}})^2 + \omega_0^2(\frac{1}{3}\Delta z_{target}^2 + b_{min}^{target}\Delta z_{target})/z_r^2} , \tag{2.9}$$

where Δz is the target thickness and a_{min}^{target} is z_{min}^{target} (with a similar definition for b_{min}^{target}). As one can see, having a thick target slightly complicates the zIDS subtraction and detailed examples of its application are discussed in our previous work [94].

2.6.2 Temporal pulse evolution

2.6.2.1 Intensity pulse envelope

In addition to the spatial laser intensity profile, the laser pulse also has a temporal intensity profile, i.e. $\mathbf{I}(\rho, z, t) = I(\rho, z)\mathcal{I}(t)$, where $I(\rho, z)$ is the spatial profile described in equation 2.6 and $\mathcal{I}(t)$ is the temporal intensity profile. In this dissertation and generally in ultrashort laser work, $\mathcal{I}(t)$ is assumed to be a Gaussian and of a temporal width corresponding to the Fourier transform of the frequency profile, a.k.a. the Fourier transform limited (FTL) pulse, *unless explicitly stated otherwise*. Cases in which the pulse shape does deviate from these assumptions will be discussed momentarily. For now, letting the aforementioned assumptions be true yields the pulse seen in figure 2.8(a). Namely,

$$\mathbf{I}(\rho, z, t) = \frac{I_0}{1 + z^2/z_r^2} \exp\left[-\frac{2\rho^2}{\omega_0^2(1 + z^2/z_r^2)}\right]\mathcal{I}(t) = I(\rho, z)\exp\left(-\frac{t^2}{2\sigma^2}\right) = I(\rho, z)\exp\left(-\frac{4\ln(2)t^2}{\tau^2}\right) , \tag{2.10}$$

where $I(\rho, z)$ is expressed in equation 2.6, σ is the standard deviation, and τ is the temporal full-width at half-maximum (FWHM) of the laser pulse in intensity and corresponds to the FTL

[29] This is not of concern when the change in pulse shape is negligible in comparison to the original shape (e.g. a 790 nm 45 fs Fourier-transform-limited pulse going through a 1 mm fused silica beam splitter will emerge with less than a 1% increase in width). However, if one wishes to use ultrashort pulses, the dispersion is no longer negligible (e.g. a 790 nm 8 fs Fourier-transform-limited pulse will emerge from a 1 mm fused silica beam splitter with a width of almost 15 fs along with pre- and post-pulses). Therefore, the zIDS method, which requires no attenuating optics, is preferable to and more accurate than the IDS method when using ultrashort pulses.

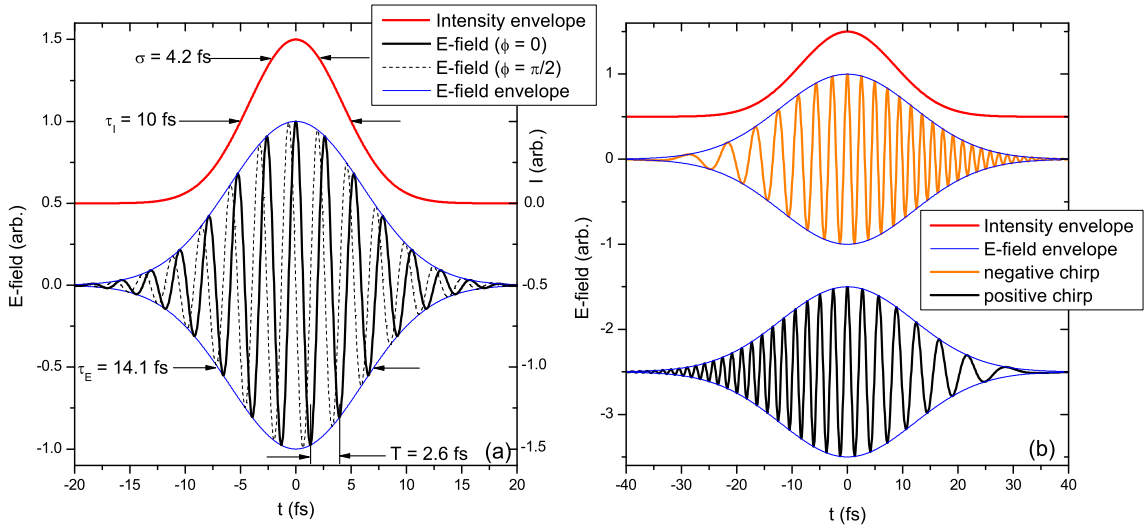

Figure 2.8: (a) Intensity envelope and electric field for a τ=10 fs Fourier transform limited 790 nm laser pulse given at different carrier envelope phases, ϕ_{CEP}. Note that τ and σ are marked for the intensity envelope and that they differ from those for the electric-field envelope. The period T for this 790 nm pulse is also marked. (b) A schematic of a positively (top) and a negatively (bottom) chirped pulse of the same width τ=20.

pulse. Thus, τ and I_0 uniquely characterize a FTL laser pulse envelope at a given point (ρ, z). However, it is important to remember that the effect under study may not be dependent directly upon these parameters. For example, the process under examination may depend upon the slope of the intensity envelope, $d\mathbf{I}/dt$. Therefore, when we describe the laser pulse with τ and I_0 it is to uniquely describe the pulse being used and not to imply that the measured results are directly dependent upon these quantities.

2.6.2.2 Electric field time dependence

CEP So far the laser pulse was described entirely in terms of its intensity profile, but there is, of course, more to the story — the electric field.[30] For the FTL pulse, the electric field is simply

$$E(\rho, z, t, \omega, \phi_{\text{CEP}}) = \sqrt{\frac{2\mathbf{I}(\rho, z, t)}{c\epsilon_0}} \cos(\omega t + \phi_{\text{CEP}}) \ , \tag{2.11}$$

[30]In this dissertation there will be no mention of the magnetic field of the laser pulse as even at our maximum intensities, i.e. $\lesssim 10^{16}$ W/cm^2, the effect of the magnetic field is negligible. For example, if the laser intensity is 10^{16} W/cm^2, then the maximum electric field, F_E, is $F_E = 0.5$ au $= 2.7 \times 10^{11}$ V/m where as the maximum magnetic field is $F_B = F_E/c = 4 \times 10^{-3}$ au $= 9.2 \times 10^2$ Tesla.

where $c \simeq 2.997 \times 10^8$ m/s is the speed of light, $\epsilon_0 \simeq 8.85 \times 10^{-12}$ $C^2N^{-1}m^{-2}$ is the electric permittivity in vacuum, ω is the laser's angular frequency ($\omega = 2.4 \times 10^{15}$ Hz for 790 nm light), and ϕ_{CEP} is the carrier envelope phase (CEP). For long pulses where there are many laser periods, T, in the intensity envelope, i.e. $\tau \gg T$, the CEP is inconsequential as the maximum electric field strength varies very slowly from one cycle to the next. However, when dealing with short, i.e. few-cycle, pulses as shown in figure 2.8(a), the CEP can play a significant role.[31] In this dissertation, *unless explicitly stated otherwise*, we use laser pulses with random CEP. This is to say, the CEP from one pulse to the next is allowed to vary freely, and over the course of a measurement, which is typically comprised of a few million laser shots, the CEP distribution is uniform.

Chirp The FTL pulse is, of course, the pulse with the shortest possible temporal duration. However, the pulse can be "stretched" in time by introducing dispersion [110]. For now only second-order group-velocity dispersion, i.e. chirp, will be considered. Standard optical materials, e.g. fused silica, introduce a positive chirp while some specially designed optics, e.g. chirped mirrors or prism pairs, can produce negative chirp. If a pulse has a positive or negative chirp, then different frequency components will arrive at different times, i.e. with positive chirp redder low-frequency components arrive before the bluer high-frequency components and the opposite for negative chirp as shown in figure 2.8(b). This temporal arrangement of frequencies can affect the experimental yield of a process, e.g. a sequential process requiring high energy photons for a preliminary step and lower energy photons for a secondary step is more likely given a negatively chirped pulse (e.g. [127]). In general, we attempt to limit the pulse duration to the FTL as discussed in appendix A.4.2. However, if chirp is intentionally introduced, it will be explicitly stated and quantified.

Polarization In addition to changing the frequency of the electric field of a laser pulse, one can also manipulate the polarization of the laser pulse. In our experiments we use only linear and

[31] CEP effects have been a hot topic for a few years now and have been the subject of a great deal of interesting experimental and theoretical work, e.g. [3, 54, 103–105, 107, 109, 124–126].

circular polarization.[32] In the case of circular polarization, the form of the electric field deviates slightly from the linear case above yielding

$$E_{\text{circular}}(\rho, z, t, \omega, \phi_{\text{CEP}}) = \left[\sqrt{\frac{2\mathbf{I}(\rho, z, t)}{c\epsilon_0}}\cos(\omega t + \phi_{\text{CEP}})\right]\left[\sin(\omega t + \phi_{\text{pol}})\widehat{x} + \cos(\omega t + \phi_{\text{pol}})\widehat{y}\right], \quad (2.12)$$

where ϕ_{pol} is the polarization phase. Note, however, that I_0 is now a factor of 2 less than that measured in equation 2.5, as the absolute value of the electric field $|E|$ is no longer modulated by a sine wave. In other words, if one uses a laser pulse with the same power and spatiotemporal properties, the maximum electric field in the circular case is less by $\sqrt{2}$, i.e. $E_{\text{max}}^{\text{linear}} = \sqrt{2}E_{\text{max}}^{\text{circular}}$ [110].

Pulse shaping In addition to the elementary laser pulse shape variations we use, i.e. intensity I_0, pulse width τ, and linear/circular polarization, there are much more complex ways to shape the pulse [128, 129]. In these pulse-shaping measurements one has much greater control of the electric field as a function of time [130]. This superior control means that there are more parameters and correspondingly a much larger parameter space to explore. This large space makes determining the dependence of a process on all the parameters virtually impossible. Thus, pulse-shaping measurements typically employ genetic algorithms [131–133] to maximize some desired result, e.g. dissociation. However, it is most often quite difficult, if not impossible, to coax a physical picture out of the process in question in this manner. Therefore, we have decided to limit our parameter space, for the time being, to those dimensions discussed above so that a physical interpretation of the measurements is more apparent.

[32] For broad frequency bandwidth laser pulses, the quarter wave-plate used to convert the linear pulse into a circular pulse does introduce some frequency-dependent ellipticity. However, we typically use circular polarization for qualitative comparison to linear polarization, e.g. to determine the effect of rescattering, and therefore are not bothered by the deviation from a true circularly polarized pulse.

Chapter 3

Hydrogenic Diatomic Molecular Ions

3.1 Introduction

As we are trying to understand the dynamics of molecules in intense ultrashort laser fields, it makes sense to start by examining the *simplest* molecule, i.e. the one with the fewest constituents. This is the hydrogen molecular ion, H_2^+, and its isotopes, D_2^+ and HD^+. As the simplest molecule in nature, H_2^+ plays a fundamental role in theoretical and experimental investigation of the interaction between intense laser fields and molecules. In recent years there have been numerous theoretical explorations of H_2^+ exposed to intense laser fields, e.g. references [9, 19, 24–28], as well as several excellent reviews, e.g. references [8, 33]. Current laser technology produces intense fields comparable to the internal Coulomb field of the molecule that activate various interesting phenomena, among which are bond softening [10–12], vibrational trapping [20, 29, 30], above threshold dissociation [13, 21, 31], zero-photon dissociation [14, 15], charge resonance enhanced ionization [16, 17], laser-induced alignment [18, 22, 23], and high-harmonic generation (HHG) [1, 32]. In an intense laser field the original electronic and nuclear motions of the molecule are distorted. Both theoretical and experimental studies have found that the intense-field phenomena are sensitive to the characteristics of the laser pulse, such as the peak intensity, wavelength, pulse duration, and shape [26, 34, 134].

Experimental investigation of the various intense-field phenomena in H_2^+ is of current interest. However, due to the obvious experimental difficulties involving studies of ion beams, most of the experiments have actually been performed using neutral H_2 as the target, e.g. references [10–

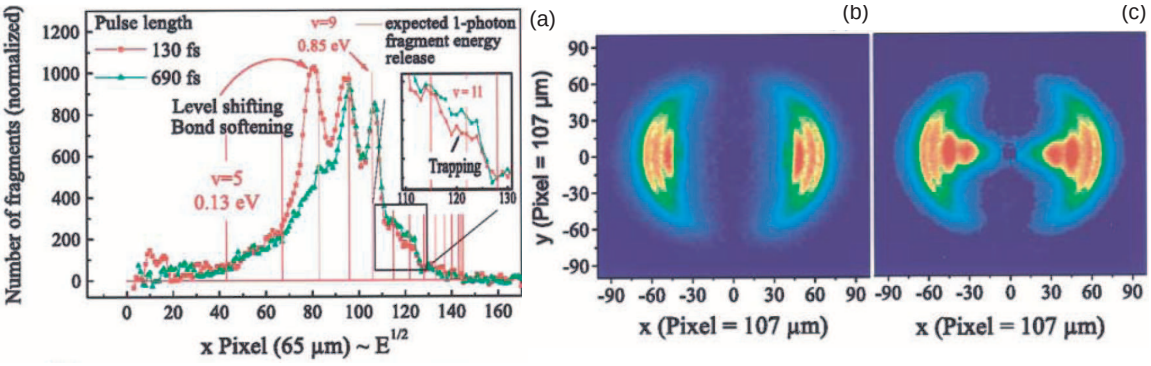

Figure 3.1: Experimental results of Figger, Hänsch, *et al.* [84] for dissociation of H_2^+. (Figure adapted from reference [84].) (a) Cut through the two-dimensional momentum projection of fragments at $y = 0$ for $\lambda = 785$ nm, $I_0 = 2.5 \times 10^{13}$ W/cm^2 pulses. (b) and (c) Two-dimensional momentum projection of neutral photofragments at a pulse energy of 1.0 mJ and a wavelength of 785 nm. (b) $\tau = 575$ fs, $I_0 = 3.5 \times 10^{13}$ W/cm^2. (c) $\tau = 135$ fs, $I_0 = 1.5 \times 10^{14}$ W/cm^2. (Figures adapted from reference [84].)

12, 14, 34, 41, 135, 136]. In these experiments, the H_2 molecule is ionized and then the daughter H_2^+ ion interacts with the light field within the same laser pulse. The major differences between neutral molecule and molecular ion studies were outlined in section 2.2 earlier. Previously, there were only a couple of groups that experimentally explored intense laser-molecule interactions using H_2^+ ion beams. Both of these groups employ intense femtosecond Ti:sapphire laser pulses at 790 nm to study the processes of laser-induced dissociation and ionization of H_2^+. Williams *et al.* [82, 91] produced an H_2^+ beam using a plasma discharge ion source. In their experiment, the kinetic energy release (KER) distribution of the H^+ fragment was measured by combining an electrostatic energy analyzer and time-of-flight (TOF) analysis. The KER distribution of the H fragment was measured separately from the TOF spectrum of H using a laser polarization along the beam direction. Hänsch and co-workers [81, 84–86] used a similar H_2^+ ion source. In their experiment, either the neutral fragment H or both H^+ and H fragments were projected onto a microchannel plate with a phosphor anode whose 2D image was recorded by a high resolution CCD camera as shown in figure 3.1. The initial 3D momentum distribution of the photofragments was reconstructed by an inverse Abel transform of the CCD image, taking advantage of the cylindrical symmetry of the molecular breakup when linearly polarized light is used.

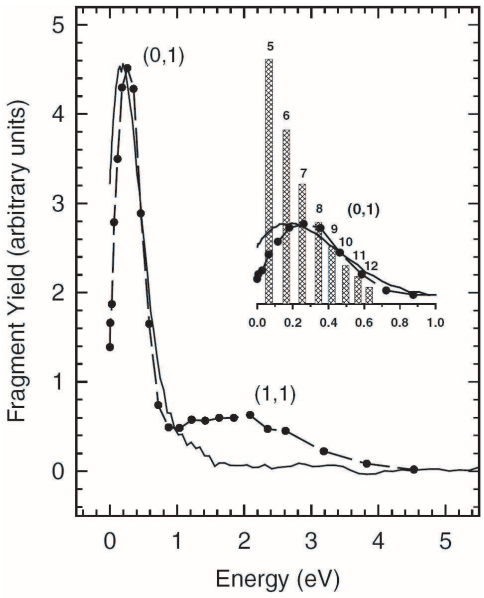

Figure 3.2: Experimental results of Williams *et al.* [82, 91] for 65 fs, $\lambda = 790$ nm, $I_0 = 3 \times 10^{15}$ W/cm^2 dissociation and ionization of H_2^+. The line represents the H atom KER spectrum and the dots represents the proton KER spectrum with a dashed curve drawn through the experimental points to guide the eye. For ease of display the (0,1) dissociation peaks have been normalized to the same peak height. The inset shows the dissociation peak on an expanded energy scale with the predicted fragment energies expected from a FranckCondon vibrational distribution of the H_2^+ ion displayed as vertical bars. The height of the bar represents the population of the particular vibrational state, normalized to the dissociation curves for v=9. (Figures adapted from reference [82].)

In the above-mentioned experiments, dissociation was clearly separated from ionization in the spectrum of neutral fragments, as ionization produces no neutral fragments. However, since both ionization and dissociation produce charged fragments, ionization is harder to isolate. This is because the H^+ spectrum measured by Williams *et al.* [82, 91] and the accumulated H^+ and H spectra measured by Pavičić *et al.* [84, 86] include a significant contribution from the dissociation channel. A complete distinction between the dissociation and ionization processes is therefore difficult. As Williams' experiment shows in figure 3.2, the KER spectrum of the proton from the ionization overlaps with that from the dissociation (especially in the region around 1 eV of energy). Although in both experiments one may obtain the abundance of the ionization channel by subtracting the spectrum of H from that of H^+, this method has some drawbacks. First, this is only accurate when there is substantial ionization compared to dissociation in the KER range of interest. Therefore, it cannot be applied near the ionization appearance intensity. Second, since the H fragments to be subtracted have to be measured in a separate experiment, this method demands a high reproducibility of the experimental conditions, which is not easy in such measurements. To solve this problem, a coincidence measurement of the fragments from each dissociation or ionization event is required. This is precisely the type of measurement presented in this dissertation.

In this chapter we report the experimental study of laser-induced dissociation and ionization

of H_2^+ in an intense femtosecond laser field through a coincidence 3D momentum imaging method. First, measurements of H_2^+ dissociation using intense 135, 45, and 7 fs pulses at 790 nm will be discussed and compared. Additionally, the measured H_2^+ dissociation distributions will be compared to both the Floquet picture discussed in section 1.4 and calculations which solve the time-dependent Schrödinger equation in the Born-Oppenheimer representation [137]. Second, measurements of H_2^+ ionization using intense ultrashort pulses will be discussed and compared to the predictions of the widely used charge-resonance enhanced ionization model (CREI) [16]. Third, we will present an alternative model to understand the observed H_2^+ KER and angular ionization distributions (in particular near the ionization appearance threshold).[33]

3.2 Dissociation of H_2^+

3.2.1 Long pulse (135 fs, 790 nm)[34]

In this section, we will start by making use of the simplified Floquet picture presented in section 1.4 to make some qualitative predictions about what type of behavior one should expect for H_2^+ laser-induced dissociation due to a $\lambda = 790$ nm, $I_0 \lesssim 10^{14}$ W/cm^2, $w = 135$ fs pulse. Then the measured data for a series of intensities at this pulse duration and wavelength will be presented and compared to the aforementioned predictions. Finally, we will use the information gained from solving the time-dependent Schrödinger equation by expanding on the Born-Oppenheimer electronic states [137] to help understand the observed features of the experimental spectra. Additionally, the techniques we use to present and interpret our data will be introduced as the need arises, thereby setting the foundation for subsequent discussions.

3.2.1.1 Predictions using the simplified Floquet picture

Distinct vibrational levels First, as the typical vibrational period of H_2^+, i.e. ~ 14 fs, is much shorter than the laser pulse, one can roughly assume that the dressed Born-Oppenheimer potential energy curves (PECs) change roughly adiabatically. In other words, the intensity envelope of

[33] Some of the results have been previously reported in our published work [36, 38, 42, 52, 92, 94–96, 138, 139].
[34] Much of the work in this section has been previously reported in our publications [36, 52, 92, 95, 96].

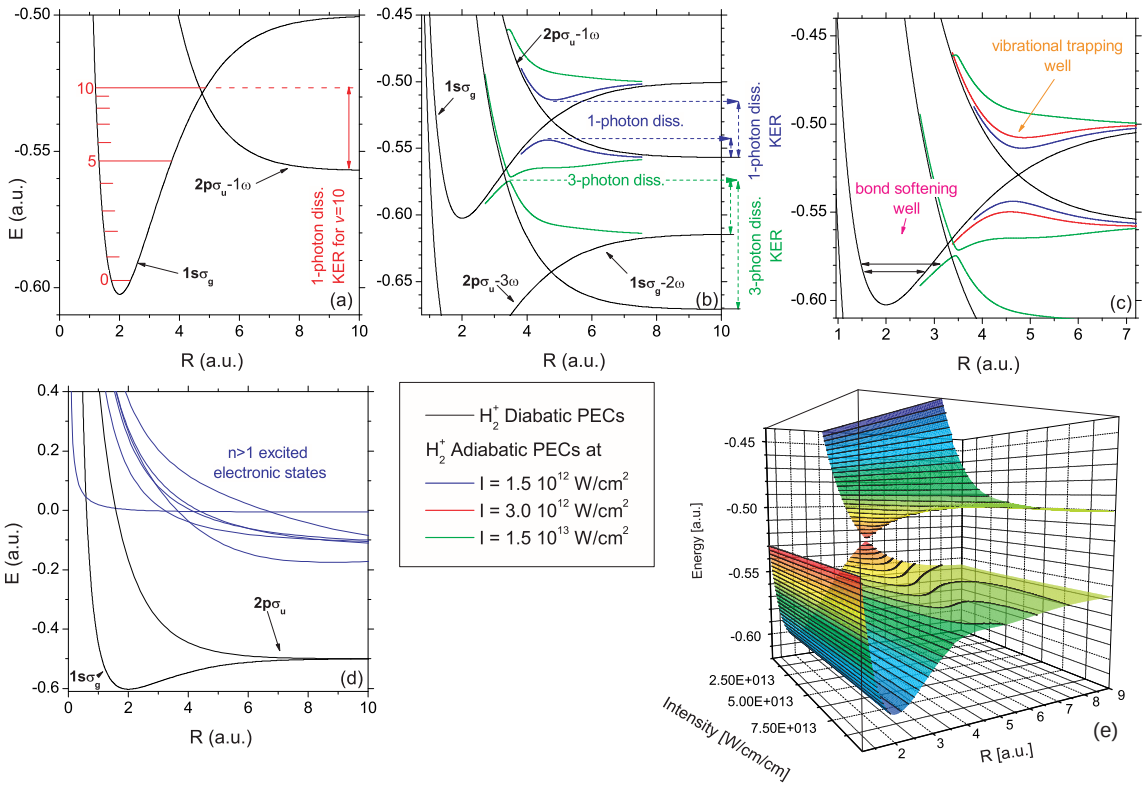

Figure 3.3: Floquet pictures used to make predictions about H_2^+ dissociation. (a) Diabatic Floquet Curves (b) Opening of the bond softening gap with intensity and 3-photon dissociation path (c) The bond softening potential well grows wider with increased intensity. (d) Excited electronic states of H_2^+. (e)A picture of the 1-photon avoided crossing opening with increasing intensity. (a) – (e) See text for details.

the laser pulse changes slowly enough that the nuclear wavefunction has time to adjust to the modified PECs. Furthermore, as the PEC curves change slowly, especially for lower laser intensities, the vibrational levels should be preserved, i.e. distinct vibrational levels should be visible and distinguishable by their kinetic energy release (KER), as shown in figure 3.3(a). For example, the PECs are basically undistorted by the laser field and thus one would expect the resonant transition from the $v = 9$ state to occur resulting in dissociation with ~ 0.8 eV of KER. Additionally, the non-resonant transitions from $v > 9$ should occur with distinct KERs, but with less probability, as they are energetically allowed but non-resonant and susceptible to vibrational trapping.

Accessibility and shifting of vibrational levels As the laser intensity is increased, one would expect that more vibrational levels would become accessible. This is exemplified in figure 3.3(b) in which the increased intensity has opened the avoided curve crossings in the adiabatic Floquet picture. This opening now allows vibrational levels $v < 9$ to dissociate via bond softening as discussed in section 1.4. Additionally, the upper — vibrational trapping — well rises and becomes less binding with increased intensity, thereby increasing the probability for dissociation of $v > 9$ vibrational levels. Thus, as the intensity increases, one would expect the range of vibrational levels that dissociate to increase both above and below the $v = 9$ resonant transition. In addition, one expects that the vibrational levels will shift with increased intensity. As shown in figure 3.3(c), the width of the lower potential well formed by the adiabatic Floquet PECs increases with increased intensity. Therefore, if the vibrational wavefunction behaves adiabatically during the laser pulse, one would expect the vibrational levels to shift to lower energies as the potential well increases in width.

Effective intensity as a function of molecular alignment In addition to the strength of the laser field, one expects that the molecular alignment with respect to the laser polarization should play an important role. In our simplified Floquet picture of H_2^+ dissociation, we have neglected all electronic states other than $1s\sigma_g$ and $2p\sigma_u$. This is because the additional electronic manifolds lie well above the the ground state dissociation limit, as shown in figure 3.3(d). Further, if the assumption that these states play a negligible role is valid, then the only two effective electronic states have the same angular momentum, i.e. $\Lambda = 0$. Thus, all transitions are parallel transitions, which is to say that the dissociation process is dependent on the square of the electric field, i.e. the intensity, along the internuclear axis. Thus the effective intensity I_{eff} seen by a molecule at angle θ is $I_{\text{eff}} = I\cos^2\theta$. Additionally, one expects that, in the weak field limit, the angular distribution of the dissociating H_2^+ molecules would have a distribution proportional to $\cos^2\theta$, where θ is the angle between the molecular axis and the laser polarization. Moreover, as is discussed in section 1.4.4.4, if the molecular wavepacket dissociates via bond softening, i.e. from a $v < 9$ state, one expects the angular distribution to be pushed towards the laser polarization, i.e. $\cos\theta = \pm 1$. Conversely, if

the nuclear wavepacket is from a $v > 9$ state and undergoes vibrational trapping, one expects the angular distribution to be pushed away from the laser polarization direction, i.e. towards lower I_{eff} where the potential well is deeper, as the wavepacket funnels into the potential well of the upper potential shown in figure 3.3(e).

Above threshold dissociation (ATD) In this section so far, only one photon transitions have been discussed. However, at intensities up to $I_0 = 2.4 \times 10^{14}$ W/cm^2 it is not unreasonable to expect multi-photon dissociation, i.e. $n_{\text{photon}} > 1$, which is typically called ATD. This is because the minimum number of photons necessary to dissociate an H_2^+ molecule is one.[35] With a 3-photon transition, vibrational states lying below the one-photon barrier formed by the avoided crossing in the adiabatic Floquet picture, i.e. the bond softening barrier, can dissociate.[36] As the laser intensity is sufficient to open the 3-photon avoided crossing, the vibrational levels dissociating through this crossing will most likely continue along the adiabatic potential crossing back to the $2p\sigma_u - 1\omega$ curve since the travel time between the two crossings is short compared to the 135 fs pulse duration. Further, this type of ATD may be, at least partially, distinguishable from the 1-photon transitions as the expected KER, i.e. the vertical distance from the 3-photon crossing to the $2p\sigma_u - 1\omega$ dissociation limit as shown in figure 3.3(b), is larger than the KER expected from 1-photon dissociation from vibrational levels $v \lesssim 11$.

3.2.1.2 Experimental results

Laser pulse characteristics Now that some qualitative predictions from the simplified Floquet picture for the laser-induced dissociation of H_2^+ have been discussed, the experimental data we measured at $\lambda = 790$ nm, $\tau = 135$ fs, and intensities up to $I_0 = 2.4 \times 10^{14}$ W/cm^2 will be presented. We measured the laser-induced dissociation of H_2^+ at five different intensities, as shown in figures 3.4(a) – (e). These measurements were performed using a $f = 200$ mm focusing lens,

[35] This can be a bit misleading as, although it is true that the minimum number of 790 nm photons necessary to dissociate H_2^+ vibrational levels $v \geq 9$ is 1, for vibrational states below the bond-softening barrier the minimum number of photons required to dissociate the molecule is ≥ 2. However, as it is extensively used in the way described above, we will stick to the common nomenclature unless otherwise specified.

[36] 2-photon transitions between $H_2^+(1s\sigma_g)$ and $H_2^+(2p\sigma_u)$ are forbidden by symmetry constraints.

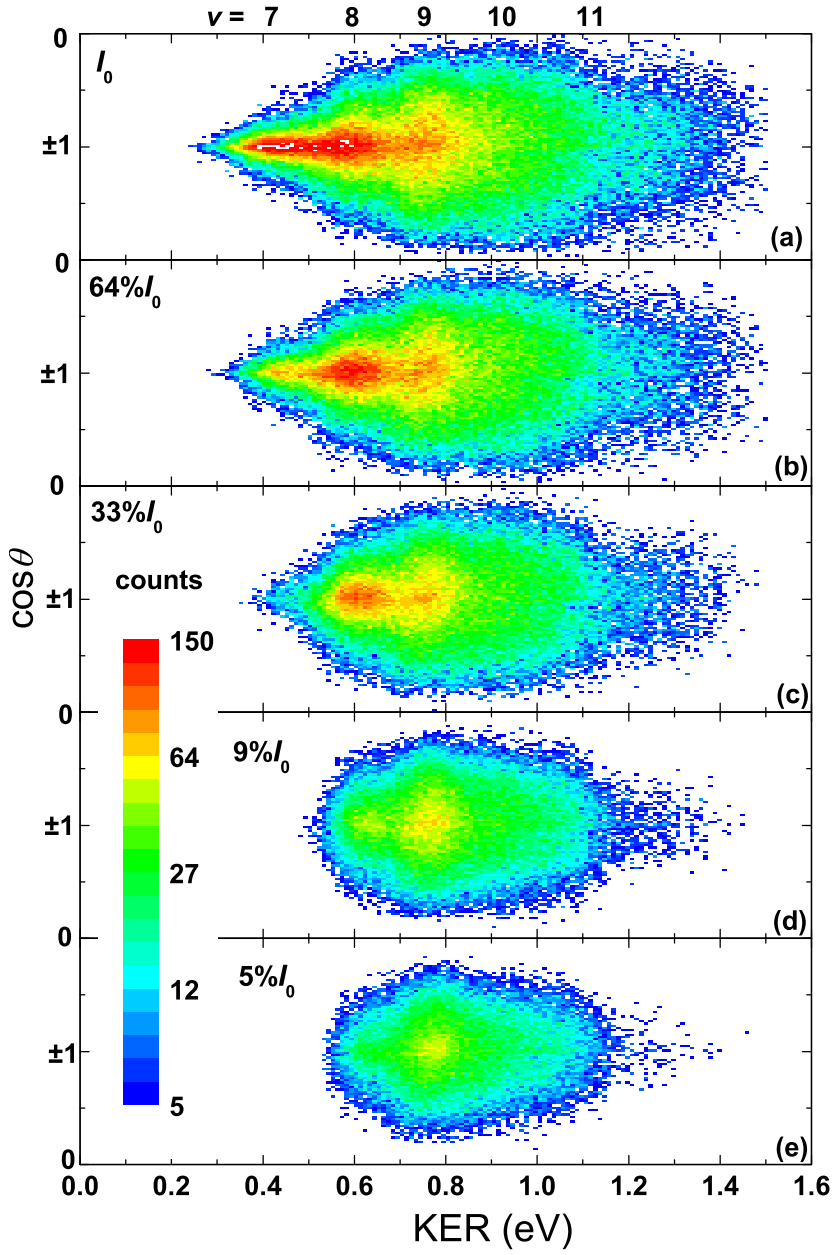

Figure 3.4: Histograms of counts vs. KER and $\cos\theta$ for H_2^+ dissociation at 790 nm, 135 fs, and intensities up to $I_0 = 2.4 \times 10^{14}$ W/cm^2. The vertical structures, i.e. the ridges with a constant KER, are formed by dissociation from the vibrational levels marked by the label at the top of the figure. The peak intensity for each data set is denoted with relation to I_0, e.g. 33% $I_0 = 7.9 \times 10^{13}$ W/cm^2. The counts are binned in $\cos\theta$ since an isotropic spherical distribution will be uniform in that representation. (a) – (e) Data taken at decreasing intensities with contributions from the entire focal volume. Note that $\cos\theta$ is plotted from 0 to -1 and then from $+1$ to 0. See text for discussion. (Figure adapted from our publication [52].)

which produced a $1/e^2$ diameter of 65 μm and a Rayleigh length of $\sim$ 2.3 mm. To reduce the peak intensity, the laser power was attenuated using neutral density (ND) filters. Note than both the lens and ND filters introduce dispersion to the laser pulse which is negligible in this case as this pulse is relatively narrow in frequency bandwidth and long in temporal duration. The additional dispersion introduced by the lens and ND filters is small. Additionally, the measurements were performed using both positive and negative chirp to ensure that the results were independent of the sign of the chirp.[37]

Accessibility of vibrational levels Now, by examining figure 3.4, one can see if the predictions made above are actually seen in the measured data. First of all, distinct vertical, i.e. constant KER, ridges are visible especially at the highest intensity. The expected KERs for dissociation from the field-free vibrational levels are marked at the top of the figure with the initial vibrational state. Furthermore, the accessibility of the various vibrational levels matches the predicted trend, which is to say that the accessible vibrational levels increase with intensity and the $v = 9$ resonant transition is the most likely and visible at the lowest intensity. Qualitatively our results are in agreement with that of Sändig *et al.* [84], who performed H_2^+ dissociation measurements prior to ours using 135 fs laser pulses. A quantitative comparison between our data and theirs is not possible, however, because they used a molecular ion beam narrower than the laser focus while we have the opposite configuration, thus resulting in significantly different intensity averaging.

Shifting of vibrational levels Additionally, if we project the plots shown in figure 3.4 onto the KER axis, as shown in figure 3.5, one observes that the structure matches the v=7 - 11 field-free vibrational levels of the ground electronic state. In figure 3.5 we show the KER distribution of figure 3.4(a), but only for the dissociation in the narrow slices of $|\cos\theta|$ denoted. Even at $|\cos\theta| > 0.9$, we barely see the v=6 peak measured by Sändig *et al.* [84]. This is because we have a smaller volume of high intensity in the interaction region. The levels higher than v=9 do not appear clearly in this figure because they tend to align away from the laser polarization, i.e. away from $\cos\theta = \pm 1$, as

[37] Both positive and negative chirp were introduced by varying the distance between the grating pair inside the compressor of the chirped-pulse amplification laser system.

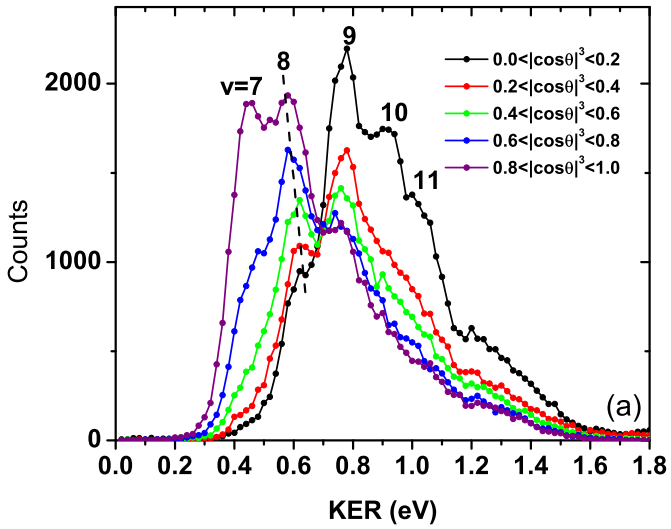

Figure 3.5: A histogram of counts vs. KER for H_2^+ dissociation at 790 nm, 135 fs, and an intensity of $I_0 = 2.4 \times 10^{14}$ W/cm^2. Each data set is formed by integrating over the specified ranges in the KER-cos θ data shown in figure 3.4(a). Note that the effective intensity is $I_{\text{eff}} = I \cos^2 \theta$ so different cos θ slices are equivalent to different peak intensities. The initial vibrational levels are denoted at the top of the figure and v=8 has a noticeable shift to lower KER with increased effective intensity. (Figure adapted from our publication [52].)

will be discussed in detail momentarily. For comparison, figure 3.5 also shows the KER distribution for other slices in $|\cos\theta|$, which are equivalent to different intensities since $I_{\text{eff}} \simeq I \cos^2 \theta$, as was discussed above. This allows one to see that the vibrational levels below the avoided crossing, e.g. v=8, shift to lower energy with increasing intensity as predicted and discussed above.

Figure Style As shown in the figure 3.4, we generally prefer to present our data in terms of KER and cos θ as the former is the quantity most easily retrieved from the Born-Oppenheimer potential energy curves and the latter has a uniform volume element for the initial isotropic spherical distribution seen in our measurements. Additionally, we typically plot cos θ from 0 to -1 then from $+1$ to 0 so that molecules aligned with the laser polarization are along the central cos $\theta = \pm 1$ axis.[38] The method in which various groups present their data varies, but the data is often presented in terms of the momentum parallel $\mathbf{p}_\parallel$ and perpendicular $\mathbf{p}_\perp$ to the laser polarization, e.g. the data of Sändig *et al.* [84] for the same process shown in figure 3.1. We can also plot the data in this manner as is shown in figure 3.6(a), which presents the same data that is shown in figures 3.4(a) and 3.6(b). The $\mathbf{p}_\parallel$-$\mathbf{p}_\perp$ plot does show the vibrational levels quite nicely, however there are some features of this type of plot that are often overlooked. In figure 3.6(a), as is typically the case, the data, which is

[38] Assuming that there is no carrier-envelope phase (CEP) effect, the measurements have $\pm z$-symmetry, i.e. $\pm \cos\theta$-symmetry in cylindrical coordinates, where z is set along the laser polarization. Therefore, the top and bottom half of the KER-cos θ distribution have redundant information. Nevertheless, we prefer to plot both halves of the data so as to show that the measurement adheres to the inherent symmetry.

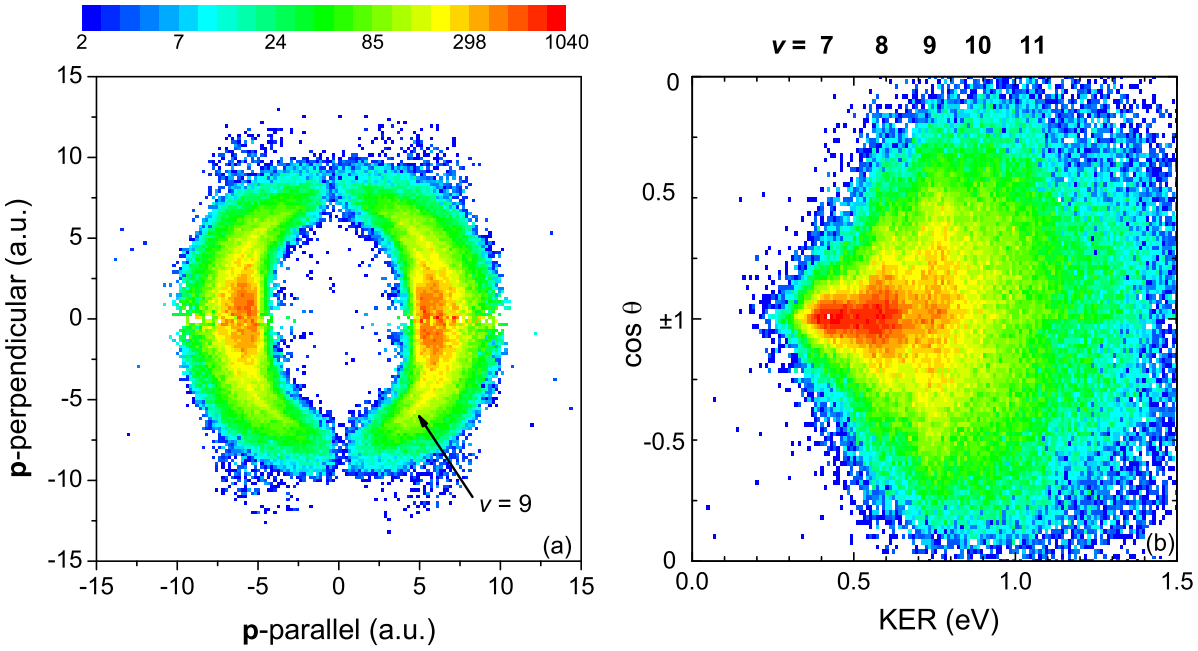

Figure 3.6: (a) A 2D histogram of counts as a function of $\mathbf{p}_\parallel$ and $\mathbf{p}_\perp$. (b) The same data plotted as a 2D histogram of counts as a function of kinetic energy release (KER) and the $\cos\theta$, where θ is the angle between the laser polarization and the internuclear axis of the molecule. See text for details.

first binned in $\mathbf{p}_\parallel$ and $\mathbf{p}_\perp$, is multiplied by the volume element, $d(\cos\theta)$, associated with an isotropic spherical distribution. This artificially inflates the number of counts near $\cos\theta = \pm 1$ making the error bar for this portion of the plot much greater than the simple statistical error associated with N counts, i.e. %error $= \sqrt{N}/N$, would suggest. Additionally, when dealing with data with ϕ-symmetry, one can reconstruct the three-dimensional data by taking the Abel transformation of the x-z-plane projection. Thus, it is important to distinguish whether the $\mathbf{p}_\parallel$-$\mathbf{p}_\perp$ plot displays the x-z-plane projection or the transformed three-dimensional data. Nevertheless, all of these plotting styles are valid and have their advantages. We simply find that the KER-$\cos\theta$ representation helps us avoid some possible confusion.[39]

[39]The freedom we have in binning data is an important advantage of the event-mode data acquisition we use, which allows us to bin the data repeatedly and in various ways without the need to include a volume element. Data that is collected in non-event mode can also be transferred to different bins, however this requires multiplication by a volume element, thereby complicating the statistical error as discussed above.

KER-$\cos^3\theta$ distributions Figure 3.6(b) reveals a strong correlation between the angular distribution and the KER. This correlation is highlighted by comparing the measured angular distribution to the one expected for photo-dissociation in the weak-field limit which has a $\cos^2\theta$ distribution. Bond softening and vibrational trapping dissociation channels are expected to deviate from this distribution as discussed above. We highlight these nonlinear effects by comparing the angular distributions to the expected $\cos^2\theta$ distribution of H_2^+ photo-dissociation in the weak-field limit [95]. If dN is the number of dissociation events that occur in the angular range $d(\cos\theta)$, then dN is proportional to the dissociation probability of a molecule aligned along $\cos\theta$ and to the number of molecules aligned inside $d(\cos)$, i.e. $dN \propto \cos^2\theta\ d(\cos\theta)$. Consequently, the distribution of the dissociation events as a function of $\cos^3\theta$ yields

$$\frac{dN}{d(\cos^3\theta)} = \text{constant}\ , \tag{3.1}$$

in the weak-field limit. Plotting $dN/d(\cos^3\theta)$ thus emphasizes deviations from the flat distribution expected for low intensities, therefore highlighting the nonlinear intensity dependencies in laser-induced dissociation.

Angular distributions for bond softening and vibrational trapping As shown in figure 3.7, this technique reveals the small deviations from the $\cos^2\theta$ distribution much more effectively that the previous plots. It is evident that dissociation from $v = 9$ is approximately uniform, i.e. adhering to the $\cos^2\theta$ weak-field limit, while dissociation from vibrational levels above and below $v = 9$ are aligned further away and closer to the laser polarization, respectively. To further illustrate this point, in figure 3.8 we have fit the $\cos\theta$-distribution as a function of KER to a $\cos^{2n}\theta$ function, thereby, confirming the previously stated assumptions that (i) if the molecular wavepacket dissociates via bond softening, one expects a $n > 1$ angular distribution and (ii) if the nuclear wavepacket undergoes vibrational trapping, one expects a $n < 1$ angular distribution [23].

Above threshold dissociation (ATD) In addition to illustrating the angular properties of bond softening and vibrational trapping, figure 3.8 also shows a strong signature of ATD. This is

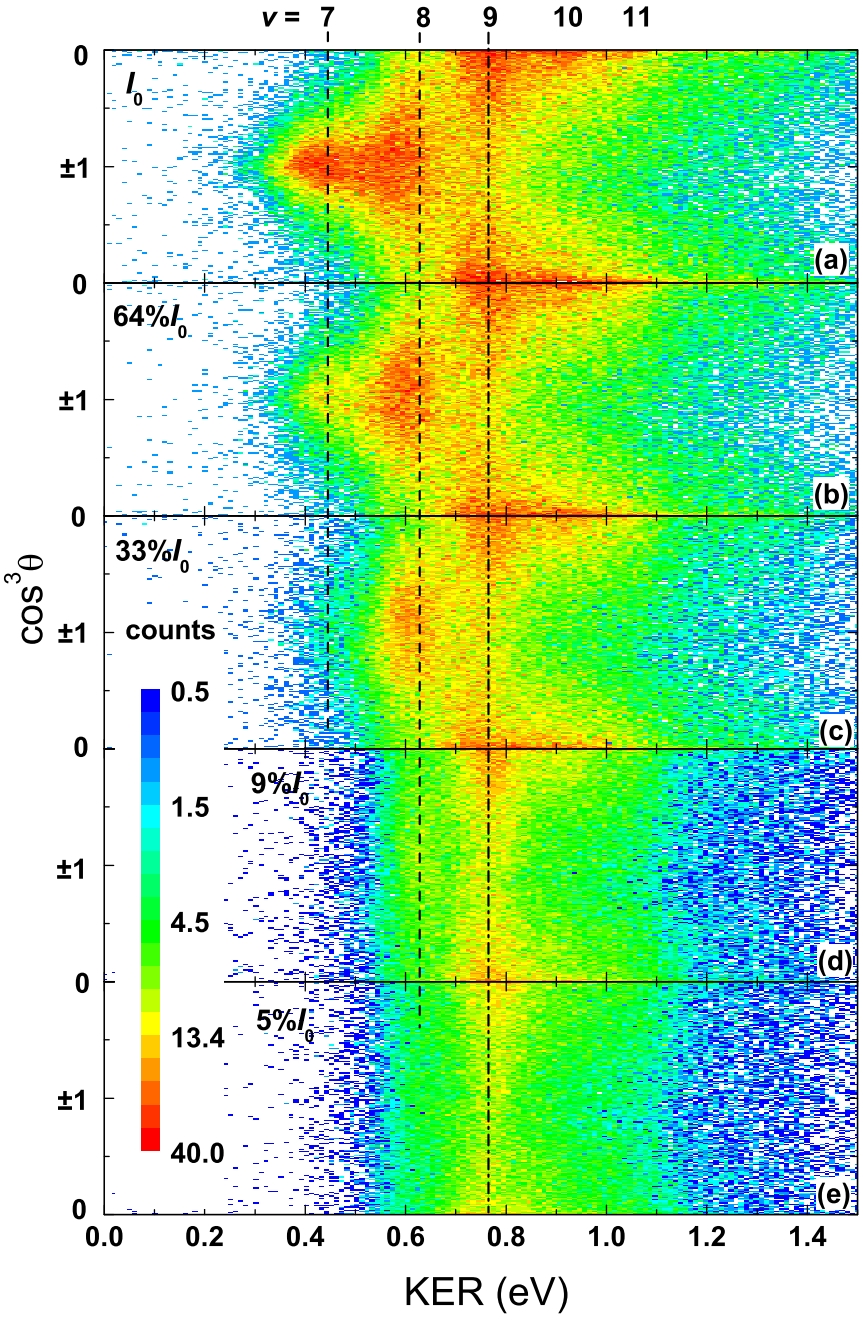

Figure 3.7: Histograms of counts vs. KER and $\cos^3\theta$ for H_2^+ dissociation at 790 nm, 135 fs, and intensities up to $I_0 = 2.4 \times 10^{14}$ W/cm^2. The vibrational levels are marked with vertical lines. Note that the deviation from the $\cos^2\theta$ predicted in the weak field limit is easily visible when the data is binned in this way. (Figure adapted from our publication [95].) See text for discussion.

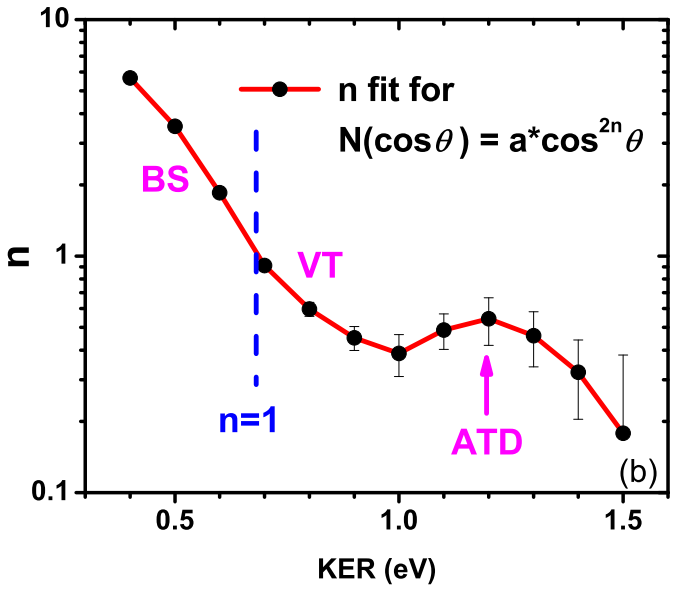

Figure 3.8: By taking a series of slices in KER and fitting the data to a $\cos^{2n}\theta$ distribution to the data we arrive at this plot of n as a function of KER. Values of $n > 1$ and $n < 1$ correspond to bond softening (BS) and vibrational trapping (VT), respectively. Note that the angular distribution for ATD deviates from the trend seen in BS and VT. (Figure taken from our publication [95].)

to say that the feature from 1.0 – 1.5 eV deviates from the behavior expected from net 1-photon dissociation. Namely, (i) the KER is generally greater than that expected from the highly populated vibrational states and (ii) the angular distribution differs from the trend seen in the 1-photon region. This dissociation mechanism will be discussed in further detail in section 3.2.1.3.

Intensity difference spectra (IDS) We now apply the IDS method, as detailed in section 2.6.1.1, to the experimental results by subtracting consecutive spectra in figure 3.4, which is reproduced in figure 3.9(left) for comparison. This results in the IDS shown in figure 3.9(right). The decomposition of the spectra of figure 3.9(left) by IDS reveals the characteristics of the laser-induced dissociation for specific intensity ranges. For the intensity range below 5% I_0 mainly a broad structure corresponding to dissociation around the avoided crossing at $v \simeq 9$ can be seen. This is the typical feature for low-intensity photodissociation and closely follows a $\cos^2\theta$-distribution expected in the weak field limit. It is notable that figure 3.9(e2) accounts for 33% of the total counts in figure 3.9(a1), although the peak intensity is 20 times smaller. This indicates that an intensity-averaged spectrum may suffer severely from the intensity-volume effect, as the IDS derivation of section 2.6.1.1 implies. In the intensity range of 5 - 9% I_0, the broad structure becomes much weaker. Instead, the bond softening channel from $v = 8$ appears stronger, which indicates that the barrier

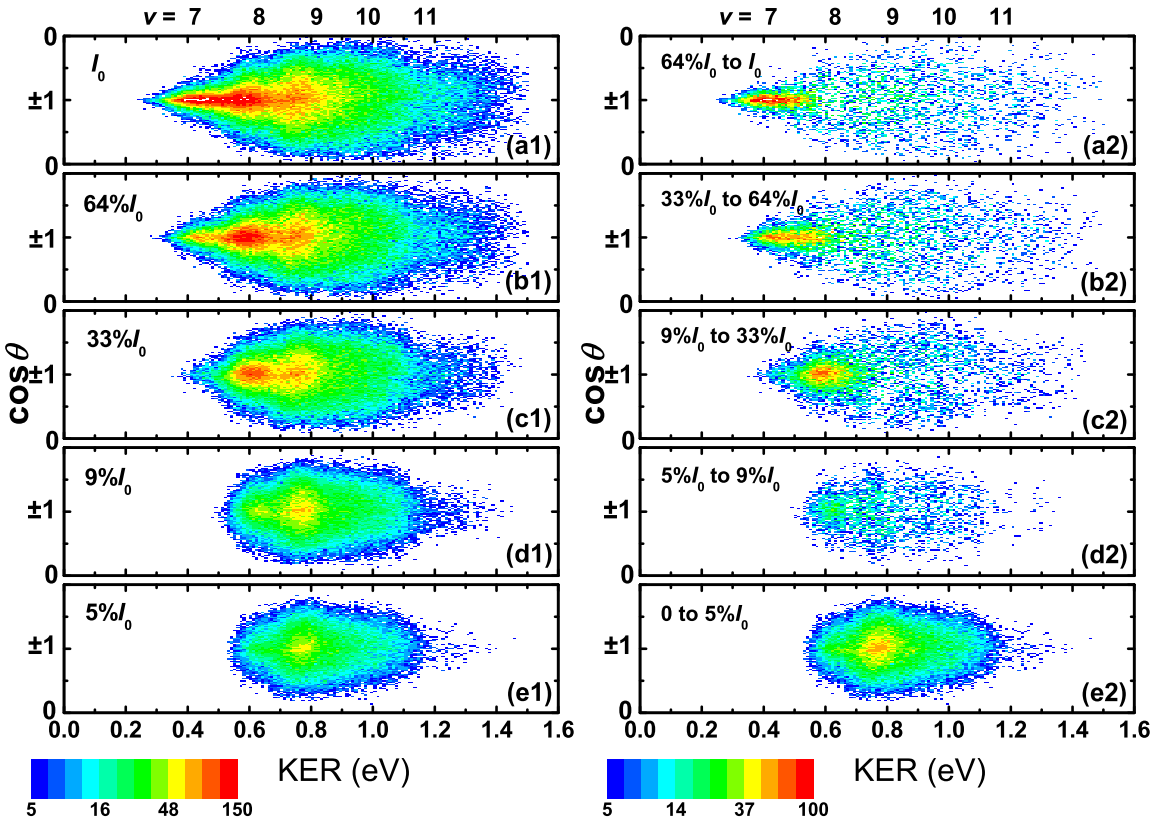

Figure 3.9: (a1) – (e1) Histograms of counts vs. KER and $\cos\theta$ for H_2^+ dissociation at 790 nm, 135 fs, and intensities up to $I_0 = 2.4 \times 10^{14}$ W/cm^2 identical to those shown in figure 3.4. (a2) – (e2) Intensity differences spectra (IDS) using the same data. See text for details and section 2.6 for a discussion of the IDS method. (Figure taken from our publication [52].)

formed by the curve crossing, see figure 3.3, is lower than this vibrational level. At higher intensity ranges, this bond-softening channel is dominant, and it shifts to lower KER in a continuous manner. The shift of the bond softening channel indicates the successive breakup of lower vibrational levels, as well as a downward energy shift of the levels at higher laser intensities. At the wavelength we used, the dissociation of H_2^+ is dominated by the coupling between the ground $1s\sigma_g$ and first excited $2p\sigma_u$ states. The effective light field for this coupling is given by $E_0 \cos\theta$, where E_0 is the amplitude of the laser pulse. It is notable that the angular distribution of the bond-softening channel is narrower for the lower vibrational levels. This indicates the strong nonlinear intensity dependence of the avoided crossing energy gap, where the required intensity is only reached when

the molecules align within a narrower cone around the laser field direction.

The dissociation from the vibrational levels above the avoided crossing, i.e. $v > 9$, forms another feature in 3.9(right). The angular distributions of the dissociation from these levels are much broader than the bond-softening channels, and are even broader than the $\cos^2\theta$ distribution of photo-dissociation at the weak field limit. Vibrational trapping can be invoked to explain this broad distribution [95]. Because at higher intensities the molecules can be trapped in the potential well above the avoided crossing, there is a reduced probability for the molecules to dissociate when they align close to the laser polarization, which results in a counterintuitive angular distribution [23]. It is notable that this vibrational trapping effect is different from the observation of perpendicular emission of fragments by Talebpour *et al.* [140] at shorter wavelengths, which was interpreted in terms of the coupling between the ground electronic state and the high-lying $3d\sigma_g$ and $3p\pi_u$ states. Although the broadening of the angular distribution of $v > 9$ levels can also be caused by saturation, figure 3.9(left) and (right) indicate that the spectrum for $v > 9$ changes when increasing the laser intensity. Therefore, we attribute the observed phenomenon to vibrational trapping rather than saturation.

3.2.1.3 Time-dependent calculations

Theoretical approach In addition to the simplified Floquet picture described above we also take advantage of more sophisticated calculations developed by Anis and Esry [137]. These calculations followed the standard route of solving the time-dependent Schrödinger equation in the Born-Oppenheimer representation. In this section we briefly describe the specific implementation. Two fundamental assumptions underlie this treatment: (i) the nuclei do not have time to rotate during the pulse and (ii) rotation after the pulse is not significant.[40] The electronic degrees of freedom are expanded on the field-free Born-Oppenheimer states, leaving coupled time-dependent

[40] For the level of agreement we seek here, these assumptions are justified. Furthermore, nuclear rotation is included in subsequent calculations when it plays an important role.

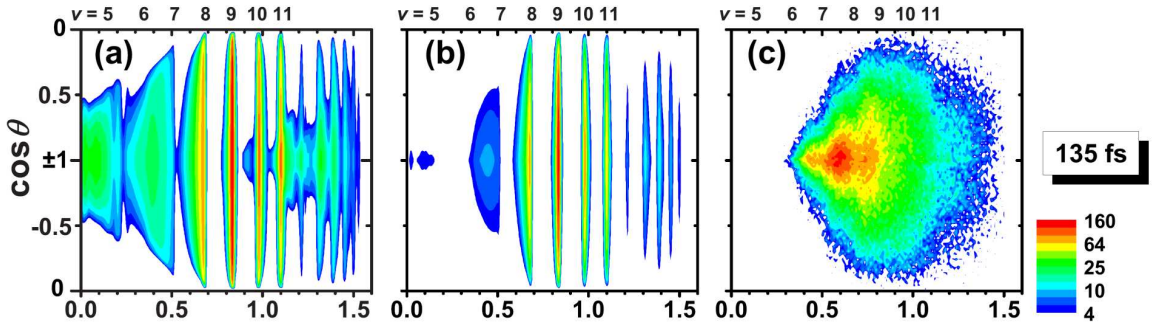

Figure 3.10: Comparison between experimental and theoretical KER-cos θ distributions of laser-induced dissociation of H_2^+ [52]. (a) Theoretical, 135 fs, 10^{14} W/cm^2, no intensity averaging. (b) Same as (a), but with intensity averaging. (c) Experimental, 135 fs, 1.6×10^{14} W/cm^2. (Figure taken from our publication [52].)

equations in the internuclear distance R (in atomic units):

$$i\frac{\partial}{\partial t}\mathbf{F}(R,t) = \left[-\frac{\mathbf{I}}{2\mu}\frac{\partial^2}{\partial R^2} + \mathbf{U}(R) + \mathbf{E}(R)\cdot\mathbf{D}(R)\right]\mathbf{F}(R,t) \tag{3.2}$$

The matrix $\mathbf{I}$ is the unit matrix, $\mathbf{U}(R)$ is the diagonal matrix of Born-Oppenheimer potentials, μ is the nuclear reduced mass, $\mathbf{D}(R)$ is the matrix of electronic dipole matrix elements, and $\mathbf{F}(R,t)$ is the column vector containing the radial wave function in each channel. The laser field $\mathbf{E}(t)$ is assumed to be linearly polarized along the lab frame z-axis with magnitude $E(t) = E_0 \exp(-t^2/\tau^2)\cos(\omega t)$, where $\tau = w/\sqrt{4\ln 2}$, E_0 is the amplitude of the electric field, and ω is the carrier frequency.[41]

Comparison with data The theoretical KER-cos θ distributions for laser-induced dissociation of H_2^+ at 790 nm and 135 fs, shown in figures 3.10(a) and (b), display both substantial differences and qualitative agreement with some features of the measured distribution in figure 3.10(c). The most distinct features of the theoretical distributions are the vibrational levels. These levels are seen in both the theoretical and measured data, and agree with the bond softening process discussed before for $v = 7 - 11$ in KER and angular distribution. However, the theoretical calculations show a much sharper structure in KER, which can be attributed to a combination of our finite experimental resolution and the approximations made in the theoretical calculations. Another set

[41] See references [52, 137] for detailed descriptions of these calculations.

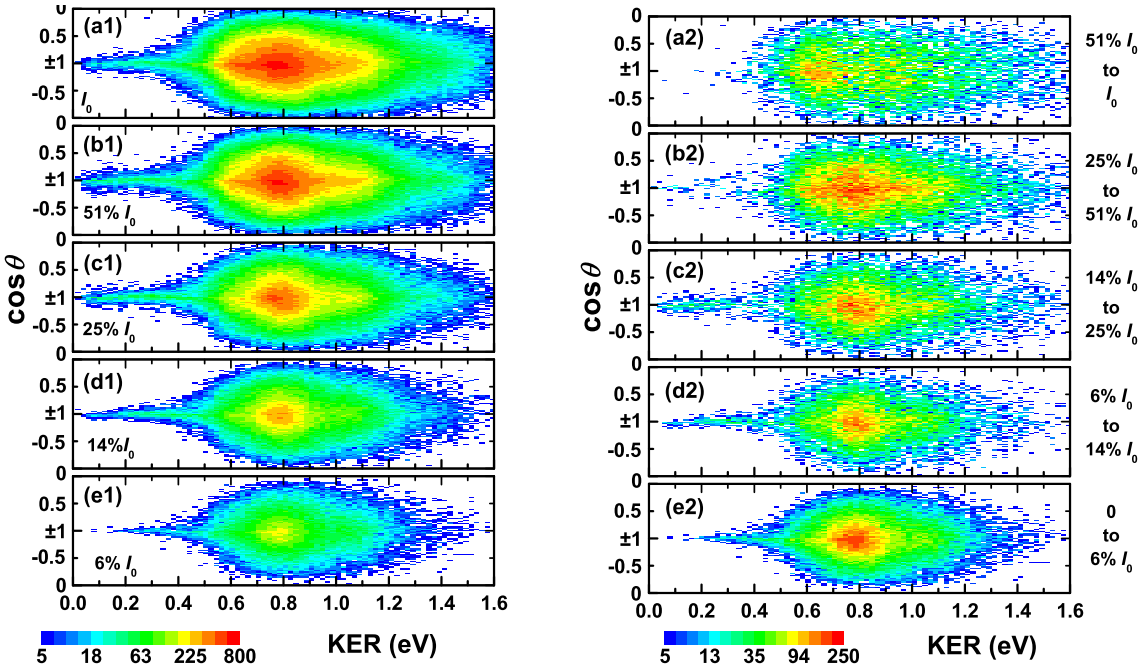

Figure 3.11: Histograms of counts vs. KER and $\cos\theta$ for H_2^+ dissociation at 790 nm, 45 fs, and intensities up to $I_0 = 2.4 \times 10^{14}$ W/cm^2. The peak intensity for each data set is denoted with relation to I_0, e.g. 51% $I_0 = 1.2 \times 10^{14}$ W/cm^2. (a1) – (e1) Data taken at decreasing intensities with contributions from the entire focal volume. (a2) – (e2) The intensity difference spectra derived from the normalized spectra of figures (a1) – (e1). See text for discussion. (Figure taken from our publication [52].)

of distinct features in the theoretical data are the series of vibrational levels with KER of 1.1 – 1.5 eV, which dissociate via net 2-photon ATD.[42] This matches the conclusions reached above from examining the experimental data in this KER range.

3.2.2 Short pulse (45 fs, 790 nm)[43]

3.2.2.1 Experimental Results

Intensity dependence Figure 3.11(left) shows the KER-$\cos\theta$ distribution of laser-induced dissociation of H_2^+ in a $\tau = 45$ fs Fourier transform limited laser pulse with peak intensities up to $I_0 = 1.7 \times 10^{15}$ W/cm^2 done with the same apparatus described above.[44] The main feature of

[42] In the theoretical calculations one can distinguish the contributions from each vibrational level independently.
[43] Much of the work in this section has been previously reported in our publications [36, 52, 92, 95, 96].
[44] Using the 45 fs laser pulse we also see ionization, which will be discussed later in this chapter.

these spectra is a broad KER distribution around 0.8 eV. After applying the IDS method to these spectra, we get the spectra for each intensity range as shown in figure 3.11(right). The features at lower intensity are generally interpreted by bond softening and vibrational trapping. However, this is contradicted by the fact that the IDS spectra indicate that the feature at around 0.8 eV exists at all higher intensities. Thus, we interpret this high-intensity feature as one being produced by a form of above threshold dissociation (ATD) in which the molecular ion absorbs three photons and emits one later, resulting in a net two-photon absorption. Additionally, figure 3.11 shows that at higher intensity ranges, ATD generally has a broader KER distribution and shifts slightly to lower KER values. There is another contribution to the spectra in figure 3.11(a) which is located below about 0.4 eV and has a very narrow angular distribution. In the IDS spectra, as shown in 3.11(right), this minor feature shifts to lower KER values when the intensity increases. It becomes weaker, relative to the main feature at ~ 0.8 eV, at higher intensities and almost disappears in 3.11(a1), thereby, suggesting that this minor contribution is caused by bond softening. Both this bond softening interpretation and the above-mentioned ATD process are confirmed by the calculations, as will be shown momentarily.

Comparison of 45 and 135 fs pulses Although the 135 and 45 fs data have been shown over approximately the same intensity range, i.e. $I_0 = 0 - 2.4\times10^{14}$ W/cm^2, the spectra are dramatically different. These two figures and their corresponding IDS spectra are redisplayed in figure 3.12 to contrast the features. Some significant differences between the spectra of the long, 135 fs, and short, 45 fs, laser pulses are: (i) Figures 3.12(b) and (d) show that at higher intensities the short pulse dissociation is dominated by ATD, while in the long pulse it is mainly due to bond softening and vibrational trapping (VT). (ii) The vibrational structure seen in the 135 fs data is obscured in the 45 fs data, which is expected as the 45 fs pulse duration is approaching the vibrational period of H_2^+, which is about 20 fs for the vibration levels from which the molecules dissociate. (iii) The short pulse yields a minor bond-softening channel below 0.4 eV with a narrow angular distribution, which does not appear in the spectrum for the long pulse. The differences between the spectra from the short and the long pulses are more apparent after subtracting the contribution from lower

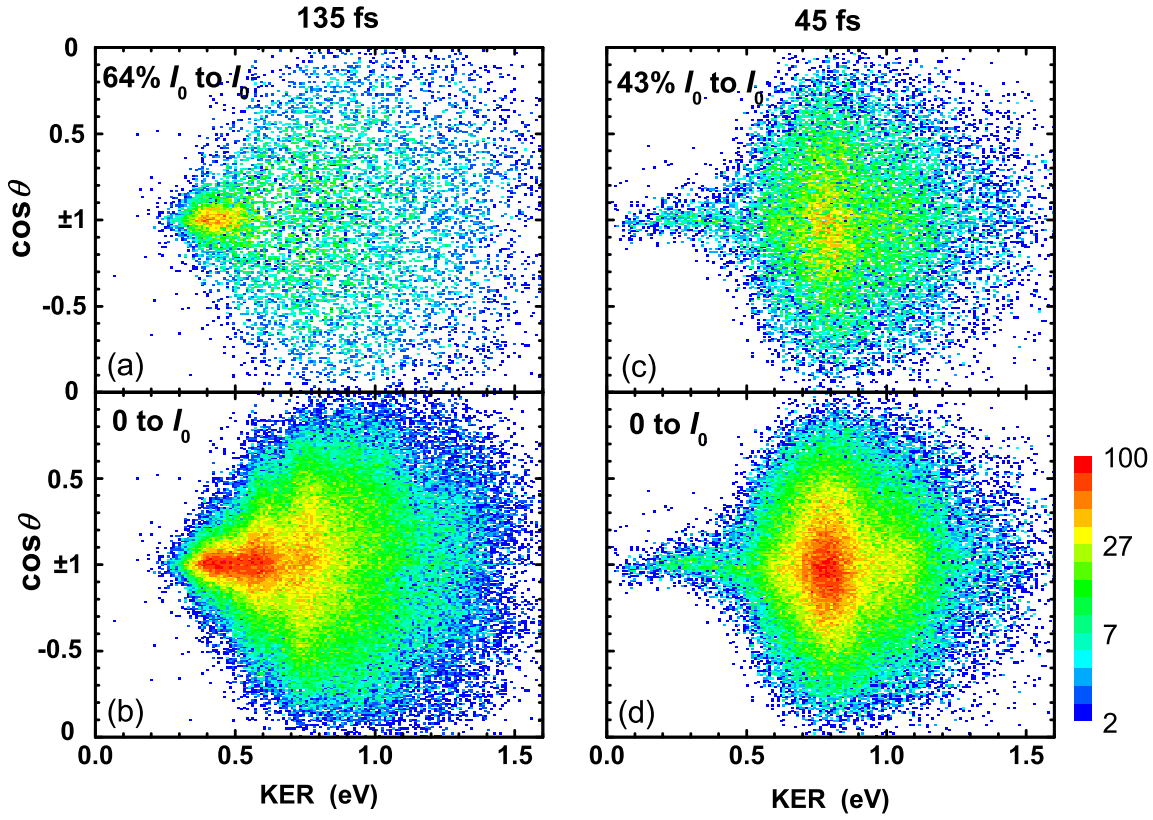

Figure 3.12: (a) and (b) H_2^+ dissociation at 790 nm, 135 fs, $I_0 = 2.4 \times 10^{14}$ W/cm^2, where (b) has contributions from the entre intensity range and (a) is an IDS slice. (c) and (d) H_2^+ dissociation at 790 nm, 45 fs, $I_0 = 2.4 \times 10^{14}$ W/cm^2, where (d) has contributions from the entire intensity range and (c) is an IDS slice. (Figure taken from our publication [52].)

intensities by the IDS method, as shown in figures 3.12(b) and (d). This method reveals that at the highest intensity the 135 fs data is dominated by bond softening from $v < 9$ vibrational states while the 45 fs data is primarily net 2-photon ATD.

3.2.2.2 Time-dependent calculations

KER contributions from vibrational states Before we compare the experimental results with the time-dependent calculations discussed above, it is helpful to show a typical KER spectrum for H_2^+ dissociation calculated by the method described above. Figure 3.13 shows the total KER distribution for H_2^+ dissociation and contributions from several selected vibrational levels. Here the pulse duration is $\tau = 45$ fs and the laser intensity is $I_0 = 5 \times 10^{13}$ W/cm^2, and no intensity averaging

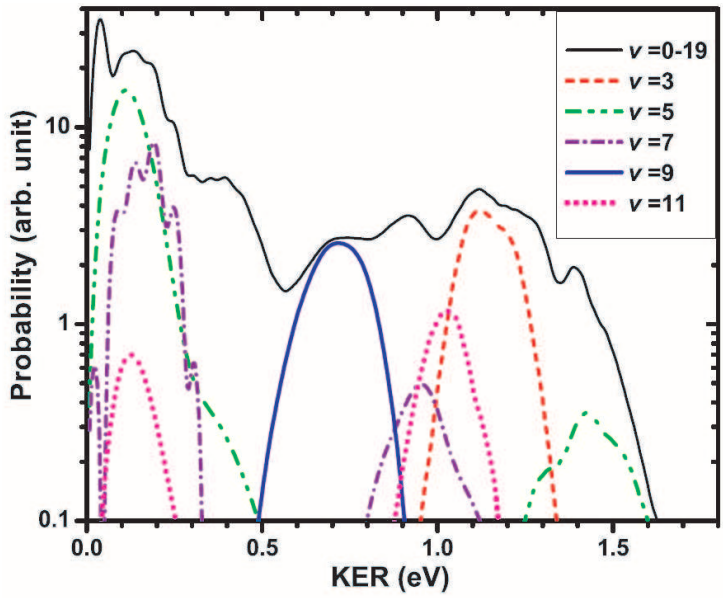

Figure 3.13: Theoretical KER distribution of laser-induced dissociation of H_2^+. The pulse duration is 45 fs, and the peak intensity is 5×10^{13} W/cm^2. The contributions from several different vibrational levels are shown. (Figure taken from our publication [52].)

is taken into account. For the total KER distribution the contribution of all levels from $v = 0 - 19$ are added incoherently. The dissociation mechanisms for $v = 9$ and 3 are straightforward. These two levels are located very close to the one-photon and three-photon avoided crossings as shown in the Floquet-style potential energy curves of figure 3.3. They are subject to bond softening (BS) and above threshold dissociation (ATD), respectively. However, other vibrational levels may have more than one dissociation pathway. For example, $v = 5$ and 7 can dissociate through both BS and ATD, where BS produces the lower KER peak, and ATD produces the higher KER peak. The $v = 11$ vibrational level is known to dissociate through VT, but can also produce very low KER at about 0.15 eV. This may be explained by the zero-photon dissociation (ZPD) mechanism suggested by Posthumus *et al.* [14].[45] In conclusion, figure 3.13 shows that each KER cannot be attributed to one vibrational level, or to one dissociation mechanism. This increases the difficulty of the interpretation of the experimentally observed KER spectrum. Furthermore, in a real experiment the KER distribution is a convolution of spectra at different intensities.

[45] In ZPD [20, 29, 30], a.k.a. below-threshold dissociation (BTD) [57], the upper adiabatic Floquet potential well, i.e. the vibrational trapping well shown in figure 3.3(e), becomes shallower with increasing laser intensity, thereby effectively lifting any part of the nuclear wavepacket bound in this well up in energy. Therefore, if the wavepacket is lifted above the $H + p$ dissociation limit in this manner, it can dissociate despite absorbing zero net photons.

Comparison to experimental data In order to elucidate the experimentally observed phenomena of laser-induced dissociation of H_2^+ at different pulse durations, the KER-$\cos\theta$ distribution shown in figure 3.14 is calculated using the same method described above. Here $\cos\theta$ *is obtained using the effective light field along the molecular axis* and no intensity averaging is done. The peak laser intensity is 1.0×10^{14} W/cm^2, and the pulse duration is 135 fs for figure 3.14(a) and 45 fs for figure 3.14(d). The intensity averaged KER-$\cos\theta$ distributions are shown in figures 3.14(b) and (e). Additionally, the experimental intensity-averaged distributions for a 135 fs, $I_0 = 1.6 \times 10^{14}$ W/cm^2 pulse and a 45 fs, $I_0 = 1.1 \times 10^{14}$ W/cm^2 pulse shown in figures 3.14(c) and (f), respectively. There is certainly not exact quantitative agreement between theory and experiment. However, we do not expect an exact quantitative agreement as (i) the calculation only includes the ground and first excited electronic states of H_2^+ and (ii) the experiments suffer from finite kinetic energy resolution and an uncertainty in the peak intensity ($\sim \pm 50\%$). In view of this, the theoretical results shown here are only intended to guide us in the interpretation of the observed phenomena.

From the calculation, shown in figure 3.14(a), we see that in 135 fs laser pulses the dissociation is dominated by one-photon absorption by the molecules initially at different vibrational levels of the ground electronic state. Although it is energetically possible for all $v \geq 5$ levels to dissociate, the levels around the avoided crossing $v = 9$ contribute the most. At about 1.2 eV a small contribution is superimposed onto the resolved vibrational structure, with a much narrower angular distribution. This minor feature is caused by net 2-photon ATD.[46] After intensity averaging, the features at lower intensities, i.e. those at smaller $\cos\theta$ values in figure 3.14(a) become dominant in figure 3.14(b).[47] The processes that occur at higher intensities, i.e. BS that produces low KER and ATD at about 1.2 eV, become less apparent. In particular, the dissociation below 0.3 eV caused by BS from the $v = 5$ and 6 levels seems to be significant in figure 3.14(a), but after intensity averaging it becomes

[46] Note that this is the feature shown in figure 3.14(d) at $\cos\theta = \pm 1$ and KER$\sim$ 1.0 eV. Furthermore, as processes involving a net even or a net odd number of photons are distinguishable in the theoretical calculations and the feature in question has been determined to involve an even number of photons, this feature cannot be due to bond softening, i.e. a net one-photon process. Recall, that this is also supported by the experimental results shown in figures 3.12(c) and (d) (and in more detail in figures 3.11(a2) – (e2)), which, in contrast to the bond softening shown in figures 3.12(a) and (b), show that this feature does not move to lower KER with increased intensity.

[47] Recall that the effective laser field is given by $E_0 \cos^2\theta$ and that intensity averaging always enhances the lower intensity contributions.

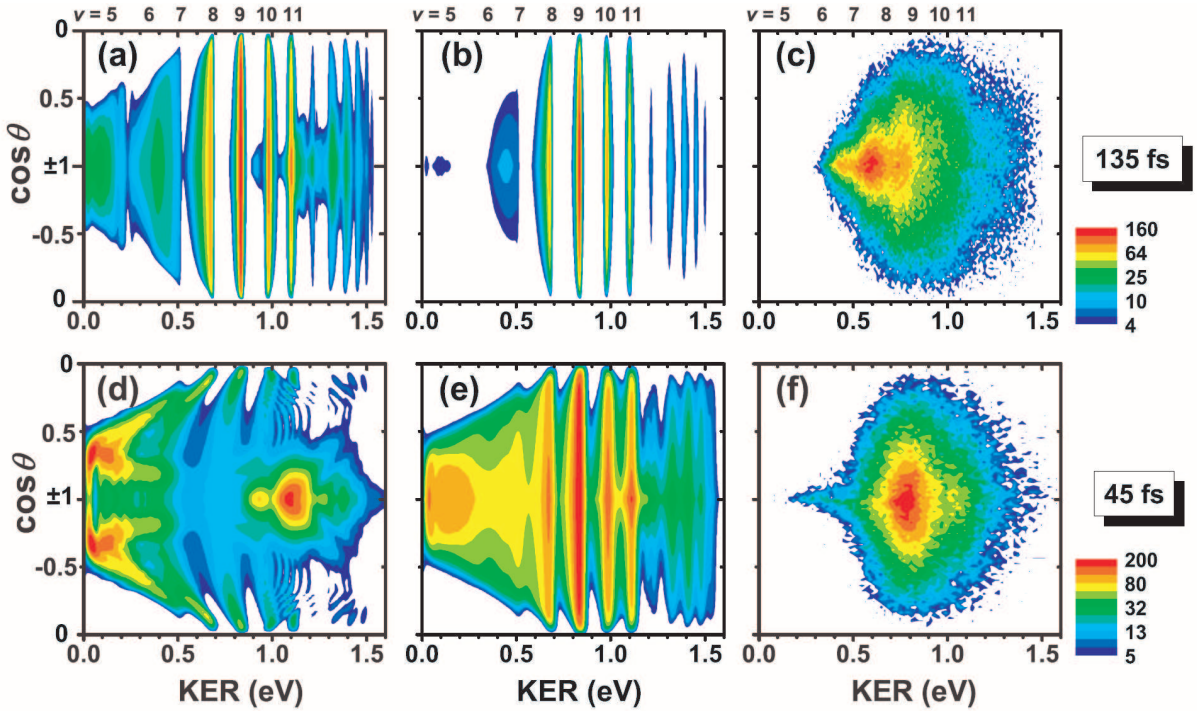

Figure 3.14: Comparison between experimental and theoretical KER-cos θ distributions of laser-induced dissociation of H_2^+. (a) Theoretical, 135 fs, 1.0×10^{14} W/cm^2, no intensity averaging. (b) Same as (a), but with intensity averaging. (c) Experimental, 135 fs, 1.6×10^{14} W/cm^2. (d) Theoretical, 45 fs, 1.0×10^{14} W/cm^2, no intensity averaging. (e) Same as (d), but with intensity averaging. (f) Experimental, 45 fs, 1.1×10^{14} W/cm^2. The vibrational structure through bond softening and bond hardening are labeled. (Figure taken from our publication [52].)

barely noticeable except for a spike around 0.1 eV. The BS and VT channels are reproduced in figure 3.14(c) except for the dissociation below 0.1 eV which is not observed in our measurements due to the finite size of the Faraday cup used to block the ion beam.

In figure 3.14(d), where 45 fs laser pulses are used, the calculated KER spectrum has two contributions. Below 1.2 eV BS takes place peaking at $|\cos\theta| \sim 0.35$ and above 1.2 eV the theoretical spectrum is dominated by ATD, which has a wide KER range and no vibrational structure.[48] After intensity averaging, figure 3.14(e) shows that the BS and VT channels are greatly enhanced, while ATD is in the background of the KER-cos θ distribution. Additionally, BS

[48] In figure 3.14, one can see that the theoretical calculations and experimental results do not match too well, e.g. in figures 3.14(d) and (e) bond-softening peaks outside $|cos\theta| = 1$. We believe that most of these discrepancies are due to the assumptions used in these calculations, e.g. no molecular rotation.

below 0.5 eV becomes narrow in angular distribution and now peaks at $\cos\theta = \pm 1$ due to intensity averaging.

The features present in the theoretical distributions, discussed above, help us to explain the experimental results, as shown in figure 3.14(f). Below 0.5 eV in the experimental results, BS produces a narrow angular distribution stripe. Above 0.5 eV, the observed feature, which has roughly a $\cos^2\theta$ angular distribution and a 0.6 eV KER spread, is thought to be a mixture of BS and VT at lower intensities, as well as ATD at higher intensities. Additionally, as expected, the theoretical predictions shown in figures 3.14(b) and (e) indicate the the vibrational structure washes out as the laser pulse duration is shortened and begins to approach the H_2^+ vibrational period. This trend is supported by the experimental data shown in figures 3.14(c) and (f) where the clear vibrational structure of the 135 fs pulse is wiped out for the 45 fs pulse.

3.2.3 Ultrashort pulse dissociation (7 fs, 790 nm)[49]

3.2.3.1 Simplified Floquet picture

Since the discovery of above-threshold ionization of atoms [141], the molecular analogue — above-threshold dissociation (ATD) — has been widely anticipated [13, 21]. Strangely, in spite of early experimental evidence for high-order[50] ATD of H_2^+ at 532 nm and 1064 nm wavelengths [10, 11, 142], detection using 800 nm light has proven difficult. Against this trend, an observation of a relatively weak high-order ATD has very recently been reported using a variationally cold target of HD^+ [56].

Detailed inspection using the Floquet representation for the light-dressed states (e.g. [33]) of H_2^+ reveals why high-order ATD is normally obscure. Figure 3.15 shows the diabatic $1s\sigma_g$ and $2p\sigma_u$ Born-Oppenheimer potentials, shifted in energy by the number of absorbed photons. Both of these states converge to the $H^+ + H(1s)$ atomic limit. For laser intensity $\gtrsim 10^{12}$ W/cm^2, the adiabatic potentials, which include the effects of the laser-molecule coupling, are more appropriate. The resulting adiabatic pathways for dissociation are indicated in figure 3.15 with arrows. This figure reveals why high-order ATD is difficult to observe with longer pulses, e.g. the 45 and 135 fs data

[49] Much of the work in this section has been previously reported in our publications [42].
[50] For convenience the absorption of three or more photons will be refereed to as "high-order" processes.

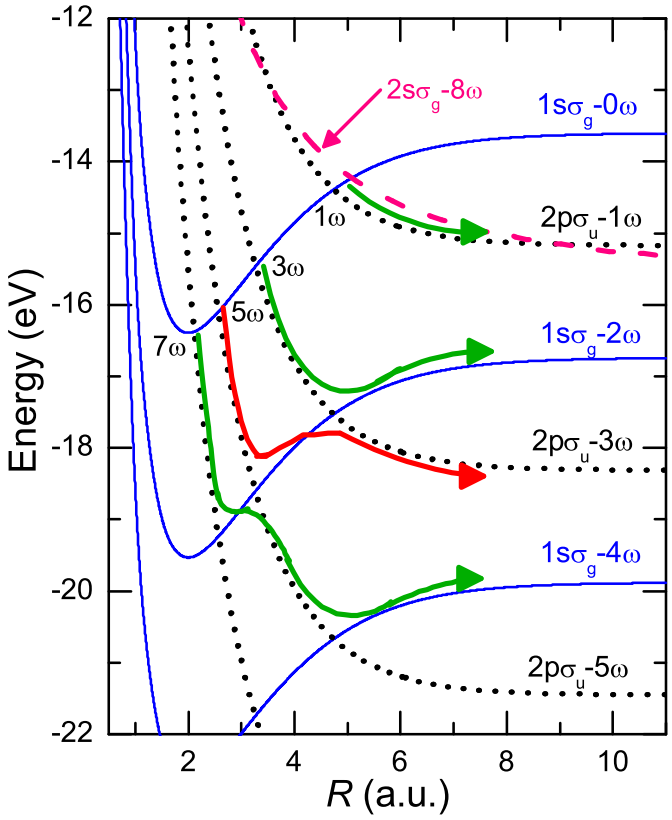

Figure 3.15: Field-free Born-Oppenheimer potential energy curves for H_2^+, dressed by net absorbed number of photons, $n\omega$. The red dissociation pathway is discussed in the text. (Figure adapted from our publication [42].)

discussed above. Namely, if there is enough intensity to allow the dissociating nuclear wave packet to adiabatically pass from its initial position in the $1s\sigma_g$ potential well out through a laser-induced avoided crossing, then the dissociating wavepacket will most likely continue along the adiabatic dissociation pathway, i.e. reducing the net number of absorbed photons and the dissociation KER at the next crossing, if the laser intensity stays relatively unchanged. For example, given a high laser intensity, a low lying vibrational state can (i) dissociate through the 5ω avoided crossing onto the $|2p\sigma_u - 5\omega\rangle$ state by absorbing 5 photons, then (ii) cross adiabatically onto the $|1s\sigma_g - 2\omega\rangle$ state by emitting 3 photons, and finally (iii) pass through the avoided crossing onto the $|2p\sigma_u - 3\omega\rangle$ state by absorbing 1 photon, as is shown in figure 3.15.

Whether the molecule follows these adiabatic pathways or more diabatic ones depends on the intensity of the laser pulse when the dissociating wave packet passes through the crossing. For example, at low intensity, i.e. $\sim 10^{12}$ W/cm^2, dissociation is dominated by one-photon absorption, depleting the population of high vibrational states, $v \simeq 9$. At higher intensity, the three-photon

crossing $|1s\sigma_g\rangle \rightarrow |2p\sigma_u - 3\omega\rangle$ opens, with population from the low-v states dissociating. This population tends to end up in the net two-photon channel $|1s\sigma_g - 2\omega\rangle$ via re-emission of a photon at the second crossing encountered along this pathway. For the same reasons, the observation of net three-photon ATD $|2p\sigma_u - 3\omega\rangle$ requires an initial absorption of five photons as discussed in the example above, net four-photon ATD requires absorption of seven photons, and so on. The fact that dissociation follows the adiabatic pathway makes observation of high-order ATD difficult.

In this section we explore the possibility of blocking the paths that lead from high-order ATD to low-order ATD via channel closing so as to enhance the high-order processes.[51] We do so using laser pulses that are intense enough to open the first ATD crossing with the ground state, but also short enough to "switch off" before the dissociating H_2^+ wavepacket can reach the later curve crossings along its path. In this way we can control the dissociation path of the molecule, forcing it into the harder-to-access high-order ATD channels. In addition to experimental measurements and theoretical calculations for the ultrashort pulse laser-induced dissociation of H_2^+ we also use its isotopologues, i.e. HD^+ and D_2^+, to effectively shorten the laser pulse duration.[52] Moreover, we identify a new ATD mechanism: excitation to the $H(2l)$ states of H_2^+ accompanied by the absorption of an excess number of photons, which is absent in all previous interpretations of ATD based solely on $H(1s)$ states.

3.2.3.2 Experimental method

This experiment was done under the same conditions previously described, except for the fact that we did not use a fused silica lens to focus the laser beam or neutral density (ND) filters to attenuate the power as the large frequency-bandwidth needed to support ultrashort pulses is extremely sensitive to dispersion (see section 2.6 and appendix A.4.2 for details). Instead, we used a 90° off-axis parabolic mirror to focus the laser beam and scanned the z-position of the focus to attenuate the intensity [94, 121–123] (see appendix A.3.4.1 and section 2.6.1.1, respectively, for

[51] In addition to dissociation, we observe a large ionization yield for laser pulses of this intensity and pulse duration. The dissociation channel will be focused on for now and ionization will be discussed later in this chapter.

[52] More massive isotopologues move at a slower speed given the same energy as $v = \sqrt{2E/\mu}$, thus effectively making the laser pulse duration shorter with respect to the travel time of the nuclear wavepacket.

details). This way the laser pulse was insured to have approximately the same temporal profile for measurements at different peak intensities. Additionally, in these measurements the carrier-envelope phase (CEP) was not locked, thereby washing out any CEP effects given the large number of laser shots used in each measurement (see section 2.5.3 for details on the CEP).

3.2.3.3 Time-dependent calculations

In the theoretical approach [137], the time-dependent Schrödinger equation is solved in the Born-Oppenheimer representation, including nuclear rotation, nuclear vibration, and electronic excitation, but neglecting the Coriolis and all non-adiabatic couplings. As ionization is omitted from the theory, the intensities explored are limited to those below the ionization threshold. This theoretical approach is a generalization of the previously discussed formulation for aligned molecules in section 3.2.1.3 which is solved using a similar numerical scheme [52]. However, in this approach, the molecule is also allowed to rotate in the laser field. To obtain distributions to compare to our KER-cos θ experimental data, the scattering solutions for each electronic channel are superposed to obtain a solution that asymptotically behaves as an outgoing plane wave [143]. The projection of the total time-dependent wave function after the pulse on this scattering solution gives the KER-cos θ distribution.

Figures 3.16(a) and (b) show the dissociation probability for the $v = 9$ and 3 states of H_2^+ from our time-dependent calculations, respectively. These states exemplify precisely the difficulties involved in observing high-order ATD from H($1s$) states, which will be referred to as ATD_1 hereafter, namely, the almost negligible probability for mechanisms requiring more than net two-photon absorption. To identify the different mechanisms in the figures, we use the facts that for ATD_1 the net absorption of an even or odd number of photons leads to dissociation on the $1s\sigma_g$ or $2p\sigma_u$ state, respectively. The tick marks may be used as a guide to the expected positions of the resulting peaks, showing also the contributions from the H($2l$) manifold. For $v = 9$, one-photon dissociation dominates as $v = 9$ is near resonance with the 1ω crossing. For low vibrational states, where contributions to high-order ATD are anticipated to be largest, e.g. $v = 3$, which is resonant with the 3ω crossing, the three-photon probability is still more than two orders of magnitude below

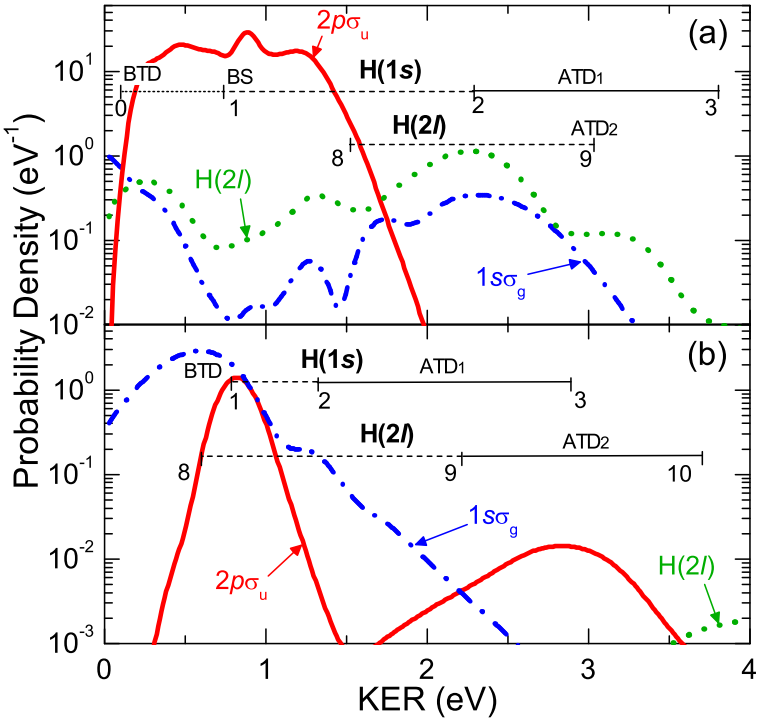

Figure 3.16: (a) Dissociation probability of the $v = 9$ H_2^+ level (10 fs, 10^{14} W/cm^2 pulse) showing final population contributions for the H($1s$) $1s\sigma_g$ and $2p\sigma_u$ and H($2l$) electronic states. (b) same as (a) for $v = 3$. Tick marks with labels denote net photons absorbed, indicating diabatic energy release from the initial v state to $E(R = \infty)$. (Figure adapted from our publication [42].)

the one and two-photon probabilities. Such a rapid decrease in probability for high-order ATD is evident in the early experimental work of Bucksbaum *et al.* [10] on H_2 at 532 nm.

Figure 3.16 also shows that the high vibrational states, e.g. $v = 9$, have a strong contribution to ATD from H($2l$) states, i.e. ATD_2, showing multiple peaks from the absorption of excess photons. As the H($2l$) states shown in figure 3.3(d) lie many photon energies above the H($1s$) manifold, such excitations are normally neglected in literature. However, as illustrated in the theoretical work of Nguyen-Dang *et al.* [144], their involvement can be important, and indeed is necessary, to explain observations of perpendicular transitions [140, 145] at 400 nm. In addition, Gibson *et al.* [146] recently reported a direct measurement of net eight-photon excitation of the H_2^+ $2s\sigma_g$ state using 800 nm light. Our results show both that the inclusion of excitation to the H($2l$) manifold is essential and that there is a non-negligible probability for ATD involving the H($2l$) states. In particular, the probability of ATD_2 is found to outweigh that of high-order ATD_1 in cases such as the one displayed in figure 3.16, further emphasizing the suppressed nature of the latter.

Figures 3.17(a) and (b) show Franck-Condon averaged (weighted average over all v states)

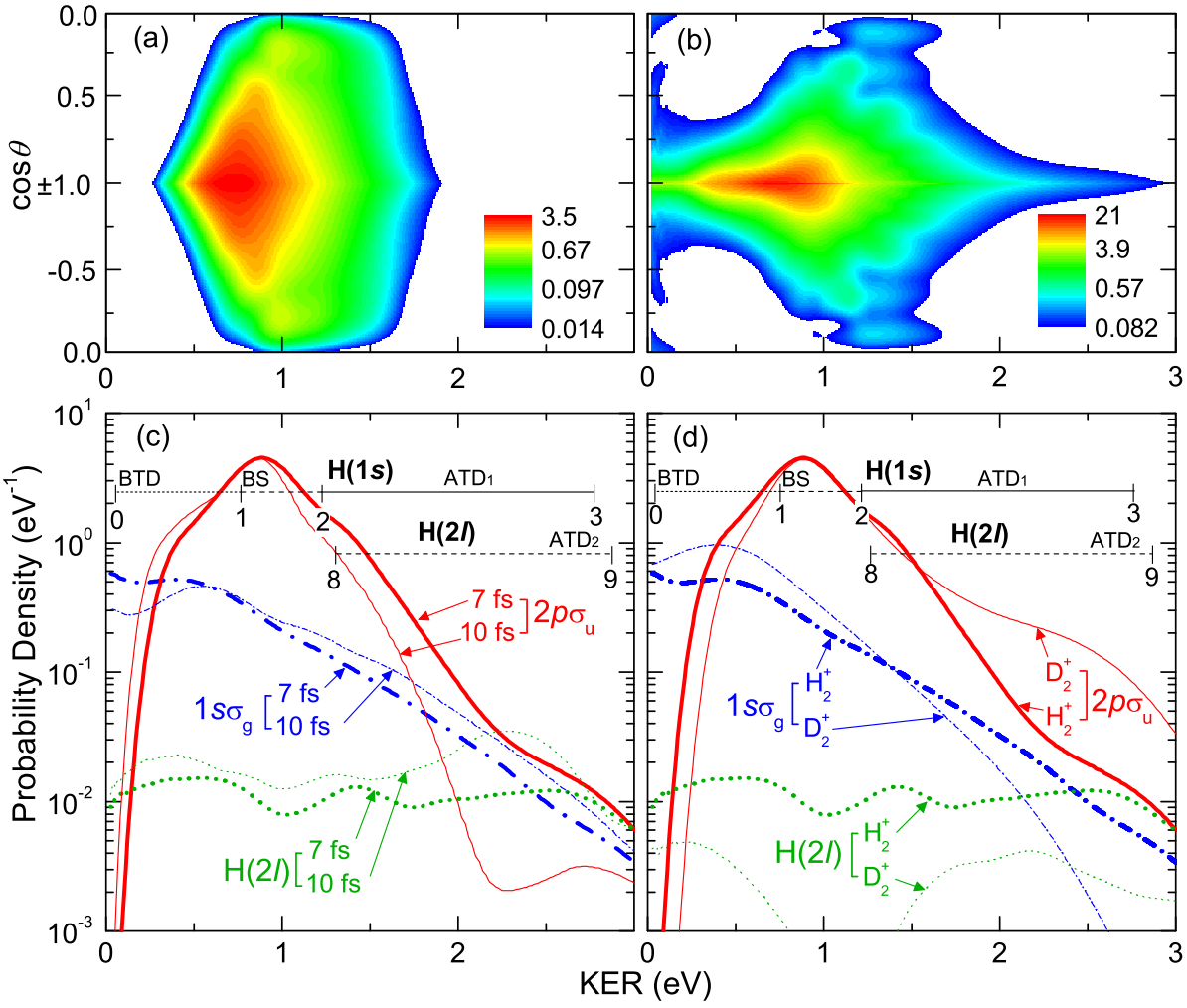

Figure 3.17: (a) Calculated KER-cos θ probability density (in units of $10^2(\cos\theta\text{eV})^{-1}$) maps for H_2^+ using 7 fs 2×10^{13} W/cm^2 pulses. (b) Same as (a) for 10^{14} W/cm^2. (c) Dissociation probability density at 10^{14} W/cm^2 for a 7 fs and 10 fs pulse showing $1s\sigma_g$, $2p\sigma_u$, and H($2l$) contributions with the peak value of their sum normalized. (d) Same as (c) for 7 fs H_2^+ and D_2^+ comparison. All probability densities are Franck-Condon averaged over all v states. Ticks with labels denote net photons absorbed, indicating diabatic energy release from curve crossings with the ground state to $E(R = \infty)$. (Figure taken from our publication [42].)

dissociation probabilities for a 7 fs pulse, as a function of kinetic energy release (KER) and $\cos\theta$. At 2×10^{13} W/cm^2 dissociation is almost exclusively due to one-photon absorption, as shown in figure 3.17(a). The angular distribution is characteristic of bond-softening (BS) [10, 13, 21] as illustrated previously for longer pulses, e.g. reference [52] and the 135 fs data above. However, increasing the intensity to 10^{14} W/cm^2 leads to several changes, as shown in figure 3.17(b). First, the overall spectrum becomes much narrower in angle. This is consistent with the fact that ATD requires a high effective field along the molecular axis to drive high-order parallel $\sigma \rightarrow \sigma$ transitions. Hence, by geometric alignment, ATD will preferentially dissociate those molecules aligned with the field. Second, the spectrum develops a striking high KER tail. To understand this tail, figure 3.17(c) shows a decomposition of this spectrum into the individual state contributions, revealing that while one-photon absorption is still the dominant channel, the tail is a mixture of ATD_1 and ATD_2 processes via three and nine photon transitions, respectively (see tick marks).

Comparison of the 7 fs results to a 10 fs pulse in figure 3.17(c) shows that the three-photon probability, i.e. $2p\sigma_u$ with KER $\sim$ 2.5 eV, is enhanced by almost an order of magnitude for the shorter pulse. Simultaneously, the two-photon probability, i.e. $1s\sigma_g$ with KER $\sim$ 1.8 eV, drops. This suggests that flux is being channeled from one process to the other — exactly the result sought to show closing of the $|1s\sigma_g - 2\omega\rangle \rightarrow |2p\sigma_u - 3\omega\rangle$ crossing. An additional order of magnitude enhancement in the three-photon probability is achievable by replacing H_2^+ with D_2^+, as is shown in figure 3.17(d). This isotopic dependence is caused by the more massive D_2^+ nuclear wavepacket taking longer to reach the $|1s\sigma_g - 2\omega\rangle \rightarrow |2p\sigma_u - 3\omega\rangle$ crossing. Thus, rather than following the adiabatic 2ω pathway, channel-closing diverts it into the 3ω channel. Interestingly, figure 3.17(c) and (d) show that ATD_2 follows the reverse trend to the high-order ATD_1 enhancement, getting suppressed for D_2^+ and shorter pulses. This would suggest that ATD_2 is similarly affected by channel-closing. A Floquet picture incorporating the H($2l$) states, as illustrated for $|2s\sigma_g - 8\omega\rangle$ in figure 3.15(a), shows that the excited states may indeed cross the dissociative $|2p\sigma_u - 1\omega\rangle$ curve at larger R, e.g. $|1s\sigma_g\rangle \rightarrow |2p\sigma_u - 1\omega\rangle \rightarrow |2s\sigma_g - 8\omega\rangle$. As the second step of such a sequence is time-delayed with respect to the first, the use of short pulses will, therefore, suppress the H($2l$)

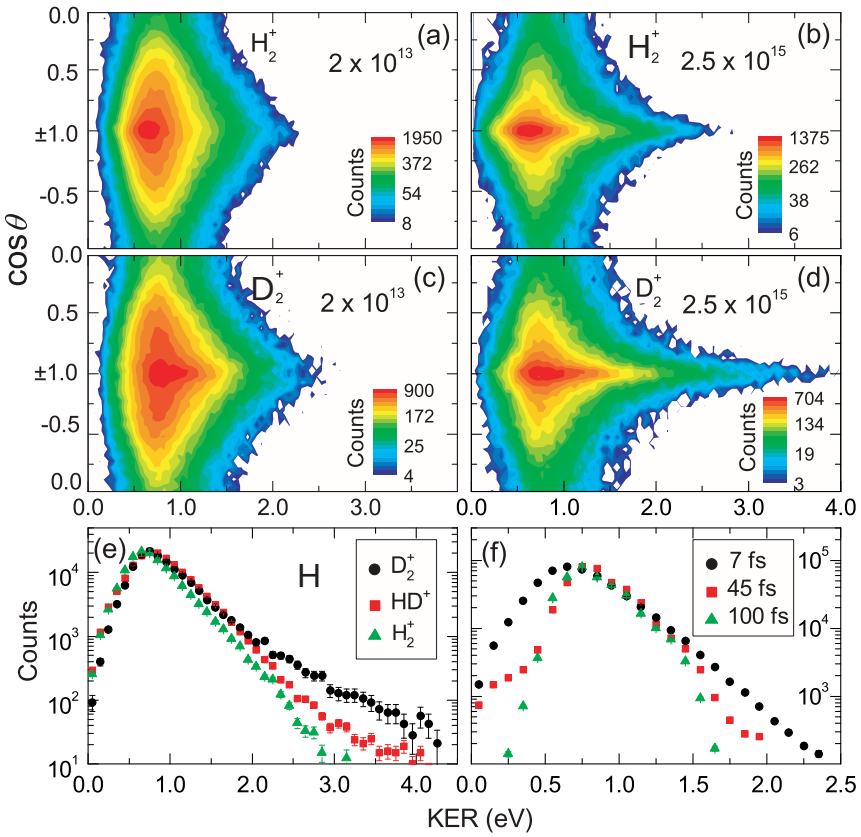

Figure 3.18: (a) and (b) Measured KER-cos θ distributions for dissociation of H_2^+ using 7 fs pulses at intensities shown (in units of W/cm^2). (c) and (d) Same as (a) and (b) for D_2^+. (e) Total dissociation yield as a function of KER for H_2^+, HD^+, and D_2^+ at 7.5×10^{15} W/cm^2 normalized to the peak number of counts. (f) Same as (e) for H_2^+ at different pulse durations of 7 fs, 45 fs, and 100 fs at similar peak intensity ($6.5 - 8.6 \times 10^{14}$ W/cm^2). (Figure taken from our publication [42].)

excitation step. These calculations indicate the largest suppression is for the $2s\sigma_g$ and $3p\sigma_u$ states.

3.2.3.4 Experimental results and interpretation

Figures 3.18(a) – (d) show the measured dissociation spectra of H_2^+ and D_2^+ for both low, 2.0×10^{13} W/cm^2, and high, 2.5×10^{15} W/cm^2, intensities.[53] The higher intensity does not match that given in figure 3.17(b) since the theory was limited to intensities below the onset of ionization, i.e. $\sim 2 \times 10^{14}$ W/cm^2. However, experimentally, the goal was to magnify the effects of ATD which are more apparent at high intensity, despite some ionization (~14%) that will deplete, particularly, the higher-order ATD channels. In addition, as a general rule, the experiment involves large focal volume averaging effects that act to reduce the effective intensity — the reason for the small ionization fraction at 2.5×10^{15} W/cm^2. These are not accounted for in this theory, and therefore

[53] We have excluded HD^+ from this discussion because of its heteronuclear nature which allows both transitions with even and odd numbers of photons between all states. For example, the $|1s\sigma\rangle \rightarrow |2p\sigma - 2\omega\rangle$ transition, which is forbidden for H_2^+ and D_2^+, is allowed for HD^+. Therefore, only H_2^+ and D_2^+ are considered so as to make a clean comparison.

experiment and theory should be compared only qualitatively.

At low intensity, the distributions observed for H_2^+ and D_2^+ are quite similar. This agrees with the calculated distribution shown in figure 3.17(a), which indicates that dissociation is predominantly one-photon, and hence we do not expect there to be a strong isotopic dependence. At higher intensity, this is not the case. Experiment and theory reveal similar distributions for H_2^+ despite the large difference in intensity, supporting our assertion of a lower overall effective intensity for the experiment. Most importantly, the signature high-KER tail is clearly observed. Moreover, it extends to almost the same maximum KER ($\sim$2.7 eV) as the theoretical prediction suggesting that it could similarly be a mixture of ATD_1 and ATD_2.

Comparison of H_2^+ to D_2^+ shows that this tail gets amplified and reaches much higher KER ($\sim$4.0 eV) for the more massive species. Recalling that in figure 3.17(d) ATD_2 was predicted to be suppressed and ATD_1 enhanced for D_2^+, the high KER enhancement is likely from three-, or more, photon ATD_1. This is also in agreement with our channel-closing argument. The mass dependence is elucidated in figure 3.18(e), which shows the signal, integrated across all angles, for all three isotopologues at an intensity of 7.5×10^{15} W/cm^2. While the low-energy parts are similar, the high-energy portions display a progressive increase in KER with increasing mass.

As a final test to show explicitly the temporal dependence of high-order ATD, we increased the pulse duration from 7 fs to 100 fs for H_2^+ while maintaining approximately the same peak intensity, as shown in figure 3.18(f). The high energy part of the spectrum clearly becomes enhanced for shorter pulse duration in agreement with the rest of our observations. Rather intriguingly, the low energy part (<0.5 eV) is also enhanced showing a strong pulse-length dependence. This contribution is most likely due to an increase in below-threshold dissociation (BTD), i.e. the portion of the nuclear wavepacket trapped in the vibrational trapping potential energy well being driven up in energy such that it can dissociate along $|1s\sigma_g - \omega\rangle$ potential with the absorption of zero net photons.

Another mechanism that, in principle, can explain the high KER we have seen is a five-photon transition following the adiabatic pathway to $|2p\sigma_u - 3\omega\rangle$. We believe this decay mechanism to be unlikely, however, because it requires a higher intensity than the three-photon transition. In

addition, calculations at 10^{14} W/cm^2 shows that the dominant contribution to the high KER observed comes from the vibrational states around the three-photon crossing with $1s\sigma_g$, and not the five-photon crossing (see pathways in figure 3.15). Nevertheless, we cannot rule out the possibility of at least weak five-photon contributions. There are a number of ways to experimentally test our argument. For example, laser pulse shaping could be used to produce a rapidly falling pulse to favor channel-closing without affecting the five-photon ATD rate. Alternatively, selecting a specific initial vibrational state would allow the different mechanisms to be separated much more cleanly, just as they were in the theoretical calculation.

3.3 Ionization of H_2^+

3.3.1 Introduction

At the high laser intensities used in our measurements, i.e. $\sim(10^{14}$–$10^{16})$ W/cm^2, the H_2^+ molecular ion can ionize as well as dissociate. In the ionization process, i.e. $H_2^+ + n\hbar\omega \rightarrow p + p + e^-$, the electron is removed from the system and the molecule fragments. In this section, our H_2^+ data will be compared to two models of ionization used to predict laser-induced molecular ionization structure. First, the charge resonant enhanced ionization (CREI) model developed by Zuo and Bandrauk [16] will be discussed. Second, the unified Floquet (UF) model developed by Esry *et al.* [38, 139] in conjunction with the measurements from our experimental group will be used to interpret the unexpected KER structure near the ionization appearance intensity.

3.3.2 Charge resonant enhanced ionization (CREI)[54]

3.3.2.1 Introduction

As has been seen in multiple measurements (e.g. [86, 147, 148]), ultrashort laser-induced ionization of H_2^+ produces a low KER feature which is interpreted as an enhancement to the ionization probability at internuclear distances, R, larger than the equilibrium distance. This phenomenon is commonly invoked in order to explain the low kinetic energy release (KER) of the "Coulomb exploding" protons (see, for example, the reviews [8, 33]). Zuo and Bandrauk [16] suggested that

[54] Much of the work in this section has been previously reported in one of our publication [38, 138, 139].

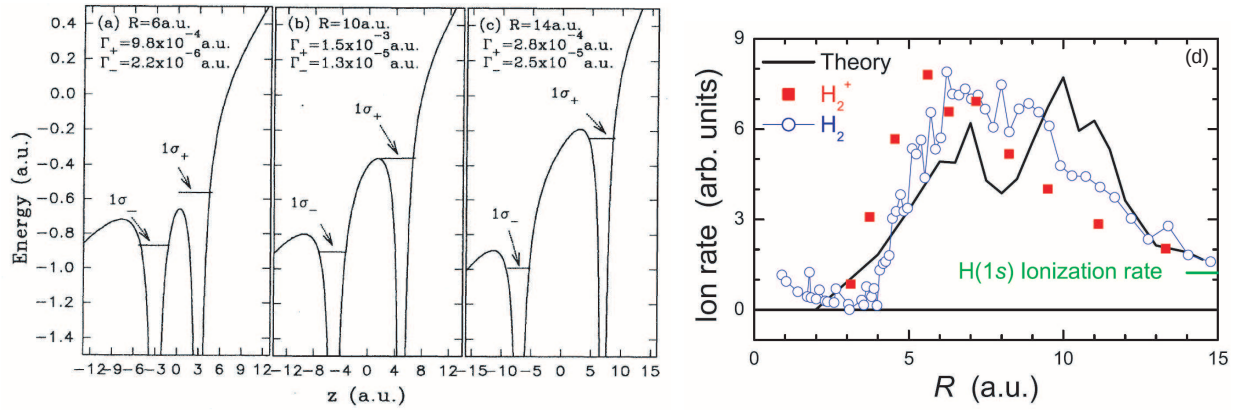

Figure 3.19: (a) – (c) The double well potential of H_2^+ in a dc electric field. (Taken from reference [16].) (d) Ionization rate as a function of the H_2^+ internuclear distance, R (H_2^+ data for $I_0 = 3\times10^{15}$ W/cm^2 from reference [82], H_2 data for $I_0 = 3.2 \times 10^{14}$ W/cm^2 from reference [135], and theory from reference [16]). (Taken from our publication [138].)

this enhancement in ionization is due to charge resonance enhanced ionization (CREI) around some critical internuclear distances that are larger than the equilibrium bond length of H_2^+. Their calculations predicted two prominent peaks in the ionization rate centered about an internuclear distance, R, of 7 and 10 a.u.. In a simplified two Coulomb-well model, CREI occurs when the bound state in the upper well is above the potential barrier between the two wells, as shown in figures 3.19(a) – (c). Therefore, one would expect CREI to be independent of the laser color and shift slowly to smaller R with increasing laser intensity [16]. This prediction initiated both further theoretical work on the KER structure of CREI and experimental work trying to reveal it (e.g. [148–150]).

Gibson *et al.* [135] and Williams *et al.* [82] tailored their experimental conditions to enable the study of CREI, the former using a transient H_2^+ formed early in the laser pulse from H_2 and the latter using a H_2^+ molecular ion beam. These measurements are in good agreement with each other and with the theoretical prediction that ionization is enhanced for stretched molecules. However, as shown in figure 3.19(d), the data does not support the prediction of a large second maximum

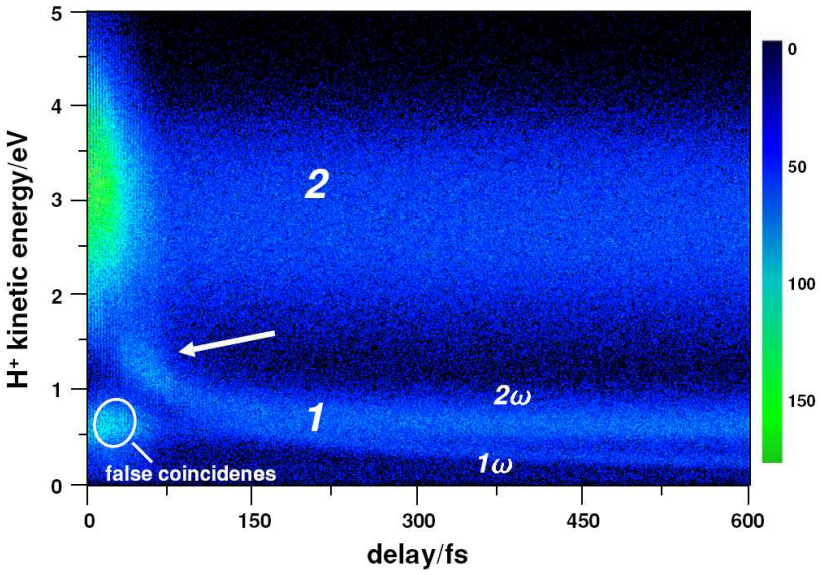

Figure 3.20: Pump-probe measurement of H_2^+ ionization/dissociation by Ergler *et al.* [39]. This experiment was performed starting from a neutral H_2 target and is plotted as a function of KER and the delay between two identical 25 fs laser pulses. The intensity of each pulse was 2×10^{14} W/cm^2. The arrow indicates an enhancement of the H_2^+ ionization rate attributed to ionization at $R \sim 10 - 11$ a.u.. (adapted from reference [39].)

around R=10 a.u..[55] It has been suggested that the second enhanced ionization peak is hard to observe because of depletion by ionization at the first enhanced ionization. Furthermore, the second enhanced ionization peak yields low KER, therefore making it hard to distinguish from the fragments of dissociation in these experiments [82].

Recently, Ergler *et al.* [151] reported that they found a clear signature for the second enhanced ionization maximum using a pump-probe technique.[56] The measured KER and ionization rate as a function of time delay between the two pulses allows the identification of the dissociation pathway before ionization by the second pulse [151, 152]. This measured time delay is then converted to internuclear distance information using classical motion on the $2p\sigma_u$ potential energy curve. However, this recent evidence for the second enhanced ionization peak, which is denoted by the arrow in figure 3.20, may be in question as it appears at the time delay where H_2^+ ionization of the 1-photon and 2-photon dissociating processes overlap and the pump-probe pulses are not well separated in time. To make the situation even more interesting, ongoing experimental efforts to uncover this structure [39, 153] have reached nearly opposite conclusions about its existence.

[55] It is important to note that in both experiments, the internuclear distance was evaluated from the measured KER in order to compare the experimental data to "frozen"-nuclei calculations. To perform this transformation, one has to adopt some model, and doing so will affect the results as will be discussed momentarily. Explicitly, the latter group used the Coulomb explosion model (i.e., KER = $1/R$), while the former subtracted the average dissociation energy of the H_2^+ from the measured KER before employing the Coulomb explosion model.

[56] The pump-probe technique is discussed in section 2.4.

In this section we will present measurements of the ionization of an H_2^+ beam for which ionization is directly separated from dissociation along with the results of a pump-probe measurement starting from H_2 conducted by Cocke's experimental group (e.g. [153]). The results of both these measurements reveals no evidence for the elusive second enhanced ionization peak, but rather a single broad KER peak. Furthermore, it is argued that the predicted structure in the ionization probability for frozen nuclei is washed out by the motion of the nuclei during the laser-molecule interaction and by intensity averaging. The H_2^+ measurements presented here were performed under identical conditions to those of the 45 fs H_2^+ dissociation discussed in section 3.2.2.

3.3.2.2 Results and discussion

Molecular ion beam measurement The measured KER, displayed in figure 3.21(a), clearly shows a single broad peak around 4.7 eV and not a double-peak structure. This distribution is similar to the one measured previously [82], but the uncertainty at the low KER end has been removed. It is expected that the interaction between the laser field and the H_2^+ will initiate dissociation of the vibrational states within the energy gap at the avoided crossing, as shown in figure 3.21(b). Taking the v=9 state, which is expected to be the first state to dissociate, and adding the kinetic energy gained during the dissociation up to $R = 7$ a.u. (where the first CREI peak is expected) to the energy gain for the Coulomb repulsion at this distance yields 4.6 eV, thus suggesting that the measured KER peak is associated with the first enhanced ionization peak. In contrast, ionization at R=10, where the second CREI peak is expected, yields about 3.4 eV and the data does not show any significant structure around this energy. Neither does it show any contribution at the low KER ($\lesssim$1.5 eV) as reported recently by Pavičić *et al.* [85] for enhanced ionization of a D_2^+ beam exposed to $\sim 1 \times 10^{14}$ W/cm^2, 350 fs laser pulses. The structure they observed around R=8, 11 and 15 a.u. might be due to multi-photon resonances near the ionization appearance intensity [38].

One may argue that the pulse intensity might drop before the dissociating H_2^+ stretches to R=10 a.u., thus suppressing the ionization there. However, given that the data shown above illustrates that the dissociation of the v=9 state begins at intensities below 10^{13} W/cm^2 [52], we expect the intensity to still be increasing during the passage through R=10 a.u. for a 40 fs laser pulse as it takes

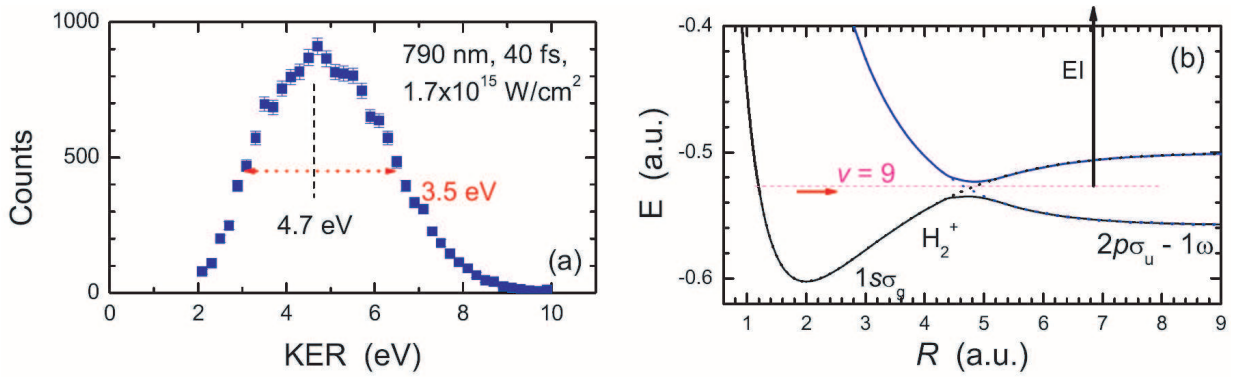

Figure 3.21: H_2^+ measurements. (a) Measured KER distribution of H_2^+ and (b) a schematic PEC diagram for the H_2^+ ionization and dissociation. The arrow labeled EI (enhanced ionization) marks the internuclear distance where ionization is expected to be enhanced. (Figure taken from our publication [138].)

about 13 and 22 fs for the H_2^+ to stretch from the curve crossing to R=7 and 10 a.u., respectively.[57] Another concern is that the population of the v=9 state was depleted by the enhanced ionization around R=7 a.u.. However, our data suggests the contrary, as the measured rate of dissociation of this vibrational state is not negligible, thus indicating that a significant fraction of the H_2^+ molecules passed through both enhanced ionization regions without being ionized. That said, we should be cautious about identifying contributions to dissociation from specific vibrational states solely based on their KER, as we have seen above that KER is often not enough to distinguish one dissociation process from another [52, 82].

Depletion To further investigate if depletion of the dissociation nuclear wavepacket due to ionization at the first CREI critical distance is the reason for the absence of a second ionization peak, Esry *et al.* [137, 139] computed the time evolution of each vibrational state during the laser pulse used in our experiment.[58] Molecules are assumed to be aligned and the time evolution is performed starting with a field-free vibrational state (each vibrational state is treated independently) well before the laser pulse. The time evolution is then carried out until the peak of the laser pulse at

[57] This is approximated using classical motion of the nuclei on the adiabatic Floquet potential energy curves.

[58] The same procedure of solving the time-dependent Schrödinger equation in the Born-Oppenheimer representation as described in section 3.2.1.3 was used here.

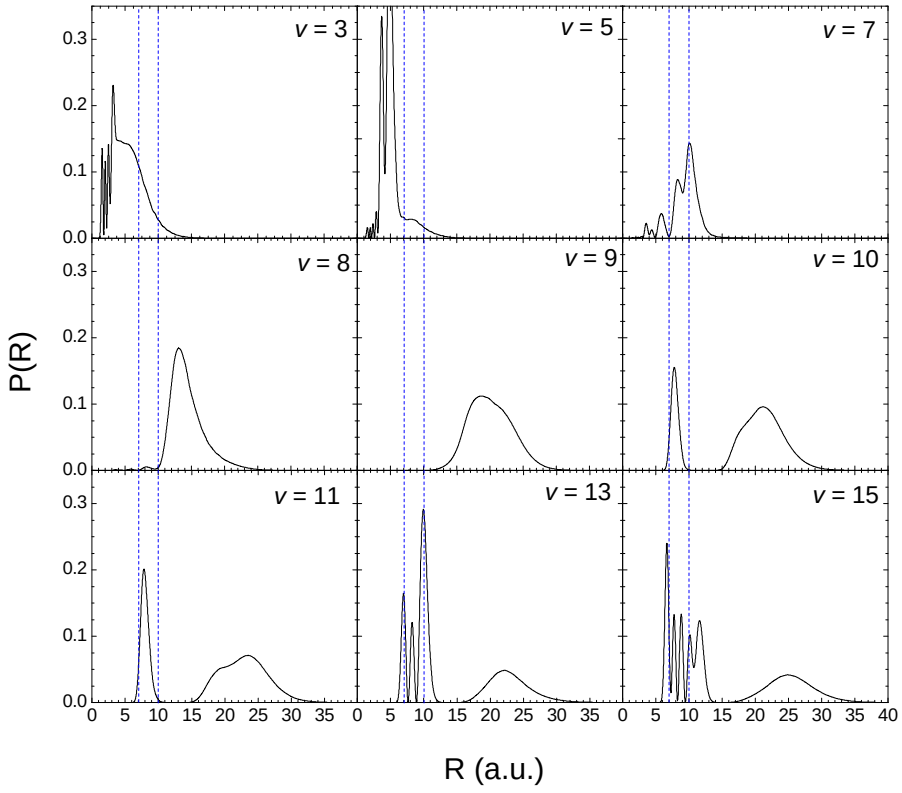

Figure 3.22: Calculated probability distribution of the H_2^+ nuclear wavepacket for various v-states, i.e. $|\Psi_v(R)|^2$. The H_2^+ molecule is aligned with the laser field and subjected to a $I_0 = 10^{14}$ W/cm^2, $\tau = 45$ fs laser pulse. Each vibrational state is treated separately and allowed to evolve in time from well before the pulse to the peak of the laser pulse. The particular vibrational state is displayed in the corresponding frame. The vertical lines mark the critical distances expected from CREI [16]. (Adapted from reference [139]. See text for discussion.)

which time the probability distribution of the nuclear wavepacket is retrieved. For example, in figure 3.22 the aligned H_2^+ molecule is exposed to a $I_0 = 10^{14}$ W/cm^2, $\tau = 45$ fs, $\lambda = 790$ nm laser pulse and the probability distribution for several initial vibrational states are plotted as a function of R at the peak of the laser pulse, i.e. at the instant when ionization is most likely. From these distributions, one can see that there is significant probability for the nuclear wavepacket to be near one or both of the critical distances for various initial vibrational states as shown in the Franck-Condon averaged distributions shown in figure 3.23. Therefore, depletion at the first critical distance should not have an effect on ionization at the second critical distance.

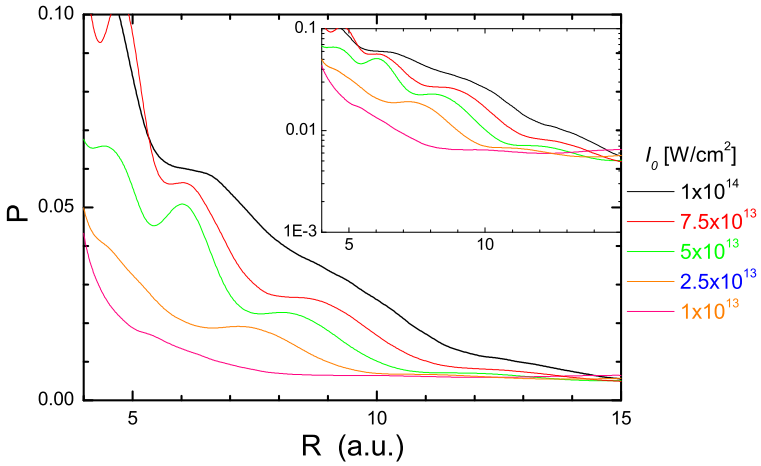

Figure 3.23: The probability distribution of the Franck-Condon averaged H_2^+ nuclear wavepacket, P, as a function of internuclear distance, R. The H_2^+ molecule is aligned with the laser field and subjected to a $I_0 = 10^{14}$ W/cm^2 $\tau = 45$ fs laser pulse. Each vibrational state is treated separately and allowed to evolve in time on the adiabatic Floquet potential-energy curves from well before the pulse to the peak of the laser pulse. The initial vibrational population is weighted by the Franck-Condon factors for the vertical transition from H_2. (inset) same as main figure, but on a log scale. (Adapted from reference [139]. See text for discussion.)

Pump probe measurement To further remove the uncertainty due to depletion, we will also consider the results from a pump-probe measurement for which depletion at a smaller R cannot occur [138, 153]. The pump-probe measurements were conducted by Cocke's experimental group using a cold target recoil ion momentum spectroscopy (COLTRIMS) technique described in detail in section 2.4 and elsewhere [152]. In brief, a cold supersonic jet of molecular hydrogen (D_2 was used for practical reasons) was crossed with a linearly-polarized laser beam from the same Ti:Sapphire source described in the H_2^+ measurement above. Shorter laser pulses of about 10 fs, i.e. the ultrashort pulses described in section 3.2.3, were used to reduce the overlap in time between the pump and the probe. The pump pulse, with a peak intensity of 3×10^{14} W/cm^2, ionized the D_2 target molecules and also launched the nuclear wave packet of the reaction channel of interest, namely bond softening. This pulse was followed by a more intense probe pulse, with a peak intensity of 9×10^{14} W/cm^2. The time delay between the two pulses was scanned over a 100 fs range while maintaining a good spatial overlap as explained by Alnaser *et al.* [152].

The peak intensity of the pump pulse was kept low enough to minimize contributions from

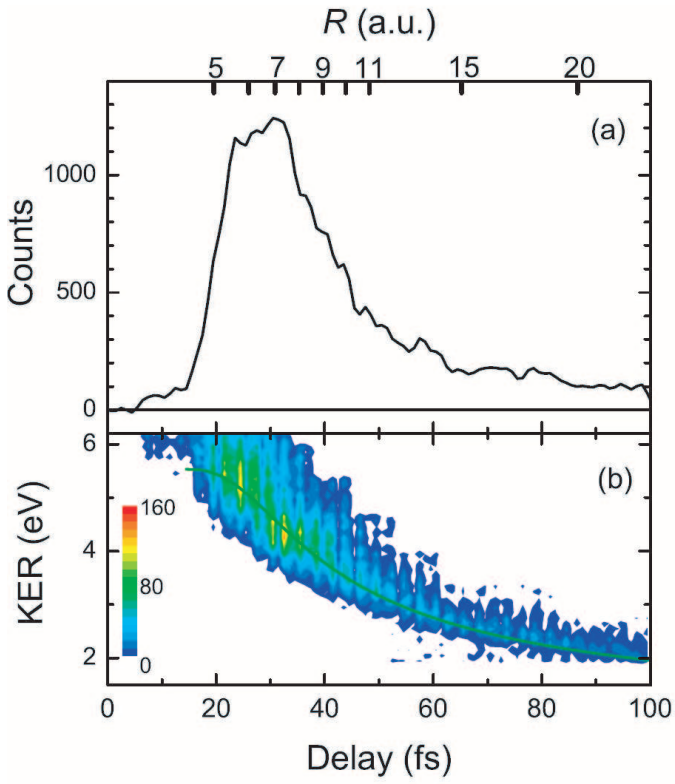

Figure 3.24: D_2 pump-probe measurements. (a) Measured time-delay distribution (note the associated value of R marked on the top axis), and (b) measured time delay-KER distribution. Note that the data in (b) follow the calculated bond softening (BS) dissociation path - solid line (see text). (Figure taken from our publication [138].)

ATD.[59] The bond softening and above threshold dissociation mechanisms can be tracked in time and distinguished from each other by the trace they follow on a KER vs time-delay plot (see, for example, references [40, 152]). It has been shown by Alnaser *et al.* [152] that only bond softening has a significant contribution to the time delay-KER data shown in figure 3.24(b). Furthermore, they showed that this data is described well by a classical time evolution of the dissociating D_2^+ molecule on the $2p\sigma_u$ state starting from the curve crossing with the $1s\sigma_g$ state a short time (∼12 fs, i.e. roughly the time it takes the nuclear wave packet of D_2^+ to reach the crossing) after the pump pulse (see line in figure. 3.24). This model allows the evaluation of the internuclear distance as a function of time and the conversion from time delay to R shown on the top axis of figure 3.24(a). It can clearly be seen from this distribution that ionization is enhanced around R=7 a.u. and, more importantly, that the second enhanced ionization peak around R=10 a.u. is missing. Independent of any model used to convert time delay to R, the raw data exhibits a single enhanced ionization

[59] This is a difficult configuration to obtain as it takes $\gtrsim$ 10 (790 nm) photons to ionize H_2 and only an additional 2 photons to facilitate ATD in the resulting H_2^+.

peak in agreement with our H_2^+ results shown before.

3.3.2.3 Summary

Both the ionization of an H_2^+ ion beam and the pump-probe measurements of a D_2 target yield the same qualitative result. Namely, ionization is enhanced at large R, but instead of the predicted double-peak structure, only a single broad peak is observed. It is important to note that in both measurements, the KER is a measurable, but the internuclear distance R is not. Thus, the best comparison with theory can be accomplished if theory computes the measurable quantities for each experiment directly. In addition, it is important to include the nuclear vibrational motion in the ionization calculations. Freezing the nuclei for the computation of the ionization probability might simplify the problem, but there is no realistic way to measure the ionization of stretched molecules while keeping the nuclei frozen.[60] Moreover, the dissociation energy is not negligible in comparison with the Coulomb explosion energy in the case of enhanced ionization at large R.

Lacking calculations of the specific observable quantities in both measurements, we are forced to convert the KER data to an internuclear distance in order to compare with theory, in particular with the predicted structure. As a byproduct, this conversion facilitates a direct comparison of the two measurements. Following the success of the classical time-evolution model in fitting the time delay-KER distribution of ionization from the bond softening dissociation of D_2 [152], we applied a similar model to the dissociation of the H_2^+ target. As discussed previously, we expect the v=9 state to dissociate through the energy gap, shown in figure 3.21(b), early in the laser pulse and gain a kinetic energy $E_D(R)$ with respect to the $2p\sigma_u$ curve. Upon ionization at R, the protons gain an additional energy of $1/R$, thus resulting in a measured KER $= E_D(R)+1/R$, where $E_D(R) = E_{v=9} - E_{2p\sigma_u-1\omega}(R)$. Using this model, the measured KER distribution shown in figure 3.21(a) was converted to the R distribution shown in figure 3.25(a), where it is also compared with the distribution derived from the pump-probe measurements. The agreement between the two is very good except for the high R tail which is associated with the low KER (or long time

[60] Although an attosecond probe pulse would effectively remove nuclear change in internuclear distance during the probe, the non-zero velocity of the nuclear wavepacket may play an important role in the ionization yield.

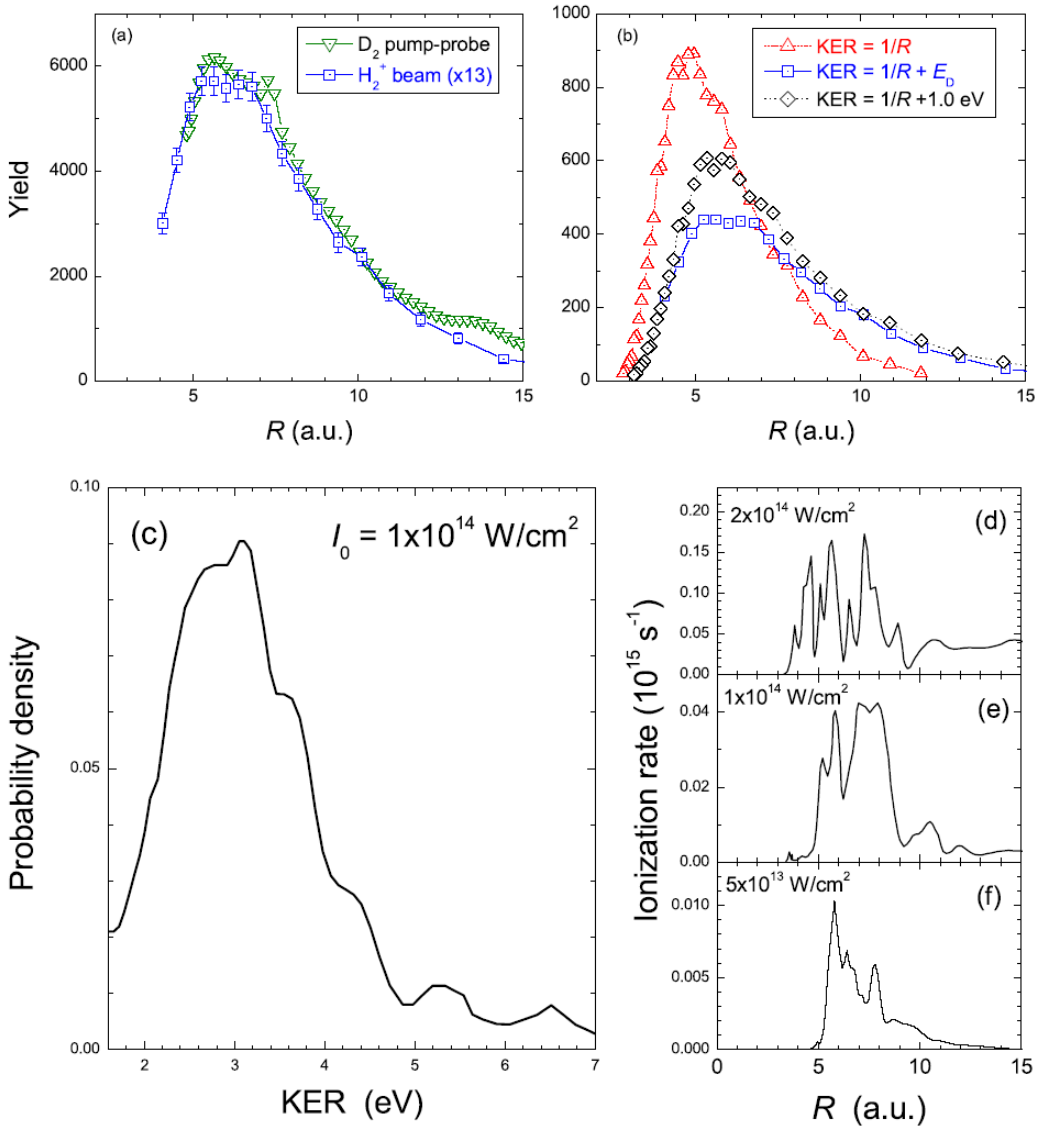

Figure 3.25: (a) The measured ionization rate as a function of internuclear distance, R, derived from the H_2 pump-probe and H_2^+ molecular-ion beam measurements (see text). (b) comparison of a few models used to convert the measured KER to R. Explicitly, the Coulomb explosion model for which KER $= 1/R$, subtracting the average dissociation, i.e. $\langle E_D \rangle = 1.0$ eV, energy KER $- 1.0 = 1/R$ [135], and our model, i.e. KER $- E_D(R) = 1/R$ (see text). (c–f) CREI theory from Chelkowski *et al.* [154]: (c) proton KER spectrum including nuclear motion, and (d-f) frozen nuclei calculation for a few peak intensities. Note that the KER range in (c) matches the relevant range of R in (d-f). (Figure taken from our publication [138].)

delay) data that is of lesser quality. This conversion, however, is very sensitive to the model used to transform the KER to R, as shown in figure 3.25(b), and it should be used with caution. Furthermore, converting the measured H_2^+ KER distribution using the $E_D(R)$ that is expected for a net 2-photon ATD pathway yields a similar result. This reinforces the statement above preferring a direct comparison with theoretical calculations of the measurable quantities. However, in spite of these limitations, the data strongly suggests the existence of a single broad enhanced ionization peak.

There are a couple of reasons which are most likely responsible for the absence of the predicted second peak. First, and most important, the nuclear motion washes out the KER structure, e.g. in the calculations by Chelkowski *et al.* [154] for a 40 fs, 600 nm laser pulse interacting with H_2^+ shown in figure 3.25(c). In addition, as shown in figures 3.25(d)–(f), the structure in the ionization rate changes significantly with laser intensity, which is important as the spatial distribution of intensities imposes an intensity averaging on any measurement (see section 2.6), further smearing any expected structure. If there is any hope to observe such structures in the ionization rate, it is crucial to have calculations including these effects to suggest under what conditions they might be observed.

In this section, we presented compelling experimental evidence suggesting that H_2^+ ionization for high intensity short laser pulses is enhanced for a wide range of internuclear distances, approximately around R=7 a.u.. This distribution was found to be structureless. More importantly, it is suggested that the structure predicted by frozen nuclei calculations is washed out by nuclear motion, and that intensity-averaging effects should smear any structure further.

3.3.3 The unified Floquet picture[61]

3.3.3.1 Introduction

Charge-resonance enhanced ionization (CREI), as discussed above, is a mechanism often used to describe the molecular ionization process (e.g. $H_2^+ \rightarrow p+p+e^-$). This mechanism [16] is an extension of the atomic tunneling picture of strong field ionization [8] to H_2^+. However, the two-center nature

[61] Much of the work in this section has been previously reported in our publications [38].

of H_2^+ is a nontrivial change which leads to enhanced ionization at particular internuclear distances. In contrast to this picture, in this section we will discuss a mechanism we recently proposed [38] for molecular ionization near the appearance intensity that produces a sequence of peaks in the nuclear kinetic energy spectrum separated by the photon energy. While much is understood about the laser-induced ionization and dissociation of simple molecules [8, 16, 33], a model that describes the nuclear dynamics for both processes on an equal footing has been lacking until recently. Just such a model will be described in this section and supported by experimental data from our measurements of H_2^+ ionization.[62] Our interpretation is based on the Floquet picture [53] described in detail in section 1.4, which, unlike the aforementioned CREI description, includes nuclear motion during an intense laser pulse. In this picture, we will use the same concepts previously discussed, e.g. bond softening (BS), vibrational trapping (VT), and above-threshold dissociation (ATD), to describe both ionization and dissociation using a single picture.

The unified Floquet (UF) model presented here [38] describes both dissociation and ionization from a multiphoton point of view. That is to say, in a regime where the Keldysh parameter γ is $\gtrsim 1$. The Keldysh parameter [8],

$$\gamma = \sqrt{\frac{E_b}{2U_p}}\ , \tag{3.3}$$

where E_b is the electronic binding energy and U_p is the ponderomotive energy,[63] is often used to quantify what constitutes "high" and "low" laser intensities. When $\gamma \gg 1$, the system is said to be in the multiphoton regime; and when $\gamma \lesssim 1$, in the tunneling regime. Therefore, as we will be describing ionization via a series of n-photon transitions, we need to be in the multiphoton regime where there is explicit reference to photons. However, the separation of intense laser-matter interactions into two regimes constitutes more a guideline than strict rules as both can be useful for $\gamma \approx 1$ and each picture is sometimes useful in the other regime.[64] In typical H_2^+ experiments [36, 82, 84, 85] where $\lambda = 790$ nm and $I_0 = 10^{14}$ - 10^{15} W/cm^2, γ hovers within about a factor of

[62] Although we will base our discussion on the ionization of H_2^+ in a linearly polarized laser field, the essential ideas and benefits of our model should generalize to more complicated systems.

[63] U_p is the cycle-averaged energy of a free electron in the laser field and is proportional to I/ω^2, where I is the laser intensity and ω is its carrier frequency.

[64] The standard description of H_2^+ dissociation in terms of the adiabatic Floquet potentials is fundamentally a multiphoton one, while the CREI picture is based on tunneling.

2 of unity for the whole range of internuclear distance R. Therefore, our multiphoton description should yield an interpretation complementary to that based on tunneling in this $\gamma \approx 1$ regime. Furthermore, as we want γ to be as small as possible, our model should work best for ionization at intensities near the appearance intensity.

3.3.3.2 Unified Floquet (UF) model

The primary goal of the model created by Esry [38] is to be able to treat both ionization and dissociation of molecules within a single self-consistent picture including nuclear motion. The essence of the model is to reduce the problem, as much as is possible, to effective Born-Oppenheimer potential curves so that we can understand the dynamics in terms of the simple curve crossings used to predict H_2^+ dissociation behavior above. We introduce the Born-Oppenheimer curves representing ionization in a manner exactly analogous to the dissociation curves. While these curves, in principle, represent the whole continuum of possible photoelectron energies, for the purposes of our model we only draw the curve representing the field-free ionization threshold, i.e. $E_{\text{electron}} = 0$. Upon inclusion of the photon label, these ionization threshold curves, i.e. $1/R - n\omega$, cut across the dissociation curves as shown in figure 3.26(b).[65] These ionization threshold potential curves can be viewed as an analogy to the Floquet picture, or they can be viewed as simply a convenient way to count photons. In our model, however, all photon counting – whether for dissociation or ionization – is carried out in exactly the same way in a single picture.

It is clear from figure 3.26(b) that critical values of R occur where the ionization threshold potentials cross the dissociation potentials. We expect that these crossings will correlate to enhancements in the nuclear KER spectrum when the intensity is just above the threshold for ionization. In other words, the model predicts that, for intensities near the ionization appearance intensity, there will be structure in the KER corresponding to ionization at internuclear distances matching the positions of the curve crossings shown in figure 3.26(b).[66] Further, we expect this structure to disappear as

[65] Dipole selection rules do not restrict these curves since continuum electron states of all symmetries exist at each energy.

[66] Many of these crossings can be interpreted as a manifestation of resonantly-enhanced multiphoton ionization (REMPI). In fact, Madsen and Plummer [155] have shown that REMPI does enhance the ionization rate at critical R values in nonperturbative Floquet calculations for H_2^+.

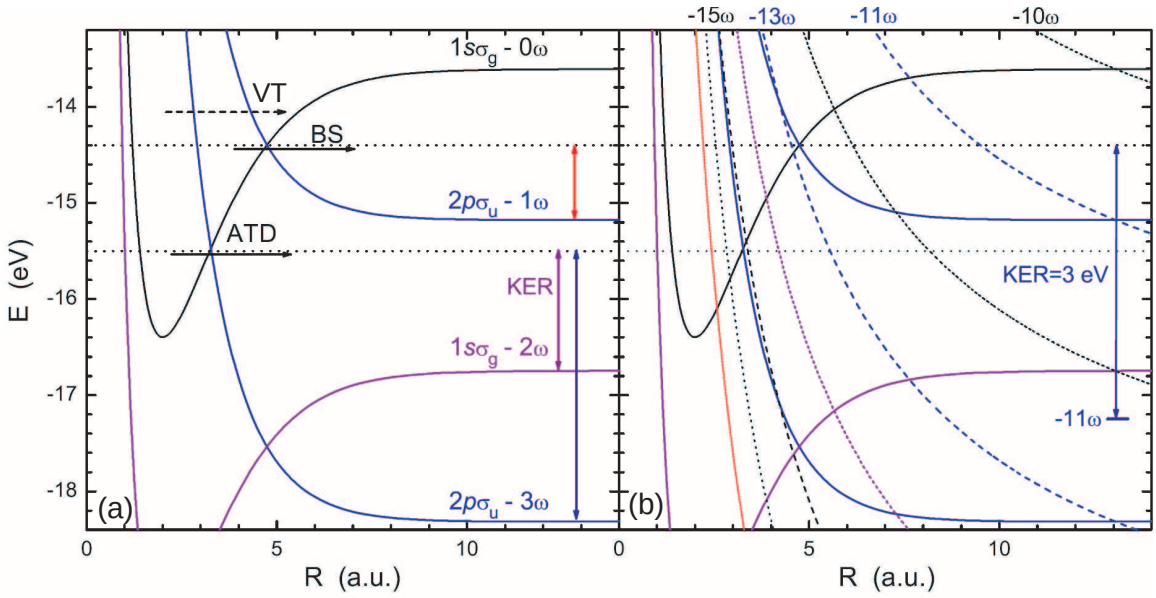

Figure 3.26: (a) The diabatic Floquet potentials for H_2^+. Besides the molecular quantum numbers, each curve carries a photon number label. (b) The same as (a), but including the ionization threshold potentials. Bond softening (BS), vibrational trapping (VT), and above-threshold dissociation (ATD) are discussed in section 3.2.1.1. (Figure taken from our publication [38].)

the intensity is increased since the coupling gets stronger, driving transitions over a wider range of R, yielding broader KER peaks.

To determine which crossings in figure 3.26(b) are most important we can assert three general rules. First, as we are in the multiphoton regime, transitions requiring the fewest number of photons will dominate. Second, the laser pulse needs to be long enough for the nuclear wavepacket to reach the crossing.[67] Third, the pulse must be intense enough to drive the transition when the nuclear wavepacket passes through the crossing. These principles are certainly more qualitative than quantitative. Therefore, although the relative widths of these transitions and intensities cannot be predicted quantitatively, the qualitative trends in KER peak position can be discerned. Furthermore, given a particular experimental spectrum, we can predict both how it will change with the laser parameters and the angular distribution of the nuclear fragments for each KER peak

[67] The nuclei in H_2^+ take about 2.7 fs to move 1 a.u. with 1 eV of kinetic energy. A more detailed discussion of the propagation of various vibrational states with respect to the laser pulse's intensity envelope is discussed in section 3.3.2.2 and shown in figures 3.22 and 3.22.

via the number of photons involved in the transition.

To exemplify the model, let us consider the dissociation and ionization of H_2^+ in a 790 nm, $\gtrsim 10^{14}$ W/cm^2 laser pulse using figure 3.26(b). First, as the intensity rises to $\sim 10^{12}$ W/cm^2 on the leading edge of the pulse, nuclear vibrational states $v \simeq 9$ can move via bond softening (BS) from $|1s\sigma_g\rangle$ to $|2p\sigma_u - 1\omega\rangle$. Second, the dissociating wave packet can ionize via the crossings with the $|1/R - 13\omega\rangle$ to $|1/R - 10\omega\rangle$ ionization curves. This two-step process will lead to KER peaks corresponding to each of the likely $|2p\sigma_u - 1\omega\rangle \rightarrow |1/R - n\omega\rangle$ crossings, i.e. if the $|2p\sigma_u - 1\omega\rangle$ and $|1/R - n\omega\rangle$ cross at R_n, then the KER should peak around $1/R_n + E_D$, where E_D is the kinetic energy of the dissociating nuclear wavepacket at the instant of ionization. These peaks form a sequence separated by $\sim \hbar\omega$, and are the result of a qualitatively new mechanism for molecular breakup, i.e. a two-step process involving dissociation (BS in the example above) and molecular ATI, which we call above threshold Coulomb explosion (ATCE) or more generally BS-UFI which denotes bond softening (BS) followed by unified Floquet picture ionization (UFI).

Considering only H_2^+ dissociation via BS for a moment, the specific crossing $|2p\sigma_u - 1\omega\rangle \rightarrow |1/R - n\omega\rangle$ at which the dissociating wavepacket ionizes is roughly determined from the pulse duration. This is because the nuclear wavepacket will begin to experience BS at $\gtrsim 10^{14}$ W/cm^2 and will tend to ionize at the peak of the laser pulse. Therefore, the most effective ionization crossing will be the one which intersects the $|2p\sigma_u - 1\omega\rangle$ state at an internuclear distance R_I that corresponds to the distance traveled by the nuclear wavepacket in the amount of time it takes the laser pulse to rise from $\gtrsim 10^{14}$ W/cm^2 to its peak.[68] For example, ionization at the $|1/R - 13\omega\rangle$ crossing can occur if the pulse intensity ramps up fast enough that the dissociating wavepacket has not yet traveled beyond the $|1s\sigma_g\rangle \rightarrow |2p\sigma_u - 1\omega\rangle$ avoided crossing when the intensity reaches its peak.[69] The resulting peak will produce a KER of $\lesssim 6.1$ eV and likely be fairly broad due to the large $|1s\sigma_g\rangle \rightarrow |2p\sigma_u - 1\omega\rangle$ coupling. As the pulse becomes longer, the nuclear wavepacket will have a longer time to travel along the $|2p\sigma_u - 1\omega\rangle$ before ionizing. Additionally, the $|1s\sigma_g\rangle \rightarrow |2p\sigma_u - 1\omega\rangle$

[68] The exact intensity when BS begins to occurs is dependent upon the vibrational level, v. Additionally, higher vibrational levels will have higher nuclear kinetic energy, which is equivalent to an increase in the nuclear wavepacket velocity, and a decreased transit time to a particular crossing.

[69] This requirement is less restrictive than it might appear since the wavepackets velocity decreases substantially in this crossing.

coupling becomes weaker with an increase in R. Thus, for longer pulses, the effective ionization curve $|1/R - n\omega\rangle$ (i) will require fewer photons, i.e. smaller n, (ii) will intersect the $|2p\sigma_u - 1\omega\rangle$ curve at larger internuclear distance R_n, (iii) will produce a sharper KER peak due to the smaller $|1s\sigma_g\rangle \rightarrow |2p\sigma_u - 1\omega\rangle$ and $|2p\sigma_u - 1\omega\rangle \rightarrow |1/R - n\omega\rangle$ couplings, and (iv) will produce KERs with smaller values, i.e. $\sim 1/R_n + E_D$. For example, the nuclear wavepacket takes approximately 8.5 and 23.5 fs to reach the $|2p\sigma_u - 1\omega\rangle \rightarrow |1/R - 12\omega\rangle$ at $R \simeq 7$ and $|2p\sigma_u - 1\omega\rangle \rightarrow |1/R - 11\omega\rangle$ at $R \simeq 13$ a.u., respectively. The KER peaks expected from these channels are 4.5 eV for $|1/R - 12\omega\rangle$ and 3.0 eV for $|1/R - 11\omega\rangle$. The ionization probability from $|1/R - n\omega\rangle$ for $n < 11$ is expected to be small as these states intersect $|2p\sigma_u - 1\omega\rangle$ at much larger distances, e.g. $R_{10} \simeq 45$ a.u..

Up to this point we have only considered ionization in the UF picture being initiated via BS. However, as we have shown in the H_2^+ dissociation discussed earlier in this chapter, VT and ATD are also important dissociation mechanisms that must be considered. In both of these cases, the initial dissociation step will be followed by ionization at the crossing with the $|1/R - n\omega\rangle$ curve. For example, for ionization in the unified Floquet picture preceded by ATD, which will be labeled ATD-UFI, the nuclear wavepacket will dissociate via the $|1s\sigma_g\rangle \rightarrow |2p\sigma_u - 3\omega\rangle$ avoided crossing and then ionize near the peak of the laser pulse at the $|1s\sigma_g - 2\omega\rangle \rightarrow |1/R - n\omega\rangle$.[70] The pulse width dependence for ATD-UFI will follow the same trend as BS. However, the nuclear wavepacket will (i) move faster after the initial curve crossing due to the larger kinetic energy gained from the energy difference between the $|1s\sigma_g\rangle \rightarrow |2p\sigma_u - 3\omega\rangle$ avoided crossing and the $|1s\sigma_g - 2\omega\rangle$ asymptotic value and (ii) require an intensity greater than BS to achieve the initial dissociation step as the $|1s\sigma_g\rangle \rightarrow |2p\sigma_u - 1\omega\rangle$ avoided crossing opens at lower intensity than the $|1s\sigma_g\rangle \rightarrow |2p\sigma_u - 3\omega\rangle$ avoided crossing.

3.3.3.3 Experimental evidence for unified Floquet model ionization (UFI)

790 nm data Now that the predictions from UF have been put forth, we will examine our experimental data for H_2^+ ionization near the appearance intensity. Figure 3.27 shows KER spectra

[70] The wavepacket is assumed to follow the $|2p\sigma_u - 3\omega\rangle \rightarrow |1s\sigma_g - 2\omega\rangle$ adiabatic pathway as discussed in section 3.2.3.

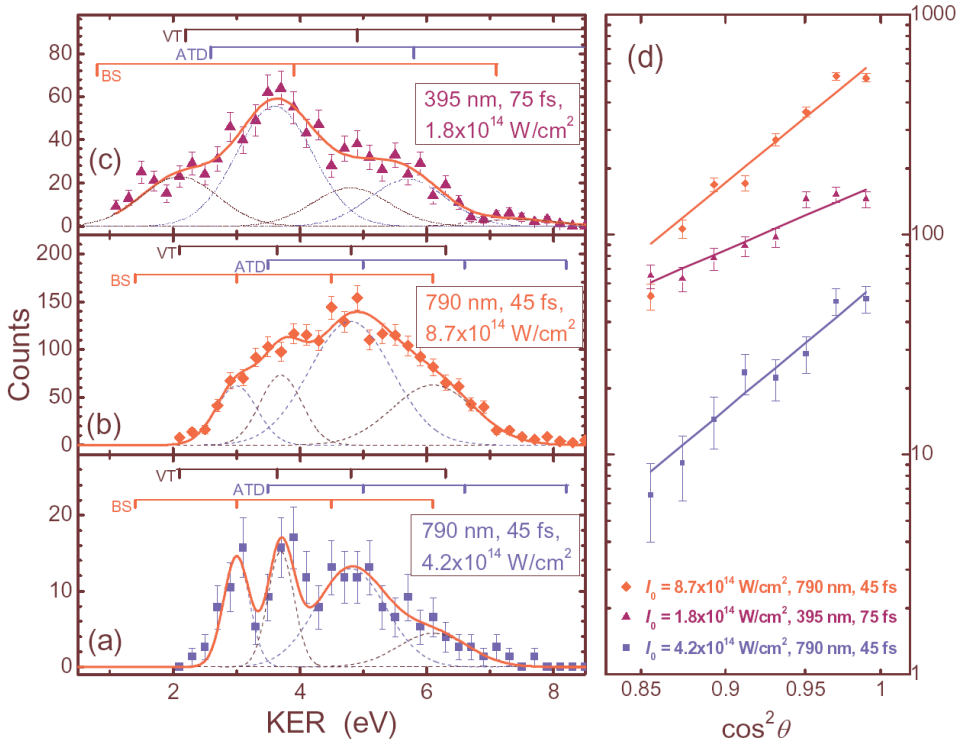

Figure 3.27: (a) - (c) Experimental ionization KER spectra. The vertical bars indicate the predicted KER peak locations, grouped by initiating mechanism. The tic marks denote the KER expected from UFI via one of the $|1/R - n\omega\rangle$ states preceded by BS, VT, and ATD. (d) Experimental log-log angular distributions corresponding to the spectra (a) - (c). (Figure adapted from our publication [38].)

that were obtained using the method described for the 45 fs pulses in section 3.2.2. Figures 3.27(a) and (b) are data from near the appearance intensity and data from ∼2 times this intensity, respectively. The predicted structure is readily apparent in the appearance intensity data, figure 3.27(a) and, as expected from the peak broadening arguments given above, washes out as the intensity is increased in figure 3.27(b). To quantify the peaks in these figures, we fit the KER distribution of figure 3.27(a) with a sum of four Gaussians. The fit was restricted to Gaussians centered at the predicted locations sharing a common width.[71] The same positions were then used in figure 3.27(b) with larger widths to account for intensity broadening. Thus, between the two panels, there were effectively only 12 free parameters. The quality of the fits suggests that our

[71] Where there were multiple pathways leading to nearly the same KER (i.e. ±0.2 eV), the Gaussian combines the peaks and has a larger width.

model does indeed have descriptive and predictive powers.

While the abundance of crossings makes a one-to-one, peak-to-pathway identification difficult, the 4 peaks in figures 3.27(a) and (b) can easily be accounted for by one or more of the predicted pathways. Furthermore, none of the peaks occurs at unexpected positions in KER. The 3 eV peak is cleanly associated with the $|1s\sigma_g\rangle \rightarrow |2p\sigma_u - 1\omega\rangle \rightarrow |1/R - 11\omega\rangle$ BS-UFI pathway. The source for the second prominent peak at 3.8 eV likely includes contributions from VT, BS (shifted by strong one-photon coupling), and ATD initiated UFI. The 4.8 eV peak is also likely a combination of peaks, this time from 12ω ionization of the VT states and 13ω ionization following ATD. In addition to KER, this model allows for the prediction of the angular distribution of the nuclear fragments. Assuming that all transitions involved in both ionization and dissociation are parallel, i.e. $\Delta\Lambda = 0$, an n-photon transition gives a $\cos^{2n}\theta$ distribution. For ionization initiated by BS and ATD, we expect primarily 11- to 13-photon and 11- to 12-photon ionization, respectively. To check the measured distributions, figure 3.27(d) shows the experimental angular distributions plotted so that the expected $\cos^{2n}\theta$ behavior appears as a straight line with a slope proportional to n. The data fall nicely along a straight line with n lying between 12 and 13, which is in agreement with our prediction. Thus our model and experimental data are consistent in both KER and angular distributions for 790 nm.

395 nm data In the CREI model, the critical internuclear distances depend on the electric field strength and are independent of the wavelength being used. However, the frequency plays an essential role in the UF model. Therefore, after determining where we expected to see UFI peaks for frequency doubled, $\lambda = 395$ nm, pulses (see tic marks in figure 3.27(c)), we performed the experiment to test our model. The ionization and dissociation distributions for H_2^+ at $\lambda = 395$ nm are significantly different as compared to 790 nm pulses. The potential energy curves will be analogous to those for 790 nm light with double the energy spacing, i.e. twice the photon energy. Applying the same kind of analysis discussed above, our model predicts that the angular distribution should have a 6 - 7-photon character, i.e. $\cos^{2n}\theta$ with $n = 6 - 7$, and primary KER peaks at around 2.2 eV for VT, 3.8 eV for BS, and 5.7 eV for ATD. The measured angular distribution, shown

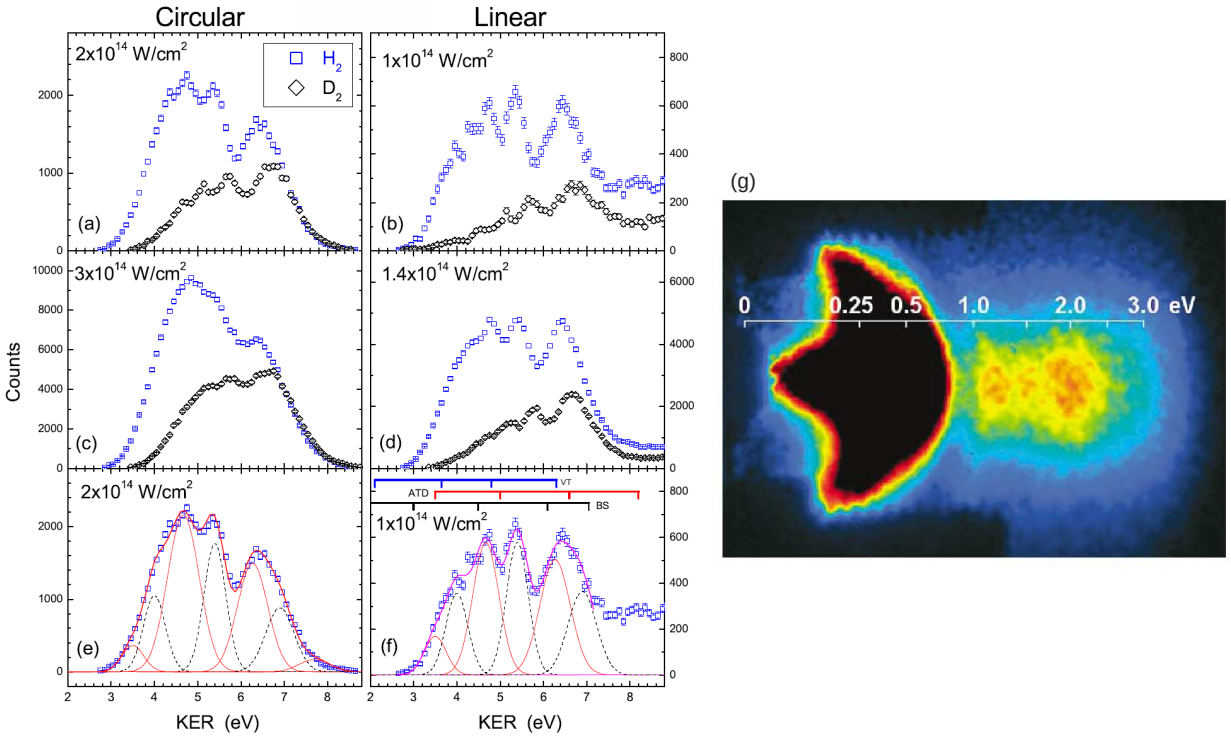

Figure 3.28: (a) – (f) H_2^+ and D_2^+ Coulomb explosion KER spectra from Staudte *et al.* [88]. Panels (e) and (f) show our model fit, both individual peaks and total. The bars in (f) indicate the diabatic peak positions grouped by mechanism. (g) Projected velocity distribution of the fragments from the photodissociation and Coulomb explosion channel of D_2^+ at an intensity of 10^{14} W/cm^2 and pulse duration of 350 fs. The color scale is adjusted to the signal in the Coulomb explosion (CE) channel. Note that this panel displays the KER per fragment and not the total KER. Thus, the KER scale should be multiplied by two when comparing to our data. (Figures (a) – (f) and (g) taken from references [139] and [85], respectively.)

in figure 3.27(d), gives a $\cos^{2n}\theta$ fit with $n = 6.6 \pm 1.0$, which is in excellent agreement with the expected 6 - 7-photon character. Additionally, the measured KER spectrum shown in figure 3.27(c) also agrees well with the predictions. In fact, the 395 nm KER structure can be more readily associated with specific pathways than the 790 nm data since the higher photon energy leads to a comparative sparsity of crossings. For example, the main 3.8 eV peak arises from a $|1s\sigma_g\rangle \rightarrow |2p\sigma_u - 1\omega\rangle \rightarrow |1/R - 6\omega\rangle$ pathway. The remaining KER peaks at 2.2, 4.8, 5.7, and 7.0 eV come from UFI initiated by VT, VT, ATD, and a mixture of BS and VT, respectively.

Measurements by other groups[72] Furthermore, the UF model of ionization is consistent with measured data from other groups. For example, figures 3.28(a) – (h) show the KER distributions measured by Staudte *et al.* [88]. In addition to the structure itself, figures 3.28(a) – (h) show other curious features. First, the peaks for H_2^+ are in essentially the same positions for all intensities and for both linearly and circularly polarized light. Moreover, all peaks for D_2^+ shift only slightly to higher KER relative to H_2^+. The peak positions for circularly polarized light can be explained using the same UF model as linear polarized light if one assumes that for the parallel transitions most important here, only the projection of the electric field on the molecular axis matters. Therefore, since care was taken in the experiment [88] to insure that the maximum field was the same for both polarizations, it is thus not surprising that the spectra look similar within the framework of our UF model. There are, however, clear differences between the results at the two polarizations. For energies above roughly 7.5 eV, the differences are due primarily to rescattering effects, which are beyond the present model. Below 7.5 eV, our model does apply, and the differences can be ascribed to geometrical alignment.[73] For circularly polarized light a larger fraction of the isotropic distribution of molecules experience a higher intensity on average, thereby effectively giving the circular polarization measurement a higher average intensity than the linear measurement at the same peak electric field. Furthermore, our model predicts that higher intensities tend to broaden the peaks and contain a higher proportion of large R, i.e. low-KER, peaks since the pulse retains enough intensity at the long times needed to reach the large-R crossings. Therefore, the measurements by Staudte *et al.* [88] as shown in figures 3.28(a) – (h) agree with both the KER structure and the KER shifts due to intensity and polarization predicted by the UF model.

Another example of an H_2^+ ionization experiment that is consistent with the UF model is the projected velocity distribution for D_2^+ measured for a 10^{14} W/cm^2, 791 nm, 350 fs pulse, shown in figure 3.28(g) [85]. Pavičić *et al.* interpret the three distinct ionization peaks seen in their data

[72] Much of the work in this section has been previously reported by Esry *et at.* [139].

[73] Assuming that only the projection of the electric field on the internuclear axis is important, the effective temporal intensity envelope for the linear and circular cases are $I^{\text{eff}}_{\text{lin.}} = I_0 \cos\alpha$ and $I^{\text{eff}}_{\text{cir.}} = I_0 \cos\beta$, respectively, where I_0 is the true cycle-averaged intensity envelope as a function of time, α is the angle between the polarization direction and the internuclear axis, and β is the angle between the *plane* of the laser polarization and the internuclear axis. Notice that for the circular case the number of molecules which have $I^{\text{eff}} \simeq I_0$ is much greater than in the linear case as the entire polarization plane experiences $I^{\text{eff}} = I_0$ and not just those molecules aligned along the polarization axis.

as CREI-like ionization corresponding to the critical distances of 8, 11, and 15 a.u. [85]. However, these peaks do not match the $R = 7$ and 10 a.u. predicted by CREI and are in very good agreement with the three predominant peaks of our 790 nm data shown in figure 3.27(a). Note that figure 3.28(g) is a projected velocity distribution and not the Abel transform of this data in terms of $p_{\parallel}$ and $p_{\perp}$. Thus, the true KER peaks are slightly shifted to higher values of KER with respect to those appearing in the figure, thereby improving the agreement between the two data sets.

3.3.3.4 Summary

In this section we have built upon the Floquet picture to produce a simple, self-consistent model for the nuclear dynamics involved in both dissociation and ionization. Our model incorporates all of the interpretive power of the Floquet potentials for dissociation and extends the same power to ionization, thereby enabling us to identify various ionization mechanisms, e.g. BS-UFI and ATD-UFI. Furthermore, experimental data for the ionization of H_2^+ near the ionization appearance intensity for both 790 and 395 nm laser pulses is in agreement with the predictions of the UF model. Although not all ionization mechanisms are uniquely distinguishable in this model, e.g. the 5.0 eV peak in figure 3.27(a), the predictive power has proven to be substantial. Additionally, the model's dependence on intensity, pulse length, and carrier frequency makes it quite useful in designing new experiments. Further, the ambiguous identifications discussed above should be easily removed by implementing and interpreting a pump-probe style experiment that retrieves the timing information inherent in the potential curves, thereby giving clear pathway assignments. Finally, we note that, although the increased number of potential energy curves will make the interpretation more complex, our model can be applied to molecules other than H_2^+, just as the Floquet language has been used for dissociation in other molecules.

3.4 Conclusions

In this chapter, we have presented detailed state-of-the-art intensity and pulse-width dependent measurements of laser-induced ionization and dissociation of H_2^+. The dissociation measurements

have given us a great deal of insight into the ultrashort pulse laser-induced dynamics of H_2^+ in terms of the unified Floquet picture and are supported by more sophisticated time-dependent calculations performed by Esry's theoretical group [137]. Additionally, the ionization measurements have allowed for both a detailed investigation of the charge resonance enhanced ionization (CREI) model and the development of a new model — the unified Floquet (UF) model — for molecular ionization near its appearance intensity.

Chapter 4

Multi-Electron Diatomic Molecular Ions

4.1 Introduction

There is a great deal of ongoing theoretical and experimental work concerned with understanding the dynamics of diatomic molecules in intense short pulse laser fields. However, interpretation of the experimental results for multi-electron molecules has been crude compared to the extensive theoretical and experimental studies of H_2-laser interactions discussed in chapter 3 and in several excellent papers and reviews [8–10, 13, 16–18, 33–35, 41, 43–49, 142, 151, 156–158]. This is mainly due to the more complex electronic structure of multi-electron diatomic molecules as is evident in figure 4.1 for O_2^+. The abundant work with H_2 has given rise to a conceptual understanding of molecular dissociation in terms of the Floquet picture, as discussed in previous chapters. Others have used parts of this picture to reduce the number of possible electronic states involved in the laser-induced ionization and dissociation of multi-electron molecules. For example, Hishikawa *et al.* used angular distributions to limit possible dissociation pathways [159], and Alnaser *et al.* used kinetic energy release (KER) to find initial and final states in double ionization [136]. Taking this one step further, by combining all the information given by the Floquet picture with a complete intensity-dependent 3D momentum imaging technique, we have suggested a method to uniquely determine the laser-induced dissociation pathways of a multi-electron diatomic molecule [37].

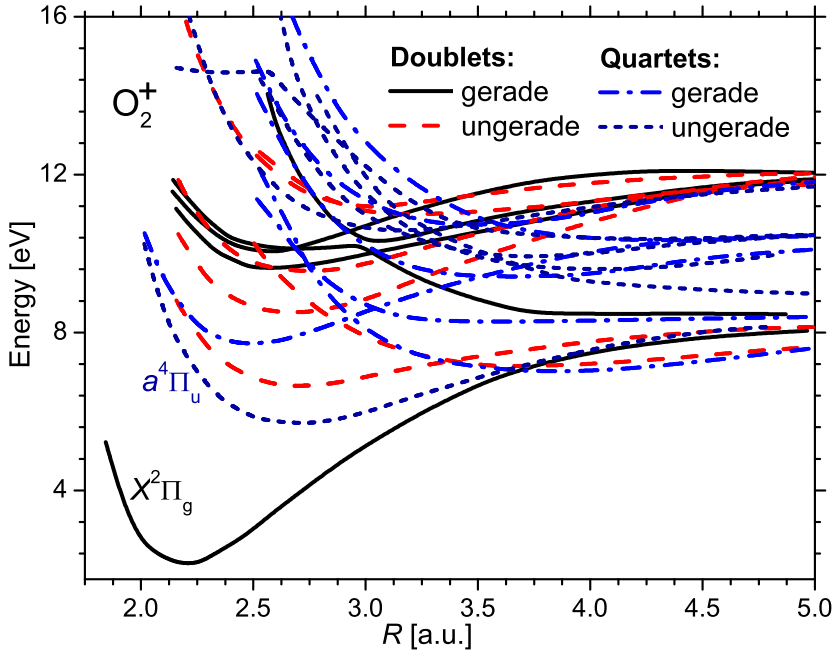

Figure 4.1: O_2^+ Born-Oppenheimer PECs [125]. The doublet and quartet states are separated into gerade and ungerade groups and the two possible initial electronic states in this experiment, $X\,^2\Pi_g$ and $a\,^4\Pi_u$, are labeled. (Figure taken from our publication [37].)

As before, we will be using the diabatic Floquet representation with the same notation, e.g. $|2p\sigma_u - 1\omega\rangle$ is the $2p\sigma_u$ state shifted down by the energy of 1 photon. The dissociating nuclear wave packet can make a transition at any crossings between such dressed states that obey the molecular dipole selection rules. Furthermore, the transition probability at each crossing is proportional to the absolute square of the dipole matrix element. In contrast to the diabatic Floquet picture, which is most appropriate for laser intensities in the perturbative regime, the adiabatic Floquet representation is best suited for laser fields beyond the perturbative regime. However, one can still use the diabatic representation for intense laser pulses by including the effect of the laser field strength in the coupling terms between these states. For example, this scheme was used successfully to interpret the dissociation of Na_2^+ by both experimentalists [160] and theorists [161]. Furthermore, this simplified representation helps one quickly explore possible dissociation pathways without the additional calculations needed to generate the adiabatic potential energy curves for each laser intensity.

In this chapter we will discuss laser-induced fragmentation of three of the multi-electron diatomic molecular ions studied by our group — O_2^+, ND^+, and N_2^+. These three molecules are chosen since they have distinct and different fragmentation features, yet the predominant features in each can

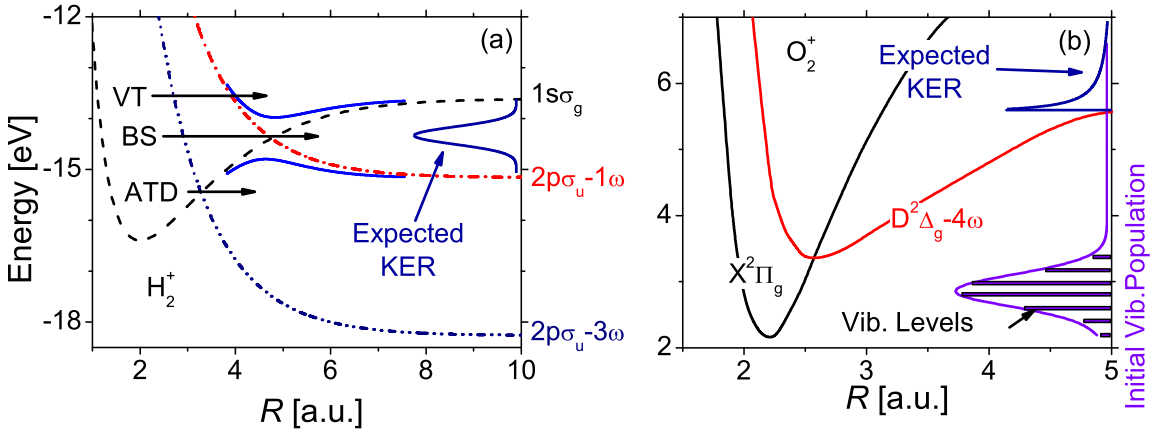

Figure 4.2: (a) A schematic Floquet picture of the H_2^+ diabatic PECs with adiabatic PECs superimposed at the one-photon crossing (solid lines) for $\lambda\sim$790 nm. The processes of bond softening (BS), vibrational trapping (VT), and above-threshold dissociation (ATD) are depicted. (b) The initial vibrational distribution of the O_2^+ doublet ground state and a possible dissociation pathway discussed in the text. The expected KER distributions for the $|X\,^2\Pi_g\rangle \rightarrow |D\,^2\Delta_g - 4\omega\rangle$ and BS pathways are displayed in (b) and (a), respectively. Note that only the relative heights in these distributions are meaningful. (Figure taken from our publication [37].)

be explained by extending the relatively simple methods discussed in the previous chapter on H_2^+.

4.2 O_2^+ dissociation pathways[74]

4.2.1 Introduction

As seen in previous chapters and now in figure 4.2(a), the small number of effective PECs in H_2^+ allows one to interpret the adiabatic Floquet picture rather easily, thus giving rise to the concepts of bond-softening, vibrational trapping, and above-threshold dissociation [8, 10, 13, 43]. In contrast to the relatively simple picture for H_2^+, multi-electron diatomic molecules such as O_2^+ create a diabatic Floquet picture with a plethora of PEC crossings, allowing for a multitude of laser-induced dissociation pathways, referred to simply as pathways below. A discussion of the interactions of a variety of "small" molecules, in particular diatomic, with intense laser fields is found in the detailed reviews by Codling and Frasinski [162], as well as Posthumus [8], and references therein. The behavior of the oxygen molecule in intense laser fields, in particular, has been studied for many

[74]Much of the work in this section has been previously reported in one of our publications [37].

years (see, for example, references [58, 112, 136, 152, 159, 162–172]). More specifically, these studies of the dissociative ionization of O_2 spanned a variety of wavelengths, pulse durations, and intensities along with various levels of ionization. However, unambiguous determination of the dissociation pathways using a picture as elegantly simple as the H_2^+ Floquet picture has been absent until lately. Recent kinematically complete studies of the dissociation into $O^+ + O^+$ following double ionization had sufficient resolution to identify the transient electronic state of O_2^+ [136].

In this work, we utilize an O_2^+ beam target and coincidence three-dimensional momentum imaging to perform measurements with similar resolution for the dissociation of O_2^+ into $O^+ + O$ without the need for the laser to first ionize the target. Furthermore, we use what is known about the dynamics of H_2^+ in intense laser fields, where non-perturbative behavior dominates, as a foundation for determining the most probable dissociation pathways of O_2^+ from the measured intensity-dependent momentum distribution of the dissociation fragments. The abundance of photo-dissociation pathways in the diabatic Floquet picture of O_2^+ may make this task seem insurmountable. However, by evaluating the dissociation distribution, most, if not all, non-contributing pathways can be eliminated. This is accomplished using four conditions outlined here and discussed in detail momentarily. First, the intensity at which a dissociation feature is predominant, I_{pred}, is related to the sum of absorbed and emitted photons, n, required along the pathway, i.e. higher n corresponds to higher I_{pred}. Second, the shape and position of the KER peak generated by a particular pathway is influenced by the shape of the PECs comprising it. Third, the number of transitions favoring internuclear alignment parallel and perpendicular to the laser polarization required along a pathway will determine the angular distribution of the breakup channel. Fourth, all transitions involved in a pathway must obey the molecular dipole selection rules. In addition, we assume that all relevant dipole transition matrix elements for the pertinent allowed transitions are of comparable magnitude.

4.2.2 Experimental method

In this experiment we used basically the same setup described in the 135 and 45 fs H_2^+ measurements of chapter 3 (with further details in appendices A and B), namely, a $\lambda = 790$ nm pulse with a

Fourier-transform limited duration of $\tau = 35$ fs and a pulse energy of about 1 mJ. The pulse is stretched to 40 ± 5 fs due to the dispersion of our optics. This linearly polarized pulse, which is focused by an $f = 200$ mm fused silica lens, is incident upon the center of the ion beam, and the laser polarization, laser propagation, and ion beam are normal to one another. The fragments from the dissociation, O^+ and O, are separated in time by the constant weak electric field of a spectrometer in the ion beam direction [36, 37, 52, 92].

An 8 keV O_2^+ ion beam was produced in the same electron cyclotron resonance (ECR) ion source discussed in appendix section A.2. The electron impact ionization in the ion source produces an O_2^+ beam that is predominantly in the $X\,^2\Pi_g$ and $a\,^4\Pi_u$ electronic states, the former comprising about 2/3 and the latter about 1/3 of the beam [67]. $X\,^2\Pi_g$ is the electronic ground state of O_2^+, and $a\,^4\Pi_u$ is metastable and the lowest lying quartet state. For the sake of brevity, only the dissociation of O_2^+ at intensities up to 10^{15} W/cm^2 will be discussed here.

Under the conditions of this study, dissociation of highly excited vibrational states of O_2^+ plays an important role. The lowest electronic states in both the doublet and quartet manifolds of this molecular ion have a broad vibrational population. Typically, molecular ions produced by electron impact ionization in an ion source have a population distribution roughly determined by the Franck-Condon factors (see, for example, [66] for the population of H_2^+). Deviations from the Franck-Condon distribution can occur, especially when ionization of higher electronic states, which feed the lower state by cascades, are significant. This is the case for the $a\,^4\Pi_u$ state of O_2^+ [173]. However, the resulting vibrational population is still broad and falls off for the highest vibrational states. Furthermore, it is important to note that in the upcoming interpretation of the dissociation data, the only relevant facts are that high vibrational states of O_2^+ have significant population and that the population of these states, particularly for the doublet, falls off for very high vibrational states.

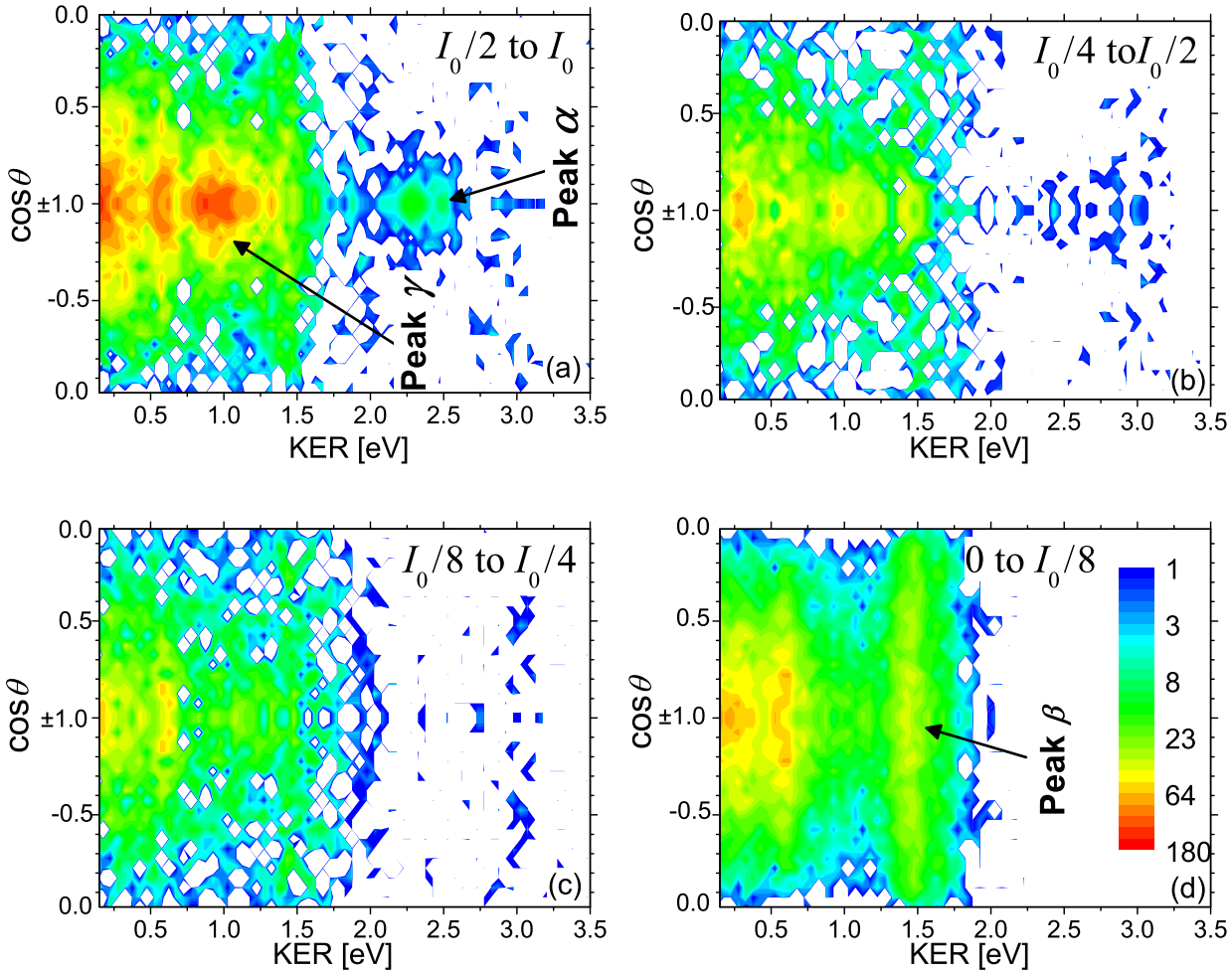

Figure 4.3: Experimental data for the dissociation of O_2^+ in a 40 ± 5 fs 790 nm laser field, where $I_0 = (1.3 \pm 0.5) \times 10^{15}$ W/cm^2 and θ is the angle between the laser polarization and the internuclear axis of O_2^+. (a) – (d) The contributions of four different intensity slices, which comprise the total ion-laser interaction volume, as a function of KER and $\cos\theta$. (Figure taken from our publication [37].)

4.2.3 Results and discussion

4.2.3.1 Determining laser-induced dissociation pathways

As one can see from the intensity-dependent KER-cos θ distributions in figure 4.3, the rich electronic structure of O_2^+ produces numerous distinct features,[75] which give us insight into the dissociation pathways. Although the number of electronic states in O_2^+ is formidable, the intensity-dependent laser-induced dissociation distributions provide three pieces of information about the pathway of a particular channel.

First, since the IDS method allows one to determine at what intensity each feature is predominant, one can narrow down the possible number of photons and transitions involved in a particular pathway. In general, features appearing at higher intensities require more photons than those appearing at lower intensities. Furthermore, if one can determine the pathway for any feature, that feature can then be used as an intensity benchmark for other features. For example, if (i) there are two features labeled δ and ε, which appear at intensities I_δ and I_ε, respectively, (ii) δ is known to correspond to a pathway requiring three photons, and (iii) $I_\varepsilon < I_\delta$, then the pathway leading to ε requires three or less photons. In this way, lower and upper bounds can be placed on the number of photons involved in the pathway leading to a feature by the identification of other features.

Second, the position and shape of the KER distribution for each peak, as seen in figure 4.4(a), allows one to determine the height and general shape of the barrier over which the vibrational wave packet dissociates. This can easily be seen in the contrast between the expected KER distributions from the curves displayed in figures 4.2(a) and (b). The BS pathway in H_2^+ will produce a KER distribution peaking around 0.8 eV as that is the position of the diabatic Floquet curve crossing above the $|2p\sigma_u - 1\omega\rangle$ dissociation limit. The width of the KER peak should correspond to the gap between the adiabatic curves weighted by the vibrational population. In contrast, the O_2^+ PECs, shown in figure 4.2(b), will produce a KER distribution peaked at 0 eV that dies off exponentially with KER. This is because the $|D\,^2\Delta_g - 4\omega\rangle$ dissociation limit is above the PEC crossing and the vibrational distribution of $X\,^2\Pi_g$ tails off exponentially at this point.

[75] The separation between adjacent vibrational levels in O_2^+ is < 0.25 eV. Thus, features separated by $\gtrsim 0.5$ eV are assumed to be due to O_2^+ electronic structure.

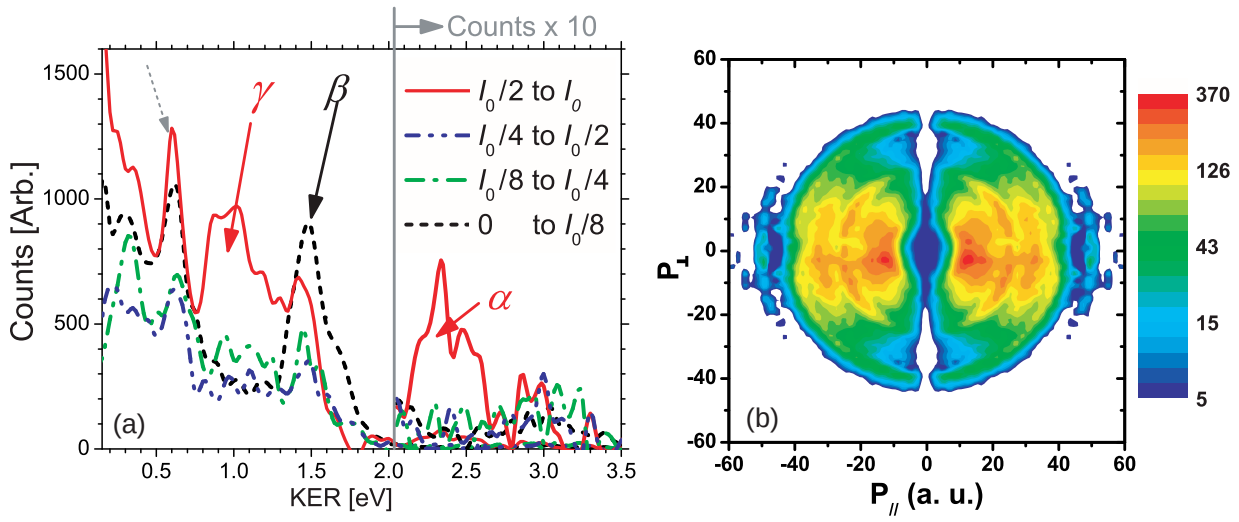

Figure 4.4: (a) The measured KER distributions of O_2^+ dissociation for the same four intensity slices shown in figure 4.3 integrated over $\cos\theta$. Lines indicate splines through the data points and the dissociation pathways yielding the KER peaks labeled as α, β and γ are discussed in the text. (Figure taken from our publication [37].) (b) Distributions of O_2^+ dissociation for $I_0 = (1.3 \pm 0.5) \times 10^{15}$ W/cm^2, i.e. the same as figure 4.3(a), as a function of $p_{\parallel}$ and $p_{\perp}$. Note that the data was multiplied by the $d(\cos\theta)$ volume element, as discussed in section 3.2.1.2.

Third, the angular distribution of a particular feature points to the number and type of transitions involved in its pathway by way of the angular momentum quantum number Λ. Each transition from one potential curve to another can be classified as either a parallel transition ($\Delta\Lambda = 0$), which depends on the laser field strength parallel to the internuclear axis, or a perpendicular transition ($\Delta\Lambda = \pm 1$), which depends on the laser field perpendicular to the O_2^+ axis. Furthermore, only different pathways that begin and end on the same PECs can interfere. Therefore, pathways with unique ending and/or starting points can be treated incoherently. The vast majority of O_2^+ pathways fall under the latter case. Thus, one would expect a solitary KER-$\cos\theta$ feature produced by a single pathway to have a $\cos^{2n}\theta \sin^{2m}\theta$ distribution, where n and m are the number of photons emitted and absorbed in parallel and perpendicular transitions along the pathway, respectively [159].[76]

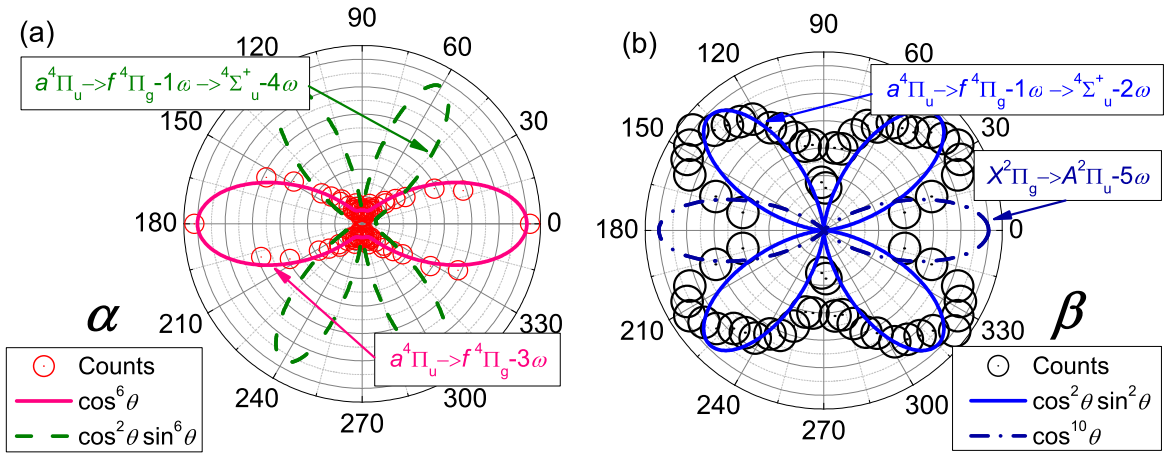

Figure 4.5: The measured angular distributions for two O_2^+ dissociation features. Panels (a) and (b) correspond to a range of KER values within peaks α and β, respectively. The size of the data symbols represents the error, and data for $\theta > 180°$ is mirrored for display purposes. Fits corresponding to possible dissociation pathways described in the text are shown as lines. Note that with the aforementioned laser pulse, the molecule is predicted to rotate only slightly (i.e. the axial recoil approximation is valid) [18, 58]. Therefore, we neglect the effect of these angular distortions here. (Figure taken from our publication [37].)

4.2.3.2 Examples

Peak α To illustrate this procedure, we will detail the determination of pathways that lead to two distinct KER-$\cos\theta$ features, α and β as denoted in figures 4.3 and 4.4(a). The most distinct feature of channel α is its sharp peak around the laser polarization, as seen in figure 4.5(a). This peak is best fit by a $\cos^{2n}\theta$ function if $n=3$. Therefore, after implementation of the aforementioned transition rules, the pathway can be assumed to have only parallel transitions, as any perpendicular transitions along the pathway would create an angular distribution greatly different from the one measured. Thus, the pathway must consist of $X\,^2\Pi_g$ followed by $^2\Pi$ states or $a\,^4\Pi_u$ followed by $^4\Pi$ states, provided that the axial-recoil approximation is valid. Furthermore, pathways involving more than five photons can be excluded as the error in the $\cos^{2n}\theta$ fit of the data doubles from its minimum at $n = 3$ if $n > 5$. This greatly reduces the number of combinations, allowing us to determine that the pathway producing the 2.3 eV KER peak is most likely the three-photon

[76] Plotting the $p_\parallel$-$p_\perp$-distribution as shown in figure 4.4(b) can be helpful in identifying distinct KER and angular features in the measured data, as discussed in the preceding two paragraphs.

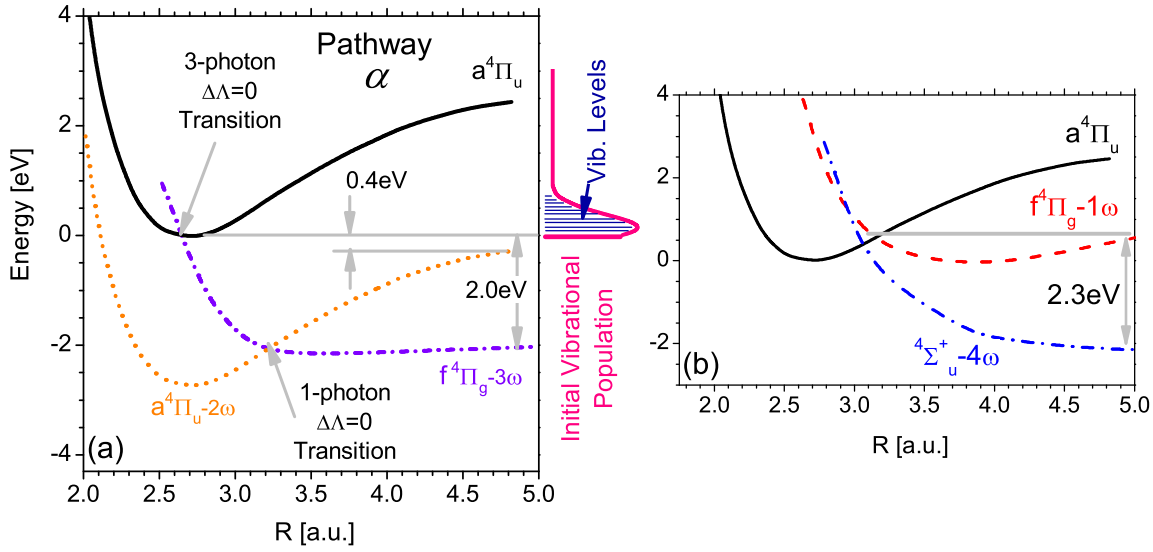

Figure 4.6: (a) The pathway for α and the approximate initial vibrational population of the $a\,^4\Pi_u$ state (see text). (b) A pathway leading to the measured KER peak for α, but failing to produce the observed angular dependence. (Figure taken from our publication [37].)

ATD, $|a\,^4\Pi_u\rangle \rightarrow |f\,^4\Pi_g - 3\omega\rangle$, pathway shown in figure 4.6(a) (the 2.3 eV is the sum of the 2.0 eV marked on the figure and the vibrational energy, as explained in section 4.2.3.3). Other doublet and quartet pathways, such as $|a\,^4\Pi_u\rangle \rightarrow |f\,^4\Pi_g - 1\omega\rangle \rightarrow |\,^4\Sigma_u^+ - 4\omega\rangle$ (see figure 4.6(b)), which produce the correct KER but the wrong angular distribution, fulfill some requirements, but only $|a\,^4\Pi_u\rangle \rightarrow |f\,^4\Pi_g - 3\omega\rangle$ fulfills *all* the necessary conditions.

Peak β The most probable pathway leading to channel β will be determined using the same set of tools described above with the additional information gained by determining the pathway for α. Since channel β is predominant at a much lower intensity than channel α, one can assume that the pathway producing β requires a total emission and absorption of three or fewer photons, if the relevant transition matrix elements are comparable. Furthermore, all pathways starting from the $X\,^2\Pi_g$ state can be excluded, as pathways starting from this state that involve three or less photons will produce KER distributions peaked at zero as discussed earlier. Thus, the benchmark, channel α, and the selection rules have made the task of determining the pathway producing β much less arduous. Furthermore, the angular distribution, shown in figure 4.5(b), clearly indicates

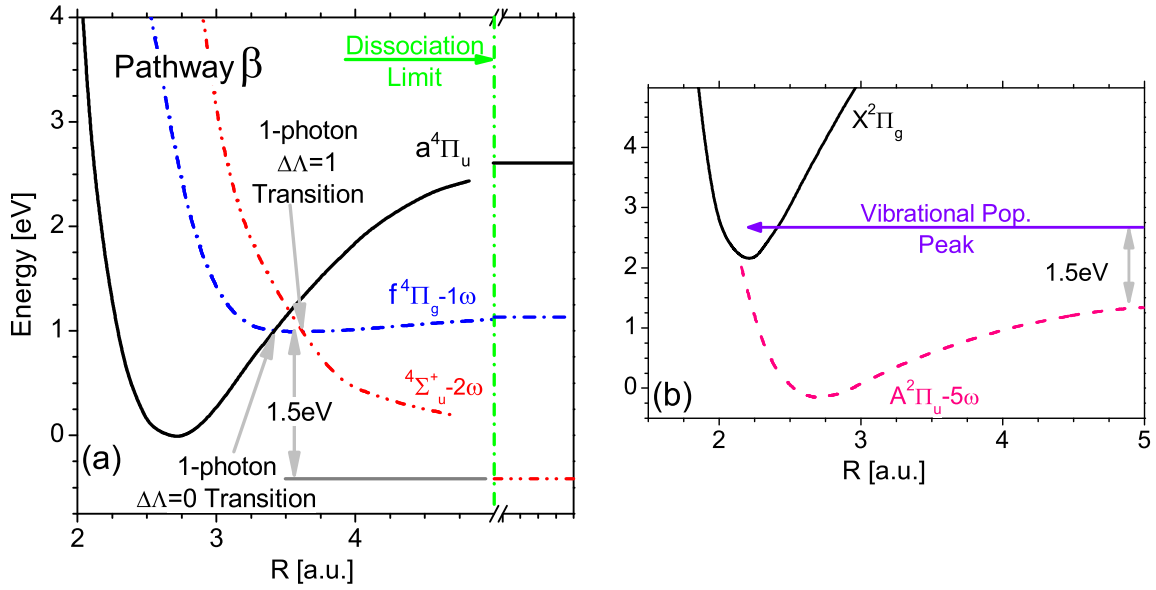

Figure 4.7: (a) The pathway for β as discussed in the text. (b) A pathway starting from the doublet ground state, $X\,^2\Pi_g$, which leads to the measured KER peak for β, but fails to produce the observed angular and intensity dependence. (Figure taken from our publication [37].)

that the pathway must include both parallel and perpendicular transitions, as the distribution does not peak at 0° or 90°. These requirements and the axial-recoil approximation leave only one possible pathway, namely $|a\,^4\Pi_u - o\omega\rangle \rightarrow |f\,^4\Pi_g - 1\omega\rangle \rightarrow |\,^4\Sigma_u^+ - 2\omega\rangle$, which is analogous to a "double bond-softening" pathway as shown in figure 4.7(a). Again, other pathways, such as $|X\,^2\Pi_g\rangle \rightarrow |A\,^2\Pi_u - 5\omega\rangle$ shown in figure 4.7(b), will produce a KER distribution peaking around 1.5 eV; however, all will generate an angular distribution inconsistent with the data and require more photons than indicated by the intensity dependence of this feature.

4.2.3.3 Comparison with previous work

Though the main objective of this section is to present the experimental method that allows us to identify the specific dissociation pathways in a many-electron molecule, it is interesting to compare the dissociation pathways we have identified with those previously found by Hishikawa *et al.* [159]. It is important to note that in their measurements the O_2 gas target was first ionized, creating O_2^+, and subsequently dissociated by the same laser pulse. In contrast, in our measurements the ionization

by the laser is not necessary since the O_2^+ is generated by electron impact ionization. Therefore, some differences between the two measurements might be expected. The most noticeable difference is that in addition to features strongly aligned along the laser polarization like those observed by Hishikawa *et al.* [159], we also observe dissociation pathways that involve perpendicular transitions, which result in an angular distribution that is not tightly aligned along the laser polarization. They identified two dissociation pathways of the $a\,^4\Pi_u$ state of O_2^+, which we will discuss below in further detail. Earlier work on the dissociation of O_2^+ [166, 167] cannot be compared in detail because significantly shorter wavelengths were used. However, some of the KER structures observed in this work have similar features to those observed earlier.

Before comparing specific dissociation pathways to previous measurements, it is worth noting that the features we presented originate from the $a\,^4\Pi_u$ state and not from the $X\,^2\Pi_g$ O_2^+ ground state. In some previous studies, dissociative ionization through the $a\,^4\Pi_u$ state has been suggested to explain some observations [159, 164]. In other studies, there was no indication for this intermediate state, and all the observations were consistent with ionization through the O_2^+ $X\,^2\Pi_g$ ground state [165–167].

Peak α The first dissociation pathway, denoted as channel α above, involves a transition from the initial $|a\,^4\Pi_u\rangle$ to the final $|f\,^4\Pi_g - 3\omega\rangle$ state through the 3-photon gap, as shown in figure 4.6(a). This dissociation pathway, identified also by Hishikawa *et al.* [159], yields a KER of about 2.0 eV for the v=0 state of $a\,^4\Pi_u$. (All vibrational levels bound in the PECs of interest were computed using the phase-amplitude method [174].) Higher vibrational states will also contribute, somewhat broadening and shifting the KER distribution to higher values, namely 2.3 eV with about 0.5 eV FWHM in our measurements. However, the yield of this path decreases rapidly with increasing v due to decreasing wave-function overlap (as is typical in this kind of curve crossing dynamics — predissociation is another example [43]) and consequent decrease in vibrational population, thus limiting the width of the KER peak for this process.

Note that after making the $|a\,^4\Pi_u\rangle \rightarrow |f\,^4\Pi_g - 3\omega\rangle$ transition, the O_2^+ dissociating along this pathway can either (i) continue along the $|f\,^4\Pi_g - 3\omega\rangle$ curve and dissociate as discussed above

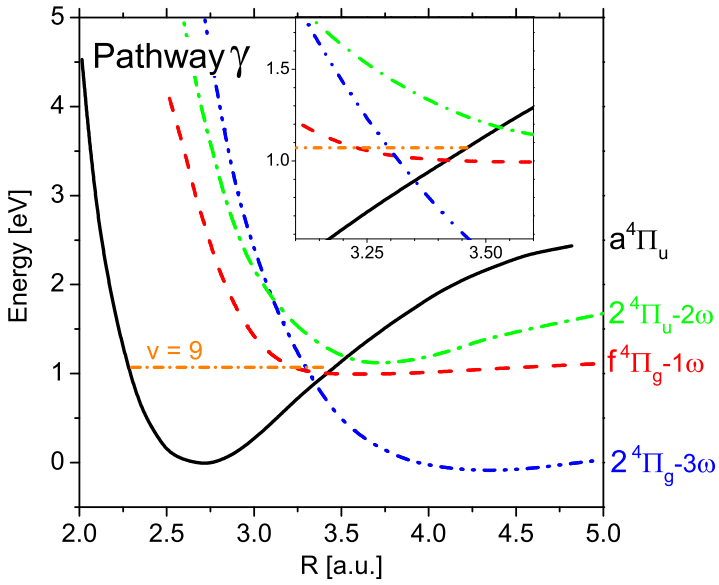

Figure 4.8: Pathway for γ as discussed in the text. The vibrational level nearest to the crossing is marked. The inset is an expanded view of the PEC crossings. (Figure taken from our publication [37].)

or (ii) cross to the $|a\,^4\Pi_u - 2\omega\rangle$ state through a 1-photon transition as indicated in figure 4.6(a). The dissociating O_2^+ reaches the $|f\,^4\Pi_g - 3\omega\rangle \rightarrow |a\,^4\Pi_u - 2\omega\rangle$ crossing ~10 fs after the 3-photon transition has occurred. At this time the 40 fs FWHM laser pulse used in our measurements still provides strong 1-photon coupling. Thus, a significant fraction of the dissociating wave packet is expected to make the transition to the $|a\,^4\Pi_u - 2\omega\rangle$ final state yielding a smaller KER of about 0.4 eV for the v=0 state. This contribution should shift to higher KER values in a similar way as the α peak, thus resulting in about 0.7 eV (this feature is marked by a dashed arrow in figure 4.4(a)). Both these KER features, namely a 2.3 eV peak from the $|a\,^4\Pi_u\rangle \rightarrow |f\,^4\Pi_g - 3\omega\rangle$ pathway and a 0.7 eV peak from the $|a\,^4\Pi_u\rangle \rightarrow |f\,^4\Pi_g - 3\omega\rangle \rightarrow |a\,^4\Pi_u - 2\omega\rangle$ pathway, appear in the highest intensity data shown in figures 4.3 and 4.4. Furthermore, the latter is more likely as expected. Note that the 0.7 eV peak appears also at lower intensities suggesting contributions of additional dissociation pathways, and therefore we cannot determine the branching ratio between these two pathways.

Peak γ The second dissociation pathway suggested by Hishikawa *et al.* [159] involves a sequence of transitions though one-photon crossings, explicitly, $|a\,^4\Pi_u\rangle \rightarrow |f\,^4\Pi_g - 1\omega\rangle \rightarrow |2\,^4\Pi_u - 2\omega\rangle \rightarrow |2\,^4\Pi_g - 3\omega\rangle$, which yields a KER of about 0.8 eV. All these suggested crossings involve parallel transitions (i.e. Π to Π) and thus result in a strong angular alignment of the nuclear fragments

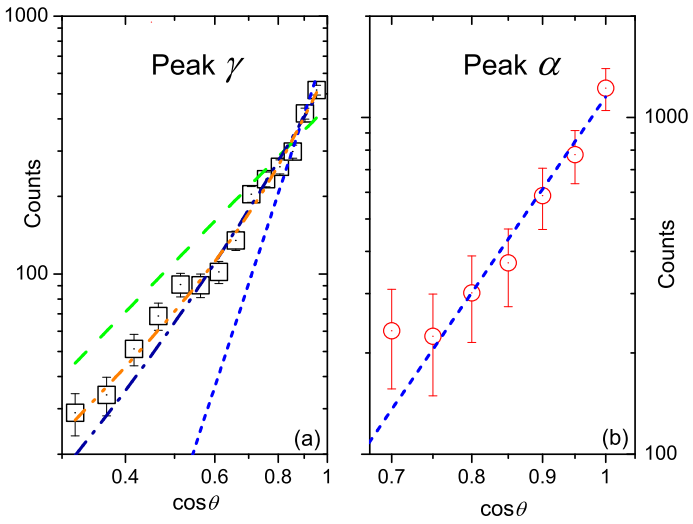

Figure 4.9: (a) and (b) Log-log-plots of the measured yield (symbols) as a function of $\cos\theta$ for the γ and α dissociation pathways, respectively. The lines shown in the figures are fits to the data of $N_0 \cos^6\theta$ (short-dashed blue line), $N_0 \cos^2\theta$ (long-dashed green line), $N_0 \cos^2\theta + N_1 \cos^4\theta$ (dash-dot dark-blue line), and $N_0 \cos^2\theta + N_1 \cos^6\theta$ (dash-dot-dot red line). The last distribution fits the data in panel (a) best, but also the mixed $\cos^2\theta + \cos^4\theta$ distribution is consistent with the data as discussed in the text. The data in panel (b) nicely fit by a $\cos^6\theta$ distribution. (Figure taken from our publication [37].)

along the laser polarization. Furthermore, this dissociation pathway is expected to be more efficient than the aforementioned 3-photon pathway as it requires three one-photon couplings rather than a direct three photon transition, and thus it should occur even at lower intensities. This KER peak around 0.8 eV also appears in our data, but it vanishes at low intensities as can be seen in figures 4.3 and 4.4(a). Moreover, (i) this peak appears at the same intensity range as the peak labeled α, which is associated with a 3-photon ATD dissociation pathway as discussed above, and (ii) it has a strongly aligned angular distribution. This suggests that a multiphoton mechanism of a similar order is involved, explicitly, the $|a\,^4\Pi_u\rangle \rightarrow |f\,^4\Pi_g - 1\omega\rangle \rightarrow |2\,^4\Pi_g - 3\omega\rangle$ dissociation pathway, which is shown in Fig. 4.8 and later referred to as 1+2-photon ATD because the second transition involves a 2-photon coupling. The dissociation pathway suggested here will have the same KER distribution as the one suggested previously [159] because (i) it accesses the same vibrational population through the initial $|a\,^4\Pi_u\rangle$ to $|f\,^4\Pi_g - 1\omega\rangle$ crossing, which occurs around $v = 9$, and (ii) it has the same $|2\,^4\Pi_g - 3\omega\rangle$ dissociation limit. However, assuming dipole transition matrix elements of comparable magnitude, the current pathway will occur only at intensities higher than the previously suggested pathway due to the 2-photon transition. This example demonstrates the impact of the intensity difference method on one's ability to determine the correct dissociation pathway.

It is also notable that the γ peak in figure 4.4(a) seems to sit on top of a wider KER distribution, which is visible at the lower intensities shown in the figure. This broad energy tail is most likely due to the $|a\,^4\Pi_u\rangle \rightarrow |f\,^4\Pi_g - 1\omega\rangle$ dissociation shown in figure 4.8, which produces a KER distribution similar to the one shown in figure 4.2(b) because the crossing is below the dissociation limit. This parallel 1-photon transition, typically referred to as bond-softening [10, 12], is expected to yield a $\cos^2\theta$ angular distribution. Furthermore, we cannot totally exclude contributions from the dissociation of highly excited vibrational states of the $X\,^2\Pi_g$ ground state of O_2^+ through the crossing with the $|A\,^2\Pi_u - 1\omega\rangle$ state, which is also expected to yield a $\cos^2\theta$ angular distribution. However, the population of such highly excited vibrational states ($v \gtrsim 30$) is expected to be negligible. Due to this KER tail, the angular distribution of the γ peak is a mixture of a $\cos^2\theta$ distribution from the aforementioned 1-photon process and a $\cos^6\theta$ distribution from the 1+2-photon ATD discussed above. This angular distribution nicely fits the data as shown in figure 4.9. However, the data is also consistent with a mixed $\cos^2\theta + \cos^4\theta$ distribution illustrating the difficulty in eliminating possible pathways based only on their angular distribution. Nevertheless, we have not found a 2-photon pathway which involves only parallel transitions and yields 0.8 eV, thus we conclude that the pathway suggested above is the most likely one.

Peak β The dissociation pathway, denoted as channel β above, has a wider angular distribution and peaks at a KER of ~ 1.5 eV. We identified the dissociation pathway to be a sequence of two 1-photon transitions, namely $|a\,^4\Pi_u\rangle \rightarrow |f\,^4\Pi_g - 1\omega\rangle \rightarrow |\,^4\Sigma_u^+ - 2\omega\rangle$ as explained earlier. It is important to note that this dissociation pathway appears at lower laser intensities than the previous two pathways as expected for the lower number of photons involved in these transitions. Furthermore, this dissociation pathway involves similar vibrational states of the $a\,^4\Pi_u$ electronic state as the 3-photon ATD pathway to the $|2\,^4\Pi_g - 3\omega\rangle$ state, namely $v \sim 7 - 9$. Finally, this dissociation pathway, which dominates our low intensity spectra, was not observed previously [159], most likely because the need to first ionize the neutral oxygen target sets a limit on the lowest intensities at which one can study O_2^+ dissociation.

4.2.4 Summary

In summary, using the intensity dependence, the shape and position of the KER peak, the angular distribution, and the dipole selection rules, one can determine the most probable laser-induced dissociation pathway(s) for a feature that has a distinct dissociation momentum distribution. Furthermore, once the pathway leading to a particular feature in the spectra is determined, it can be used as an intensity benchmark to set the upper or lower limit of photons required along another pathway of interest. This method can be extended to other features in the KER-cos θ distribution of O_2^+ and is expected to work for any diatomic molecule in a laser field that is measured with a complete 3D intensity-dependent momentum imaging technique. It is important to note that in order to apply this method a few assumptions need to be valid, namely (i) the axial-recoil approximation, (ii) dipole transition matrix elements for the relevant allowed transitions are of comparable magnitude, and (iii) the conditions allowing the use of the IDS method [96].

Employing this method, we have investigated a few of the O_2^+ dissociation pathways in an intense 40 fs laser pulse and identified them as (i) α — a 3-photon ATD pathway strongly aligned along the laser polarization occurring predominantly at intensities above 6×10^{14} W/cm^2, (ii) β — a dissociation channel involving two one-photon transitions, one parallel and one perpendicular, that happens mainly at lower intensities below about 10^{14} W/cm^2, and (iii) γ — a 1+2-photon ATD pathway occurring at similar intensities as α. All of these are dissociation pathways of the $a\,^4\Pi$ metastable state of O_2^+.

4.3 ND^+ dissociation pathways[77]

4.3.1 Introduction

In this section we will use the pathway identification techniques described, with regards to O_2^+ above, to determine the dissociation pathways of ND^+ and investigate the dependence of the dissociation branching ratio of ND^+ (the ratio of $N+D^+$ to the total dissociation yield) on intensity in the strong-field regime. The NH^+ radical is an important astrophysical species as it is believed to play

[77] Much of the work in this section has been previously reported in one of our publication [50].

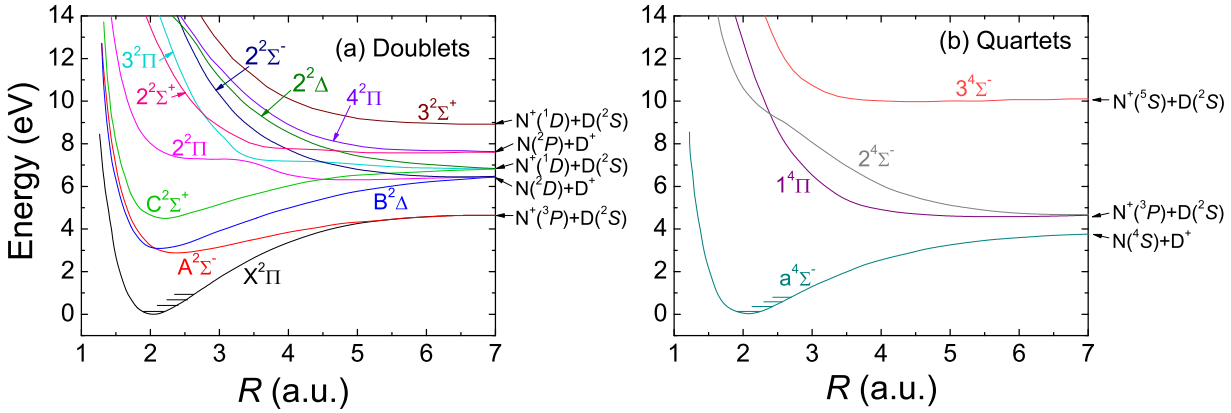

Figure 4.10: Potential energy curves of ND^+ for the lowest-lying (a) doublet, and (b) quartet states. Potential energy is given with respect to the bottom of the ground $X^2\Pi$ state well. Computed energies for the lowest few vibrational states are indicated by horizontal lines. Curves have been reproduced from reference [182].

a vital role in the synthesis of ammonia in dense interstellar media [175], as well as being formed by various reaction mechanisms in other environments such as the gas tail of comets [176] (see also reference [177] for a brief review). So far, however, the search for it in space has been unfruitful. Nevertheless, a number of spectroscopy-style measurements [178–181], as well as theoretical works on the electronic structure of NH^+ [177, 182–187], have been performed over the years leading to relatively detailed information on its molecular structure.

From an intense-field perspective, ND^+ is also an interesting target to probe as it has an alternating sequence of dissociation limits into (a) $N^+ + D$ and (b) $N + D^+$ (see figure 4.10), each spaced in energy by between 0.3–1.5 eV, just less than one photon energy at 795 nm wavelength (1.56 eV). Thus, we pose the question: how does the branching ratio of these dissociation channels depend on the laser field strength? This query is timely since much emphasis is currently placed on selectively determining the outcome of a particular reaction mechanism. Indeed, ND^+ would seem a target well-suited for future studies on state-selective control of dissociation. In this section we address the question of the $N^+ + D$ and $N + D^+$ dissociation branching ratio intensity-dependence and discuss the intense-field dissociation dynamics of this molecule.

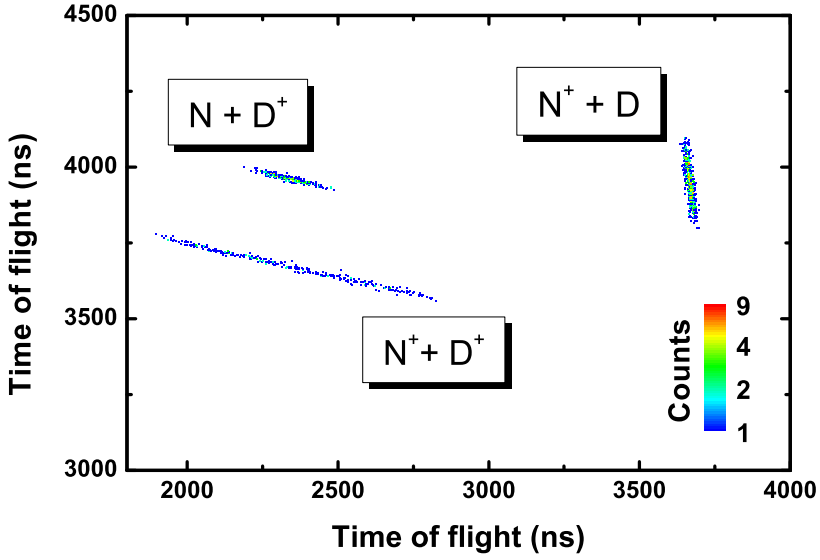

Figure 4.11: Coincidence time-of-flight spectrum for the dissociation and single ionization fragmentation channels of ND^+ plotted as a function of the time-of-flight of the first and second particles, for particle pairs that conserve momentum. (Figure taken from our previous publication [50].)

4.3.2 Experimental method

This experiment was performed in the same manner as the O_2^+ measurements (described in detail in appendices A and B), hence only the salient points will be relayed here. The ND^+ ions are formed from deuterated ammonia (ND_3) by electron impact ionization in an electron cyclotron resonance (ECR) ion source as discussed in appendix A.2. They are formed as a mixture of ground $X^2\Pi$ and metastably excited $a^4\Sigma^-$ states, although the ratio of these populations is unknown. In this measurement it is also important to recall that the primary ND^+ beam is collected in a small on-axis Faraday cup (2 mm diameter) near the center of the detector as detailed in appendix A.2. Due to the large mass ratio of N to D (7:1), slow nitrogen fragments may be blocked by the Faraday cup while fast deuterium fragments may travel outside the detector face. We estimate that our setup allows the kinetic energy release (KER) to be measured in the range 0.1<KER<3.3 eV. In figure 4.11 we show a plot of the flight time of the first particle to arrive at the detector versus that of the second for those event pairs that conserve momentum. Each of the measured channels, i.e. $(N^+ + D)$, $(N + D^+)$, and $(N^+ + D^+)$, are clearly identifiable and separable, thereby illustrating the importance and power of the coincidence measurement. This allows us to precisely determine the branching ratio of the dissociation channels for a given intensity measurement. The laser used in this study is the same as described in the previous O_2^+ section except that (i) the pulses were

focused on target using an off-axis parabolic mirror (f=203 mm), (ii) a higher peak intensity of I_0~2.6×10^{15} W/cm^2 was achieved, and (iii) the z-position of the focus was used to attenuate the intensity [94, 121–123] (see section 2.6.1.1 and appendix A.3.4.1 for details).

To the best of our knowledge, the exact vibrational population distribution of the $X^2\Pi$ and $a^4\Sigma^-$ states of ND^+ prepared from ammonia through electron-impact, i.e. $ND_3 + e^- \rightarrow ND^+ + D_2 + 2e^-$, is unknown. However, since the equilibrium N–D bond length of ND_3 (1.91 a.u. [188]), is close to that of the ND^+ $X^2\Pi$ and $a^4\Sigma^-$ states (i.e. 2.02 and 2.06 a.u. [182]), the vibrational population is likely to be relatively low-lying. Using a model potential energy surface cut for the N–D bond of ammonia [188] and applying a Franck-Condon projection of its ground state wavefunction onto the ND^+ states, we estimate that ~90% of the vibrational population is in the v=0 state of the $X^2\Pi$ and/or $a^4\Sigma^-$ electronic states. This is consistent with the narrowness of the observed KER distributions, particularly that in figure 4.12(a). Hence, ND^+ prepared in this way seems to be a nice example of a vibrationally cold target. [78]

4.3.3 Results and discussion

4.3.3.1 KER for ND^+ dissociation

Shown in figures 4.12(a) and (b) are the KER spectra for the dissociation of ND^+ into channels (a) $N^+ + D$ and (b) $N + D^+$, respectively, at a selection of intensities. The total number of dissociation events for the $N^+ + D$ channels at 4.0×10^{13} and 3.3×10^{13} W/cm^2 in figure 4.12(a) have been normalized to the 2.6×10^{15} W/cm^2 $N^+ + D$ dissociation counts. The counts of the competing $N + D^+$ channel are shown relative to the respective $N^+ + D$ count in figure 4.12(b). By taking the ratio of the total counts in the spectrum for each channel, to the total number of dissociation events, we obtain the branching ratios of these channels. The shaded areas of the spectra denote possible regions of loss in the KER distributions where low momenta N/N^+ fragments may be blocked by the Faraday cup as discussed above. Due to the loss of N^+ fragments from $N^+ + D$ dissociation events for which the KER is observed to be small (i.e. < 0.1 eV), the

[78] Indeed, achieving ground vibrational state molecular ions has been a goal for some time for intense-field studies and has only recently been demonstrated for HD^+ by using an electrostatic storage device [56].

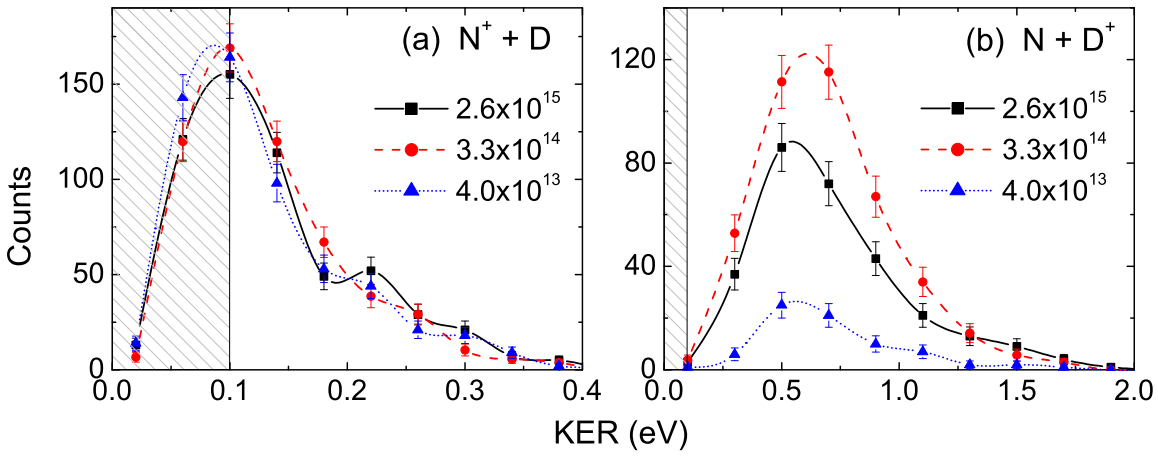

Figure 4.12: (a) Kinetic energy release (KER) distribution spectra for the dissociation of ND^+ into (a) $N^+ + D$ (KER $\sim$ 0.0–0.4 eV), and (b) $N + D^+$ (KER $\sim$ 0.0–2.0 eV) at intensities indicated (in units of W/cm^2). The total number of counts in the spectra of (a) have been normalized to one another. The same normalization factors are used in spectra (b). The shaded regions denote regions of expected loss due to the Faraday cup, see text for details. (Figure taken from our previous publication [50].)

question of where the KER distribution actually peaks between 0.0 and 0.1 eV remains open for future studies.

Before embarking on how to decipher the dissociation pathways from the spectra, let us examine a few of the intriguing aspects of the data. First, one may have noted the large difference in KER range for the two channels; $N^+ + D$ spans the range of approximately 0.0 – 0.4 eV, while $N + D^+$ spans the range of approximately 0.0 – 2.0 eV. The difference in KER range can be attributed to the dissociation pathways leading to that specific channel, which we identify in the upcoming discussion. Also intriguing is the narrow energy spread of the peaks, particularly the ~0.1 eV FWHM peak of $N^+ + D$. As discussed above, we believe the population of the ground state of ND^+ is almost entirely in a single vibrational level (v=0) for these experiments. Therefore, the initial state of the system is well-defined and will not produce a large spread in the final energy distribution. Second, the absence of any higher, i.e. >1.0 eV, KER dissociation peaks[79] is due to the shallow nature of the electronic states involved in the dissociation. Additionally, the potential energy curves of figure

[79]The absence of >1.0 eV KER dissociation peaks may be considered atypical for other small diatomic molecules, e.g. O_2^+ discussed in section 4.2 and reference [37].

4.10(a) show that for the doublet states all of the lowest-lying potential curves are either attractive, or only slightly repulsive, for internuclear distance $R > 2$ a.u.. Therefore, dissociation on these potentials is likely to lead to low KER. Finally, it was observed in these experiments that the total rate of ND^+ dissociation at the highest intensity (2.6×10^{15} W/cm^2) was more than one order of magnitude lower than for H_2^+ dissociation under similar laser and ion beam conditions, indicating that ND^+ is difficult to dissociate because of the large number of photons involved.

4.3.3.2 Laser-induced dissociation pathways for ND^+

Introduction To determine the likely dissociation paths of ND^+ leading to the products $N^+ + D$ and $N + D^+$, we will draw on the technique discussed above in section 4.2 and reported in reference [37]. To briefly recap the basic rules are as follows.

1. Assuming the spin-orbit coupling is negligible, the doublet and quartet states are not mixed by the laser interaction due to spin-transition selection rules, e.g. doublet and quartet states do not mix.

2. The KER peak position will, at least roughly, correspond to the energy difference between the initial vibrational state and the dissociation limit, as detailed in figure 4.2.

3. The general KER distribution profile for each KER peak will correspond to the shape of the dissociation pathway.

4. The lower the intensity a feature appears as, the fewer the total number of absorbed/emmited photons along the pathway.

5. In the weak field limit, the angular distribution will be $\cos^{2n}\theta \sin^{2m}\theta$, where n and m are the number of photons involved in parallel ($\Delta\Lambda = 0$) and perpendicular ($\Delta\Lambda = \pm1$) transitions, respectively [159].

As the ND^+ has a very low-lying vibrational population, dissociation directly via the high-lying doublet ($3^2\Pi$, $2^2\Sigma^-$, $2^2\Delta$, $2^2\Sigma^+$, $4^2\Pi$, $3^2\Sigma^+$) and quartet ($1^4\Pi$, $2^4\Sigma^-$, $3^4\Sigma^-$) states would require the absorption of many photons (approximately 7 – 11), which renders vertical transitions

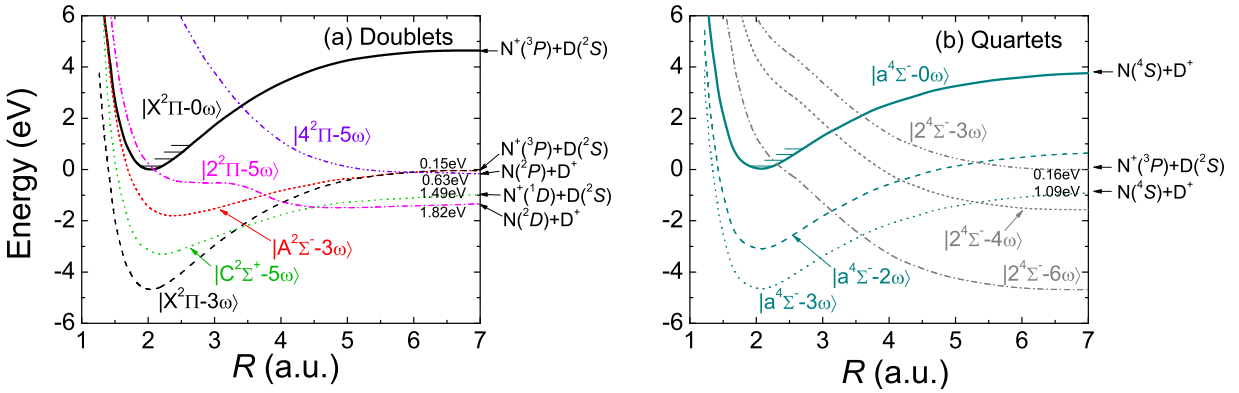

Figure 4.13: A selection of dressed potential energy curves of ND^+ for the (a) doublet and (b) quartet states. Computed energies for the lowest few vibrational states are indicated by horizontal lines. The numbers adjacent to certain dissociation limits correspond to the expected kinetic energy release for dissociation from that state starting from the v=0 vibrational level of the $X^2\Pi$ or $a^4\Sigma^-$ states. Field free curves have been reproduced from reference [182]. (Figure taken from our previous publication [50].)

to these states unlikely. In addition, the centroid of the observed KER distributions shown in figure 4.12 is inconsistent with the highly repulsive nature of these states which should lead to a KER$\gg$1 eV. To further narrow down the dissociation paths, we consider individually all remaining dissociation paths and eliminate those that are inconsistent with the data using the Floquet picture and previously enumerated guidelines.[80] In figure 4.13, to save congestion, we plot only the dressed potential energy curves that we have identified as relevant dissociation pathways for the doublet and quartets states of ND^+. Note that we have assumed the transition dipole to be significant allowing all photon numbers to be associated with each state which for a light system like ND^+ is a reasonable assumption.

N^+ + D pathway For N^+ + D, figure 4.12(a) shows that the KER distribution is peaked at or below 0.1 eV with an uncertainty in the exact value due to losses by the Faraday cup. Thus, for N^+ + D the dressed dissociation limit must be nearly equal in energy to the bottom, i.e. $v = 0$ state, of the field-free $X^2\Pi$ or $a^4\Sigma^-$ potential wells. The $|C^2\Sigma^+ - 5\omega\rangle$ and $|3^2\Pi - 5\omega\rangle$ states

[80] This approach is equivalent to the alternative representation often used where excitations between states are indicated as vertical transitions, resonant with an integer number of photons, e.g. reference [146].

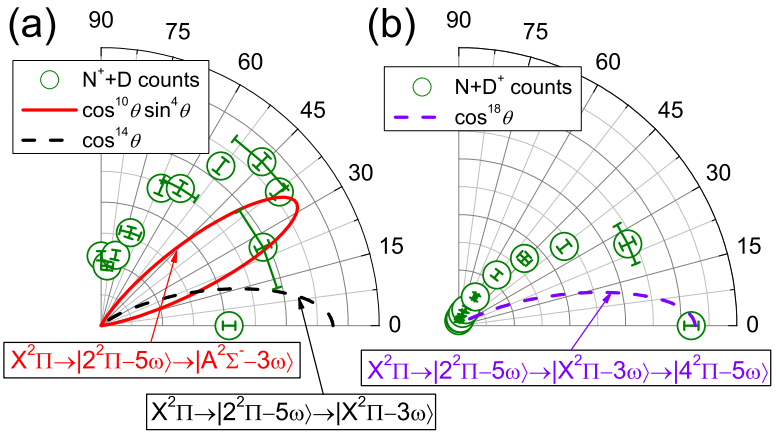

Figure 4.14: The measured angular distributions of ND^+ for (a) $N^+ + D$, and (b) $N + D^+$. The data points with error bars denote observed distributions, and the lines denote model distributions for the transitions indicated. (Figure taken from our previous publication [50].)

can be ruled out as final states as they would result in too large of a KER value, i.e. ∼1.49 eV. Thus, for the doublets shown in figure 4.13(a) the only possible final states that conform to this restriction are the $|A^2\Sigma^- - 3\omega\rangle$ and $|X^2\Pi - 3\omega\rangle$ states, which both result in a KER of about 0.15 eV. This is in relatively close agreement with the data.[81] However, as neither the dressed $A^2\Sigma^-$ nor the $X^2\Pi$ states form a direct curve crossing with the bottom of the field-free ground state well the dissociative wavepacket must first make a transition through an intermediate state. The most suitable candidate is the $|2^2\Pi - 5\omega\rangle$ state, which forms an avoided crossing with the $|A^2\Sigma^- - 3\omega\rangle$ state at $R = 3.7$ a.u. and with the $|X^2\Pi - 3\omega\rangle$ state at $R = 4.0$ a.u., as shown in figure 4.13. Hence, the bound ND^+ molecule first absorbs 5 photons to get excited to the $2^2\Pi$ state, before re-emitting 2 photons to transit onto the $A^2\Sigma^-$ or $X^2\Pi$ states.

To distinguish between the $A^2\Sigma^-$ and $X^2\Pi$ states, we will consider the angular distribution of the fragments. According to the rules listed above, the $X^2\Pi \rightarrow |2^2\Pi - 5\omega\rangle \rightarrow |A^2\Sigma^- - 3\omega\rangle$ transition should give, roughly, a $\cos^{10}\theta \sin^4\theta$ distribution, whereas the $X^2\Pi \rightarrow |2^2\Pi - 5\omega\rangle \rightarrow |X^2\Pi - 3\omega\rangle$ transition gives, roughly, a $\cos^{14}\theta$ distribution. Even though there is a higher level of uncertainty in the data at 90° emission angle as those particles are most susceptible to losses from the Faraday cup, the measured angular distribution of $N^+ + D$ displayed in figure 4.14(a) clearly shows that the distribution is not peaked along the laser polarization. Thus the pathway involving the $A^2\Sigma^-$

[81] Furthermore, as the expected KER value is calculated from the energy difference between v=0 and the dressed dissociation limit at R=∞, one may expect a small shift of the KER to lower energy as the v=0 state may get Stark-shifted downwards in energy by the laser field. This would improve the agreement with the observed value.

state is likely to be dominant.

There are a couple of alternative paths that would also produce low KER $N^+ + D$ fragments involving the quartet states. First, as shown in figure 4.13(b), the transition sequence $|a^4\Sigma^-\rangle \rightarrow |2^4\Sigma^- - 6\omega\rangle \rightarrow |a^4\Sigma^- - 2\omega\rangle \rightarrow |2^4\Sigma^- - 3\omega\rangle$ will give a KER of about 0.16 eV. However, each step of the sequence involves a $\Sigma \rightarrow \Sigma$ transition, hence the total angular distribution, like the $|X^2\Pi - 3\omega\rangle$ distribution, would be expected to be strongly peaked along the laser polarization which is inconsistent with the data shown in figure 4.14(a). Second, one must consider direct excitation of the $X^2\Pi$ (v=0) state to the vibrational continuum due to the permanent dipole moment of ND^+. This could proceed through the absorption of 3 photons ($|X^2\Pi - 3\omega\rangle$) and would result in KER=0.15 eV. However, as this mechanism involves a direct $\Pi \rightarrow \Pi$ coupling the dissociation fragments should be aligned with the laser polarization ($\cos^6\theta$). Therefore, we can again exclude this mechanism on the basis of its angular distribution. Furthermore, we believe the probability of this mechanism occurring at this wavelength to be small. Thus, through process of elimination, we conclude that the $|X^2\Pi\rangle \rightarrow |2^2\Pi - 5\omega\rangle \rightarrow |A^2\Sigma^- - 3\omega\rangle$ pathway is the favorable dissociation mechanism leading to $N^+ + D$.

$N + D^+$ pathway A similar logic may be applied to unravel the dominant mechanism in the case of $N + D^+$, which has a KER distribution peaked at about 0.6 eV with a FWHM value of ∼0.6 eV and an angular distribution highly aligned with the laser field (see figures 4.12 and 4.14(b), respectively). Furthermore, since this technique has already been demonstrated several times, we will simply state our conclusions. The measured $ND^+ \rightarrow N + D^+$ dissociation most likely occurs along the path $X^2\Pi \rightarrow |2^2\Pi - 5\omega\rangle \rightarrow |X^2\Pi - 3\omega\rangle \rightarrow |4^2\Pi - 5\omega\rangle$, which produces an angular distribution of $\cos^{18}\theta$. Whilst the predicted and observed angular distributions agree well in terms of the main dissociation direction, the observed distribution is much broader than the model prediction, as was also the case for $N^+ + D$.

Uncertainty in angular distribution There is a clear discrepancy both in the angle at which the distributions are peaked and in the width of the angular distributions. There are a number of

possible reasons that may contribute to this difference. First of all, the low KER of the $N^+ + D$ channel means that the N^+ fragments form a small spatial distribution near the center of the position-sensitive detector. This leads to a relatively large level of uncertainty in the angular measurement which is denoted by the error bars (in angle) added to select data points in figure 4.14. These alone do not fully account for the difference. Another source for the difference could be the simplicity of the model used to generate the fit which neglects interference terms from different transitions. Namely, in this model we use an incoherent sum over the pathways rather than the more correct coherent sum. Explicitly, the angular probability distribution is approximated by taking the sum of the squared transition amplitude for each pathway, as opposed to the square of the sum over all transitions. Thus the cross terms that give rise to interference are omitted. Such interference may act to slightly broaden or skew the actual distribution. Additionally, the difference may be an indication of weaker contributions from alternative pathways that also involve a mixture of parallel and perpendicular transitions. Lastly, the laser-induced alignment of the molecule both during and after the pulse may skew the angular distribution somewhat.

4.3.3.3 Branching ratios

Having established the most probable dissociation paths, we now examine the dependence of the $N^+ + D$ and $N + D^+$ branching ratio on laser intensity. The results are displayed in figure 4.15 as the ratio of the number of $N + D^+$ counts to the total number of dissociation counts. This ratio has been measured over the intensity range 2×10^{13} – 3×10^{15} W/cm^2. While there is some uncertainty in the absolute magnitude of this branching ratio due to a possible loss in counts of $N^+ + D$ below KER = 0.1 eV, this should not affect the relative change in the ratio from one intensity to another. This follows from the fact that the overall shape of the $N^+ + D$ KER distribution shown in figure 4.12(a) is insensitive to laser intensity. Thus any percentage loss at one intensity will be the same for all intensities, thereby decreasing only the overall magnitude of the ratio. The ratio may decrease further by the lower detection efficiency of the D fragment compared to D^+, but again will not affect the trend of the ratio as a function of intensity. By estimating the maximum loss of counts for $N^+ + D$, and accounting for the difference in detection efficiencies, we plot on

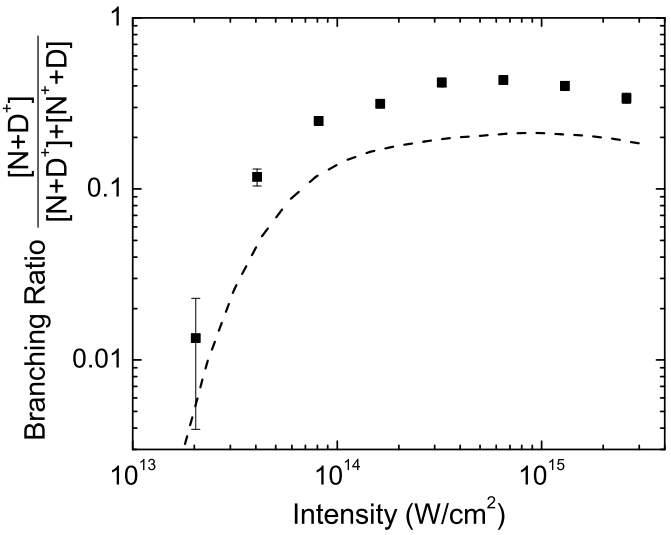

Figure 4.15: Branching ratio for dissociation of the N + D^+ channel. The dashed curve is a lower limit estimate of the absolute value of this ratio allowing for Faraday cup losses and detection efficiency (see text). (Figure taken from our previous publication [50].)

the figure a lower limit for the ratio, shown by the dashed curve. [82]

The clear trend of the branching ratio is a rapid decrease in the relative number of N + D^+ counts for intensities below 10^{14} W/cm^2. This trend is also observed directly in the raw data, as N + D^+ is seen to effectively "switch off" at lower intensities. Qualitatively, the result indicates that it is more difficult to dissociate ND^+ to N + D^+ than to N^+ + D, thus requiring higher intensity. This conclusion is consistent with our assignment of dissociation pathways since we found that the $4^2\Pi$ final state leading to N + D^+ requires absorption of 2 photons more than the $A^2\Sigma^-$ state that gives N^+ + D. The branching ratio tends to flatten off beyond an intensity of $\sim 3 \times 10^{14}$ W/cm^2 suggesting that both channels reach saturation. We note that figures 4.15 and 4.12(b) show that at the highest intensities the branching ratio decreases slightly. At these intensities the dissociation dynamics will be complicated by the opening of new dissociation paths and the onset of ionization, which we see above $\sim 5 \times 10^{14}$ W/cm^2.

Recently, Korolkov *et al.* [189] reported a similar study into the intensity-dependent branching

[82] Estimating the maximum signal loss in channel N^+ + D, we extrapolate the exponential decay portion of figure 4.12(a), i.e. KER>0.1 eV, back to KER=0.0 eV and integrate the relative yields of the extrapolated and observed data.

ratio of DCl^+. Deuterium chloride, like ND^+, is an interesting system where the lowest dissociation limits into $D^+ + Cl$ and $D + Cl^+$ are separated by ∼0.9 eV (less than one 800 nm photon), the latter being the lower limit. Korolkov *et al.* find a similar intensity dependence for the branching ratio of D^+/Cl^+ to that reported here for ND^+. However, their study was hampered by the fact that they started from a neutral gas target of DCl (rather than an ion beam of DCl^+) which subsequently limited the range of intensities they could study due to the need to first ionize DCl molecules, and then dissociate the resulting DCl^+, within the same laser pulse. Moreover, there were additional effects that inhibited a direct measurement of the DCl^+ dissociation branching ratio. For example, Korolkov *et al.* found that the intensity that gave maximum rate of change in the branching ratio depended sensitively on the chirp of the laser pulse. They attributed this to the fact that different chirps would populate the DCl^+ molecule in a different range of initial vibrational states, which affects the branching ratio. In our study this effect is circumvented as the ND^+ ions are formed by electron-impact in the ion source, and furthermore, they form a vibrationally cold target. In addition, in the DCl^+ experiment, the branching ratio was inferred from the ratio of the D^+/Cl^+ ions formed. However, ionization to DCl^{2+} followed by decay into $D^+ + Cl^+$ would inherently have an adverse effect on the branching ratio. Such an example underlines the advantage of the method used here where the dissociative fragments (both ion and neutral) are measured in coincidence.

4.3.4 Summary

In summary, in this section we have presented a concise analysis of the intense-field dissociation of the astrophysically important species, ND^+. This was facilitated by our kinematically complete, coincidence 3D imaging technique, which allowed a clean measurement of the branching ratio of the two possible dissociation channels, $N^+ + D$ and $N + D^+$. These distributions lead us to conclude that, in the intensity range 2×10^{13} – 3×10^{15} W/cm^2, dissociation is most likely dominated by the $X^2\Pi$ ground state of ND^+, proceeding via the $A^2\Sigma^-$ state for production of $N^+(^3P) + D(^2S)$, and the $4^2\Pi$ state for production of $N(^2P) + D^+$. Additionally, the ratio of the two dissociation channels was found to be very sensitive to intensity, the $N + D^+$ channel dropping rapidly in rate with decreasing intensity below ∼10^{14} W/cm^2.

4.4 N_2^+ laser-induced ionization and dissociation[83]

4.4.1 Introduction

The final diatomic molecular ion that will be considered in this dissertation is N_2^+ as it is similar to the other diatomic molecules discussed so far yet produces some intriguing and unexpected features. First of all, at the highest intensities we measure a *surprising* distinct dissociation feature at very high ($\sim$ 6 eV) KER. Second, we also measure a KER distribution for ionization that stretches beyond the Coulomb-explosion/direct-ionization limit. In this section, we will explore the probable ionization and dissociation mechanisms responsible for these and other predominant features in the measured 3D momentum distributions.

4.4.2 Experimental

In this experiment we used the 790 nm ultrashort pulse, detailed in appendix A.3, to produce $\tau = 7^{+2}_{-1}$ fs pulses with intensities up to $I_0 = 6.0 \times 10^{15}$ W/cm^2. Lower intensities were achieved by scanning the $f = 203$ mm off-axis parabolic mirror focal position, i.e. by using the intensity scanning technique described in section 2.6 [94, 121]. The target is a 9keV N_2^+ molecular ion beam, which has some unique properties. Most importantly, the N_2^+ beam is vibrationally cold and predominantly in its electronic ground state. This is due to large Franck-Condon overlap of the ground state of N_2 with the low vibrational states of N_2^+ [190, 191], as detailed in appendix A.2.1.1. For the N_2^+ ions produced in an ion source by electron impact, i.e. via vertical transitions, most of the population is distributed among the three lowest electronic states, namely, the ground state $X\,^2\Sigma_g^+$ and the metastable $A\,^2\Pi_u$, and $B\,^2\Sigma_u^+$ states [68–70]. These states are shown in figure 4.16(a) along with some additional relevant PECs of N_2^{q+} with q$\leq$2. The radiative lifetime of the different vibrational levels of the N_2^+ metastable states are a few tens of microseconds for the $A\,^2\Pi_u$ and a few nanoseconds for the $B\,^2\Sigma_u^+$. So, the electronic and vibrational population distributions will change from when they are first produced in the ion source to when the ions reach the interaction region, i.e. after the transit time of $\sim$ 20 μs in our set up. We have calculated the

[83] Much of the work in this section has been previously reported in our publication [51].

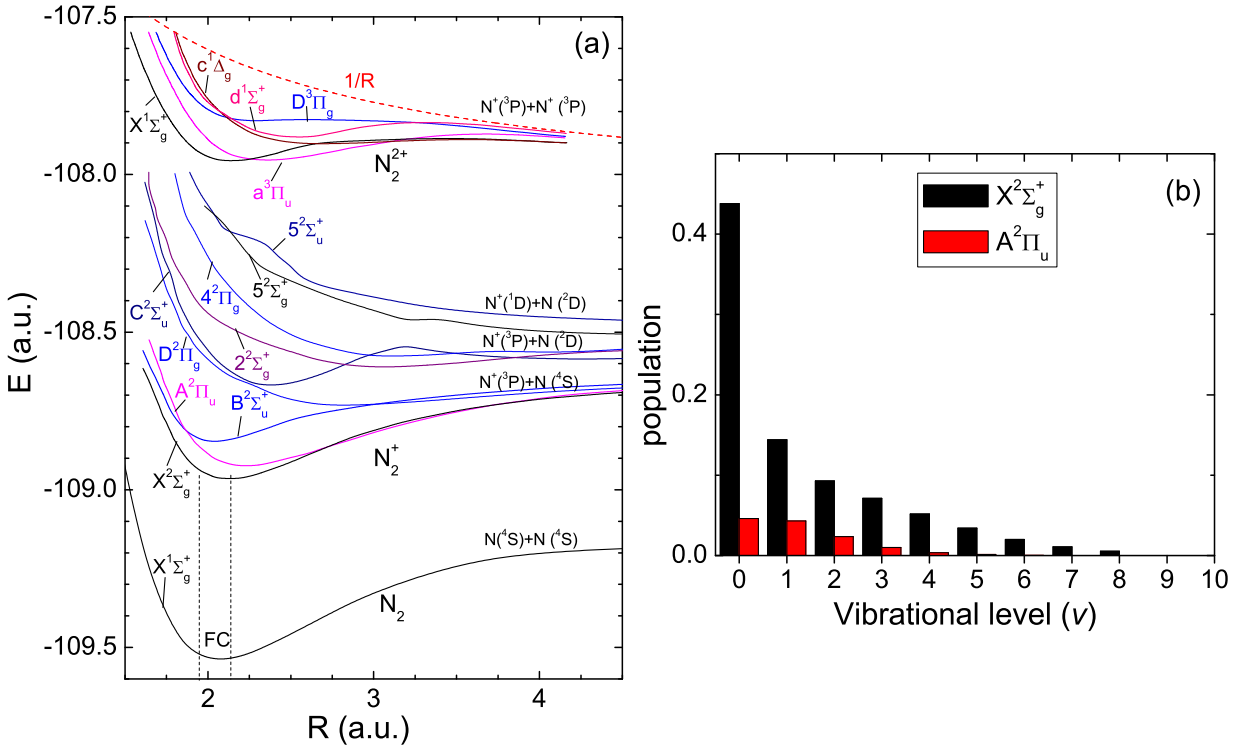

Figure 4.16: (a) A simplified potential energy curve diagram of N_2^{q+}(q≤2) showing only a selection of the lowest lying curves for each q. The PEC of N_2 is taken from [191], N_2^+ from [193] and N_2^{2+} from [194]. The dashed vertical lines represent the Franck-Condon (FC) region. The zero of the energy is for the fully stripped N^{7+}+ N^{7+}+14e^- limit. (b) Calculated vibrational population distribution of N_2^+ in the interaction region following decay of metastable states from the source. (Figure adapted from our previous publication [51].)

overall vibrational population distribution in the aforementioned electronic states at the interaction region by applying the method described by Crandall *et al.* [69] and using the data from references [69, 192]. The resulting vibrational population of the ions in the interaction region is shown in figure 4.16(b). At the interaction point, the $X\,^2\Sigma_g^+(v=0)$ state is most highly populated (> 40%) with only a small amount of population remaining in the $A\,^2\Pi_u$ state (total population <13%) and virtually no population in the $B\,^2\Sigma_u^+$ state. Furthermore, more than (83%) of the population is in $X\,^2\Sigma_g^+(v$ = 0–7) states, i.e. within 1.5 eV (roughly the energy of 1 photon) of the bottom of the potential well.

4.4.3 Dissociation

The KER distributions for the 7 fs, 790 nm laser-induced dissociation of N_2^+ (often referred to as the (1,0) channel) at 6.5×10^{14} and 6.0×10^{15} W/cm^2 are displayed in figures 4.17(a) and (b), respectively. For the lower intensity, the results display a sole low energy peak centered around 0.6 eV and extending up to ∼2.5 eV. This KER range is consistent with other studies of N_2^+ [195–197], however the other studies find distributions peaked around 0.0 eV (for 25 fs, 10^{14} W/cm^2 pulses) [197], 1.2 eV (for 33 fs, 10^{15} W/cm^2 pulses) [195], and 1.8 eV (for 55 fs, $\sim 10^{16}$ W/cm^2 pulses) [196].[84] In addition to the low KER peak shown in figure 4.17(a), the KER spectrum measured at higher intensity (6.0×10^{15} W/cm^2) shown in figure 4.17(b) has an additional KER peak around 6.1 eV. *Such a high KER feature from the non-ionizing dissociation of a simple molecule is rather surprising and has not been reported previously.* Note that this may very well be due to the strength of our coincidence time-of-flight experimental technique, described in appendix B, which allows us to uniquely separate dissociation and ionization channels even when they have the same KER [36, 52].

4.4.3.1 Dissociation pathways

Low kinetic energy release To determine the dissociation pathways we will use the same technique described when discussing O_2^+ and ND^+ above [37, 50]. The main difference between this case and those is that the angular. distributions for the two dissociation peaks are not sharply peaked (See insets in figures 4.17(a) and (b).) That is to say that the $\cos\theta$ distributions have significant contributions along both $\cos\theta = 0$ and $|\cos\theta| = 1$. This implies that perpendicular transitions, as well as the dominant parallel transitions, play an important role in the dissociation. For the low KER peak, through a process of eliminating pathways that do not agree with the

[84] The reason for this difference is unclear and further investigation is required.

measured dissociation distribution, we find three important pathways,

$$\alpha \equiv |\mathrm{X}\,^2\Sigma_g^+\rangle \rightarrow |\mathrm{C}\,^2\Sigma_u^+ - 7\omega\rangle$$
$$\beta \equiv |\mathrm{X}\,^2\Sigma_g^+\rangle \rightarrow |\mathrm{D}\,^2\Pi_g - 6\omega\rangle$$
$$\gamma \equiv |\mathrm{X}\,^2\Sigma_g^+\rangle \rightarrow |2\,^2\Sigma_g^+ - 8\omega\rangle\ ,$$

which are shown in figure 4.17(c) and we believe comprise the bulk of the dissociation yield. First, α is a parallel transition which contributes the bulk of the counts and should produce a distribution near $|\cos\theta| = 1$ and 0.6 eV. Second, β is a perpendicular transition which will yield dissociation around around $\cos\theta = 0$ and 1.0 eV, i.e. just above the maximum of the KER peak. Third, γ is a parallel transition that will result in a 1.6 eV KER that may contribute to the tail of the KER distribution.

High kinetic energy release As shown in figures 4.17(a) and (b), the surprising high KER ($\sim$6 eV) dissociation peak is observed only at high intensities ($\sim 6 \times 10^{15}$ W/cm^2), which strongly suggests that the dissociation mechanism(s) responsible for this peak require a larger number of photons than the previously discussed low-KER peak. Furthermore, the inclusion of more photons makes accessing electronic states from higher manifolds, e.g. $\mathrm{N}^+(^3P) + \mathrm{N}(^2D)$ and $\mathrm{N}^+(^1D) + \mathrm{N}(^2D)$ shown in figure 4.16(a), more likely. Additionally, figure 4.17(b-inset) reveals a broad angular distribution which suggests contributions for dissociation pathways with a variety of angular dependencies. Figure 4.17(d) shows some examples of dissociation pathways that conform to the measured data, i.e. $|X\,^2\Sigma_g^+\rangle \rightarrow |4\,^2\Pi_g - 10\omega\rangle$, $|X\,^2\Sigma_g^+\rangle \rightarrow |5\,^2\Sigma_g^+ - 12\omega\rangle$ and $|X\,^2\Sigma_g^+\rangle \rightarrow |5\,^2\Sigma_u^+ - 13\omega\rangle$.[85] We note, however, that there are a number of additional pathways that can contribute to KER in the observed range but have been omitted from the figure for clarity. Involvement of multiple dissociation pathways is also supported by the hints of structure in the high KER peak shown in figure 4.17(d).

[85] Note that the high KER produced by these pathways also depend upon the nuclear wavepacket not making additional transitions to states with lower energy dissociation limits as is discussed in reference to the high KER tail seen in dissociation of H_2^+ in section 3.2.3

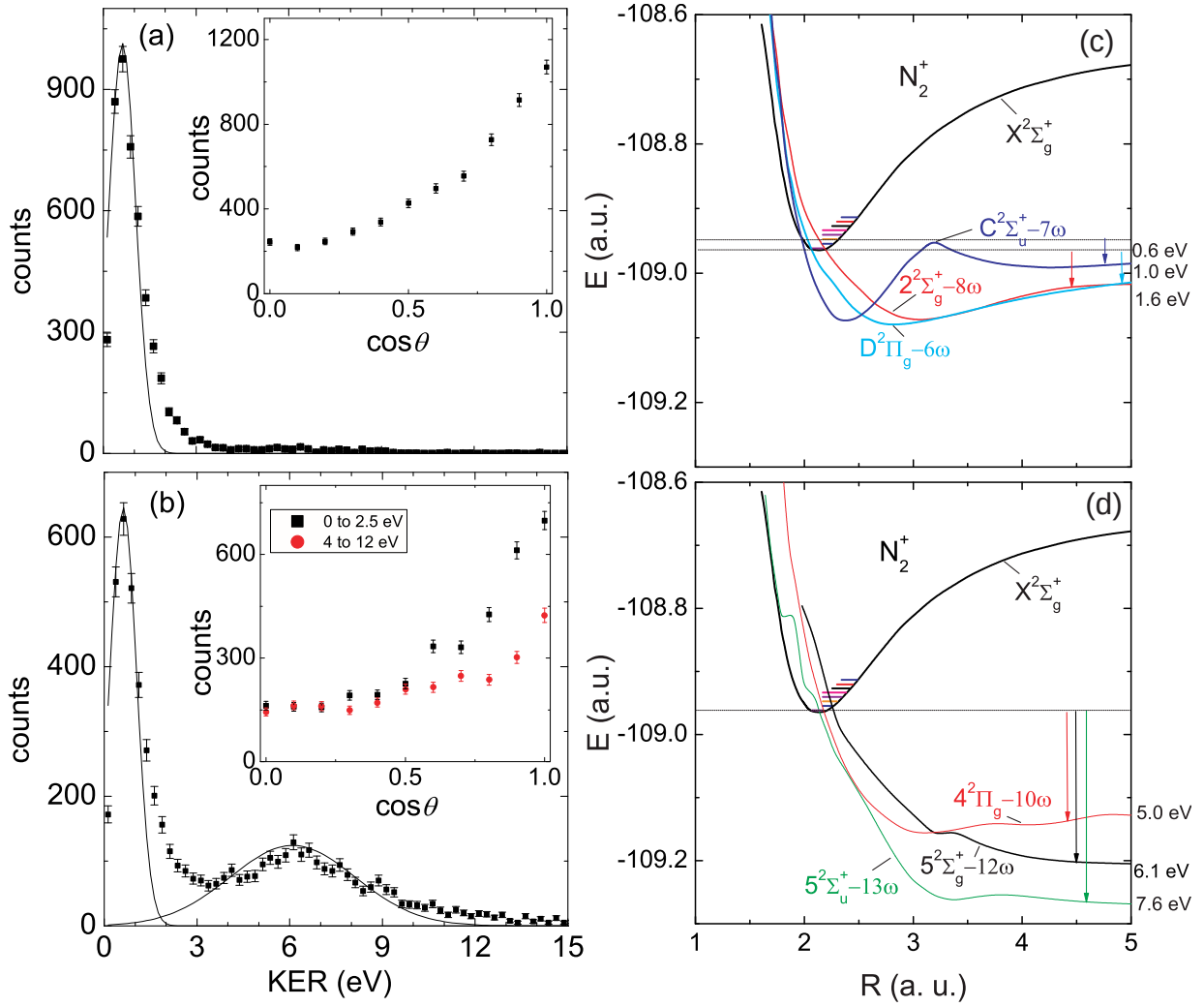

Figure 4.17: (a) – (b) Measured KER distributions for dissociation of N_2^+ using 7 fs pulses at intensities (a) 6.5×10^{14} W/cm^2, and (b) 6.0×10^{15} W/cm^2 with corresponding angular distributions, in inset, plotted versus $|\cos\theta|$. The error bars denote the statistical errors in the data. The fitted curves are Gaussian distributions centered at the peak of the measured KER distribution and only used as a guide. (c) – (d) Dressed-states diabatic picture of N_2^+ illustrating dissociation pathways that lead to (c) low and (d) high, KER dissociation (see text). The short lines within the potential well represent the different vibrational levels and the horizontal lines near the bottom of the potential represent the initial energy of the dissociation wavepacket. (Figure adapted from our previous publication [51].)

Electronic structure Since the initial vibrational population of N_2^+ is concentrated around the equilibrium distance, the number of states that are likely to be coupled to the initial $X\,^2\Sigma_g^+(v\simeq 0)$ state are severely limited by the requirement that they cross through the small region occupied by these low vibrational states of $X\,^2\Sigma_g^+$ (see figures 4.17(a) and (b)). This requirement leaves us with two basic subsets of curves groups that lead to dissociation: low-lying shallow potentials that lead to low KER, and higher lying steep potentials that lead to high KER in dissociation. The highly excited electronic states associated with the removal of inner valence electron are steeper than the lower lying electronic states because of the reduced screening of the nuclear potential. The ground state $X\,^1\Sigma_g^+$ of N_2 is $(1\sigma_g)^2\ (1\sigma_u)^2\ (2\sigma_g)^2\ (2\sigma_u)^2\ (1\pi_u)^4\ (3\sigma_g)^2$ and that of N_2^+ is obtained by removing one electron from the $(3\sigma_g)$ orbital, i.e. $X\,^2\Sigma_g^+$ is represented by $(1\sigma_g)^2\ (1\sigma_u)^2\ (2\sigma_g)^2\ (2\sigma_u)^2\ (1\pi_u)^4\ (3\sigma_g)^1$. The shallower excited state $D\,^2\Pi_g$ of N_2^+ is represented by $(1\sigma_g)^2\ (1\sigma_u)^2\ (2\sigma_g)^2\ (2\sigma_u)^2\ (1\pi_u)^4\ (1\pi_g)^1$, i.e. the outer valance electron from $(3\sigma_g)$ is excited to the $(1\pi_g)$ orbital. In the case of steeper excited states, one of the inner valence electrons goes to the outer orbital. For example, one of the electrons leaves the inner valence $(2\sigma_g)$ orbital in the steeper $5\,^2\Sigma_g^+$ state of N_2^+ [193, 198, 199].

4.4.3.2 Rate

Before proceeding, it is interesting to note that the large number of photons required to dissociate N_2^+ (6 – 13 photons) is reflected in the measured dissociation rates. For example, at 6.0×10^{15} W/cm^2 the dissociation rate of N_2^+ is about a factor of two lower than O_2^+ under similar ion and laser beam conditions, because the dominant dissociation paths for O_2^+ require 1 – 4 photons [37]. Similarly, the dissociation rate is approximately a factor of 20 lower than H_2^+, which requires only 1 – 2 photons to dissociate [42]. Hence, one observes directly a link between the large multiphoton nature of the dissociation pathways we have identified and the difficulty in breaking N_2^+ in an intense laser field.

4.4.4 Ionization

Under these experimental conditions we see ionization of N_2^+, which fragments to $N^+ + N^+$ (usually referred to as the (1,1) channel), in addition to dissociation. For our lower intensity KER measure-

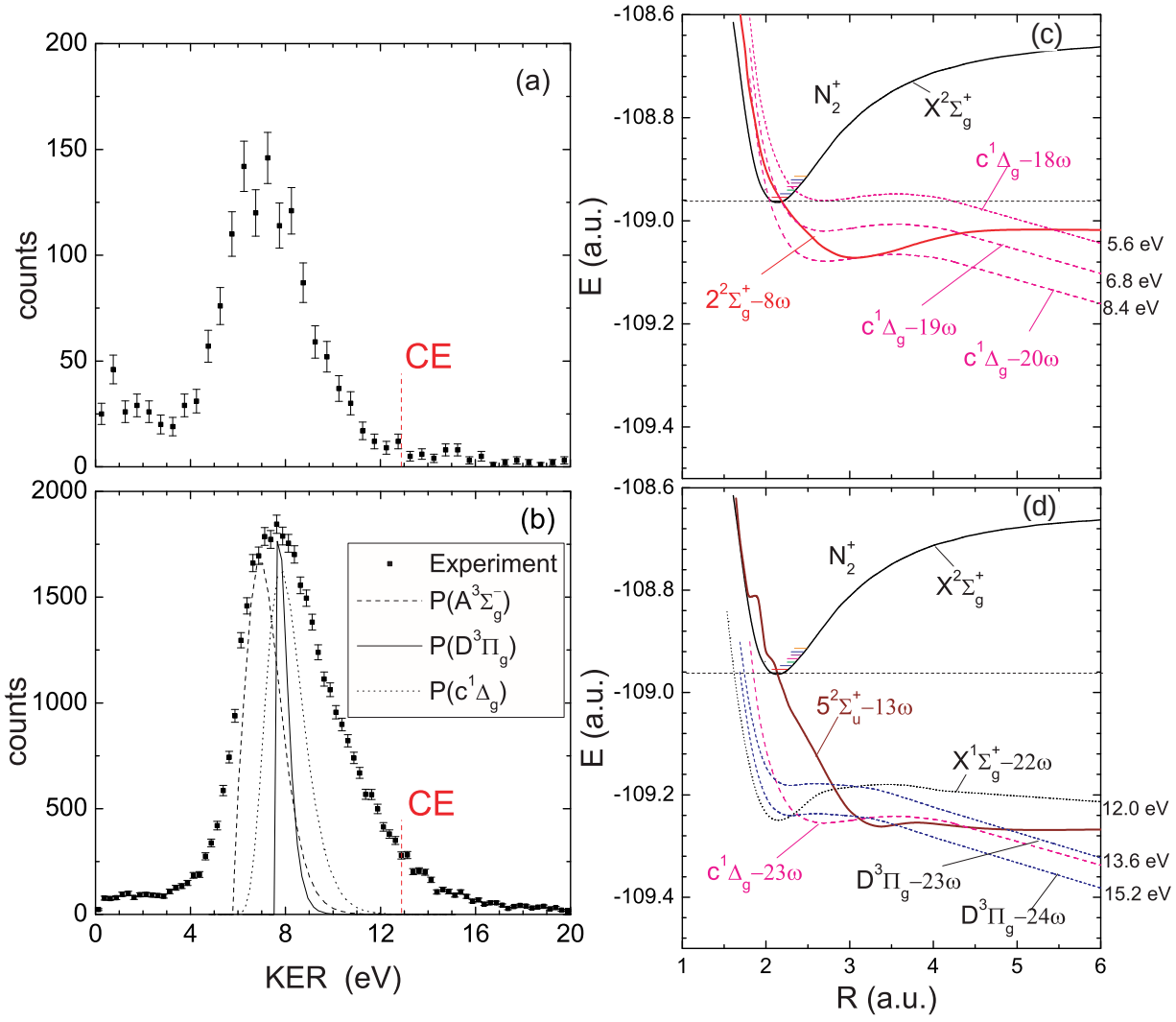

Figure 4.18: (a) – (b) Measured KER distributions for ionization of N_2^+ using 7 fs pulses at intensities (a) 6.5×10^{14} W/cm^2 and (b) 6.0×10^{15} W/cm^2. A few probability distributions (arbitrary yields) expected for direct ionization to the c $^1\Delta_g$ (dotted line), D $^3\Pi_g$ (solid line), and A $^3\Sigma_g^-$ (dashed line) states of N_2^{2+} are also shown. The dotted vertical lines indicate the energy corresponding to Coulomb explosion(CE) of N_2^+. The error bars denote the statistical error in the data. (c) – (d) Dressed-states picture of N_2^+ incorporating both dissociation (solid) and ionization (broken) curves that illustrate the dissociative ionization pathways. The pathways shown in (c) and (d) are believed to lead to the low and high KER in ionization shown in (a) and (b), respectively (see text for discussion). (Figure adapted from our previous publication [51].)

ment at 6.5×10^{14} W/cm^2 shown in figure 4.18(a), we observe a KER peak centered around 7 eV with a width of about 4 eV. The very low KER counts ($\lesssim 2$ eV) are likely to be false coincidences of N^+ fragments arising from the more dominant $N^+ + N$ dissociation channel at this intensity. The main peak of the distribution is comparable to the KER value measured in the majority of studies starting with N_2, using both similar [112] and longer [195–197, 200–203] pulses.

4.4.4.1 Direct ionization

There are two possible mechanisms that could lead to KER in the range of 6 – 12 eV. The first — direct ionization — directly promotes the nuclear wavepacket from the initial $N_2^+[X\,^2\Sigma_g^+(v \simeq 0)]$ state onto the N_2^{2+} manifold of states, i.e. a single quasi-instantaneous vertical transition. As a zeroth order approximation, the KER for such a process is typically estimated as $1/R_0$in a.u., which arises from pure Coulomb explosion of the product fragments and is marked by the dashed line labeled CE in figure 4.18(a). However, most of the low lying N_2^{2+} states have shallow potentials in the direct ionization region and lie well below the $1/R$ Coulomb curve, as shown in figure 4.16(a). Thus, they would yield lower KER than expected for pure Coulomb explosion. Using the true shape of the N_2^{2+} potentials, we have estimated the results of the vertical transition by projecting the N_2 ground state wavefunction onto some relevant N_2^{2+} states,[86] as shown in figure 4.18(b). This leads to KER values in the 6 – 12 eV range seen at 6.5×10^{14} W/cm^2, but does not explain the unexpected extension for ionization KER at 6.0×10^{15} W/cm^2 to well beyond the Coulomb explosion limit marked in figure 4.18(b).

4.4.4.2 Low KER indirect ionization

In addition to direct ionization, we have seen that indirect ionization (ionization initiated by dissociative stretching of internuclear distance), e.g. CREI and ATCE for H_2^+ ionization discussed in section 3.3, is an important process. However, this type of mechanism typically produces lower KER than is expected for direct ionization as the ionization step occurs for stretched molecules which have less potential energy (i.e. $V = 1/R$ decreases with increasing R). Nevertheless, as the

[86] Following the interpretation of Voss *et al.* [112] the $D^3\Pi_g$ state is the most probable dissociation route for such direct ionization.

likely dissociation pathways were identified above, we will examine some possible indirect ionization pathways to determine the range of KER that these processes can produce. For example, a wavepacket dissociating on the $|2\,^2\Sigma_g^+ - 8\omega\rangle$ curve shown in figure 4.17(c) may cross onto the dressed $|c\,^1\Delta_g - 19\omega\rangle$ or $|c\,^1\Delta_g - 20\omega\rangle$ states at R=2.4 or 3 a.u., respectively, giving KER in the range $\sim$ 6.5 – 8.5 eV (see figure 4.18(c)). However, this is only possible if the nuclear wavepacket can reach the second crossing, e.g. $|2\,^2\Sigma_g^+ - 8\omega\rangle \rightarrow |c\,^1\Delta_g - 19\omega\rangle$, while the laser pulse is still "on". To check this condition, we have estimated classically the time it takes a dissociating N_2^+ wavepacket to reach these crossings with the N_2^{2+} states at $R \sim$(2.5 – 3.0) a.u. and find it to be typically $\sim$ 7 fs, within the duration of the laser pulse. Furthermore, as shown in figure 4.16(a), there is a large density of accessible N_2^{2+} states, in addition to c $^1\Delta_g$, leading to the same $N^+(\,^3P) + N^+(\,^3P)$ dissociation limit. Each of these may contribute slightly different KER values resulting in a broadening of the observed KER distribution. Thus, we are not able to distinguish here between the contributions from the aforementioned direct and indirect ionization pathways.

4.4.4.3 High KER indirect ionization

Although the unexpected extension of ionization KER at 6.0×10^{15} W/cm^2 to well beyond the Coulomb explosion limit marked in figure 4.18(b) has still not been explained, we have learned that the nuclear wavepacket has sufficient velocity to enable indirect dissociation for even the ultrashort $\simeq$ 7 fs pulses used in this measurement. Additionally, we have found that a reduction of the internuclear distance R at which ionization occurs (i.e. the mechanism which typically accounts for an increase in ionization KER with increased intensity) cannot account for the highest portion of the KER distribution as, even in the limit of direct ionization, KERs above $\sim$ 12 eV cannot be reached. Furthermore, as we see 20-photon indirect ionization, e.g. $|X\,^2\Sigma_g^+\rangle \rightarrow |2\,^2\Sigma_g^+ - 8\omega\rangle \rightarrow |c\,^1\Delta_g - 20\omega\rangle$, at 6.5×10^{14} W/cm^2 and 13-photon dissociation, e.g. $|X\,^2\Sigma_g^+\rangle \rightarrow |5\,^2\Sigma_u^+ - 13\omega\rangle$, at 6.0×10^{15} W/cm^2, it is apparent that pathways involving one or more 10- to 15-photon transitions are accessible at the highest intensity. Thus, let us consider an ionization pathway which starts with the steepest and most energetic dissociation pathway found to be effective above 6.0×10^{15} W/cm^2 — the $|X\,^2\Sigma_g^+\rangle \rightarrow |5\,^2\Sigma_u^+ - 13\omega\rangle$ dissociation pathway. As shown in figure 4.18(d), this state intersects

the ionized $|c\,^1\Delta_g - 23\omega\rangle$ and $|D\,^3\Pi_g - 24\omega\rangle$ states at $R \sim 3$ a.u.. Furthermore, assuming classical nuclei, the nuclear wavepacket travels from the initial $|X\,^2\Sigma_g^+\rangle \rightarrow |5\,^2\Sigma_u^+ - 13\omega\rangle$ transition to the ionization crossing in ~ 5 fs. This short travel time is necessary in this case as the pulse width ($\tau \simeq 7$ fs) is short and the first 13-photon and second 11- or 12-photon transitions require the high intensities available only within a few fs of the peak of the laser pulse. Therefore, we find it likely that the $\gtrsim 12$ eV tail in the KER distribution is caused by the ionization of stretched molecules, e.g. via pathways such as $|X\,^2\Sigma_g^+\rangle \rightarrow |5\,^2\Sigma_u^+ - 13\omega\rangle \rightarrow |D\,^3\Pi_g - 23\omega\rangle$ and those shown in figure 4.18(d). This contradicts the trend seen in section 3.3 for H_2^+ in which increasing KER in ionization is believed to correspond to a decrease in the internuclear distance R at which the ionization occurs, i.e. KER=$1/R$ in a.u.. This is because the H_2^{++} potential energy curve, i.e. $1/R$ in a.u., decreases with increasing internuclear distance while the N_2^{++} potential curves are relatively flat in the region from the N_2^+ equilibrium distance to $\sim$4 a.u., as shown in figure 4.18(d).

4.4.5 Summary

In this section, we have presented the results of dissociation and ionization of N_2^+ in an intense ultrashort laser pulse using a coincidence 3D momentum imaging technique that has allowed us to completely separate the dissociation and ionization channels despite their overlap in KER. Furthermore, we find two surprising features in the ultrashort laser-induced fragmentation of this molecule. First, in dissociation there is a distinct KER peak with an unusually high KER, which we have assigned to multiphoton excitation to a group of steep PECs belonging to the excited N_2^+ manifold(s). Second, for high intensities, the ionization KER extends beyond the typical limits of pure Coulomb explosion and direct ionization, which we believe is due to the counterintuitive concept that ionization of a stretched molecule can indeed enhance the energy released from the system in some cases.

4.5 Conclusions

In this chapter, we have presented detailed state-of-the-art intensity dependent measurements of laser-induced ionization and dissociation of O_2^+, ND^+, and N_2^+. The measured 3D momentum distributions for dissociation have been interpreted by extending the Floquet picture developed in previous chapters to multielectron diatomic molecules, thereby yielding probable dissociation pathways for the dominant dissociation features. Additionally, we have interpreted the measured ionization of N_2^+ using the unified Floquet (UF) model discussed in chapter 3. In addition to the data presented here, we have measured laser-induced fragmentation of other diatomic molecular ions, e.g. CO^+ and CD^+, and have seen dissociation, ionization, multi-electron ionization, e.g. $CO^+ \rightarrow C^{2+} + O^{2+}$, and even asymmetric breakup following ionization [169], e.g. $N_2^+ \rightarrow N^{2+} + N$. Although these measurements have been omitted form this dissertation for brevity, the general rules for determining fragmentation pathways retain their predictive and interpretive power.

Chapter 5

Polyatomic Molecular Ions[87]

5.1 Introduction

The H_3^+ molecular ion is an important benchmark in the understanding of laser-matter interactions because its status as the simplest polyatomic molecule places H_3^+ at the threshold between the relatively well understood diatomic molecule-laser interactions and the increasing complexity of polyatomic molecule-laser interactions. Thus, we envision H_3^+ playing the same fundamental role in the understanding of polyatomic systems in intense laser fields as H_2^+ has played for diatomic molecules. Furthermore, it is only recently that *ab initio* calculations (i.e. via direct numerical solution of the time-dependent Schrödinger equation) of two electron systems in intense laser fields have become possible [204–210]. Therefore, we hope that such treatments can be extended to the two-electron system — H_3^+.

In addition to its benchmark status, H_3^+ also plays an important role in many diverse areas of physics. For example, H_3^+ is believed to be the most abundant charged molecular species in interstellar clouds [211, 212], key to planetary ionospheres [213], the prototype for molecular formation in ion-sources [214], and important in thermonuclear reactions [214]. For these reasons H_3^+ has been the subject of many theoretical studies, including a few in the ultrashort-laser community: for example, molecular high-order harmonic generation (HHG) [4, 5], three-body photo-fragmentation

[87] Much of the work will be reported in a publication in preparation which we plan to submit to a top journal. Furthermore, as these journals typically require publications to be novel, information pertaining to the measured results of laser-induced fragmentation of H_3^+ will be limited.

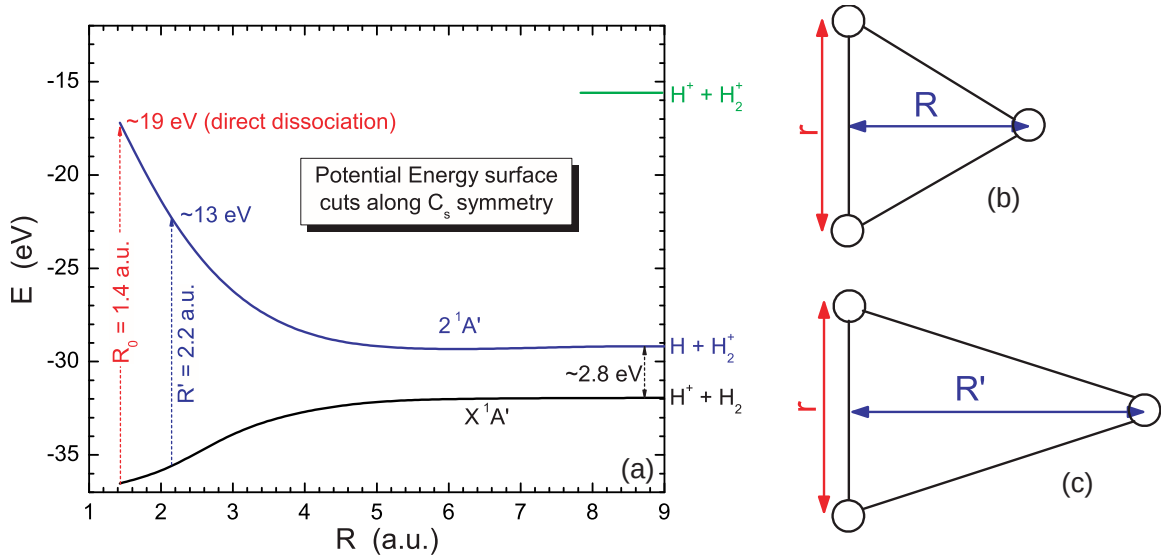

Figure 5.1: (a) Selected cuts of H_3^+ potential energy surfaces taken from reference [225]. For these cuts, the internuclear distance between the bound H_2 and H_2^+ are set to their respective equilibrium distances and kept constant for $X\,^1A'$ and $2\,^1A'$, respectively. (This is commonly known as the C_s symmetry where stretching occurs along the R-axis.) The ground electronic state of H_3^+ is the $X\,^1A'$ state which dissociates to the $[H^+ + H_2]$ limit and the lowest lying two-body fragmentation electronic state is the $2\,^1A'$ state which goes to the $[H+H_2^+]$ limit. (b) A schematic of the coordinate system being used for H_3^+. (c) An example of stretching in the R-dimension.

[215], enhanced ionization [216], and dissociative recombination (DR) in polyatomic molecules [217].

Intense laser-induced processes have previously been measured in more complex triatomic molecules, e.g. the changes in geometry of H_2O [59], CO_2 [218], NO_2 [219], and SO_2 [220] and Coulomb explosion of OCS [221]. In addition to triatomic molecules, intense laser-induced processes have been measured for even more complex polyatomic molecules, e.g. acetylene to vinylidene transitions in C_2H_2 [153], fragmentation of C_6H_6 [222], the dynamics of CH_4 [223], and many others [224]. Although these molecules are readily available and easier to fragment with intense ultrafast laser pulses than H_3^+, the large number of electrons requires one to make more assumptions when performing calculations and complicates the fundamental understanding that H_3^+ may yield.

5.2 Difficulties in measuring laser-induced fragmentation of H_3^+

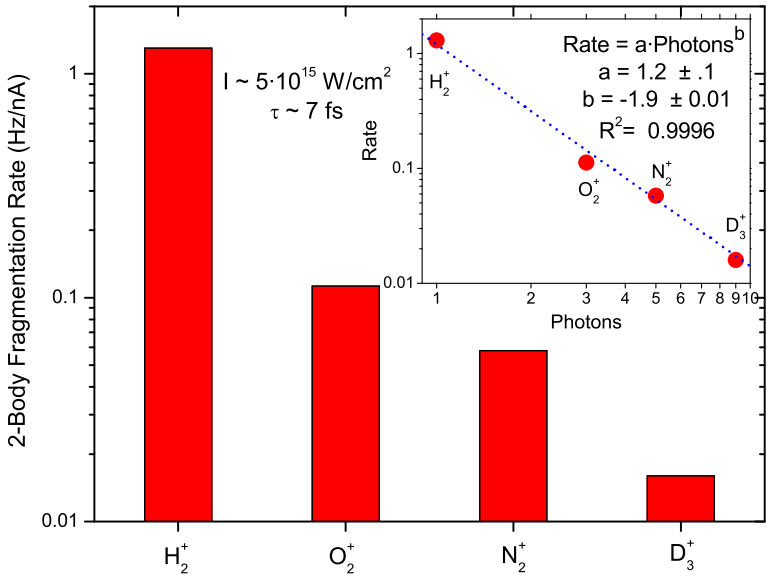

Figure 5.2: Laser-induced fragmentation rates for the dominant two-body dissociation channels of H_2^+, O_2^+, N_2^+, and D_3^+ for 7 fs, 5×10^{15} W/cm pulses, namely $[H + H^+]$, $[O + O^+]$, $[N + N^+]$, and $[D^+ + D_2]$, respectively. (inset) Log-log plot of the dissociation rate as a function of minimum number of photons needed to dissociate that molecular ion. (see text for discussion).

Introduction Measuring the laser-induced fragmentation of H_3^+ has proven to be an extremely difficult task for our group and the molecular ion beam community as a whole. Because of its importance, as discussed above, several experimental groups in addition to our own (e.g. Zajfman *et al.* at The Weizmann Institute of Science, Israel, Williams *et al.* at Queens University Belfast, U.K., and Paulus *et al.* at Texas A&M and Friedrich-Schiller-Universität Jena, Germany) have tried to measure laser-induced fragmentation of H_3^+. However, all have failed until our recent success. In this section, we will discuss the difficulties in measuring laser-induced fragmentation of H_3^+.[88]

Dissociation rate First, by examining the potential energy curves (PECs) of H_3^+, e.g. those shown in figure 5.1(a), one sees that H_3^+ is strongly bound. Quantitatively, the $H + H_2^+$ dissociation limit of the ground $X\,^1A'$ state is $\sim$ 4.6 eV above the minimum at $R \simeq 1.4$ a.u. and a direct

[88]Note that the discussion in this chapter concerning why other groups have failed to measure H_3^+ laser-induced fragmentation will be limited as we are in direct competition with these groups and are therefore unaware of all aspects of their measurement attempts. Nevertheless, the reasons we have failed to measure this process until recently will be discussed and compared to the known aspects of experiments by others.

vertical transition to the lowest lying dissociative electronic state, i.e. $2\,^1A'$, would require $\sim$ 19 eV, i.e. about 13 photons at 790 nm. Furthermore, we believe that the vibrational population is peaked at or below $R \simeq 2.2$ a.u. as denoted by the vertical arrow in figure 5.1(a).[89] Thus, even the populated excited vibrational states of H_3^+ would require a minimum of $\sim$ 13 eV, i.e. $\sim$ 9 photons at 790 nm, to dissociate. This means that dissociation (i.e. a vertical transition to a dissociative state) from a populated vibrational state of H_3^+ is greater than for any of the other molecules discussed in this dissertation, namely H_2^+, O_2^+, and N_2^+ which require at least 1, 3, and 5 photons, respectively. Furthermore, we have found that, not surprisingly, the laser-induced dissociation rate for a particular molecular ion increases as this energy gap decreases. This relationship is illustrated in figure 5.2, which shows the laser-induced dissociation rate of H_2^+, O_2^+, and N_2^+ with 7 fs, $5{\times}10^{15}$ W/cm^2 pulses.[90] One would expect that the dissociation rate of H_3^+ should be < 0.06 Hz/nA (i.e. less than that of already challenging measurement of N_2^+), which is confirmed by our measurements in which the $(H + H_2^+)$ dissociation rate is found to be 0.016 Hz/nA as shown in figure 5.2. This means that for every nA of beam current one will detect one true dissociation event per $\sim$60,000 laser pulses.[91]

Additionally, we have found that the relationship between the dissociation rate of the primary dissociation channel and the minimum number of photons needed to dissociate that molecular ion adheres to a power law. This relationship is shown in figure 5.2(inset) where the function $\text{Rate} = 1.2 \cdot \text{Photons}^{-1.9}$ fits the data points nicely. In general, this trend serves as a very rough, yet helpful, rule-of-thumb in our measurements, which allows us to quickly estimate the dissociation rates we should expect.

Since the probability of measuring an H_3^+ laser-induced dissociation event per nA of current and per laser pulse is so small, a high ion beam current density, a high laser repetition rate, and a low level of background noise are necessary to measure this process. In our measurements we use a 1

[89] The reason behind our assumptions about the vibrational population will be discussed momentarily.

[90] In this discussion, including figure 5.2, we report the rate of coincidence detection of the particular fragmentation channels, which includes the probability for detecting all nuclear fragments, i.e. the detector efficiency. When quoting a rate in units of Hz/nA, we are assuming a laser repetition rate of 1 kHz.

[91] Note that we neglect the laser-ion beam overlap, i.e. the intensity volume effect discussed in section 2.6, and assume that the difference in intensity volume effects between measurements is small.

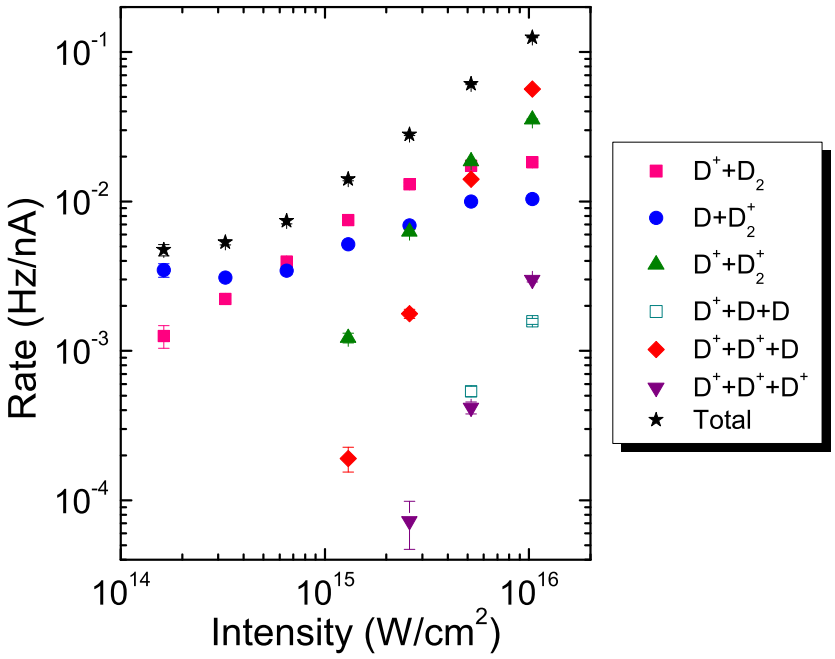

Figure 5.3: Laser-induced fragmentation rates of D_3^+ as a function of intensity. Note that as the intensity was decreased using the zIDS method discussed in section 2.6.1.2, the volume intensity volume effects differs from intensity to intensity. Therefore, there is some deviation in the trends below 10^{15} W/cm^2.

kHz laser repetition rate [102] which gives us an advantage over Williams *et al.* as they typically run at 10 Hz [196]. However, Williams *et al.* typically run with an H_3^+ ion beam of $\simeq$100 nA [226] while we typically have $\sim$10 nA. Nevertheless as the product of ion beam current and laser repetition rate is what is important here, their group would have to measure approximately ten times as long as our group to collect the same statistics (all else being equal). Additionally, other than the emerging ion beam studies of Paulus *et al.* [227] and Zajfman *et al.* at The Weizmann Institute of Science, Israel [228], we are the only group which uses a coincidence time-of-flight method (refer to section 2.3) to measure laser-induced molecular fragmentation. Thus, we have the distinct advantage of being able to "pull" true fragmentation events out of a very large background. This means that despite all the background accumulated from the $\sim$60,000 laser pulses per nA needed to see a single ionization event, we can still "weed-out" the true H_3^+ fragmentation events with certainty using those techniques discussed in chapter 2 and the appendices.

Intensity Second, as shown in figure 5.3, the dissociation rate decreases dramatically with a decrease in intensity. Thus, measurements at $\sim10^{14}$ W/cm^2, e.g. those done by Zajfman *et al.* [228], have a rate about an order of magnitude lower than those done with intensities $\sim10^{16}$ W/cm^2.

Therefore, all the features making measurement of H_3^+ laser-induced fragmentation problematic, as discussed in the previous section, are that much more difficult to overcome. Thus, in addition to the other requirements, a high laser intensity is essential to this measurement.

Three-body breakup Third, laser-induced fragmentation of H_3^+ can lead to both two- and three-body breakup channels. In fact we find that the dominant fragmentation channel in our measurements at $\sim 10^{16}$ W/cm^2 is $H_3^+ + n\hbar\omega \rightarrow H + p + p$ (figure 5.3). Furthermore, experimental techniques which do not utilize coincidence (e.g. Williams *et al.* [82] and Figger, Hänsch *et al.* [81]) do not detect three-body breakup channels well as all three fragments take away energy from a 3-body breakup, thereby spreading their flight times, which makes it difficult to distinguish true events from the background. Even in our coincidence time-of-flight (CTOF) measurements, 3-body breakup channels are more difficult to identify as they do not form a sharp straight line in the CTOF spectrum, as shown in figures 5.4(a) and (b). In our case this problem is resolved/improved by requiring that the center-of-mass of the molecular fragments falls within a small gate.

Three-body fragmentation also presents detection challenges. The main difficulty is detecting three fragments which may not be well separated in time and/or space. For example, when we perform a triple-coincidence measurement for Coulomb explosion of H_3^+, i.e. $H_3^+ + n\hbar\omega \rightarrow p + p + p$, the spectrometer will not distinguish the protons, i.e. particles with identical mass-to-charge ratios, and only the fragmentation energy will separate the protons at the detector plane. This means that the time and/or position signals may not be distinguishable, thereby making data analysis challenging, as is discussed in appendix D. Additionally, as the detection efficiency for an MCP detector is typically $\sim$30% [93], the probability of detecting all three fragments from a true three-body fragmentation event drops to $\sim$3% as compared to $\sim$10% for two-body breakup.

Formation of H_3^+ Fourth, as H_3 is a metastable molecule [231], it cannot be used/introduced directly as a gas target. Rather, one must produce H_3^+ or one of its isotopologues by other means. One can use H_2 gas to produce H_3^+ through the ($H_2^+ + H_2 \rightarrow H_3^+ + H$) reaction inside an ion source [214]. The vibrational population of the $X\,^1A'$ state produced from this process has been

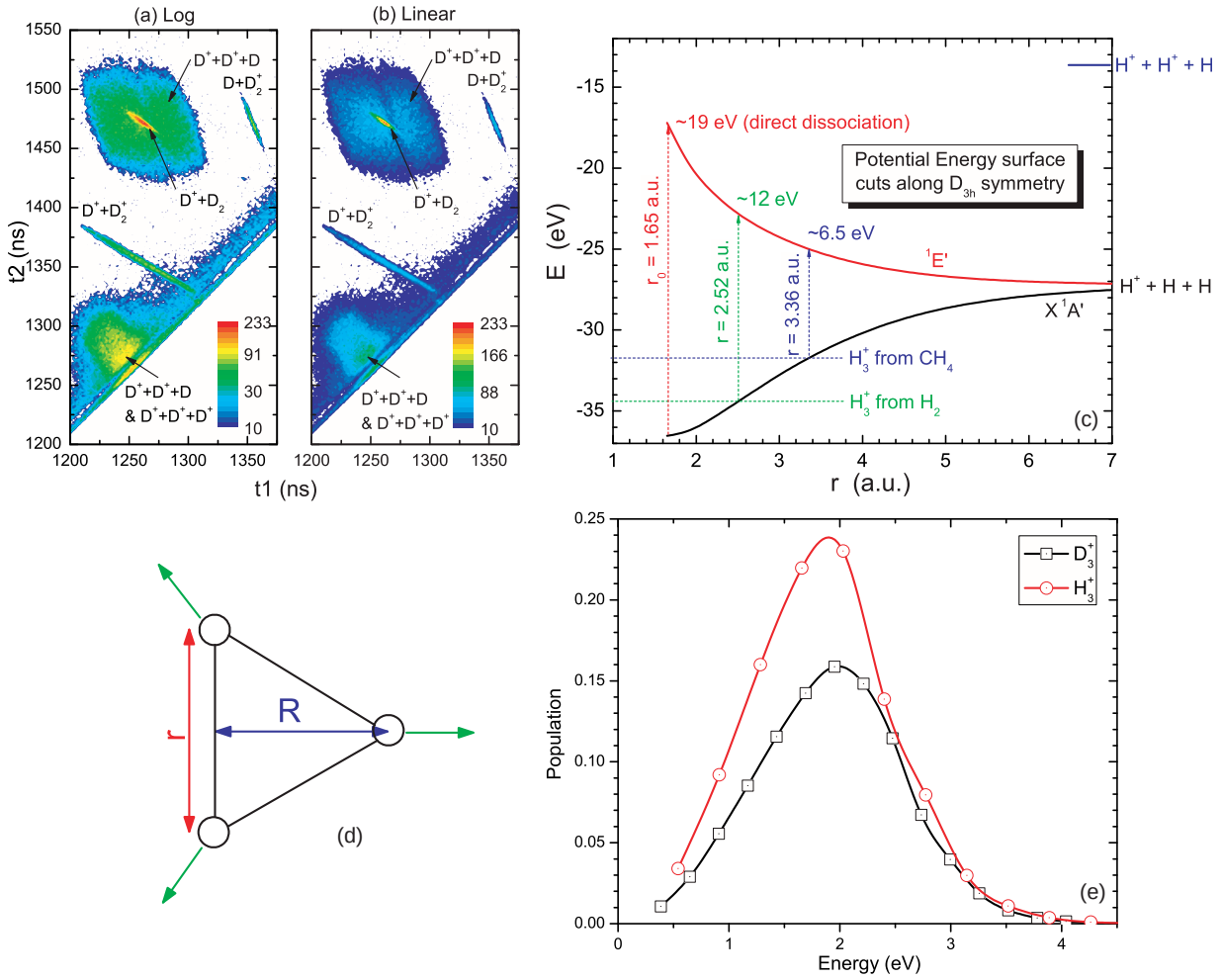

Figure 5.4: (a) and (b) Coincidence time-of-flight histograms for D_3^+ on a logarithmic and linear scale, respectively. The fragmentation channels are denoted on the figures. Note that the 3-body fragmentation channels form a broad distribution in this plot while 2-body fragmentation results in sharp linear features (see text for discussion). (c) Selected cuts of H_3^+ potential energy surfaces taken from reference [225]. For these cuts, all H-H bond lengths are kept equal and the molecule is allowed to stretch as an equilateral triangle. The ground electronic state of H_3^+ is the $X\,^1A'$ state which goes to the $(p + H + H)$ limit and the lowest lying three-body fragmentation electronic state is the $^1E'$ state which goes to the same limit. (d) A schematic of the D_{3h} symmetry. (e) The vibrational population of H_3^+ and D_3^+ expected from the $(H_2^+ + H_2 \rightarrow H_3^+ + H)$ reaction inside our ion source [229, 230]. Each point represents a vibrational level, the curve is only added to guide the eye, the energy scale starts from $E = 0$ at the bottom of the $X\,^1A'$ potential energy surface, and the peak of this distribution is denoted in panel (c) by the green lines.

calculated, as shown in figure 5.4(e) [229, 230]. Alternatively, we have produced H_3^+ in our ion source through dissociative electron impact ionization, e.g. $CH_4 + ne^- \rightarrow H_3^+ + X^{q+}$. Furthermore, as this process is approximately instantaneous, one would expect that the vibrational population of the resulting H_3^+ molecular ion would be roughly determined by the H-H-H bond configuration(s) in the parent molecule. For example, in the CH_4 ground state, the H nuclei are separated by 3.36 a.u. and form equilateral triangles [232], thus the projection onto the daughter H_3^+ molecular ion should have a broad vibrational population as the ground state is an equilateral triangle with sides of 1.65 a.u. [225]. This puts the center of the vibrational wavefunction ~5 eV above energy minimum in the D_{3h} cut of the $X\,^1A'$ electronic ground state, which gives one a very rough idea of the peak of the vibrational distribution, as shown in figure 5.4.[92] In this way, we have tried to tailor the H_3^+ vibrational distribution by choosing various parent molecules. Furthermore, as shown in figure 5.4(a) for the CH_4 H-H bond length of 3.36 a.u., populating high-lying vibrational states means that fewer photons are required for dissociation. Therefore, we expect that both the rate of dissociation is likely to increase for a given intensity and dissociation itself is likely to occur at lower intensities.[93]

Crossing the laser and molecular ion beams Fifth, in intense laser-molecular ion beam measurements, the ion beam is typically $\lesssim$500 μm in diameter and the laser focal spot size is typically ~20 μm in diameter (FWHM) which makes it difficult to cross the two beams inside a vacuum chamber. Thus, one typically uses the yield of the laser-induced fragmentation process itself to maximize the laser-ion beam overlap, as discussed in appendix A and specifically in section A.4. However, the laser-induced fragmentation rate of H_3^+ is very small, as discussed above (see figure 5.3). Thus, we use one of two techniques utilizing "test molecular ions" to cross the two beams: (i) A molecular ion beam with the same mass-to-charge ratio as the desired H_3^+ beam can

[92] The dissociative electron impact ionization of CH_4 in our ion source likely distributes the vibrational population over other electronic potential energy surfaces in addition to the $X\,^1A'$ electronic ground state.

[93] We have performed measurements utilizing both methods of D_3^+ production, i.e. ($D_2^+ + D_2 \rightarrow D_3^+ + D$) and ($CD_4 + ne^- \rightarrow D_3^+ + X^{q+}$), and have not seen any significant effect on the laser-induced fragmentation rates. Nevertheless, a more detailed study is needed to make confident statements about the comparison between absolute fragmentation rates. When starting from D_2 gas, our ion source produces a D_3^+ molecular ion beam with approximately 20 times the current of that seen when starting from CD_4.

be used to cross the beams before switching to the H_3^+ beam. (ii) Alternatively, as described in appendix A.2.2.1, the mass-to-charge ratio of the molecular ion beam is magnetically selected, so a molecular ion beam with a different mass-to-charge ratio can be used to cross the beams before switching to the H_3^+ beam by properly scaling the magnetic fields. Both of these methods have significant drawbacks: (i) It may be difficult to find a molecular ion beam that has the same mass-to-charge ratio as the desired H_3^+ beam and a laser-induced-fragmentation rate large enough to perform the beam crossing optimization.[94] Additionally, one needs to make sure that if there is a residual component of the "test" molecular ion in the beam, this molecule does not interfere with the measurement, e.g. if HD^+ is used as the test ion beam and it remains after switching to H_3^+, then the $(H_3^+ \rightarrow H + H_2^+)$ breakup channel is indistinguishable from the $(HD^+ \rightarrow H + D^+)$ breakup channel. (ii) If magnetic selection is used to switch from the test molecular ion to H_3^+, one must have sufficient control of the magnetic field to ensure that the beams cross well. Furthermore, both techniques require that the ion source conditions required to produce the test and H_3^+ molecular ion beams do not differ enough to significantly effect the ion beam trajectory.

Isotopologues of H_3^+ Sixth, the isotopologue of H_3^+ used may have significant effects on the measurement. First, as discussed above, one does not want to use the H_3^+ isotopologue that has some fragmentation channels that overlap with those from secondary beams with the same mass-to-charge ratio. This includes all beams from the ion source, not just the residual "test" molecular ions discussed in the previous section. For example, if one uses a mixture of H_2 and D_2 gas or HD gas to produce the desired H_2D^+ beam then there will be a beam of D_2^+ with a nearly identical mass-to-charge ratio with which to contend. Second, the velocities of the nuclei produced by laser-induced fragmentation of H_3^+ depend upon the isotopologue used. For example, assuming symmetric fragmentation into the $p + p + p$ channel with a kinetic energy release (KER) of 25 eV, H_3^+ will produce protons with velocities of 40 mm/μs while D_3^+ will produce deuterons with velocities of 28 mm/μs and HD_2^+ will produce a proton and two deuterons with velocities of 49

[94] Recalling that this rate is roughly proportional to the ion beam current, one needs to have a molecular ion that is "easily" fragmented and produces a "large" ion current.

and 24 mm/μs, respectively. Consequently, collection of all fragments, i.e. ensuring that none of the fragments impact outside the detector, while maintaining spatial separation of fragments with different velocities, can be difficult. However, isotopologues of H_3^+ may also be beneficial as one can "tag" one of the nuclei, e.g. in the process ($D_2H^+ + n\hbar\omega \rightarrow d + p + D$) all fragments are distinguishable.

Overcoming the difficulties Although we were able to overcome the difficulties associated with measuring laser-induced fragmentation of H_3^+, it took many attempts/failures and corresponding improvements before we were successful. In fact it took us more than three years and seven attempts to accomplish this measurement. On our first attempts with H_3^+ and D_3^+ we were not confident the beams were overlapped and in retrospect the laser intensity was below the fragmentation threshold anyway. To ensure we were crossing the beams, in the next attempt we used a mixed beam of H_2D^+ and D_2^+. This allowed us to verify that the beams crossed by tuning on D_2^+ dissociation. However, as there was still no signature of H_2D^+ fragmentation, e.g. $[p+d+H]$, we concluded that increases in laser beam intensity and ion beam density were necessary to succeed. These suspicions were reinforced by a subsequent study of N_2^+ in which our improvements in laser focusing and ion optics[95] allowed us to measure fragmentation of this strongly bound molecular ion with significantly less effort than in previous attempts. Additionally, we determined that a moderate beam of D_3^+, i.e. ~ 0.5 nA, could be derived from CD_4 in our ion source. We expected that this D_3^+ beam would be vibrationally excited and therefore easier to fragment than D_3^+ from D_2 gas for the reasons discussed above. Using the combination of higher laser intensities ($\sim 10^{16}$ W/cm^2), a vibrationally excited D_3^+ beam, and long collection times, we finally saw undisputable evidence of D_3^+ fragmentation, e.g. both two- and three-body breakup. After performing a series of long runs using this beam, we went back to a D_3^+ beam from D_2 gas to check our suspicion about the importance of an excited vibrational population. Although we are not sure why, this suspicion turned out to be incorrect, or at least insignificant, as the resulting measurement of laser-induced fragmentation of D_3^+ beam

[95]The improvement in ion optics increased our ion current by about a factor of 5 and the laser intensity at the interaction region was increased by reducing the number of mirrors along our transport line and replacing our fused silica lens with a parabolic mirror.

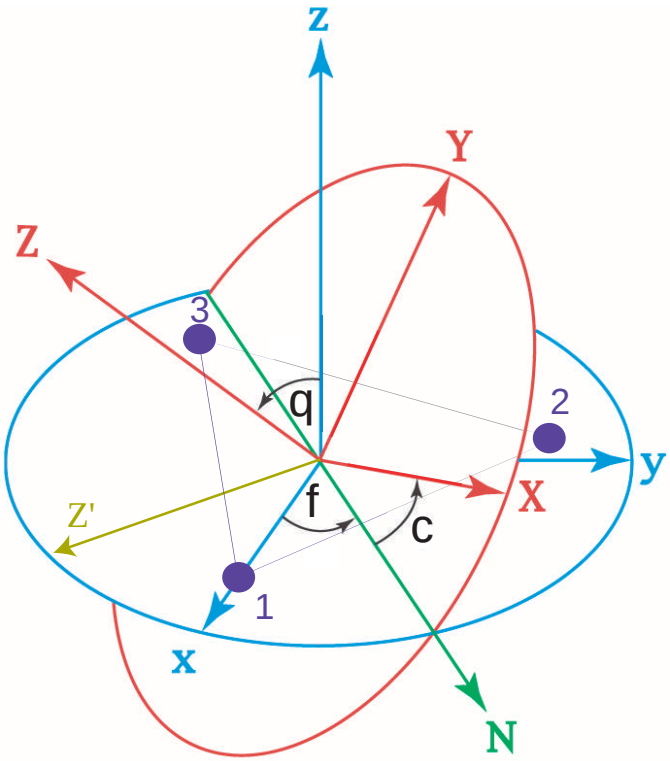

Figure 5.5: Definition of Euler angles. The molecule is in the x-y-plane and the laser polarization is along the Z-axis. Thus the angle between the laser polarization and the normal to the molecular plane is θ and the angle between the projection of the laser polarization and the vector from the molecular center-of-mass to nucleus 1, i.e. the x-axis, is χ. Additionally, N is the intersection of the plane perpendicular to the laser polarization and molecular plane.

from D_2 gas resulted in virtually the same fragmentation rate per nA of current. Thus, as the D_3^+ beam from D_2 is 20 times stronger than that from CD_4, i.e. 10 nA compared to 0.5, we have proceeded to take high statistics measurements of laser-induced fragmentation of D_3^+ in hopes of understanding the intense-field dynamics of this prototypical polyatomic molecule.

5.3 Interesting phenomena in laser-induced fragmentation of H_3^+

Molecular alignment Although specific results will not be discussed in detail here, it is worth noting that the three-center nature of H_3^+ necessitates a more complex analysis of the laser-induced dynamics. For example, we can determine whether the molecule prefers to break in or out of the plane of the laser polarization along with the angular dependence of fragmentation on the relationship between the laser polarization direction and the molecular axes.[96] One expects to see geometric alignment, i.e. preferential breaking for certain molecular orientations with respect to the laser field, in both of theses dimensions analogous to that seen in diatomic molecules, e.g. see

[96]The Euler angles shown in figure 5.5(a) are typically used for this kind of analysis.

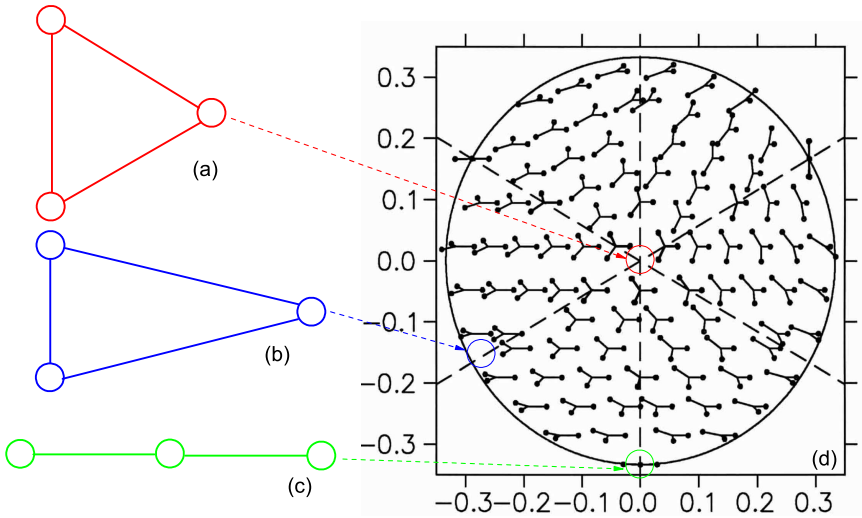

Figure 5.6: Three-body geometry and Dalitz plot. (a) – (c) equilateral, isosceles, and linear geometries, respectively. (d) The legend of a Dalitz plot displaying sample geometries and their position on the plot. Note that positions of (a) – (c) are circled on this plot. Additionally, the Dalitz plot repeats itself every 120° for indistinguishable particles.

[23]. Additionally, it is likely that the laser pulse dynamically aligns the molecule, i.e. rotates the molecular axes, producing effects analogous to those seen for diatomic molecules, e.g. see [18, 22, 58, 156, 233].

Molecular geometry Triatomic molecules also have two more internuclear degrees of freedom than diatomic molecules, as exemplified in figure 5.6. Therefore, one can also study the role the three-dimensional molecular geometry plays in intense-field-molecule interactions.[97] For example, we can determine which symmetries are more difficult to fragment into three bodies, i.e. determine if it is easier to break equilateral, isosceles, or linear geometries.[98] Furthermore, coupling of the molecular geometry and the aforementioned molecular alignment may answer/pose interesting questions, e.g. for equilateral geometries, is it easier to remove electrons when the laser polarization is parallel or perpendicular to the molecular plane and how does this vary with geometry?

Example To exemplify the aforementioned concepts, let us consider laser-induced 3-body fragmentation via single ionization, i.e. $D_3^+ + n\hbar\omega \rightarrow D^+ + D^+ + D$. First of all, a high intensity, i.e. $> 10^{15}$ W/cm^2, is required to measure this process, since the process is sure to require many

[97] Although it is beyond the scope of this dissertation, it is worth noting that the difficulty of the standard techniques of inferring the original molecular structure using Coulomb explosion imaging, e.g. see [39, 202], is significantly increased for polyatomic molecules, specially those made of constituents of similar mass.

[98] To make absolute statements of this nature, one must know the initial distribution of geometries.

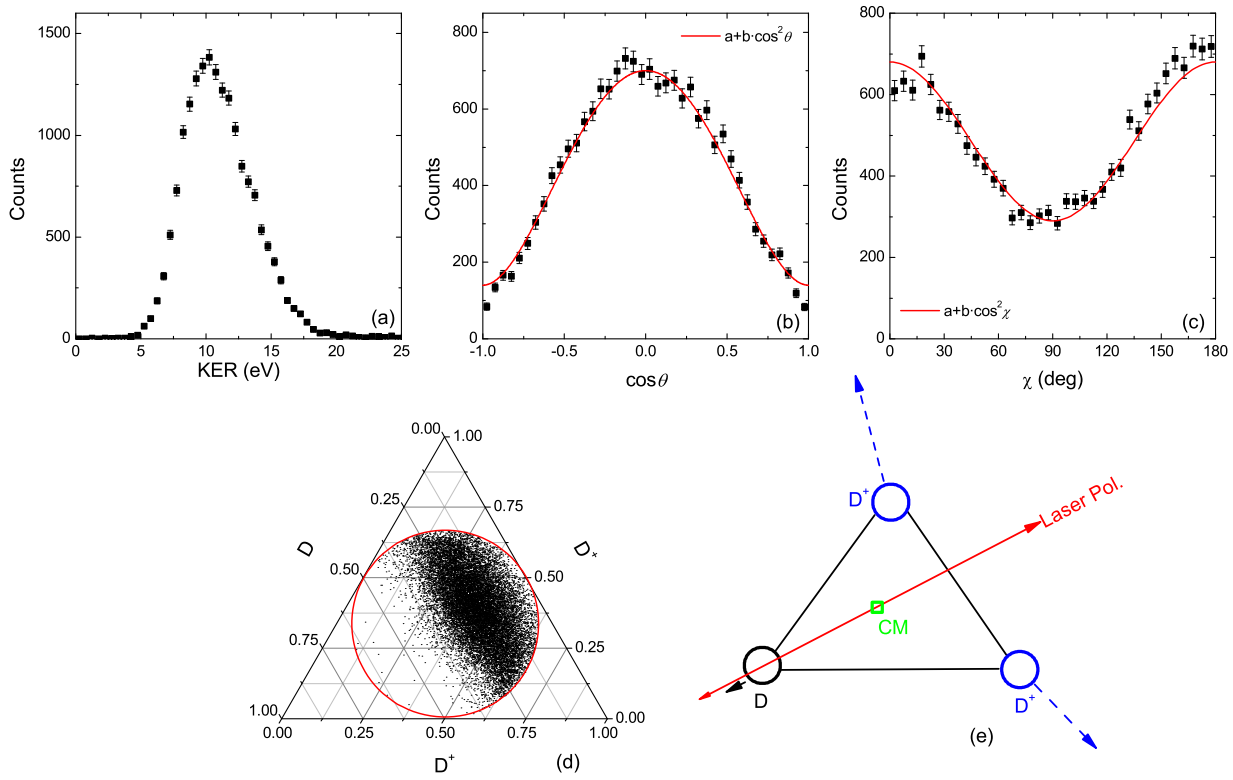

Figure 5.7: Laser induced fragmentation data for $D_3^+ + n\hbar\omega \rightarrow D^+ + D^+ + D$ at $I = 10^{16}$ W/cm^2 and 7 fs. (a) A histogram of events as a function of kinetic energy release (KER). (b) A histogram of events as a function of $\cos\theta$, where θ is the angle between the laser polarization and the normal to molecular plane. (c) A histogram of events as a function of χ, i.e. the angle between the vector from the center-of-mass to the neutral D particle and the projection of the laser polarization. The fit lines in (b) and (c) are only intended to guide the eye. (d) A Dalitz plot of the momentum carried away by each of the fragments. (e) A schematic of the preferred molecule-laser orientation for $D^+ + D^+ + D$ breakup with schematic momentum vectors (dashed lines). (See text for discussion.)

photons as the $[D^+ + D^+ + D]$ dissociation limit lies over 20 eV above the bottom of the ground $X\,^1A'$ state well, see figure 5.4(c). We hope to determine the reaction pathway(s) by examining the D_3^{2+} potential energy surfaces with a $[D^+ + D^+ + D]$ dissociation limit. This pathway must also conform to the observed KER of 5 – 15 eV peaking at 10 eV (see figure 5.7(a)). Additionally, we find that fragmentation events of this type are more likely when the molecule and laser polarization are in the same plane, i.e. $\theta = \pm 90°$ and $\cos\theta = 0$. This distribution of fragmentation events as a function of alignment is shown in figure 5.7(b), which has a $\cos^{2n}\theta$ distribution with $n \simeq 1$. We also see that fragmentation preferentially occurs when the laser-polarization is in the same direction as

the neutral fragment (see figures 5.7(c) and (e)). Finally, the Dalitz plot, i.e. figure 5.7(d), shows that in this reaction the neutral fragment takes away significantly less energy than the charged particles.

5.4 Summary

Although a comprehensive analysis of this H_3^+ laser-induced fragmentation data is yet to be completed, two important issues have been addressed in this chapter. First, we have discussed the numerous obstacles that had to be overcome to facilitate our measurement of the laser-induced fragmentation of H_3^+. Second, we have shown that the addition of a third nucleus significantly enriches/complicates our understanding/interpretation of intense laser-molecule interactions.

Chapter 6

Concluding Remarks and Future Direction

In conclusion, an event mode, coincidence time-of-flight experimental method used to measure laser-induced fragmentation of molecular ion beams has been developed. We have been measuring the laser-induced fragmentation of the prototype diatomic molecule, H_2^+, so as to gain a fundamental understanding of laser-molecule interactions in the intense, ultrashort regime. These studies have yielded an understanding of laser-induced ionization and dissociation in terms of the unified Floquet picture. This picture and experimental technique is then extended to the study of multielectron diatomic molecules yielding a method to determine the probable laser-induced fragmentation pathways of these molecules. Finally, our experimental apparatus and techniques, which are improved continuously, have now evolved to the point at which laser-induced fragmentation of the prototype triatomic molecular ion, H_3^+, has been measured.

At present, we are analyzing measurements of laser-induced fragmentation of several interesting diatomic and polyatomic molecules, e.g. CO^+, CO^{++}, H_3^+, CO_2^+, and CD_4^+, which further extend our understanding of intense laser-molecular ion interactions. In addition to continued studies of molecular ions with interesting/unusual features, the group plans to expand its experimental capabilities in the near future. As a relatively small ion beam current density presently limits the detection rate, the ion source and ion optics will be upgraded. Hopefully, this will facilitate measurements of time-dependent processes using a pump-probe technique. The improvements

needed for electron detection capabilities are also being planned. This capability would allow for the coincidence measurement of the momentum of all constituents of a laser fragmented molecular ion — electrons in addition to charged and neutral nuclei. Finally, the group will continue to utilize the advancements in laser technology achieved by Prof. Z. Chang's group and others to facilitate novel measurements, e.g. carrier-envelope phase dependence along with attosecond and high-order harmonic pulse phenomena.

Bibliography

[1] P. P. Corso, E. Fiordilino, and F. Persico, J. Phys. B: Atomic, Molecular and Optical Physics **40**, 1383 (2007).

[2] E. Gagnon, P. Ranitovic, X.-M. Tong, C. L. Cocke, M. M. Murnane, H. C. Kapteyn, and A. S. Sandhu, Science **317**, 1374 (2007).

[3] M. Nisoli, G. Sansone, S. Stagira, S. De Silvestri, C. Vozzi, M. Pascolini, L. Poletto, P. Villoresi, and G. Tondello, Phys. Rev. Lett. **91**, 213905 (2003).

[4] A. D. Bandrauk, S. Barmaki, and G. L. Kamta, Phys. Rev. Lett. **98**, 013001 (2007).

[5] A. D. Bandrauk and H. Yu, Phys. Rev. A: Atomic, Molecular, and Optical Physics **59**, 539 (1999).

[6] A. Baltuka, T. Udem, M. Uiberacker, M. Hentschel, E. Goulielmakis, C. Gohle, R. Holzwarth, V. S. Yakovlev, A. Scrinzi, T. W. Hnsch, and F. Krausz1, Nature **412**, 611 (2003).

[7] M. Hentschel, R. Kienberger, C. Spielmann, G. A. Reider, N. Milosevic, T. Brabec, P. Corkum, U. Heinzmann, M. Drescher, and F. Krausz1, Nature **414**, 509 (2001).

[8] J. H. Posthumus, Rep. Prog. Phys. **67**, 623 (2004).

[9] V. N. Serov, A. Keller, O. Atabek, and N. Billy, Phys. Rev. A: Atomic, Molecular, and Optical Physics **68**, 053401 (2003).

[10] P. H. Bucksbaum, A. Zavriyev, H. G. Muller, and D. W. Schumacher, Phys. Rev. Lett. **64**, 1883 (1990).

[11] A. Zavriyev, P. H. Bucksbaum, H. G. Muller, and D. W. Schumacher, Phys. Rev. A: Atomic, Molecular, and Optical Physics **42**, 5500 (1990).

[12] A. Zavriyev, P. H. Bucksbaum, J. Squier, and F. Saline, Phys. Rev. Lett. **70**, 1077 (1993).

[13] A. Giusti-Suzor, X. He, O. Atabek, and F. H. Mies, Phys. Rev. Lett. **64**, 515 (1990).

[14] J. H. Posthumus, J. Plumridge, L. J. Frasinski, K. Codling, E. J. Divall, A. J. Langley, and P. F. Taday, J. Phys. B: Atomic, Molecular and Optical Physics **33**, L563 (2000).

[15] A. Giusti-Suzor and F. H. Mies, Phys. Rev. Lett. **68**, 3869 (1992).

[16] T. Zuo and A. D. Bandrauk, Phys. Rev. A: Atomic, Molecular, and Optical Physics **52**, R2511 (1995).

[17] S. Chelkowski, A. Conjusteau, T. Zuo, and A. D. Bandrauk, Phys. Rev. A: Atomic, Molecular, and Optical Physics **54**, 3235 (1996).

[18] M. Uhlmann, T. Kunert, and R. Schmidt, Phys. Rev. A: Atomic, Molecular, and Optical Physics **72**, 045402 (2005).

[19] I. Maruyama, T. Sako, and K. Yamanouchi, J. Phys. B: Atomic, Molecular and Optical Physics **37**, 3919 (2004).

[20] L. J. Frasinski, J. H. Posthumus, J. Plumridge, K. Codling, P. F. Taday, and A. J. Langley, Phys. Rev. Lett. **83**, 3625 (1999).

[21] G. Jolicard and O. Atabek, Phys. Rev. A: Atomic, Molecular, and Optical Physics **46**, 5845 (1992).

[22] J. H. Posthumus, J. Plumridge, L. J. Frasinski, K. Codling, A. J. Langley, and P. F. Taday, J. Phys. B: Atomic, Molecular and Optical Physics **31**, L985 (1998).

[23] L. J. Frasinski, J. Plumridge, J. H. Posthumus, K. Codling, P. F. Taday, E. J. Divall, and A. J. Langley, Phys. Rev. Lett. **86**, 2541 (2001).

[24] L.-Y. Peng, I. D. Williams, and J. F. McCann, J. Phys. B: Atomic, Molecular and Optical Physics **38**, 1727 (2005).

[25] A. Kondorskiy and H. Nakamura, Phys. Rev. A: Atomic, Molecular, and Optical Physics **66**, 053412 (2002).

[26] K. C. Kulander, F. H. Mies, and K. J. Schafer, Phys. Rev. A: Atomic, Molecular, and Optical Physics **53**, 2562 (1996).

[27] S. Chelkowski, P. B. Corkum, and A. D. Bandrauk, Phys. Rev. Lett. **82**, 3416 (1999).

[28] B. Feuerstein and U. Thumm, Phys. Rev. A: Atomic, Molecular, and Optical Physics **67**, 063408 (2003).

[29] G. Yao and S.-I. Chu, Phys. Rev. A: Atomic, Molecular, and Optical Physics **48**, 485 (1993).

[30] A. Giusti-Suzor and F. H. Mies, Phys. Rev. Lett. **68**, 3869 (1992).

[31] T. D. G. Walsh, L. Strach, and S. L. Chin, J. Phys. B: Atomic, Molecular and Optical Physics **31**, 4853 (1998).

[32] T. Zuo, S. Chelkowski, and A. D. Bandrauk, Phys. Rev. A: Atomic, Molecular, and Optical Physics **48**, 3837 (1993).

[33] A. Giusti-Suzor, F. H. Mies, L. F. DiMauro, E. Charron, and B. Yang, J. Phys. B: Atomic, Molecular and Optical Physics **28**, 309 (1995).

[34] A. Rudenko, B. Feuerstein, K. Zrost, V. L. B. de Jesus, T. Ergler, C. Dimopoulou, C. D. Schröter, R. Moshammer, and J. Ullrich, J. Phys. B: Atomic, Molecular and Optical Physics **38**, 487 (2005).

[35] H. Niikura, F. Légaré, R. Hasbani, A. D. Bandrauk, M. Y. Ivanov, D. M. Villeneuve, and P. B. Corkum, Nature **417**, 419 (2002).

[36] I. Ben-Itzhak, P. Q. Wang, J. F. Xia, A. M. Sayler, M. A. Smith, K. D. Carnes, and B. D. Esry, Phys. Rev. Lett. **95**, 073002 (2005).

[37] A. M. Sayler, P. Q. Wang, K. D. Carnes, B. D. Esry, and I. Ben-Itzhak, Phys. Rev. A: Atomic, Molecular, and Optical Physics **75**, 063420 (2007).

[38] B. D. Esry, A. M. Sayler, P. Q. Wang, K. D. Carnes, and I. Ben-Itzhak, Phys. Rev. Lett. **97**, 013003 (2006).

[39] T. Ergler, A. Rudenko, B. Feuerstein, K. Zrost, C. D. Schroter, R. Moshammer, and J. Ullrich, J. Phys. B: Atomic, Molecular and Optical Physics **39**, S493 (2006).

[40] T. Ergler, A. Rudenko, B. Feuerstein, K. Zrost, C. D. Schroter, R. Moshammer, and J. Ullrich, Phys. Rev. Lett. **95**, 093001 (2005).

[41] J. Ludwig, H. Rottke, and W. Sandner, Phys. Rev. A: Atomic, Molecular, and Optical Physics **56**, 2168 (1997).

[42] J. McKenna, A. M. Sayler, F. Anis, B. Gaire, N. G. Johnson, E. Parke, J. J. Hua, H. Mashiko, C. M. Nakamura, E. Moon, Z. Chang, K. D. Carnes, B. D. Esry, and I. Ben-Itzhak, Phys. Rev. Lett. **100**, 133001 (2008).

[43] A. D. Bandrauk and M. L. Sink, J. Chem. Phys. **74**, 1110 (1981).

[44] D. Normand, C. Cornaggia, and J. Morellec, J. Phys. B: Atomic, Molecular and Optical Physics **19**, 2881 (1986).

[45] A. Saenz, Phys. Rev. A: Atomic, Molecular, and Optical Physics **66**, 063408 (2002).

[46] C. Cornaggia, D. Normand, J. Morellec, G. Mainfray, and C. Manus, Phys. Rev. A: Atomic, Molecular, and Optical Physics **34**, 207 (1986).

[47] R. Numico, A. Keller, and O. Atabek, Phys. Rev. A: Atomic, Molecular, and Optical Physics **56**, 772 (1997).

[48] I. Kawata, H. Kono, and Y. Fujimura, J. Chem. Phys. **110**, 11152 (1999).

[49] M. Kling, C. Siedschlag, A. Verhoef, J. Kahn, M. Schultze, Y. Ni, T. Uphues, M. Uiberackerand, M. Drescher, F. Krausz, and M. Vrakking, Science **312**, 246 (2006).

[50] J. McKenna, A. M. S. andB. Gaire, N. G. Johnson, E. Parke, K. D. Carnes, B. D. Esry, and I. Ben-Itzhak, Phys. Rev. A: Atomic, Molecular, and Optical Physics ((submitted) 2008).

[51] B. Gaire, J. McKenna, A. M. Sayler, N. G. Johnson, E. Parke, K. D. Carnes, B. D. Esry, and I. Ben-Itzhak, Phys. Rev. A: Atomic, Molecular, and Optical Physics ((in preperation) 2008).

[52] P. Q. Wang, A. M. Sayler, K. D. Carnes, J. F. Xia, M. A. Smith, B. D. Esry, and I. Ben-Itzhak, Phys. Rev. A: Atomic, Molecular, and Optical Physics **74**, 043411 (2006).

[53] S.-I. Chu and D. A. Telnov, Phys. Rep. **390**, 1 (2004).

[54] V. Roudnev and B. D. Esry, Phys. Rev. Lett. **99**, 220406 (2007).

[55] S. I. Chu, Atomic and molecular multiphoton processes in intense laser fields, in *Review of Fundamental Processes and Applications of Atoms and Ions*, edited by C. D. Lin, World Scientific, 1993.

[56] P. A. Orr, I. D. Williams, J. B. Greenwood, I. C. E. Turcu, W. A. Bryan, J. Pedregosa-Gutierrez, and C. W. Walter, Phys. Rev. Lett. **98**, 163001 (2007).

[57] J. McKenna, M. Suresh, D. S. Murphy, W. A. Bryan, L.-Y. Peng, S. L. Stebbings, E. M. L. English, J. Wood, B. Srigengan, I. C. E. Turcu, J. L. Collier, J. F. McCann, W. R. Newell, and I. D. Williams, J. Phys. B: Atomic, Molecular and Optical Physics **40**, 2607 (2007).

[58] X. M. Tong, Z. X. Zhao, A. S. Alnaser, S. Voss, C. L. Cocke, and C. D. Lin, J. Phys. B: Atomic, Molecular and Optical Physics **38**, 333 (2005).

[59] J. H. Sanderson, A. El-Zein, W. A. Bryan, W. R. Newell, A. J. Langley, and P. F. Taday, Phys. Rev. A: Atomic, Molecular, and Optical Physics **59**, R2567 (1999).

[60] J. Ullrich, R. Moshammer, R. Dörner, O. Jagutzki, V. Mergel, H. Schmidt-Böcking, and L. Spielberger, J. Phys. B: Atomic, Molecular and Optical Physics **30**, 2917 (1997).

[61] R. Dörner, V. Mergel, O. Jagutzki, L. Spielberger, J. Ullrich, R. Moshammer, and H. Schmidt-Böcking, Phys. Rep. **330**, 95 (2000).

[62] H. Schmidt-Böcking and R. Dörner, Atomic physics, http://www. atom. uni-frankfurt. de/ web/ research/ atomic/ COLTRIMS/ index. html, 2007.

[63] X. Urbain, B. Fabre, E. M. Staicu-Casagrande, N. de Ruette, V. M. Andrianarijaona, J. Jureta, J. H. Posthumus, A. Saenz, E. Baldit, and C. Cornaggia, Phys. Rev. Lett. **92**, 163004 (2004).

[64] B. Fabre, J. Posthumus, V. Adrianarijaona, J. Jureta, and X. Urbain, Laser Phys. **13**, 964 (2003).

[65] T. K. Kjeldsen and L. B. Madsen, Phys. Rev. Lett. **95**, 073004 (2005).

[66] Z. Amitay, A. Baer, M. Dahan, J. Levin, Z. Vager, D. Zajfman, L. Knoll, M. Lange, D. Schwalm, R. Wester, A. Wolf, I. F. Schneider, and A. Suzor-Weiner, Phys. Rev. A: Atomic, Molecular, and Optical Physics **60**, 3769 (1999).

[67] A. Tabché-Fouhaillé, J. Durup, J. Moseley, J. Ozenne, C. Pernot, and M. Tadjeddine, Chem. Phys. **17**, 81 (1976).

[68] N. Abramzon, R. B. Siegel, and K. Becker, J. Phys. B: Atomic, Molecular and Optical Physics **32**, L247 (1999).

[69] D. H. Crandall, W. E. Kauppila, R. A. Phaneuf, P. O. Taylor, and G. H. Dunn, Phys. Rev. A: Atomic, Molecular, and Optical Physics **9**, 2545 (1974).

[70] P. C. Cosby, J. Chem. Phys. Rev. A **98**, 9544 (1974).

[71] M. M. Shakya, *Generation of intense high harmonics: i) to test and improve resolution of accumulative x-ray streak camera ii) to study the effects of carrier envelope phase on xuv super continuum generation by polarization gating*, PhD thesis, Kansas State University, Manhattan, Kansas, U.S.A., 2007.

[72] A. Al-Khalili et al., Phys. Rev. A: Atomic, Molecular, and Optical Physics **68**, 042702 (2003).

[73] D. Zajfman, Z. Amitay, C. Broude, P. Forck, B. Seidel, M. Grieser, D. Habs, D. Schwalm, and A. Wolf, Phys. Rev. Lett. **75**, 814 (1995).

[74] D. Zajfman and Z. Amitay, Phys. Rev. A: Atomic, Molecular, and Optical Physics **52**, 839 (1995).

[75] S. Datz, R. Thomas, S. Rosén, M. Larsson, A. M. Derkatch, F. Hellberg, and W. van der Zande, Phys. Rev. Lett. **85**, 5555 (2000).

[76] R. D. Thomas, F. Hellberg, A. Neau, S. Rosen, M. Larsson, C. R. Vane, M. E. Bannister, S. Datz, A. Petrignani, and W. J. van der Zande, Phys. Rev. A: Atomic, Molecular, and Optical Physics **71**, 032711 (2005).

[77] D. Kella, P. J. Johnson, H. B. Pedersen, L. Vejby-Christensen, and L. H. Andersen, Phys. Rev. Lett. **77**, 2432 (1996).

[78] L. H. Andersen, P. J. Johnson, D. Kella, H. B. P. L., and Vejby-Christensen, Phys. Rev. A: Atomic, Molecular, and Optical Physics **55**, 2799 (1997).

[79] L. Vejby-Christensen, D. Kella, H. B. Pedersen, and L. H. Andersen, Phys. Rev. A: Atomic, Molecular, and Optical Physics **57**, 3627 (1998).

[80] H. Niikura, D. M. Villeneuve, and P. B. Corkum, Phys. Rev. Lett. **94**, 083003 (2005).

[81] D. Pavičić, *Coloumb Explosion and Intense-Field Photodissociation of Ion-Beam H_2^+ and D_2^+*, PhD thesis, Max-Planck-Institut für Quantenoptik, Garching, Germany, 2004.

[82] I. D. Williams, P. McKenna, B. Srigengan, I. M. G. Johnston, W. A. Bryan, J. H. Sanderson, A. El-Zein, T. R. J. Goodworth, W. R. Newell, P. F. Taday, and A. J. Langley, J. Phys. B: Atomic, Molecular and Optical Physics **33**, 2743 (2000).

[83] C. Wunderlich, E. Kobler, H. Figger, and T. W. Hänsch, Phys. Rev. Lett. **78**, 2333 (1997).

[84] K. Sändig, H. Figger, and T. W. Hänsch, Phys. Rev. Lett. **85**, 4876 (2000).

[85] D. Pavičić, A. Kiess, T. W. Hänsch, and H. Figger, Phys. Rev. Lett. **94**, 163002 (2005).

[86] D. Pavičić, A. Kiess, T. W. Hänsch, and H. Figger, Euro. Phys. J. D: Atomic, Molecular, Optical and Plasma Physics **26**, 39 (2003).

[87] D. Pavičić, T. W. Hänsch, and H. Figger, Phys. Rev. A: Atomic, Molecular, and Optical Physics **72**, 053413 (2005).

[88] A. Staudte, D. Pavičić, S. Chelkowski, D. Zeidler, M. Meckel, H. Niikura, M. Schöffler, S. Schössler, B. Ulrich, P. P. Rajeev, T. Weber, T. Jahnke, D. M. Villeneuve, A. D. Bandrauk, C. L. Cocke, P. B. Corkum, and R. Dörner, Phys. Rev. Lett. **98**, 073003 (2007).

[89] L.-Y. Peng, D. Dundas, J. F. McCann, K. T. Taylor, and I. D. Williams, J. Phys. B: Atomic, Molecular and Optical Physics **36**, L295 (2003).

[90] J. B. Greenwood, I. M. G. Johnston, P. McKenna, I. D. Williams, T. R. J. Goodworth, J. H. Sanderson, W. A. Bryan, A. A. A. El-Zein, W. R. Newell, A. J. Langley, and E. J. Divall, Phys. Rev. Lett. **88**, 233001 (2002).

[91] W. Newell, I. Williams, and W. Bryan, Euro. Phys. J. D: Atomic, Molecular, Optical and Plasma Physics **26**, 99 (2003).

[92] I. Ben-Itzhak, P. Q. Wang, J. F. Xia, A. M. Sayler, M. A. Smith, J. W. Maseberg, K. D. Carnes, and B. D. Esry, Nucl. Instrum. Methods Phys. Res. B **233**, 56 (2005).

[93] B. Gaire, A. M. Sayler, P. Q. Wang, N. G. Johnson, M. Leonard, E. Parke, K. D. Carnes, and I. Ben-Itzhak, Rev. Sci. Instrum. **78**, 024503 (2007).

[94] A. M. Sayler, P. Q. Wang, K. D. Carnes, B. D. Esry, and I. Ben-Itzhak, J. Phys. B: Atomic, Molecular and Optical Physics **40**, 4367 (2007).

[95] P. Q. Wang, A. M. Sayler, K. D. Carnes, J. F. Xia, M. A. Smith, B. D. Esry, and I. Ben-Itzhak, J. Phys. B: Atomic, Molecular and Optical Physics Lett. **38**, L251 (2005).

[96] P. Q. Wang, A. M. Sayler, K. D. Carnes, B. D. Esry, and I. Ben-Itzhak, Opt. Lett. **30**, 664 (2005).

[97] A. S. Alnaser, B. Ulrich, X. M. Tong, I. V. Litvinyuk, C. M. Maharjan, P. Ranitovic, T. Osipov, R. Ali, S. Ghimire, Z. Chang, C. D. Lin, and C. L. Cocke, Phys. Rev. A: Atomic, Molecular, and Optical Physics **72**, 030702 (2005).

[98] T. Niederhausen and U. Thumm, Phys. Rev. A: Atomic, Molecular, and Optical Physics **77**, 013407 (2008).

[99] R. Geller, *Electron cyclotron resonance ion sources and ECR plasmas*, Bristol, Philadelphia, 1996.

[100] M. O. Abdellahi El Ghazaly, J. Jureta, X. Urbain, and P. Defrance, J. Phys. B: Atomic, Molecular and Optical Physics **37**, 2467 (2004).

[101] F. von Busch and G. H. Dunn, Phys. Rev. A: Atomic, Molecular, and Optical Physics **5**, 1726 (1972).

[102] B. Shan, C. Wang, and Z. Chang, High peak-power kilohertz laser systems employing singe-stage multi-pass amplification, U. S. Patent No. 7,050,474, 23 May 2006.

[103] C. Li, E. Moon, H. Mashiko, C. Nakamura, P. Ranitovic, C. L. Cocke, Z. Chang, and G. G. Paulus, Opt. Express **14**, 11468 (2006).

[104] E. Moon, C. Li, Z. Duan, J. Tackett, K. L. Corwin, B. R. Washburn, and Z. Chang, Opt. Express **14**, 9758 (2006).

[105] Z. Chang, Appl. Opt. **45**, 8350 (2006).

[106] S. Ghimire, B. Shan, C. Wang, and Z. Chang, Laser Phys. **15**, 838 (2005).

[107] C. Li, E. Moon, H. Wang, H. Mashiko, C. Nakamura, J. Tackett, and Z. Chang, Opt. Lett. **32**, 796 (2007).

[108] H. Wang, C. Li, J. Tackett, H. Mashiko, C. Nakamura, E. Moon, and Z. Chang, Appl. Phys. B: Lasers Opt. (submitted 2007).

[109] H. Mashiko, C. M. Nakamura, C. Li, E. Moon, H. Wang, J. Tackett, and Z. Chang, Appl. Phys. Lett. **90**, 161114 (2007).

[110] A. E. Siegman, *Lasers*, University Science Books, Sausalito, 1986.

[111] R. W. Boyd, *Nonlinear Optics*, Achedemic Press, Amsterdam, 2003.

[112] S. Voss, A. S. Alnaser, X.-M. Tong, C. Maharjan, P. Ranitovic, B. Ulrich, B. Shan, Z. Chang, C. D. Lin, and C. L. Cocke, J. Phys. B: Atomic, Molecular and Optical Physics **37**, 4239 (2004).

[113] R. Trebino, Frequency resolved optical gating, http://www. physics. gatech. edu/ gcuo/ subIndex. html.

[114] M. J. Nandor, M. A. Walker, and L. D. V. Woerkom, J. Phys. B: Atomic, Molecular and Optical Physics **31**, 4617 (1998).

[115] V. N. Serov, A. Keller, O. Atabek, and N. Billy, Phys. Rev. A: Atomic, Molecular, and Optical Physics **68**, 053401 (2003).

[116] V. Serov, A. Keller, O. Atabek, H. Figger, and D. Pavicic, Phys. Rev. A: Atomic, Molecular, and Optical Physics **72**, 033413 (2005).

[117] S. Augst, D. D. Meyerhofer, D. Strickland, and S. L. Chin, J. Opt. Soc. Am. B **8**, 858 (1991).

[118] R. Moshammer, B. Feuerstein, D. Fischer, A. Dorn, C. Schroter, J. Deipenwisch, J. R. Lopez-Urrutia, C. Hohr, P. Neumayer, J. Ullrich, H. Rottke, C. Trump, M. Wittmann, G. Korn, and W. Sandner, Opt. Express **8**, 358 (2001).

[119] J. Ullrich, R. Moshammer, A. Dorn, R. Dorner, L. P. H. Schmidt, and H. Schmidt-Bocking, Rep. Prog. Phys. **66**, 1463 (2003).

[120] W. A. Bryan, S. L. Stebbings, J. McKenna, E. M. L. English, M. Suresh, J. Wood, B. Srigengan, I. C. E. Turcu, J. M. Smith, E. J. Divall, C. J. Hooker, A. J. Langley, J. L. Collier, I. D. Williams, and W. R. Newell, Nature Phys. **2**, 379 (2006).

[121] P. Hansch and L. D. V. Woerkom, Opt. Lett. **21**, 1286 (1996).

[122] W. A. Bryan, S. L. Stebbings, E. M. L. English, T. R. J. Goodworth, W. R. Newell, J. McKenna, M. Suresh, B. Srigengan, I. D. Williams, I. C. E. Turcu, J. M. Smith, E. J. Divall, C. J. Hooker, and A. J. Langley, Phys. Rev. A: Atomic, Molecular, and Optical Physics **73**, 013407 (2006).

[123] T. R. J. Goodworth, W. A. Bryan, I. D. Williams, and W. R. Newell, J. Phys. B: Atomic, Molecular and Optical Physics **38**, 3083 (2005).

[124] C. Li, E. Moon, and Z. Chang, Opt. Lett. **31**, 3113 (2006).

[125] C. Marian, R. Marian, and S. Peyerimhoff, Mol. Phys. **46**, 779 (1982).

[126] V. Roudnev and B. D. Esry, Phys. Rev. A: Atomic, Molecular, and Optical Physics **76**, 023403 (2007).

[127] A. Datta, S. S. Bhattacharyya, and B. Kim, Phys. Rev. A: Atomic, Molecular, and Optical Physics **65**, 043404 (2002).

[128] A. M. Weiner, Rev. Sci. Instrum. **71**, 1929 (2000).

[129] G. Steinmeyer, Appl. Opt. **45**, 1484 (2006).

[130] E. Goulielmakis, V. S. Yakovlev, A. L. Cavalieri, M. Uiberacker, V. Pervak, A. Apolonski, R. Kienberger, U. Kleineberg, and F. Krausz, Science **317**, 769 (2007).

[131] T. Brixner, N. H. Damrauer, G. Krampert, P. Niklaus, G. B. Gerber, and C. Cornaggia, J. Mod. Opt. **50**, 539 (2003).

[132] R. S. Judson and H. Rabitz, Phys. Rev. Lett. **68**, 1500 (1992).

[133] R. J. Levis, G. M. Menkir, and H. Rabitz, Science **292**, 709 (2001).

[134] E. E. Aubanel, A. D. Bandrauk, and P. Rancourt, Chem. Phys. Lett. **197**, 419 (1992).

[135] G. N. Gibson, M. Li, C. Guo, and J. Neira, Phys. Rev. Lett. **79**, 2022 (1997).

[136] A. S. Alnaser, X. M. Tong, T. Osipov, S. Voss, C. M. Maharjan, P. Ranitovic, B. Ulrich, B. Shan, Z. Chang, C. D. Lin, and C. L. Cocke, Phys. Rev. Lett. **93**, 183202 (2004).

[137] F. Anis and B. D. Esry, Phys. Rev. A: Atomic, Molecular, and Optical Physics **77**, 033416 (2008).

[138] I. Ben-Itzhak, P. Wang, A. Sayler, K. Carnes, M. Leonard, B. Esry, A. Alnaser, B. Ulrich, X. Tong, I. Litvinyuk, C. Maharjan, P. Ranitovic, T. Osipov, S. Ghimire, Z. Chang, and C. Cocke, ((in preperation) 2008).

[139] B. D. Esry and I. Ben-Itzhak, Phys. Rev. Lett. ((in preperation) 2008).

[140] A. Talebpour, K. Vijayalakshmi, A. Bandrauk, T. T. Nguyen-Dang, and S. L. Chin, Phys. Rev. A: Atomic, Molecular, and Optical Physics **62**, 042708 (2000).

[141] P. Agostini, F. Fabre, G. Mainfray, G. Petite, and N. K. Rahman, Phys. Rev. Lett. **42**, 1127 (1979).

[142] B. Yang, M. Saeed, L. F. DiMauro, A. Zavriyev, and P. H. Bucksbaum, Phys. Rev. A: Atomic, Molecular, and Optical Physics **44**, R1458 (1991).

[143] E. Charron, A. Giusti-Suzor, and F. H. Mies, Phys. Rev. A: Atomic, Molecular, and Optical Physics **49**, R641 (1994).

[144] T. T. Nguyen-Dang, H. Abou-Rachid, N. A. Nguyen, N. Mireault, J. Lévesque, K. Vijayalakshmi, and S. L. Chin, Phys. Rev. A: Atomic, Molecular, and Optical Physics **67**, 013405 (2003).

[145] K. Vijayalakshmi, A. Talebpour, T. T. Nguyen-Dang, J. Yang, A. D. Bandrauk, and S. L. Chin, Phys. Rev. A: Atomic, Molecular, and Optical Physics **62**, 053408 (2000).

[146] G. N. Gibson, L. Fang, and B. Moser, Phys. Rev. A: Atomic, Molecular, and Optical Physics **74**, 041401 (2006).

[147] X. Urbain, B. Fabre, E. M. Staicu-Casagrande, N. de Ruette, V. M. Andrianarijaona, J. Jureta, J. H. Posthumus, A. Saenz, E. Baldit, and C. Cornaggia, Phys. Rev. Lett. **92**, 163004 (2004).

[148] L.-Y. Peng, D. Dundas, J. F. McCann, K. T. Taylor, and I. D. Williams, J. Phys. B: Atomic, Molecular and Optical Physics **36**, L295 (2003).

[149] M. Plummer and J. F. McCann, J. Phys. B: Atomic, Molecular and Optical Physics **29**, 4625 (1996).

[150] M. Vafaee and H. Sabzyan, J. Phys. B: Atomic, Molecular and Optical Physics **37**, 4143 (2004).

[151] T. Ergler, A. Rudenko, B. Feuerstein, K. Zrost, C. D. Schröter, R. Moshammer, and J. Ullrich, Phys. Rev. Lett. **95**, 093001 (2005).

[152] A. S. Alnaser, M. Zamkov, X. M. Tong, C. M. Maharjan, P. Ranitovic, C. L. Cocke, and I. V. Litvinyuk, Phys. Rev. A: Atomic, Molecular, and Optical Physics **72**, 041402 (2005).

[153] A. S. Alnaser, I. Litvinyuk, T. Osipov, B. Ulrich, A. Landers, E. Wells, C. M. Maharjan, P. Ranitovic, I. Bocharova, D. Ray, and C. L. Cocke, J. Phys. B: Atomic, Molecular and Optical Physics **39**, S485 (2006).

[154] S. Chelkowski, C. Foisy, and A. D. Bandrauk, Phys. Rev. A: Atomic, Molecular, and Optical Physics **57**, 1176 (1998).

[155] L. B. Madsen and M. Plummer, J. Phys. B: Atomic, Molecular and Optical Physics **31**, 87 (1998).

[156] T. Ergler, A. Rudenko, B. Feuerstein, K. Zrost, C. D. Schroter, R. Moshammer, and J. Ullrich, Phys. Rev. Lett. **97**, 193001 (2006).

[157] T. Ergler, A. Rudenko, B. Feuerstein, K. Zrost, C. D. Schröter, R. Moshammer, and J. Ullrich, J. Phys. B: Atomic, Molecular and Optical Physics **39**, S493 (2006).

[158] T. D. G. Walsh, F. A. Ilkov, S. L. Chin, F. Châteauneuf, T. T. Nguyen-Dang, S. Chelkowski, A. D. Bandrauk, and O. Atabek, Phys. Rev. A: Atomic, Molecular, and Optical Physics **58**, 3922 (1998).

[159] A. Hishikawa, S. Liu, A. Iwasaki, and K. Yamanouchi, J. Chem. Phys. **114**, 9856 (2001).

[160] A. Assion, T. Baumert, U. Weichmann, and G. Gerber, Phys. Rev. Lett. **86**, 5695 (2001).

[161] M. Machholm and A. Suzor-Weiner, J. Chem. Phys. **105**, 971 (1996).

[162] K. Codling and L. J. Frasinski, J. Phys. B: Atomic, Molecular and Optical Physics **26**, 783 (1993).

[163] C. Cornaggia and L. Quaglia, Phys. Rev. A: Atomic, Molecular, and Optical Physics **63**, 030702 (2001).

[164] B. L. G. Bakker and D. H. Parker, J. Chem. Phys. **112**, 4037 (2000).

[165] B. L. G. Bakker, D. H. Parker, P. C. Samartzis, and T. N. Kitsopoulos, J. Chem. Phys. **112**, 5654 (2000).

[166] C. Cornaggia, J. Lavancier, D. Normand, J. Morellec, P. Agostini, J. P. Chambaret, and A. Antonetti, Phys. Rev. A: Atomic, Molecular, and Optical Physics **44**, 4499 (1991).

[167] D. Normand, C. Cornaggia, J. Lavancier, J. Morellec, and H. X. Liu, Phys. Rev. A: Atomic, Molecular, and Optical Physics **44**, 475 (1991).

[168] L. Quaglia, O. Chiappa, G. Granucci, V. Brenner, P. Millié, and C. Cornaggia, J. Phys. B: Atomic, Molecular and Optical Physics **35**, L145 (2002).

[169] C. Guo, M. Li, and G. N. Gibson, Phys. Rev. Lett. **82**, 2492 (1999).

[170] C. Guo, M. Li, J. P. Nibarger, and G. N. Gibson, Phys. Rev. A: Atomic, Molecular, and Optical Physics **61**, 033413 (2000).

[171] X. M. Tong, Z. X. Zhao, and C. D. Lin, Phys. Rev. A: Atomic, Molecular, and Optical Physics **66**, 033402 (2002).

[172] B. Walker, M. Saeed, T. Breeden, B. Yang, and L. F. DiMauro, Phys. Rev. A: Atomic, Molecular, and Optical Physics **44**, 4493 (1991).

[173] W. van Der Zande, W. Koot, J. Peterson, and J. Los, Chem. Phys. **126**, 169 (1988).

[174] E. Y. Sidky and I. Ben-Itzhak, Phys. Rev. A: Atomic, Molecular, and Optical Physics **60**, 3586 (1999).

[175] E. T. Galloway and E. Herbst, Astron. Astrophys. **211**, 413 (1989).

[176] M. Shimizu, Astrophys. Space Sci. **36**, 353 (1975).

[177] J. M. Amero and G. J. Vázquez, Int. J. Quant. Chem. **99**, 353 (2004).

[178] K. Kawaguchi and T. Amano, J. Chem. Phys. **88**, 4584 (1988).

[179] R. Colin, J. Mol. Spectrosc. **136**, 387 (1989).

[180] U. Müller and G. Schulz, Chem. Phys. Lett. **170**, 401 (1990).

[181] A. Ehbrecht, A. Kowalski, and Ch. Ottinger, Int. J. Mass Spectrosc. Ion Phys. **173**, 127 (1998).

[182] J. M. Amero and G. J. Vázquez, Int. J. Quant. Chem. **101**, 396 (2005).

[183] I. Kusunoki, K. Yamashita, and K. Morokuma, Chem. Phys. Lett. **123**, 533 (1986).

[184] J. K. Park and H. Sun, Bull. Korean Chem. Soc. **11**, 34 (1990).

[185] J. K. Park and H. Sun, Chem. Phys. Lett. **211**, 618 (1993).

[186] J. Seong, J. K. Park, and H. Sung, Chem. Phys. Lett. **57**, 79 (1996).

[187] R. Tarroni, P. Palmieri, A. Mitrushenkov, P. Tosi, and D. Bassi, J. Chem. Phys. **106**, 10265 (1997).

[188] R. Marquardt, K. Sagui, W. Klopper, and M. Quack, J. Phys. Chem. B **109**, 8439 (2005).

[189] M. V. Korolkov, H. G. Breunig, and K. M. Weitzel, Optics. Spect. **103**, 325 (2007).

[190] M. Hochlaf, G. Chambaud, and P. Rosmus, J. Phys. B: Atomic, Molecular and Optical Physics **30**, 4509 (1997).

[191] R. J. Gdanitz, Chem. Phys. Lett. **2283**, 253 (1998).

[192] F. R. Gilmore, R. R. Laher, and P. J. Espy, J. Phys. Chem. Ref. Data **21**, 1005 (1992).

[193] T. Aoto, K. Ito, Y. Hikosaka, A. Shibasaki, R. Hirayama, N. Yamamono, and E. Miyoshi, J. Chem. Phys. **124**, 234306 (2006).

[194] M. Lundqvist, D. Edvardsson, P. Baltzer, and B. Wannberg, J. Phys. B: Atomic, Molecular and Optical Physics **29**, 1489 (1996).

[195] J. P. Nibarger, S. V. Menon, and G. N. Gibson, Phys. Rev. A: Atomic, Molecular, and Optical Physics **63**, 053406 (2001).

[196] J. McKenna, M. Suresh, B. Srigengan, I. D. Williams, W. A. Bryan, E. M. L. English, S. L. Stebbings, W. R. Newell, I. C. E. Turcu, J. M. Smith, E. J. Divall, C. J. Hooker, A. J. Langley, and J. L. Collier, Phys. Rev. A: Atomic, Molecular, and Optical Physics **73**, 043401 (2006).

[197] R. N. Coffee, L. Fang, and G. N. Gibson, Phys. Rev. A: Atomic, Molecular, and Optical Physics **73**, 043417 (2006).

[198] R. E. Startmann, G. Bandarage, and R. Lucchese, Phys. Rev. A: Atomic, Molecular, and Optical Physics **51**, 1756 (1995).

[199] J. A. Nichols, D. Yeager, and P. Jorgemsen, J. Chem. Phys. **80**, 239 (1984).

[200] J. H. Posthumus, A. J. Giles, M. R. Thompson, and K. Codling, J. Phys. B: Atomic, Molecular and Optical Physics **29**, 5811 (1996).

[201] E. Baldit, S. Saugout, and C. Cornaggia, Phys. Rev. A: Atomic, Molecular, and Optical Physics **71**, 021403 (2005).

[202] C. Beylerian and C. Cornaggia, J. Phys. B: Atomic, Molecular and Optical Physics **37**, L259 (2004).

[203] S. Banerjee, G. Ravindra Kumar, and D. Mathur, Phys. Rev. A: Atomic, Molecular, and Optical Physics **60**, R25 (1999).

[204] G. Lagmago Kamta and A. F. Starace, Phys. Rev. A: Atomic, Molecular, and Optical Physics **65**, 053418 (2002).

[205] J. Parker, K. T. Taylor, C. W. Clark, and S. Blodgett-Ford, J. Phys. B: Atomic, Molecular and Optical Physics **29**, L33 (1996).

[206] A. Scrinzi and B. Piraux, Phys. Rev. A: Atomic, Molecular, and Optical Physics **58**, 1310 (1998).

[207] M. S. Pindzola and F. Robicheaux, Phys. Rev. A: Atomic, Molecular, and Optical Physics **57**, 318 (1998).

[208] L. A. A. Nikolopoulos and P. Lambropoulos, Phys. Rev. Lett. **82**, 3771 (1999).

[209] G. L. Kamta, T. Grosges, B. Piraux, R. Hasbani, E. Cormier, and H. Bachau, J. Phys. B: Atomic, Molecular and Optical Physics **34**, 857 (2001).

[210] R. Hasbani, E. Cormier, and H. Bachau, J. Phys. B: Atomic, Molecular and Optical Physics **33**, 2101 (2000).

[211] A. Dalgarno and J. H. Black, Rep. Prog. Phys. **39**, 573 (1976).

[212] W. D. Watson, Rev. Mod. Phys. **48**, 513 (1976).

[213] T. Stallard, Icarus **156**, 489 (2002).

[214] A. Aguado, O. Roncero, C. Tablero, C. Sanz, and M. Paniagua, J. Chem. Phys. **112**, 1240 (2000).

[215] U. Galster, P. Kaminski, M. Beckert, H. Helm, and U. Müller, Euro. Phys. J. D: Atomic, Molecular, Optical and Plasma Physics **17**, 307 (2001).

[216] I. Kawata, H. Kono, and A. D. Bandrauk, Phys. Rev. A: Atomic, Molecular, and Optical Physics **64**, 043411 (2001).

[217] H. Kreckel et al., Phys. Rev. Lett. **95**, 263201 (2005).

[218] A. Hishikawa, A. Iwamae, and K. Yamanouchi, Phys. Rev. Lett. **83**, 1127 (1999).

[219] A. Hishikawa, A. Iwamae, and K. Yamanouchi, J. Chem. Phys. **111**, 8871 (1999).

[220] C. Cornaggia, F. Salin, and C. L. Blanc, J. Phys. B: Atomic, Molecular and Optical Physics **29**, L749 (1996).

[221] W. A. Bryan, W. R. Newell, J. H. Sanderson, and A. J. Langley, Phys. Rev. A: Atomic, Molecular, and Optical Physics **74**, 053409 (2006).

[222] K. Ledingham, R. Singhal, D. Smith, T. McCanny, P. Graham, H. Kilic, W. Peng, S. Wang, A. Langley, P. Taday, and C. Kosmidis, J. Phys. Chem. A **102**, 3002 (1998).

[223] S. Baker, J. S. Robinson, C. A. Haworth, H. Teng, R. A. Smith, C. C. Chirila, M. Lein, J. W. G. Tisch, and J. P. Marangos, Science **312**, 424 (2006).

[224] J. Posthumus, editor, *Molecules and clusters in intense laser fields*, Cambridge University Press, Cambridge, 2001.

[225] D. Talbi and R. P. Saxon, J. Chem. Phys. **89**, 2235 (1988).

[226] J. McKenna, H_3^+ ion beam current, private communication, 2008.

[227] G. G. Paulus, Molecular ion coincidence momentum imaging, private communication, 2008.

[228] A. Diner, *Effects of pulse shape on the photodissociation of hydrogen molecular ions*, PhD thesis, Weizmann Institute of Science, Rehovot, Israel, 2008.

[229] A. Sen and J. B. A. Mitchell, J. Phys. B: Atomic, Molecular and Optical Physics **19**, L545 (1986).

[230] V. G. Anicich and J. H. Futrell, Int. J. Mass Spectrosc. Ion Phys. **55**, 189 (1984).

[231] C. Bordas, P. C. Cosby, and H. Helm, J. Chem. Phys. **93**, 6303 (1990).

[232] R. C. Weast, M. J. Astle, and W. H. Beyer, editors, *CRC Handbook of Chemistry and Physics*, CRC Press, Boca Raton, 65 edition, 1985.

[233] F. Rosca-Pruna and M. J. J. Vrakking, Phys. Rev. Lett. **87**, 153902 (2001).

[234] S. Cheng, *Ionization and capture by O^{8+} from aligned deuterium*, PhD thesis, Kansas State University, Manhattan, Kansas, U.S.A., 1991.

[235] W. Kołos, K. Szalewicz, and H. J. J. Monkhorst, Chem. Phys. **84**, 3278 (1986).

[236] B. H. Bransden and C. J. Joachain, *Physics of Atoms and Molecules*, Pearson Education Limited, Harlow, England, 2003.

[237] G. Woan, *The Cambridge Handbook of Physics Formulas*, Cambridge University Press, Cambridge, 2003.

[238] J. S. Coursey, D. J. Schwab, and R. A. Dragoset, Atomic weights and isotopic composition, http://physics. nist. gov/ PhysRefData/ Compositions/ index. html, 2001.

[239] RoentDek, Charts for roendek delay-line detectors, http://www. roentdek. com/ mitte/ doppel/ links/ fuer_charts/ charts_3. htm.

[240] J. Shepherd, S. Sobottka, and M. Williams, IEEE Trans. Nucl. Sci. **38**, 154 (1991).

[241] M. Williams, S. Sobottka, and J. Shepherd, IEEE Trans. Nucl. Sci. **38**, 148 (1991).

[242] M. Lampton and G. Penegor, Rev. Sci. Instrum. **71**, 294 (2000).

[243] O. Jagutzki, A. Cerezo, A. Czasch, R. Dorner, M. Hattas, M. Huang, V. Mergel, U. Spillmann, K. Ullmann-Pfleger, T. Weber, H. Schmidt-Bocking, and G. Smith, IEEE Trans. Nucl. Sci. **49**, 2477 (2002).

Appendix A

Experimental Procedures

A.1 Introduction

One of the most, if not the most, difficult experimental aspects of the measurements presented in this dissertation is crossing an ultra-short pulsed laser beam and molecular ion-beam under controlled conditions. This technique has been briefly outlined in several of our existing publications [36, 37, 52, 92–94, 96] and is the subject of this appendix. The procedure is split into three sections — (i) preparing a molecular-ion beam with the desired properties (e.g. non-diverging, uniform density, and high current density), (ii) preparing an ultra-short high-intensity pulsed laser beam, and (iii) crossing the two beams under known and controlled conditions.

A.2 Molecular-ion beam

A.2.1 Electron cyclotron resonance (ECR) ion source

A.2.1.1 Vibrational population

All the measurements discussed within this dissertation were performed using an electron cyclotron resonance (ECR) source[99], which produces ions (both molecular and atomic) by electron impact ionization. This process is often described as a vertical transition and the probability to be in any final vibrational state is referred to as the Franck-Condon factor (A_{if}). The probability, A_{if}, for being in a particular final state, f, given the initial state, i, is $A_{if} = |\langle\Psi_f|\Psi_i\rangle|^2$ [236, 237]. For

[99]The detailed functionality of an ECR is beyond the scope of this dissertation and is described in multiple publications (see, for example, [99]), and thus will not be discussed here.

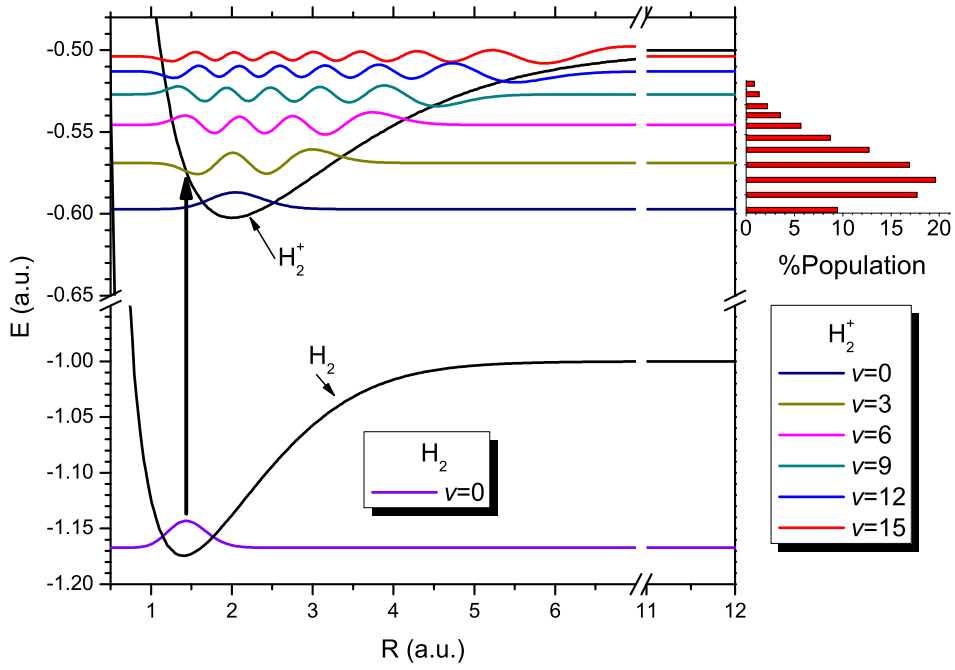

Figure A.1: Vibrational population of H_2^+ formed from H_2 electron impact ionization in an ECR. The Born-Oppenheimer nuclear potential energy curves [234, 235] for H_2 and H_2^+ are colored black and labeled. The initial vibrational wavefunction of H_2 along with several of the lower vibrational wavefunctions for H_2^+ are displayed. The bar graph displays the populations of the H_2^+ vibrational states resulting from a vertical transition from the H_2 ground state as described in the text.

example, when H_2, which is in the ground vibrational state, is fed to the ECR, the resulting H_2^+ molecular ions will be in a spread of vibrational states determined by the overlap of the initial $H_2(v = 0)$ vibrational wavefunction with the vibrational eigenstates of the H_2^+ molecular ion. This is illustrated in figure A.1 together with the vibrational population of a H_2^+ beam produced using H_2 in the source. This has also been measured by Z. Amitay et al. [66], who find that the vibrational population of H_2^+ is well approximated by the Franck-Condon factors.

A.2.1.2 Electronic and vibrational decay during flight

One must also take into account the vibrational and electronic decay of the molecular-ion beam during its flight to the interaction region, which is typically on the order of 10 μs in our measurements. This is important in cases such as N_2^+ produced from N_2 in the ECR where both the $X\,^2\Sigma_g^+$ and $A\,^2\Pi_u$ electronic states are populated. In this case, the initial population of N_2^+ electronically

decays during the flight time to the interaction region [69, 192]. Regardless of the molecular ion under investigation, a detailed understanding of the molecular state at the time of interaction is necessary if one hopes to identify the dynamics of the process(es) under study. In our case, this is done by (i) assuming a vertical transition from the parent molecule in the ECR and (ii) determining the relevant electronic and vibrational decay during the flight time to the interaction point.

A.2.2 Ion optics

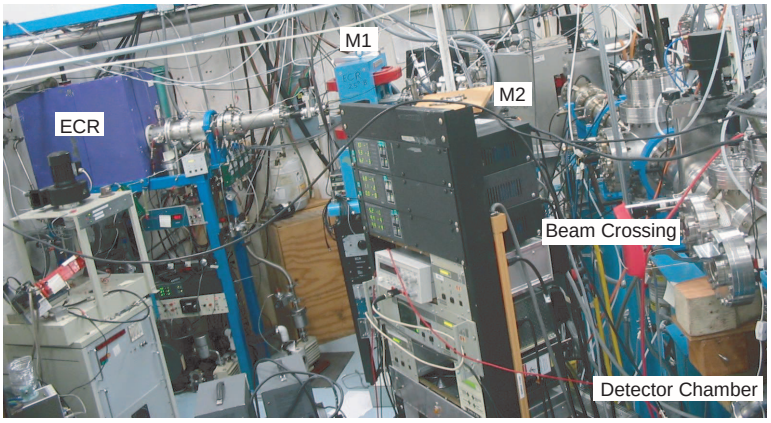

Figure A.2: Photograph of ECR ion beam line with several major elements labeled.

In our measurements, we want to have a high uniform current density molecular-ion beam that is non-diverging, collimated to roughly 1 mm diameter, and contains only one molecular species. To do this, a series of ion-beam optics are employed following the ECR ion source. The ECR ionizes the input neutral gases and accelerates the resulting ions through a set voltage, e.g. 9 kV. The elements used to select the desired molecular-ion beam are the topic of this section and are displayed in figures A.2 and A.3. Note that this section will be limited to the discussion of the properties of the ion optics as the use of these elements will be discussed in a subsequent section, i.e. appendix A.4.

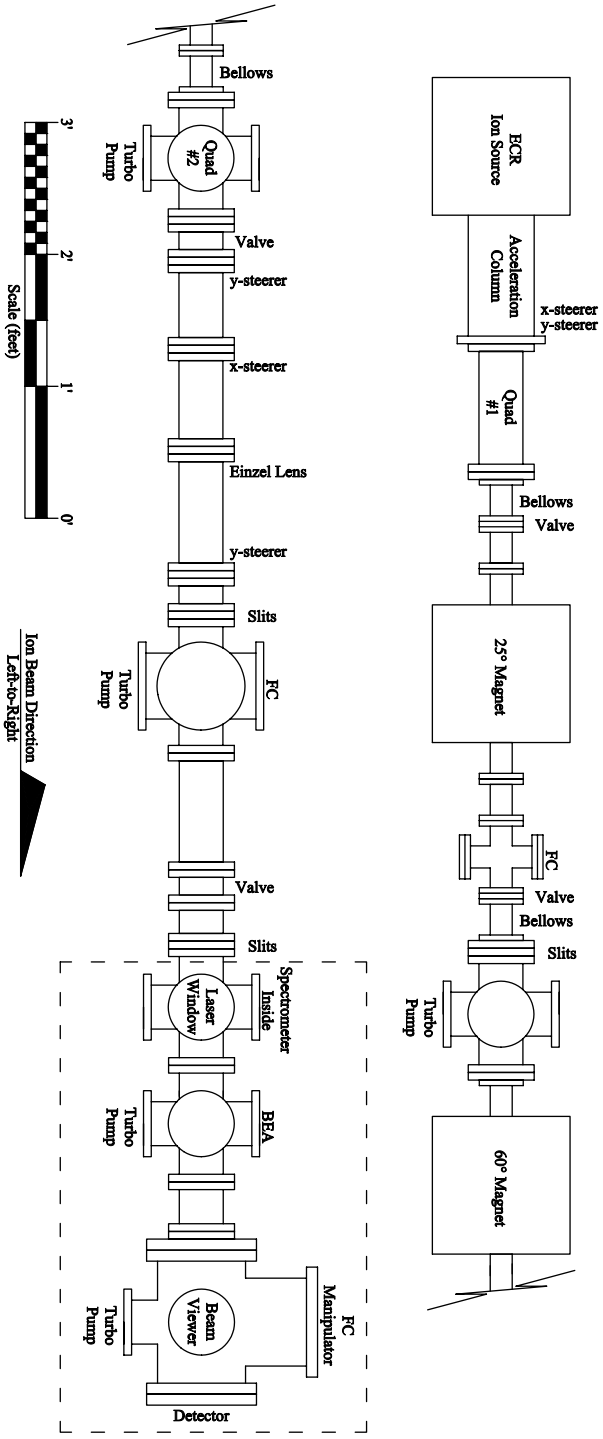

Figure A.3: The functionality of these elements is discussed in detail in the text. Note that elements in the section within the dashed box, i.e. the interaction/detection region, are also discussed in the molecular-dissociation imaging and delay-line-detector appendices, B and D, respectively.

A.2.2.1 Magnetic selection of a particular ion beam

The first order of business is selecting the desired molecular-ion. This is important because the ECR source produces ions from all gasses within the source. For example, N_2^+, O_2^+, O_2^{2+}, and many other molecular ions can all form from electron impact ionization of background gas in the source. To ensure only ions with the desired momentum-to-charge ratio make it to the interaction region, magnetic selection is employed using the magnets marked "M1"/"M2" and 25°/60° in figures A.2 and A.3, respectively. Note that there are situations in which multiple beams with "identical" mass-to-charge ratios[100] can be produced from the same gas in the ECR. For example, when producing a D_3^+ beam (mass-to-charge ratio $=m{:}q$ = 6:1 a.m.u.) from CD_4, a beam of C^{2+} ($m{:}q$=12:2) is also present. However, these two beams are not exactly identical in mass as $m_{D_3^+} = 6.0418 \neq 5.9989 = m_{C^{2+}}$ (in a.m.u.) [238]. Therefore, these beams can be separated, at least partially, by using an ultra fine (i.e. four significant figures in our case) control of the magnetic field.

A.2.2.2 Ion beam collimation

Now that an ion beam with a particular mass-to-charge ratio has been selected, one needs to collimate the beam. This is done with two types of ion optics — (i) focussing elements and (ii) truncating/confining elements. To change the divergence of the beam we use two types of focussing elements — (i) a pair of electrostatic quadrupoles and (ii) an Einzel lens. The truncating/confining elements are (i) three pairs of four-jaw slits, marked as slits in figure A.3, consisting of four movable plates which confine the ion beam to a rectangular cross-section and (ii) a 1×1 mm fixed aperture approximately 27 mm before the interaction point in the first plate of the spectrometer described in appendix B. Note that in our setup, the last set of slits and spectrometer aperture are generally used to eliminate the scatter produced from the previous apertures, which serve to cut the transverse profile of the ion beam.

[100] Note that although a magnetic field selects an ion beam based upon its momentum-to-charge ratio (p/q), the mass-to-charge ratio (m/q) will be used interchangeably as it is proportional to the square root of the momentum-to-charge ratio if it is assumed that all ions are accelerated through the same voltage (V). In other words $mv/q = m/q \cdot \sqrt{2qV/m} \propto \sqrt{m/q}$.

A.2.2.3 Ion beam steering

In addition to focussing and truncating the ion beam, we need to define the trajectory so that the ion beam passes through our spectrometer along its axis. This is done by steering the ion beam with (i) the previously mentioned magnets and (ii) electrostatic deflectors. Adjusting the current in the magnets allows one to steer the ion beam in the horizontal lab axis, i.e. the x-axis. Additional x-axis control along with y-axis control is gained by electrostatic steerers marked in figure A.3. The steerers are basically a parallel-plate capacitor design used to deflect the ion beam without changing its energy.

A.2.2.4 Ion beam collection

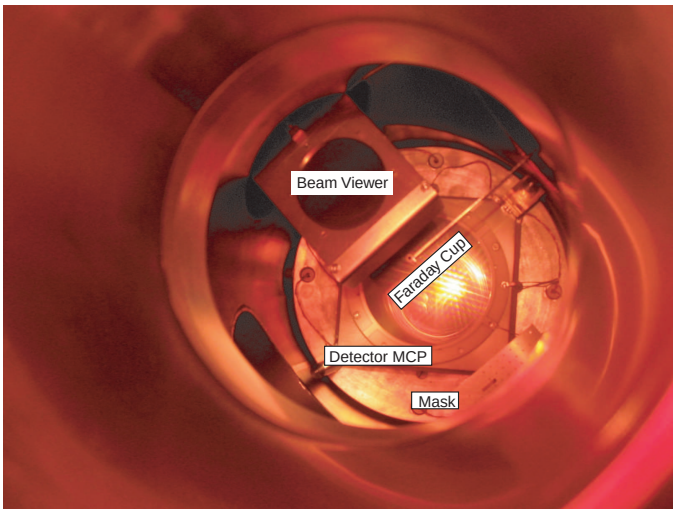

Figure A.4: Photograph of the detector chamber (from the inside) with several major components marked.

In our setup the ion beam is directed toward the face of the particle detector. This allows for the detection of neutral fragments and coincidence momentum imaging as discussed in appendix B. However, the ion beam would burn the detector and overwhelm the particle detection electronics if it were incident upon the detector surface. Therefore, a small (2 mm in diameter) Faraday cup mounted on a two-dimensional manipulator, as shown in figures A.4 and A.5, is employed. This setup allows for the collection of the primary ion beam without any major effect on the dissociating

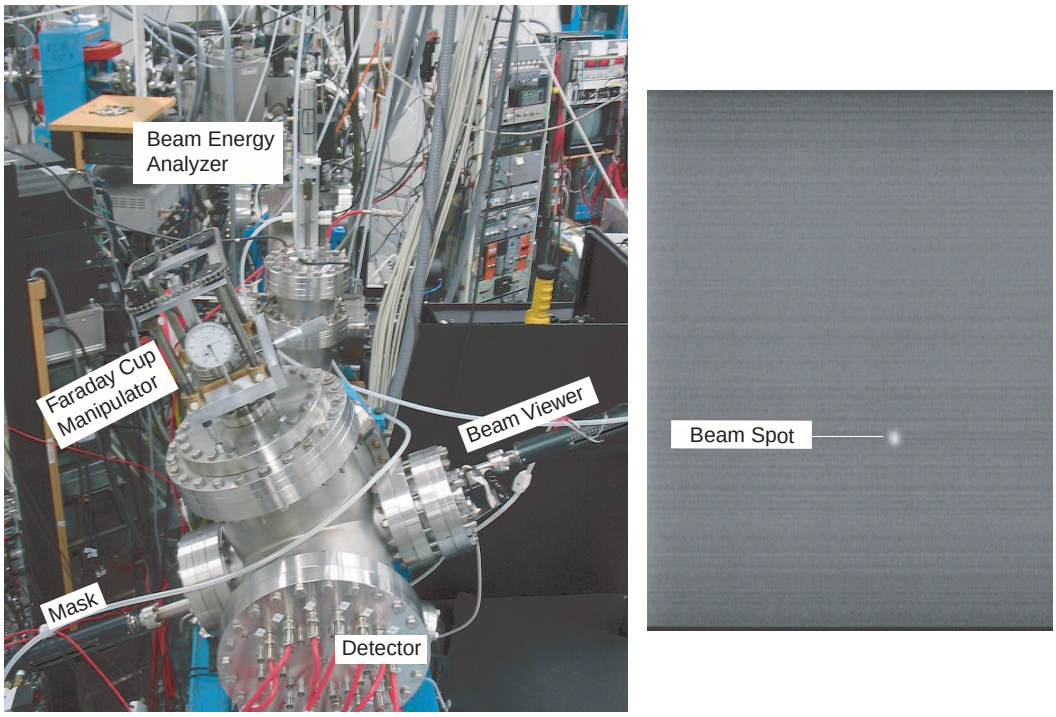

Figure A.5: (left)Photograph of the detector chamber (from the outside) with several major components marked. (right) A typical ion-beam profile as seen on the beam viewer. This spot is approximately 1.0 mm in diameter measured at half the maximum (FWHM).

fragments assuming the ion beam is smaller than the Faraday cup. This requires a beam divergence of $\lesssim 10^{-3}$, i.e. the beam that passes through the 1×1 mm fixed aperture in the spectrometer must be contained within the 2 mm diameter Faraday cup that is approximately 600 mm down stream.

Despite the Faraday cup described above, particle scatter forward from elements along the flight path are still incident upon the detector face — typically a rate of 50 – 500 kHz on the detector in our measurements. To reduce this rate and the resulting accumulated damage to the detector, the voltage on a set of deflectors, which are upstream of the interaction region, is pulsed so that the ion beam is deflected off the detector during those times when the laser is not incident upon the target ion beam. Note that the interaction takes place on the femtosecond time scale so the duty cycle of the pulsing is governed by the electronics used to create the voltage pulse. These electronics are detailed in appendix C and provide a 50μs pulse every ms (i.e. a 5% duty cycle), which eliminated 95% of the scattered particle impacts on the detector without affecting true events in any way.

A.2.3 Tuning the ion beam

In addition to the ion optics described in section A.2.2 and shown in figures A.2 and A.3, we use a beam viewer and a transparent Faraday cup to aid in the tuning of the molecular-ion beam. These elements are shown in figures A.4 and A.5. The transparent Faraday cup is labeled as a "beam-energy analyzer" (BEA). The BEA was originally designed to measure the energy of the ion beam, hence its name. However, for the purpose of this discussion the only relevant design feature is that the BEA is comprised of three high-transmission meshes and one 50% transmission mesh. These meshes can be inserted into the ion beam path and connected to a current meter. Thus, the current meter, which is connected to the 50% transmission mesh, will read a current proportional to the actual current and allow part of the ion beam through along its original trajectory. The beam viewer is comprised of two micro-channel plates (MCPs) and a Phosphorous screen, which allows one to view the shape of the ion beam. A picture of a typical ion-beam profile is shown in figure A.5.

Using these components, the molecular-ion beam optics are tuned according to the following procedure:

1. Open the four-jaw slits and set all ion optics to zero so as to let the beam through freely.

2. Optimize the current in the first Faraday cup by tuning the 25° magnet current and the ECR setting. Note that the pressure inside and the driving power to the ECR affect the production of different ions in different ways.

3. Optimize the current in the second Faraday cup by tuning the 60° magnet and ECR.

4. Insert the BEA and beam viewer and move the 2 mm Faraday cup away from the center of the detector. This allows one to see the ion-beam profile while simultaneously measuring the ion-beam current.

5. Tune all ion optics to create an ion beam that is well collimated and intense.

6. Move the 2 mm Faraday cup to the center of the ion beam.

7. With the BEA, beam viewer, and 2 mm Faraday cup in place, maximize the current in the Faraday cup while minimizing the scatter that makes it past the Faraday cup and is seen/measured by the beam viewer.

Using this process allows one to obtain the low divergence roughly collimated ∼1 mm diameter molecular-ion beam that is desired.

A.3 Laser optics

A.3.1 Introduction

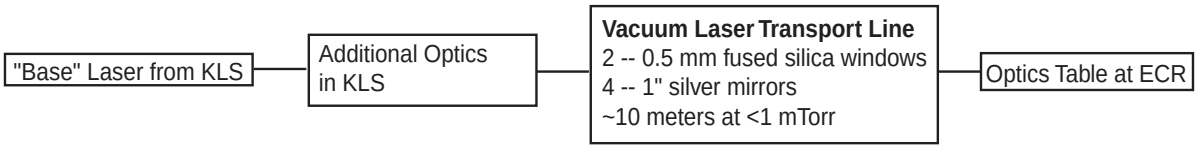

Figure A.6: Our optics setup is made of four segments — (i) the Ti:Sapphire laser, (ii) optics inside KLS, (iii) the evacuated laser transport line, and (iv) the optics adjacent to the ECR molecular-ion beam line (including a parabolic focussing mirror and focal point translation stages as detailed in figure A.7).

The laser optics used in our measurements are grouped into four major parts as depicted in figure A.6. First, the laser itself — a Ti:Sapphire oscillator, stretcher, amplifier, and compressor described in detail in multiple recent publications [102–109] — is housed inside the Kansas Light Source (KLS) facility within the J. R. Maconald Laboratory (JRM) and run by Prof. Z. Chang's research group. This laser produces 35 fs Fourier-Transform-Limited (FTL) pulses with a repetition rate of 1 kHz and ≤3 W of power at 790 nm. Second, this "basic" pulse can be altered inside KLS by using a hollow-core fiber that can produce the frequency bandwidth necessary for $\gtrsim$ 5 fs pulses. Third, the laser is transported from KLS to the ECR beam line by four remotely controlled mirrors inside an transport line, which is evacuated to minimize dispersion due to air. Fourth, there are optics following the transport line, near the interaction point, used to manipulate the laser beam properties (e.g. temporal pulse width, polarization) to produce the desired result at the interaction region.

A.3.2 Optics at interaction

A.3.2.1 790 nm pulse

To use the basic 35 fs 790 nm laser pulse, optics shown in figure A.7(top) are employed after the transport line. To produce pulses with durations above 35 fs, the compressor inside KLS is adjusted to produce a longer pulse. Note that the laser is focused into the interaction region by a 90 degree off-axis parabolic mirror on a translation stage which will be described in detail in section A.3.4.1. Additionally, the instant the laser pulse is incident upon the target is recorded with the photodiode which triggers on a fraction, $< 1\%$, of the beam intensity that passes through the periscope mirror as discussed in appendix C.

A.3.2.2 395 nm pulse

To create a second harmonic pulse, i.e. $\lambda = 395$ nm, the optics shown in figure A.7(bottom) are employed after the transport line. In this setup the basic 35 fs 790 nm laser pulse is sent into a non-linear second-harmonic generation crystal, namely a $8 \times 8 \times 0.25$ mm^3 β-BaB_2O_4 (a.k.a. BBO) crystal. This produces a 395 nm pulse which has a polarization perpendicular to the incident 790 nm pulse. This difference in wavelength and polarization orthogonality is used to separate the two collinear beams with a dichromatic beam splitter.

A.3.2.3 Ultrashort 790 nm pulse

To create an ultra short 790 nm laser pulse, several major additions must be made to the optics used. First, to get the frequency bandwidth required to support a sub-10 fs pulse, we use a hollow-core gas-filled fiber in KLS [106]. Second, chirped mirrors are used to introduce enough negative chirp to compensate for both the positive chirp produced in the hollow-core fiber and the positive chirp inherent to the subsequent transport line and optics. In our setup we typically introduce 11 reflections of chirped mirrors, which is equivalent to 350 fs^2 (or ~ 9.7 mm of fused silica) of chirp, to negate the chirp produced in the fiber and the subsequent optics. Third, fused silica wedges are used to balance the positive and negative chirp of the optics path. Note that the technique used to fine tune the wedges and minimize chirp in the interaction region, thus producing the shortest

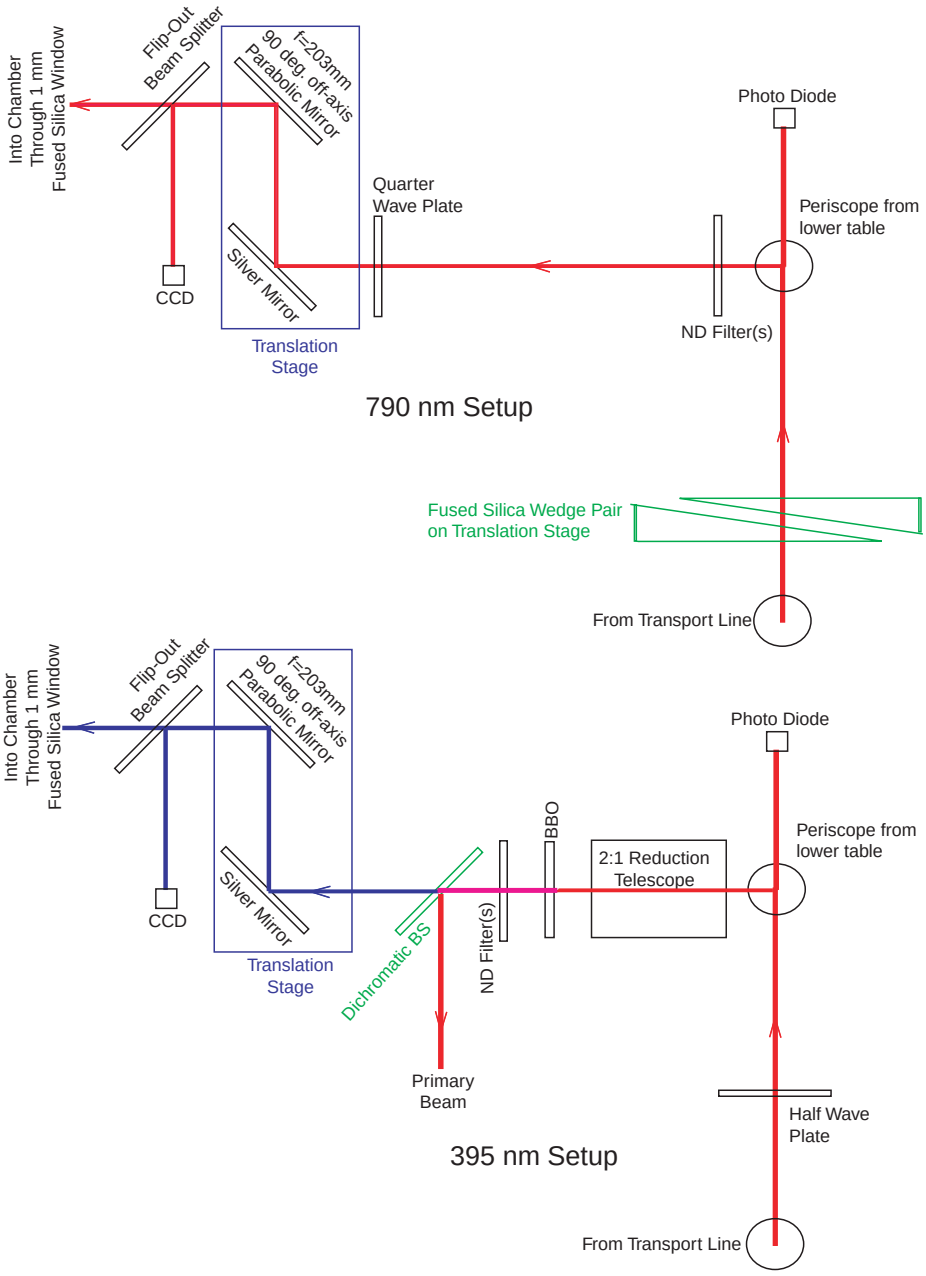

Figure A.7: Schematic of optics near ECR. (top) Optics used for 790 nm laser pulse measurements. (bottom) Optics used for 395 nm laser pulse measurements. Note that (i) while measurements are in progress, the flip-out beam splitter is removed, (ii) the quarter wave plate is only used if circular polarization is desired, (iii) the neutral density (ND) filters are removed unless CCD images or intensity difference spectrum (IDS) slices, which are discussed in section 2.6.1.1, are being taken, and (iv) the fused silica wedge pair is used with sub-10 fs pulses to balance chirp thereby achieving the shortest possible pulse.

possible pulse, is discussed in section A.4.2.

A.3.3 Pulse duration

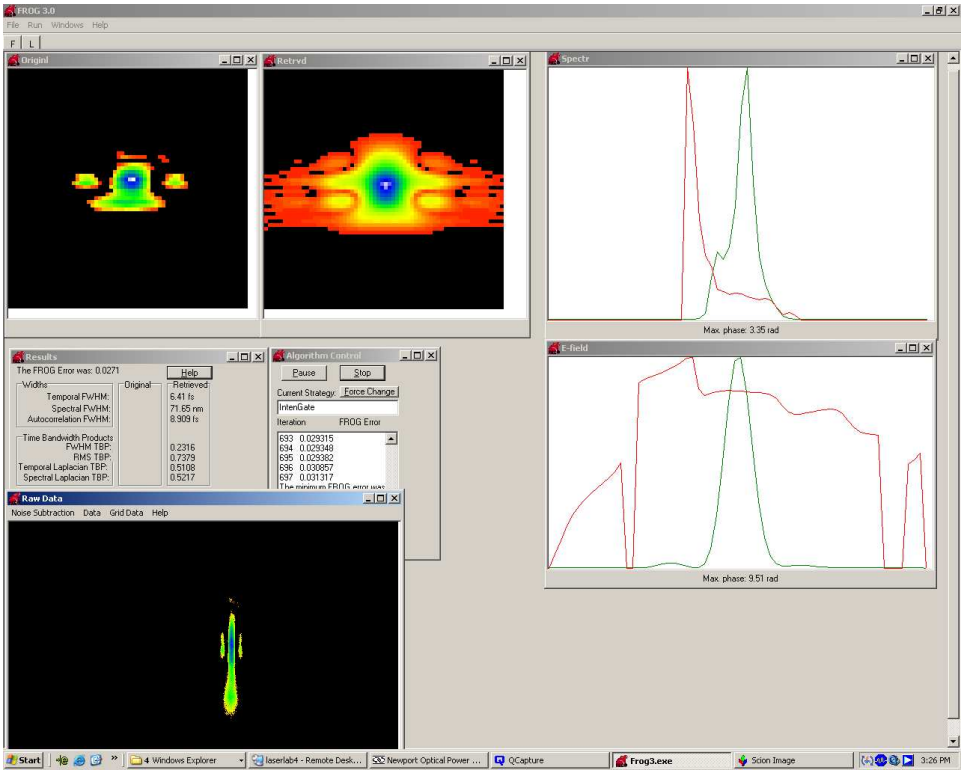

Figure A.8: Typical short pulse FROG trace. This is a sub-10 fs pulse with small pre- and post-pulses.

A.3.3.1 Measuring 790 nm pulse duration

As the interactions under study are presumed to depend upon the pulse duration and peak intensity of the second-harmonic, one needs to be able to determine those quantities. For 790 nm pulses, the pulse duration is measured after the fiber and chirped mirrors with frequency-resolved optical gating (FROG). The details of the FROG technique are beyond the scope of this dissertation and are described in detail in multiple publications, e.g. [113]. This measurement yields the pulse duration and frequency spectrum of the 790 nm laser pulses. (See figure A.8 for a typical FROG trace.) Note that the pulse durations in this dissertation refer to the full-width at half the maximum

(FWHM) in intensity of the laser pulse.

A.3.3.2 Evaluating the pulse duration of second harmonic

In the case of the second-harmonic, one needs to determine the quantities using standard nonlinear optics [110, 111] as we do not have an apparatus to measure it directly. The temporal width of the Fourier-transform limited second-harmonic pulse, $T_{2\omega}$, in terms of the pulse length of the primary beam, T_ω, is

$$\boxed{T_{2\omega} \simeq \frac{T_\omega}{\sqrt{2}}\sqrt{1+\frac{2\ln(2)}{3}\left(\frac{gL}{T_\omega}\right)^2}}, \tag{A.1}$$

where $g \simeq 200$ fs/mm is the group velocity mismatch and $L = 0.25$ mm is the thickness of the BBO crystal in our setup.

Even though this setup is efficient in generating short 395 nm pulses, e.g. if $T_\omega = 40$ fs, $T_{2\omega} \simeq 40$ fs, the 395 nm pulse is very susceptible to temporal broadening due to the chirp induced by optical elements after the BBO crystal, e.g. the dichromatic beam splitter and fused silica vacuum chamber entrance window. Therefore, to calculate a more realistic pulse duration at the interaction point, we need to include the dispersion after the BBO crystal. This yields

$$\boxed{T'_{2\omega} = T_{2\omega}\sqrt{1+\left(\frac{\alpha_{395}\ln(2)}{T_{2\omega}^2}\right)^2}}, \tag{A.2}$$

where $T_{2\omega}$ is the Fourier-transform limited second-harmonic pulse directly out of the BBO, $\alpha_{395} = 49.6L_3$ is the second-order dispersion of the second harmonic after the BBO due to fused silica, and L_3 is the thickness of fused silica through which the second harmonic travels on its way to the interaction point in mm. This means that in our setup, which requires at least a vacuum chamber window and a dichromatic beam splitter ($L_3 \geq 3.5$ mm), the minimum pulse duration given a 40 fs Fourier-transform limited primary pulse is ~ 47 fs.

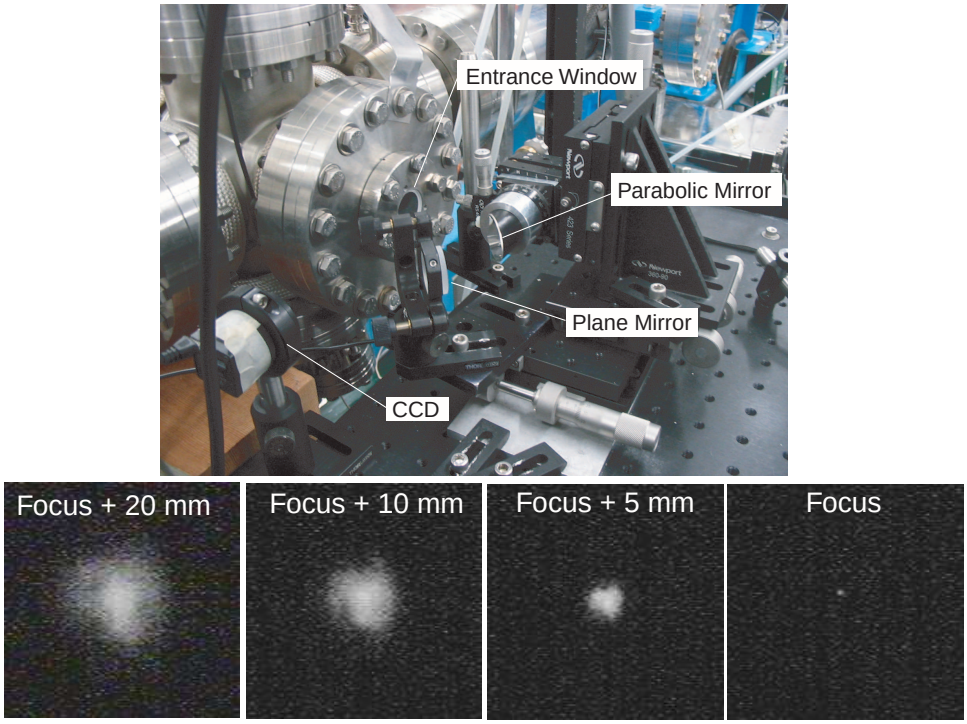

Figure A.9: (top) Photograph of the parabolic mirror mount with major components labeled. (bottom) Typical CCD images of the laser focal spot at various z-positions. Images are 150×150 pixels. See text for details.

A.3.4 90 degree off-axis parabolic mirror

A.3.4.1 Aligning the parabolic mirror

As it is rather easy to create abberations when using an off-axis parabolic mirror, this section will discuss (i) the manner in which we tune our $f = 203$ mm mirror and (ii) how the intensity profile is measured. Tuning the parabolic mirror is detailed in the following list, which refers to figures A.9 and A.10.

1. Ensure that the laser path is parallel to the optics table using an iris set at the desired height.

2. Roughly adjust all optics so that the laser beam is centered on all optical components.

3. Put the flip-out beam splitter into the beam and place the CCD camera at the mirror's focus. (Add neutral density filters as needed to give the CCD image contrast.)

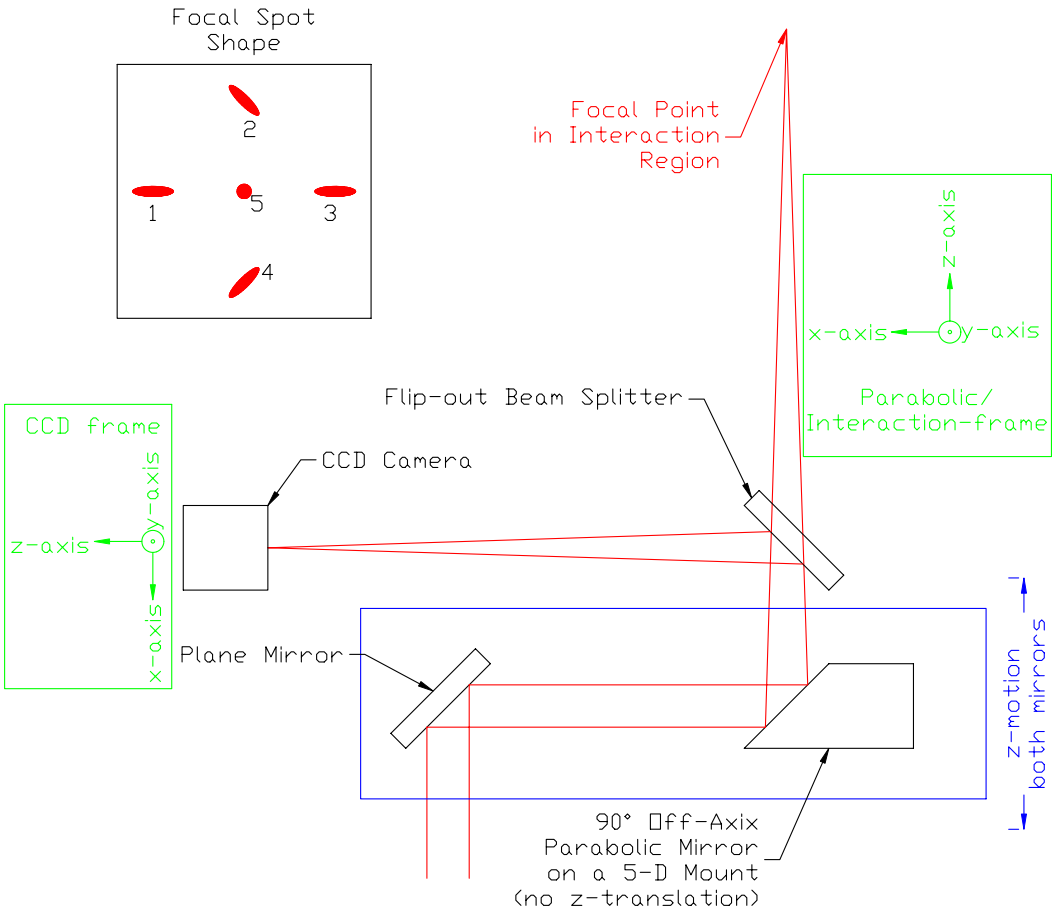

Figure A.10: Parabolic mirror schematic. (inset) The inset in the upper left shows several laser profiles. Profiles 1–4 are astigmatic profiles requiring adjustments to the parabolic mirror so that a Gaussian profile, i.e. 5, can be achieved.

4. Adjust the position of the CCD camera until the image is visible.

5. Adjust the position of the parabolic mirror until the smallest, i.e. roundest and "most Gaussian", spot is achieved. As seen in the inset to figure A.10, misalignment of the parabolic mirror will cause astigmatic abberations in the focus. These abberations can be corrected by adjusting the rotation about the y- and z-axes of the parabolic mirror.

6. The laser beam needs to be parallel in height to the optics table surface and the ion beam height to perform z-scanning intensity-difference spectrum zIDS as discussed in section 2.6.1.1. Therefore, the center of the focal spot must not move vertically when the large translation

stage, on which the plane and 90° off-axis parabolic mirrors sit, moves in the z-direction. If this is not the case, then the goniometry, which rotates the parabolic mirror about the x-axis, should be adjusted.

7. Repeat steps 4–6 until the optimum focal profile is achieved. (See the typical profile with a properly aligned parabolic mirror in figure A.9.)

To make this procedure practical and reproducible we have found several components necessary — (i) the parabolic mirror is mounted on a five-axis micrometer driven stage, i.e. rotation about all three axes and translation along the x- and y-axes, (ii) a CCD camera is used to view the image as one's eyes can be deceived by a laser spot viewed on a screen/card, (iii) no enlarging optics, e.g. a microscope objective, are used in front of the CCD camera as they may produce additional abberations to the focal spot and our focal spot is large enough to be measured with a typical CCD, i.e. at least a few pixels in diameter.

A.3.4.2 Determining the spatiotemporal intensity profile

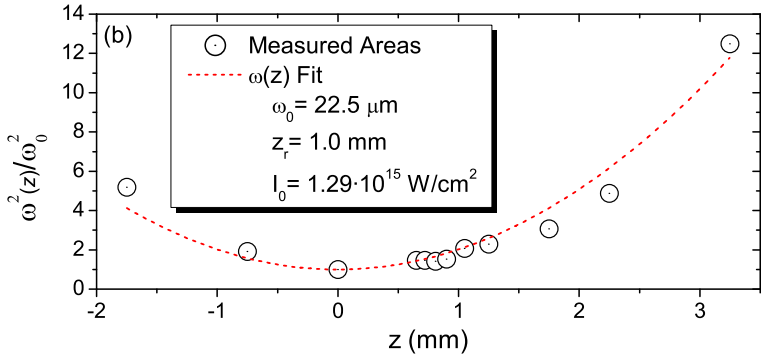

Figure A.11: Typical focal profile measured with a CCD camera.

The power of the laser (P) is measured with a power meter, the repetition rate (R) is measured with a photodiode, and the temporal full width at half the maximum in intensity ($FWHM_I$) has been measured or calculated as discussed in a previous sections. Therefore, the final piece of information necessary to determine the spatiotemporal intensity profile of the laser pulse is the spatial focal profile. The spatial focal profile is measured with the same setup used to align the

parabolic mirror, i.e. that shown in figures A.9 and A.10. This is done by adjusting the translation stage, which moves both the plane and parabolic mirrors, in the z-direction and recording the spatial profile of the laser seen on the CCD camera. The image of the focal point gives the dimension of the beam waist. In our measurements the focal point is typically ~ 25 μm (FWHM diameter in intensity) with a Rayleigh range ($z_r \sim 1$ mm) as shown in figure A.11. Assuming the laser pulse is well approximated by a Gaussian, the spatiotemporal intensity distribution of the pulse is

$$I(\rho, t) = I_0 \exp\left[-2\left(\frac{\rho}{\omega_0}\right)^2 - 4\ln(2)\left(\frac{t}{\tau}\right)^2\right] , \tag{A.3}$$

where I_0 is the peak intensity, ω_0 is the Gaussian beam waist, and τ is the temporal FWHM in intensity. Furthermore, the energy E of each pulse can be obtained by integrating over space and time, which yields

$$E = \int_{-\infty}^{\infty}\int_{0}^{\infty} I(\rho, t) \cdot 2\pi r \; dr \; dt = \sqrt{\frac{\pi}{\ln(2)}}\frac{I_0 \pi \omega_0^2 \tau}{4} . \tag{A.4}$$

Rearranging this equation yields

$$I_0 = 4\sqrt{\frac{\ln(2)}{\pi}}\frac{E}{\pi\omega_0^2\tau} \simeq 1.88\frac{E}{\pi\omega_0^2\tau} , \tag{A.5}$$

which expresses the peak intensity in terms of the pulse energy, which is simply the average power of the laser beam (P) divided by the repetition rate (R). Therefore,

$$\boxed{I_0 \simeq 1.88\frac{P/R}{\pi\omega_0^2\tau}} , \tag{A.6}$$

where P is the laser power, R is the repetition rate, ω_0 is the Gaussian beam waist (i.e. the radius using the $1/e^2$ criterion), and τ is the temporal FWHM in intensity. So, for example, if a laser pulse has duration $\tau = 45$ fs, a focal size $\omega_0 = 25$ μm, a beam power $P = 1$ W, and a repetition rate $R = 1000$ Hz, then the peak intensity is $I_0 = 2.1 \times 10^{15}$ W/cm^2. Note that in our measurements, the power of the beam is measured before the focussing element and chamber window, which have a loss of $\sim 8\%$. Therefore a factor, α, equal to the power loss from the measurement position to the interaction region is required in equation A.6, i.e. $I_0' = \alpha I_0 = 0.92 I_0 \simeq 2.0 \times 10^{15}$ W/cm^2.

A.4 Crossing the beams

A.4.1 Maximizing beam overlap in position

Now that both the basic elements of, and the procedures used to tune and measure, the laser and molecular-ion beams have been discussed, this section will describe the details of how the conditions under which the two beams interact are controlled. To find the point at which the laser's focus passes through the center of the molecular-ion beam, the following procedure is used:

1. Scan the laser focus horizontally along the ion beam, i.e. in the x-direction, until a large increase in the number of scattered photons is seen on the detector. The large photon scatter is caused by the laser beam hitting one of the rings of the time-of-flight spectrometer, as described in appendix B. Therefore, setting the x-position half way between the settings with a large scatter ensures that the x-position of the interaction point is in the appropriate place with respect to the spectrometer.

2. Scan the vertical, y, translation of the parabolic mirror, thereby moving the laser beam through the target molecular-ion beam. By plotting the dissociation yield as a function of this position, a rough profile of the beam density in y can be determined. Set the y-position of the parabolic mirror so that the laser and ion beams have the maximum overlap, i.e. the dissociation yield is maximized.

3. Scan the focal z-position, i.e. the z-translation stage with the plane and parabolic mirrors, and record the dissociation yield as a function of this position. This will create a symmetric distribution about the focal point as the focal profile is roughly symmetric in z. Set the z-position at the symmetry point. This ensures that the laser and molecular-ion beams cross at the laser focal point.

4. Repeat the procedure until no adjustments are needed.

A.4.2 Chirp compensation

A.4.2.1 Introduction

In the previous section, the method for roughly determining the amount of fused silica needed to minimize the pulse width by balancing the positive and negative chirp in our system is discussed. This method is not sufficient in the case of an ultra short, i.e. sub 10 fs, pulse because for a pulse of this width a small deviation in compensation fused silica thickness will produce a significant temporal broadening of the pulse. For example, a 790 nm 8 fs Fourier-transform-limited pulse will emerge from a 1 mm fused silica beam splitter with a width of almost 15 fs along with pre- and post-pulses while a 790 nm 45 fs Fourier-transform-limited pulse going through a 1 mm fused silica beam splitter will emerge with less than a 1% increase in width [110]. Furthermore, due to the low counting rate of our experiment, which is typically less than 10 Hz, it is impractical to look at the effects of compensation fused silica for many points. Moreover, (i) the effect of a shorter pulse is not known a priori, (ii) the effects under study might be dependent on the sign of the chirp, and (iii) the process in question may by insensitive to changes in pulse duration. Therefore, using the molecular-ion beam laser interaction as the measure for the fine chirp compensation is not practice.

A.4.2.2 Using above-threshold ionization of the background

To determine the optimum amount of chirp compensation fused silica quickly and accurately, the above-threshold ionization (ATI) yield of the vacuum background gasses is used. The molecular-ion beam is blocked from entering the interaction region, and the background gas in our vacuum system, which it typically held at $\lesssim 10^{-9}$ Torr, is ionized by the laser pulses. The yield is then recorded as a function of chirp compensation. Furthermore, since the longitudinal spectrometer separates ions with different mass-to-charge ratios (see appendix B), the yield is separated and recorded for multiple ATI channels, e.g. H_2^+, N_2^+, and H_2O^+. This results in a plot of ATI yield as a function of compensation for multiple particles with distinct mass-to-charge ratios. Furthermore, the strong dependance on peak intensity for ATI processes is well established. Thus, one can determine the position of the shortest pulse very accurately (typically $\lesssim 0.2$ mm of fused silica) and quickly.

Appendix B

Molecular-dissociation imaging

B.1 Introduction

The goal in the design of our experimental apparatus was to be able to separate different dissociation channels and derive their complete breakup dynamics, e.g. kinetic energy release, dissociation angle, etc.. We want to do this for all channels simultaneously using the measured values. We will consider the three breakup channels

$$\begin{aligned}
&\text{Dissociation 'ApB'} \rightarrow AB^{q+} + nh\nu \Rightarrow A^{q_A+} + B \\
&\text{Dissociation 'ABp'} \rightarrow AB^{q+} + nh\nu \Rightarrow A + B^{q_B+} \\
&\text{Ionization 'ApBp'} \rightarrow AB^{q+} + nh\nu \Rightarrow A^{q_A+} + B^{q_B+} + ne^- \ ,
\end{aligned}$$

where the variables q_A and q_B allow the definition to encompass all possible breakup channels and $n = q_A + q_B - q$. So for example, a measurement of the laser-induced breakup of HD^+ will have the channels

$$\begin{aligned}
&\text{Dissociation 'HpD'} \rightarrow HD^+ + nh\nu \Rightarrow H^+ + D \\
&\text{Dissociation 'HDp'} \rightarrow HD^+ + nh\nu \Rightarrow H + D^+ \\
&\text{Ionization 'HpDp'} \rightarrow HD^+ + nh\nu \Rightarrow H^+ + D^+ + e^- \ .
\end{aligned}$$

As we want to distinguish between all three channels even if their kinetic energy release (KER) and/or angular distributions overlap, we decided to employ two techniques. First, to determine which process is creating a particular charged particle, a molecular-ion beam is used so that after the molecular breakup the neutral fragments have enough velocity (i.e. approximately that of the molecular-ion beam) to be detected. In this way an ionization event can be distinguished from a dissociation if particles with different charge-to-mass ratios can be distinguished. For example, a non-ionizing dissociation of H_2^+ will produce p^++H in coincidence, i.e. from the same laser pulse, while ionization will produce p^++p^+. Second, to distinguish particles with different charge-to-mass ratios we use a longitudinal time-of-flight (TOF) spectrometer (i.e. a spectrometer with an electric field parallel to the molecular ion beam direction) to temporally separate particles with different charge-to-mass ratios. The design and effects of this spectrometer have been briefly discussed in several publications[36, 52, 92] and will be the focus of this appendix.

B.2 Event mode data collection

This temporal separation is measurable if the data is collected in "event mode", which is to say that the measured quantities are gathered and recorded for each and every laser pulse and that the information gathered for any and all individual laser pulses can be distinguished from all others.[101] This is an important aspect of of our measurements as it allows for the collection of information which is typically lost in "time integrated measurement", i.e. measurements in which the time information for each event is not recorded.[102] The event mode technique is enabled by the electronics discussed in appendix C and employed in all our measurements.

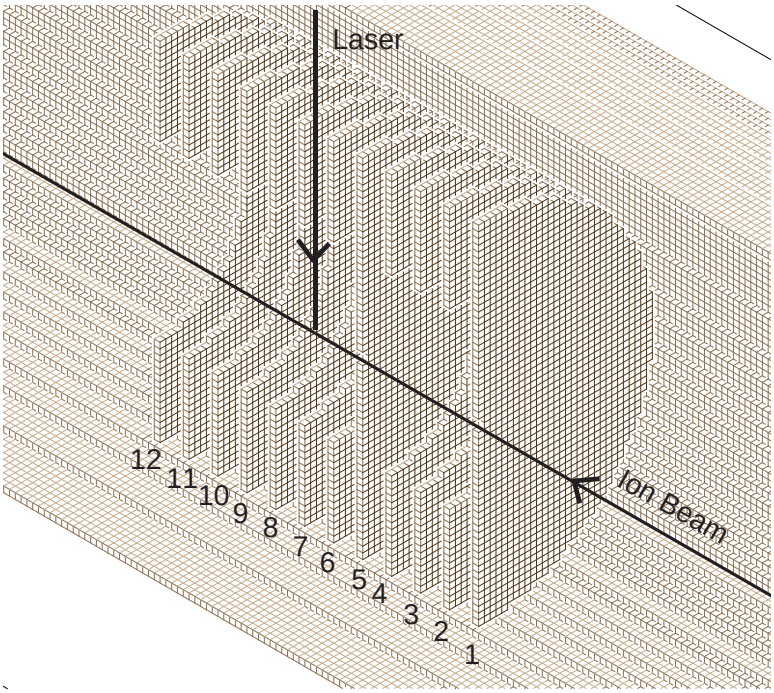

Figure B.1: SimIon 3D cross section of the spectrometer

B.3 Time-of-flight spectrometer design

The time-of-flight spectrometer used in our measurements creates an electric field in the laser-molecule interaction region. This field provides different acceleration to particles with different mass-to-charge (m/q) ratios.[103] The spectrometer is comprised of conducting rings on a common central axis, as shown in figure B.1. The rings are 1 mm thick, are spaced at a 5 mm interval (i.e. separated by a 4 mm gap), have an outer diameter of 60 mm, and have an inner diameter of 30 mm (except the first and fifth rings which have a 1 mm aperature. Ground (0 V) is applied to the

[101] Note that temporal separation can be measured with a non-event mode setup. For example, one could use fast timing electronics and logic gates to record different time gates in different bins.XXX However, when data is recorded in event mode the information is recorded at the highest possible resolution of the measurement and then binned in software. Thus, one has the advantage of being able to reanalyze the data event-by-event, i.e. rerunning the experiment virtually, as many times as necessary until the data is binned in the best way.

[102] These are referred to as time integrated measurements since they would match event mode data if one integrated the event mode data over time.

[103] It is worth noting that a longitudinal axial spectrometer could have been employed after the interaction region to gain the time separation. This type of post-interaction spectrometer does significantly simplify the data analysis discussed below, however, it must be (i) longer and/or (ii) held at a higher voltage and (iii) it is more difficult to implement as one must allow and account for the fragments' increasing spatial spread as they travel.

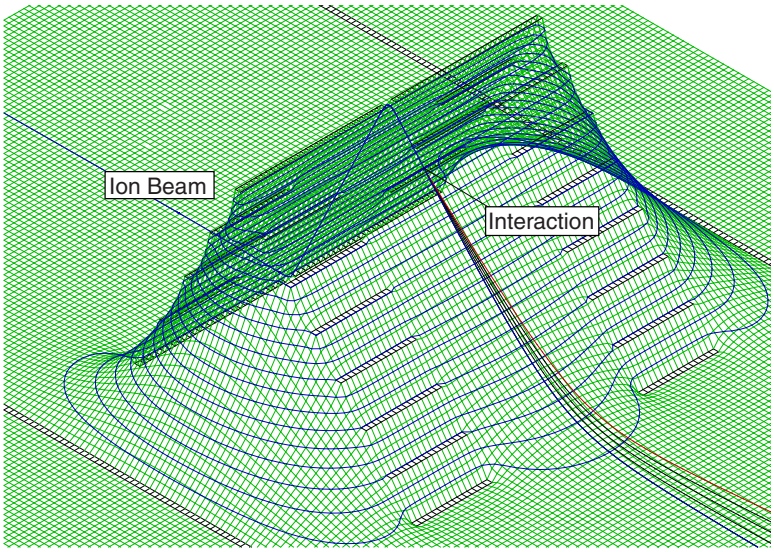

Figure B.2: A SimIon plot of the potential surface created by the spectrometer. There are 20 equally spaced potential contour lines superimposed in blue, the molecular ion beam path is marked in blue, and several typical fragment trajectories are also shown.

first and last plates,i.e. 1 and 12, while a positive voltage is applied to the fifth plate. All other plates are connected in series through an equally spaced resistor chain. With these voltages the spectrometer creates the potential surface seen in figure B.2. The laser-molecular ion interaction happens approximately on the spectrometer central axis where the voltage is 80% of the voltage applied to ring 5 (approximately half way between rings 6 and 7) and this point is designated the origin throughout this section.

B.4 Molecular dissociation imaging for diatomic molecules

B.4.1 Introduction

Remember, the goal is to be able to separate different dissociation channels and derive the complete breakup dynamics (e.g. kinetic energy release, dissociation angle, etc.) of each breakup channel from the measured values of position and time-of-flight. The TOF spectrometer described above allows for the separation of different dissociation channels and the delay-line-detector (DLD) allows for the measurement of position and TOF (i.e x, y, and t) for every particle. Thus, the goal can be

accomplished, if one can move from the measured position and time-of-flight values to momentum in the initial molecule's center-of-mass (COM) frame.

There are two ways of achieving this goal. One can either (i) create a translation matrix, which takes any set of measured values and translates it to dissociation kinematics, or (ii) model the functionality of the spectrometer in an analytical form. As the former would require a very large translation matrix to account for all the experimental variables, the latter method was chosen as it is simpler and contains intermediate steps which have physical meaning.

B.4.2 Two-region uniform field approximation

The most basic approximation of the effects of this spectrometer assumes that the spectrometer creates an ideal electric field, i.e. a uniform electric field pointing only in the ion beam direction and strictly confined to the spectrometer region. In such a configuration, the initial conditions of the interaction are easily computed from the measured quantities. In the region with the electric field, length d_1, ions will experience an acceleration, $a = qE/m$, along the ion-beam direction, which is chosen to be z. Therefore the time it takes an ion to transverse this region is

$$t_1 = \frac{-v_{0z} + \sqrt{v_{0z}^2 + 2ad_1}}{a} \tag{B.1}$$

where v_{0z} is the initial velocity and the particle is assumed to start at the origin. Additionally, the velocity of the charged particle upon exit is

$$v_1 = v_{0z} + at_1 \ . \tag{B.2}$$

Thus the entire TOF for charged particles will be

$$TOF = t_1 + t_2 = \frac{-v_{0z} + \sqrt{v_{0z}^2 + 2ad_1}}{a} + \frac{d_2}{v_1} \ , \tag{B.3}$$

where d_2 is the length of the free flight (i.e. field free) region. For neutral particles

$$TOF = t_1 + t_2 = \frac{D}{v_{0z}} \ , \tag{B.4}$$

where $D = d_1 + d_2$. Furthermore, since there is no electric field perpendicular to the ion beam direction,

$$v_x = \frac{x}{TOF} \text{ and } v_y = \frac{y}{TOF} \ , \tag{B.5}$$

where x and y are the horizontal and vertical positions of the hit on the detector relative to the spectrometer axis.

Since the idealized formula must work for neutrals as well as charged particles, the sum of the distances must match the real distance from the interaction to the detector, i.e. $d_1+d_2 = D = 774.0$ mm (as measured for our spectrometer). In addition we wish to constrain the electric field to a value corresponding to the voltage at the interaction point, i.e. $0.8V_s$. With these constraints, we used SimIon to simulate, i.e. "fly", ion trajectories with various initial conditions and found that setting $d_1 = 27.377$ mm and $d_2 = 746.623$ mm makes our model time-of-flight formula best fit the simulation.[104]

B.4.3 Modeling the focusing effects of the spectrometer

The simple model above works well for time of flight under most of the conditions in our measurements and is used as the basis for calculations from this point forward. However, the transverse (i.e. x and y) calculations do not match the SimIon results well. This is due to the distortions of the spectrometer caused by the curved potential surface as seen in figures B.2 and B.3. This field curvature acts much like a lens and thus the distortions can be described by magnification factors, which needs to be take n into account. To do this we modeled two magnification factors — (i) a magnification of the initial transverse position, M_p, and (ii) a magnification due to the transverse velocity, M_v. With these magnification factors in place, the initial transverse velocity calculation becomes

$$x_1 - M_p x_{0i} = M_v(v_{0x_i} + v_{1x})TOF \ . \tag{B.6}$$

As one can see from the equation for the relatively straightforward quantity above, the notation is going to become rather complex. Therefore, let us take a step backward and list our assumptions

[104] Typically the model TOF formula fits the SimIon simulation to within 0.25 ns, i.e. $\lesssim 0.1$ % error with respect to the total TOF, and in the worst cases that we found, the model is off by < 1 %.

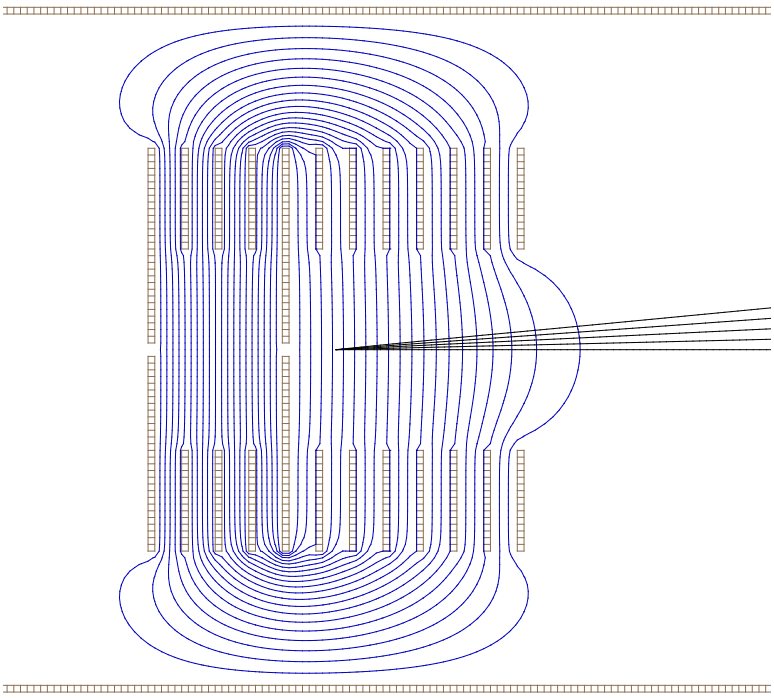

Figure B.3: A SimIon plot of the spectrometer's electric potential lines

and define all the parameters up front so that they are easy to find when needed.

B.4.4 Molecular dissociation imaging

B.4.4.1 Assumptions and definition of variables

The variables that will be used are defined in table B.1, and there are several assumptions/approximations that are enumerated below.

1. The nuclei conserve momentum
   (a) The momentum gained from and/or lost to the laser field is negligible
   (b) The momentum taken away by the freed electron(s) during the ionization process is negligible
2. The spectrometer z-component can be represented with only two regions

Variable	Definition
particle #	— 1 = the first particle to arrive at the detector and 2 = the second particle to arrive at the detector
d_1	— length of the electric field region of the ideal spectrometer ($d_1 = 27.377$ mm)
d_2	— length of the free flight region after the ideal spectrometer ($d_2 = 746.623$ mm)
D	— total length from interaction point to detector face, i.e. $D = d_1 + d_2$
E_i	— energy of the particle at the interaction point, i.e. $0.5mv^2$
E_{scl}	— the scaled particle energy, i.e. $E_i/(q * V_s)$
F	— the ratio of the ideal and real spectrometer voltages, i.e. $F = V_s/V_{ps}$
m_i	— fragment mass, e.g. m_1 is the mass of the first fragment
M	— total molecular mass, i.e. $m = m_1 + m_2 + \cdots$
$M_{p_{1,2}}$	— magnification of the initial transverse position due to the spectrometer's non-uniform field for particle 1 or 2
$M_{v_{1,2}}$	— magnification of the initial transverse velocity due to the spectrometer's non-uniform field for particle 1 or 2
q	— the particle charge in atomic units
$t_{1,2}$	— the time from the interaction point until particle 1 or 2 reaches the detector
$t'_{1,2}$	— the scaled time of flight, i.e. $t_{1,2}M_{v_{1,2}}$
$u_{1,2}$	— the scaled dissociation velocity, e.g. $u_{1z} \equiv v_{1z}/v_{0zi}$
$v_{0xi}, v_{0yi}, v_{0zi}$	— the velocity of the molecule when it interacts with the laser
$\overline{v_{0x}}, \overline{v_{0y}}, \overline{v_{0z}}$	— the **average** velocity of the molecule when it interacts with the laser
$v_{1x,1y,1z,2x,2y,2z}$	— the velocities of particle one or two (1,2) immediately after the laser interaction in the molecular center-of-mass frame
V_0	— the voltage at the origin, i.e. $0.8V_s$
V_s	— the voltage of the virtual spectrometer
V_{ps}	— the real spectrometer voltage seen on the power supply, i.e. $V_s = F \times V_{ps}$
x_{0i}, y_{0i}, z_{0i}	— the position of the molecule when it interacts with the laser with respect to the ideal position in the spectrometer (on axis and half way between plates 6 and 7)
$\overline{x_{0i}}, \overline{y_{0i}}, \overline{z_{0i}}$	— the **average** position of the molecule when it interacts with the laser
$x_{1,2}, y_{1,2}$	— the position of the first or second hit on the detector relative to the central axis of the spectrometer
$x'_{1,2}, y'_{1,2}$	— the position of the first or second hit measured on the detector face relative to the center of the detector
z'_i	— scaled initial z-position, i.e. $z'_i \equiv z_{0i}/d_1$
z''_i	— scaled initial z-position, i.e. $z''_i \equiv z_{0i}/D$
β_{ij}	— the mass ratio of 2 particles, e.g. $\beta_{12} \equiv m_1/m_2$
$\eta_{1,2}$	— proportional to the reciprocal of the scaled energy, e.g. $\eta_1 \equiv \frac{0.8qV_s}{0.5m_1v_{0z}^2} = \frac{0.8qV_s}{E_{0z}}$
$\chi_{1,2}$	— a scaled velocity, i.e. $\chi_1 = \sqrt{(1+u_{1z})^2 + \eta_1(1-z'_i)}$

Table B.1: A table of variables used in our diatomic molecular dissociation imaging.

(a) One region, i.e. $d_1 = 27.377$ mm, has a uniform electric field in the z-direction providing a constant acceleration to charged particles

(b) The second, i.e. $d_2 = 746.623$ mm, is a field-free, a.k.a. free-flight, region

3. The transverse distortions due to the spectrometer can be represented by magnification factors in initial transverse position and velocity

4. The effective laser focal spot is very small compared to the molecular-ion beam size

5. The spectrometer, molecular-ion beam, and detector are approximately on the same axis

(a) The transverse position of the interaction region, x_{0i} and y_{0i}, can only deviate slightly from the origin — the central axis of the spectrometer

(b) The longitudinal position of the interaction region, z_{0i}, can not move from the origin more that the spectrometer ring separation, i.e. $z_{0i} = 0 \pm 2$ mm

(c) The velocity of the molecular-ion beam can only deviate slightly from the central axis of the spectrometer, i.e. $v_{0xi} \ll v_{0zi}$ and $v_{0yi} \ll v_{0zi}$

(d) The detector is approximately centered on the spectrometer axis

B.4.4.2 Determining v_{1x}, v_{0xi}, and x_{0i}

The first thing to recall is that momentum will be conserved in the molecule's center of mass (CM), i.e. $\overrightarrow{p}_1 + \overrightarrow{p}_2 = 0$. Therefore, for any component of velocity in the CM frame the particles will be related by the equation

$$\boxed{m_1 v_1 = -m_2 v_2 \rightarrow v_2 = -v_1 \frac{m_1}{m_2} = -v_1 \beta_{12}}\,, \tag{B.7}$$

where $\beta_{ij} \equiv m_i/m_j$. With this in mind, one sees that the x-position of the first and second particles can be defined as[105]

$$x_1 - M_{p_1} x_{0i} = M_{v_1}(v_{0x_i} + v_{1x})t_1 = (v_{0x_i} + v_{1x})t_1' \tag{B.8}$$

[105]Note that throughout this section the y-dimension will be omitted as it is equivalent to the x-dimension.

$$x_2 - M_{p_2} x_{0i} = M_{v_2}(v_{0x_i} + v_{2x})t_2 = (v_{0x_i} - \beta_{1,2} v_{1x})t_2' \ , \tag{B.9}$$

where $t_i' = t_i M_{v_i}$. With all the equations in place, it is evident that the number of unknowns exceeds the number of equations by one. Furthermore, as our goal is to solve for v_{1x}, we must address the three coupled variables, namely v_{1x}, v_{0xi}, and x_{0i}, which are related by the equations

$$\boxed{v_{1x} = \frac{x_1' - x_2'}{t_1' + \beta_{12} t_2'} - \frac{x_{0i}(M_{p_1} - M_{p_2}) + v_{0xi}(t_1' - t_2')}{t_1' + \beta_{12} t_2'}} \ , \tag{B.10}$$

$$\boxed{v_{0xi} = \frac{x_1 \beta_{12} t_2' + x_2 t_1' - x_{0i}(M_{p_1} \beta_{12} t_2' + M_{p_2} t_1')}{(1 + \beta_{12}) t_1' t_2'}} \ , \text{ and} \tag{B.11}$$

$$\boxed{x_{0i} = \frac{x_1 \beta_{12} t_2' + x_2 t_1' - v_{0xi}(1 + \beta_{12}) t_1' t_2'}{M_{p_1} \beta_{12} t_2' + M_{p_2} t_1'}} \ , \tag{B.12}$$

which arise from manipulation of equations B.8 and B.9.

This interdependence or v_{1x}, v_{0xi} and x_{0i} makes the problem a bit more difficult. However, this can be overcome by using the knowledge that (i) for a laser beam with linear polarization in the z-direction the dissociation probability, in standard spherical coordinates, must be ϕ-independent and symmetric in $\pm\cos\theta$, and (ii) for a large data set the conditions should converge to a state where

$$\overline{v_{0x}} = \frac{1}{N} \sum_{N}^{i} v_{0xi}(\overline{x_0}) \text{ and } \overline{x_0} = \frac{1}{N} \sum_{N}^{i} x_{0i}(\overline{v_{0x}}) \ . \tag{B.13}$$

Furthermore, since the laser spot is quite small (on the order of 10 μm), the resulting deviation in x_{0i} is small and one can simply use the average value ($\overline{x_0}$) to simplify the equations and solve for v_{1x} and v_{0xi}. This is done by simply replacing x_{0i} with the constant value $\overline{x_0}$ in equations B.10 and B.11.

B.4.4.3 Determining the magnification factors

One should notice that formulae in the previous section are valid for all diatomic molecules regardless of mass and charge, i.e. for all dissociation channels. This is because these quantities only effect the times of flight, which will be discussed momentarily, and the magnification factors. The magnification factors were fit to the simulated results, i.e. SimIon trajectories, and were found to

be

$$M_p(z_{0i}, E_{scl}, q \neq 0) = M_p^0 + M_p^1 z_{0i} + M_p^2 z_{0i}^2 \tag{B.14}$$

$$M_v(z_{0i}, E_{scl}, q \neq 0) = M_v^0 + M_v^1 z_{0i} \ , \tag{B.15}$$

where

$$\begin{aligned}
M_p^0 &= 1.06502 + 0.57745\exp(-E_{scl}/18.51339) \\
&\quad + 2.03885\exp(-E_{scl}/3.33581) + 4.34746\exp(-E_{scl}/0.77558) \\
M_p^1 &= -0.00053 + 0.12686\exp(-E_{scl}/0.3933) \\
&\quad + 0.05906\exp(-E_{scl}/1.18907) + 0.04416\exp(-E_{scl}/0.39338) \\
M_p^2(E_{scl} \leq 1.75) &= -0.00027 + 0.01\exp(-E_{scl}/0.26307) \\
M_p^2(E_{scl} > 1.75) &= -2.2852 \times 10^{-6} - 2.45799 \times 10^{-5}\exp(-E_{scl}/70.57797) \\
&\quad - 9.20083 \times 10^{-5}\exp(-E_{scl}/14.0189) - 2.49711 \times 10^{-4}\exp(-E_{scl}/3.75414)
\end{aligned}$$

and

$$\begin{aligned}
M_v^0 &= 1.00246 + 0.08513\exp(-E_{scl}/3.08529) \\
&\quad + 0.02258\exp(-E_{scl}/17.64007) + 0.21143\exp(-E_{scl}/0.69256) \\
M_v^1 &= -7.09197 \times 10^{-5} - 0.0028165\exp(-E_{scl}/1.51372) \\
&\quad - 5.35257 \times 10^{-4}\exp(-E_{scl}/24.60567) - 0.0014843\exp(-E_{scl}/5.30972) \ .
\end{aligned}$$

Notice that the magnification factors depend on E_{scl}, i.e. the scaled particle energy $E_{scl} \equiv E_i/(qV_s)$, and z_{0i} and only deviate from unity for charged particles, i.e. $M_p(q = 0) = 1 = M_v(q = 0)$. The variable E_{scl} was chosen for the fit since the trajectory of all ions with the same scaled energy will be identical. Furthermore, the dependance on z_{0i} makes sense since the position of the "creation" of the ion will effect the magnification as this determines how far the ion must travel in the field region.

B.4.4.4 Determining v_{1z}

Now that the x- and y-components are well in hand let us consider the z-component, i.e. the component in the molecular-ion beam direction. In this direction the governing equations are as follows. The TOF of the first hit for both ionization and dissociation is

$$\boxed{t_1 = \frac{2d_1}{v_{0zi}\eta_1}\left[\chi_1 - (1+u_{1z})\right] + \frac{d_2}{v_{0zi}\chi_1}}, \tag{B.16}$$

where $\chi_1 = \sqrt{(1+u_{1z})^2 + \eta_1(1-z_i')}$. In contrast, the TOF of the second particle differs. For ionization

$$\boxed{t_2 = \frac{2d_1}{v_{0zi}\eta_2}\left[\chi_2 - (1+u_{2z})\right] + \frac{d_2}{v_{0zi}\chi_2}}, \tag{B.17}$$

and for dissociation

$$\boxed{t_2 = \frac{D - z_i}{v_{0zi} + v_{2z}} = \frac{D(1-z_i'')}{v_{0zi}(1-\beta_{12}u_{1z})}}, \tag{B.18}$$

where $\chi_2 = \sqrt{(1+u_{2z})^2 + \eta_2(1-z_i')}$. In addition, momentum is conserved as before

$$\boxed{m_1 v_{1z} + m_2 v_{2z} = 0 \text{ or } u_{2z} = -\beta_{12}u_{1z}}, \tag{B.19}$$

where $u_{jz} \equiv v_{jz}/v_{0zi}$. Again we have the problem that v_{1z}, v_{0zi}, and z_{0i} are all coupled together. Thus, we used the same method of determining the average value of z_{0i} so that the values of v_{1z} and v_{0zi} for each event could be determined. A numerical algorithm is employed to find the numerical solution to the simultaneous equations above. The accuracy of the numerical solution is determined by the number of iterations done by algorithm employed. In our case, we require the accuracy to be great enough that the error is negligible in comparison to the error in our measured values of position and time.

B.5 Molecular dissociation imaging for triatomic molecules

B.5.1 Molecular dissociation imaging

Using the same apparatus and basic technique described for diatomic molecules, it is also possible to measure the laser-induced dynamics of triatomic molecules. The only real difference is the addition

of one more unknown (i.e. one needs to determine $\overrightarrow{p}_3$ in addition to $\overrightarrow{p}_1$ and $\overrightarrow{p}_2$) and one more measured quantity (i.e. x_3, y_3, and t_3). With this in mind, the same notation will be used in this case as in the diatomic case with variables defined in table B.1.

B.5.1.1 Transverse components

For the transverse components x and y one has the following four equations.

$$\boxed{x_1 - M_{p_1} x_{0i} = (v_{0x_i} + v_{1x}) t'_1} \tag{B.20}$$

$$\boxed{x_2 - M_{p_2} x_{0i} = (v_{0x_i} + v_{2x}) t'_2} \tag{B.21}$$

$$\boxed{x_3 - M_{p_3} x_{0i} = (v_{0x_i} + v_{3x}) t'_3} \tag{B.22}$$

$$\boxed{0 = m_1 v_{1x} + m_2 v_{2x} + m_3 v_{3x}} \tag{B.23}$$

As in the diatomic case the number of unknowns exceeds the number of equations by one. Thus, the same approximation will be made and the average value of x_{0i} will be used, namely the constant $\overline{x_0}$. Manipulating these equations yields the following equations.

$$v_{1x} = \frac{1}{1 + \beta_{13} + \beta_{23}} \left[(1 + \beta_{23}) \frac{x_1 - M_{p_1} x_{0i}}{t'_1} - \beta_{23} \frac{x_2 - M_{p_2} x_{0i}}{t'_2} - \frac{x_3 - M_{p_3} x_{0i}}{t'_3} \right] \tag{B.24}$$

$$v_{2x} = \frac{1}{1 + \beta_{13} + \beta_{23}} \left[-\beta_{13} \frac{x_1 - M_{p_1} x_{0i}}{t'_1} + (1 + \beta_{13}) \frac{x_2 - M_{p_2} x_{0i}}{t'_2} - \frac{x_3 - M_{p_3} x_{0i}}{t'_3} \right] \tag{B.25}$$

$$v_{3x} = -(\beta_{13} v_{1x} + \beta_{23} v_{2x}) \tag{B.26}$$

$$P^{cm}_{xi} \equiv M v_{0xi} = \frac{m_1}{t'_1} x_1 - x_{0i} M_{p_1} + \frac{m_2}{t'_2} x_2 x_{0i} M_{p_2} + \frac{m_3}{t'_3} x_3 - x_{0i} M_{p_3} \tag{B.27}$$

Note that one could have eliminated the explicit dependance on x_{0i} from the equations for v_{1x}, v_{2x}, and v_{3x} in favor of v_{0xi}. However, as we see from the center of mass definition (equation B.27), v_{0xi} is a function of x_{0i}, so the effect of the assumption is that $x_{0i} \rightarrow \overline{x_0}$ is still present.

B.5.1.2 Temporal component

As in the two-body breakup case the temporal or z-component is the most complicated due to the acceleration of the electric field. Nevertheless, one can write the time-of-flight for each of the fragments as follows

$$\boxed{t_1 = \frac{2d_1}{v_{0zi}\eta_1}\big[\chi_1 - (1+u_{1z})\big] + \frac{d_2}{v_{0zi}\chi_1}} \tag{B.28}$$

$$\boxed{t_2^{ion} = \frac{2d_1}{v_{0zi}\eta_2}\big[\chi_2 - (1+u_{2z})\big] + \frac{d_2}{v_{0zi}\chi_2} \text{ or } t_2^{neutral} = \frac{D(1-z_i'')}{v_{0zi}(1+u_{2z})}} \tag{B.29}$$

$$\boxed{t_3^{ion} = \frac{2d_1}{v_{0zi}\eta_3}\big[\chi_3 - (1+u_{3z})\big] + \frac{d_2}{v_{0zi}\chi_3} \text{ or } t_3^{neutral} = \frac{D(1-z_i'')}{v_{0zi}(1+u_{3z})}}, \tag{B.30}$$

where $\chi_j = \sqrt{(1+u_{jz})^2 + \eta_j(1-z_i')}$ and momentum is still conserved, i.e.

$$\boxed{m_1v_{1z} + m_2v_{2z} + m_3v_{3z} = 0}\,. \tag{B.31}$$

Once again v_{1z}, v_{0zi}, and z_{0i} are all coupled together. We use the same method of determining the average value of z_{0i} so that the values of v_{1z} and v_{0zi} for each event can be determined. In general we do this numerically as it is simpler and more straight forward than solving the equations analytically.

Appendix C

Electronics schematics

C.1 Introduction

The discussion in this appendix will be focused on the electronics used in the experiments described within this dissertation. Specifically, the fast timing electronics used to convert the measured quantities (e.g. signals on the delay line detector (DLD) and molecular ion beam current) will be detailed. First, it is important to remember that we do our measurements in "event mode", which is to say that the measured quantities are recorded seperatly for each and every laser pulse and that the information gathered for any and all individual laser pulses can be distinguished from all others, as discussed in appendix B.2. With this in mind, there are two distinct types of electronics being used for our measurements: (i) electronics which allow us to tune/determine the "static parameters of a measurement" — parameters that have a negligible change during a measurement (i.e. from laser shot to shot over several hours) and (ii) electronics that record data in event mode.

C.2 Static parameter electronics

C.2.1 Ion beam viewer

The first task undertaken in a measurement is producing a molecular ion beam, which follows the path described in appendix A, that is (i) low-divergance, (ii) contained within our Faraday Cup

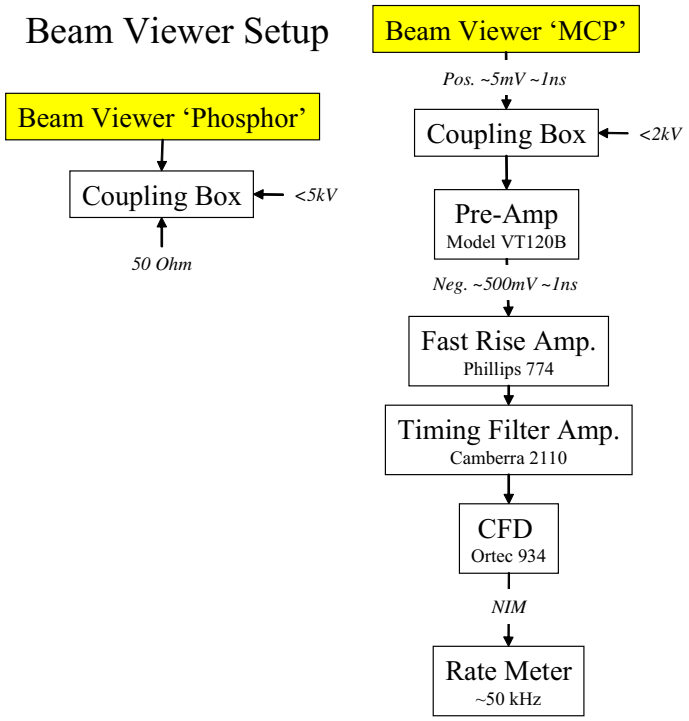

Figure C.1: Beam viewer electronics schematic.

(FC), and (iii) as dense as possible while still preserving single interaction conditions[106]. To these ends, we employ the setup shown in figure C.1 — (i) a "beam viewer" (i.e. a phosphor screen anode with two micro-channel plates (MCPs)), (ii) a 2 mm diameter FC on a two-dimensional manipulation stage, and (iii) a "semi-transparent FC" (i.e. a 30% transmission mesh attached to a current meter). In this configuration, one wants to maximize the current into the movable FC while minimizing the incident particle rate seen on the beam viewer. In this way, the ion beam is made as parallel as possible and the number of scattered particles is minimized. The semi-transparent FC is used to recognize the difference between a true current increase and a false increase in current caused by scattering off the movable FC. See figure C.1 for an electronics schematic of the beam viewer.

[106]The term "single interaction conditions" means that the number of laser-molecule interaction events in which more than one molecule interacts with the laser is negligible. This condition ensures that (i) molecule-molecule interactions do not affect the measurement and (ii) only molecule dissociates per event, thereby reducing the possibility of error in data interpretation.

C.3 Event-mode electronics

C.3.1 Time of laser-molecule interaction

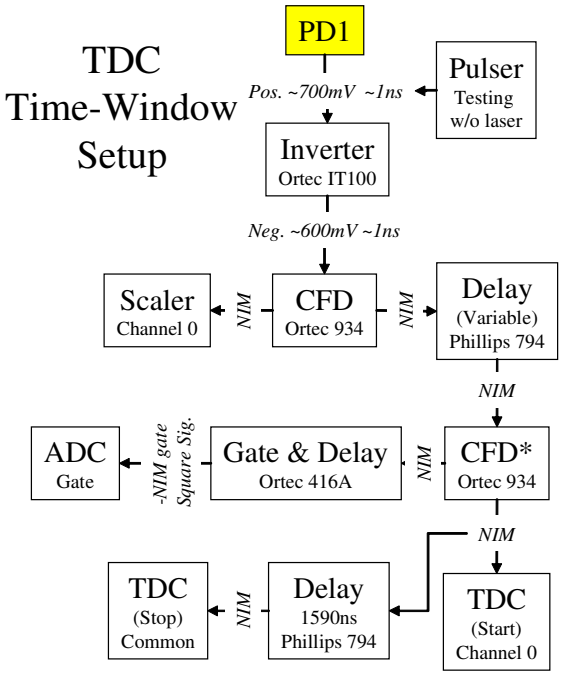

Figure C.2: Electronics schematic for determining a time window for the laser-molecule interaction. Note that the CFD unit (used after the variable delay and marked with an astrict) is simply used to split one NIM signal into three and any unit with this capability is an acceptable substitute.

The first thing we need to establish in our measurements is a time window for the laser-molecule interactions. This is done by recording the pulse output of a photo diode when the laser pulse is incident upon it, as discussed in appendix D.3.2. This signal is then converted into a standard NIM signal and used as the start in a time-to-digital converter (TDC). In other words, the laser pulse is used to start the clocks which will record all other times in our measurements. The TDC also needs a "stop" signal to know when to stop looking for additional signals to arrive and transfer the data to a computer for storage/analysis. These two signals define the window in which the TDC will record events. In figure C.2 this window is set to 1590 ns. There is also a variable delay, which delays the entire window in time. This variable delay is used to move the TDC window around so that (i) all desired events happen within the window and (ii) as many undesired events fall outside

the window as possible.

In addition to setting the TDC window, this photo diode is used in two additional ways. First, the repetition rate of this signal is recorded by a scaler to monitor the repetition rate of the laser. Second, this signal is stretched by a gate and delay generator to produce a square signal to trigger the amplitude-to-digital converter (ADC). This square signal defines the time window in which the ADC will record much in the same way as described for the TDC. The only difference is that the TDC uses two signals — one to begin and one to end the window — while the ADC uses the rising edge of the square signal to start the window and the falling edge of the same signal to the end the window.

C.3.2 Laser power

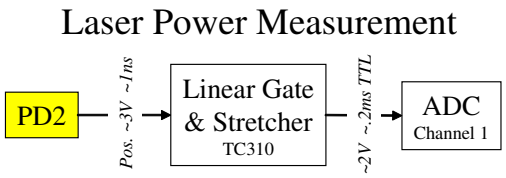

Figure C.3: Electronics schematic for monitoring the laser power.

There can be small scale deviations in the laser power over the time of a measurement. To ensure that these power fluctuations are negligible, we measure the power of each laser pulse. This is done by splitting off a small portion of the laser beam and directing it onto a photo diode, as shown in figure C.3. The intensity of this part of the beam is attenuated until it is well below the saturation of the photo diode so that the pulse height of the photodiode signal varies with intensity. The height of the photodiode signal is then recorded by an ADC and associated with all other information recorded during this pulse. The height of each pulse is then converted to a relative power using the calibration gained by measuring the height of different pulses while introducing known beam attenuations (e.g. neutral density filters). The electronics schematic for this part of our measurement is seen in figure C.3. Note that we do not use the laser power signal for each pulse to divide our measurement into different intensity groups. Rather, we use it as a

tool (i) to monitor the stability of our laser power while a measurement is in progress, (ii) to set the error bars on our laser intensity, and (iii) if necessary, to exclude portions of our data which were obtained during a time of laser instability.

C.3.3 Ion beam current

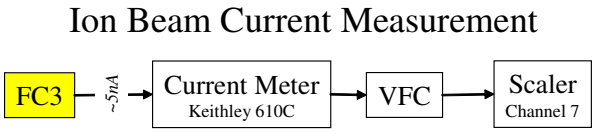

Figure C.4: Electronics schematic for monitoring the molecular ion current.

Just as the laser power can vary over the course of a measurement, the molecular ion beam current can vary. To monitor this we employ the electronics shown in figure C.4. The current is converted into a frequency by (i) converting the current into a voltage with a fast current integrator and then (ii) converting this voltage into a frequency with a voltage-to-frequency converter (VFC), which produces pulses at a frequency that is linearly proportional to the input voltage. These pulses are then summed each second by a scaler and this number is then recorded and permanently associated with the laser pulses that arrived during that second. In addition to allowing us to monitor the stability of the ion beam, this measurement is essential if one wishes to make statements about the relative yield from one measurement to another.

C.3.4 Delay-line-detector

This section will focus strictly on the electronics used in conjunction with the two-dimensional delay-line-detector (DLD), as the functionality of the DLD used in our measurements is discussed in detail in appendices D.1 through D.2. First, let us consider the particle impact time on and the signal amplification of the DLD. The amplification is determined by the difference in voltage between the MCP front plate, MCPF, and back plate, MCPB. As our detector has two MCPs, we set the voltage difference to approximately 2 kV, which corresponds to about 1 kV across each MCP. Furthermore, after removing the direct current (DC) components of MCPF and MCPB

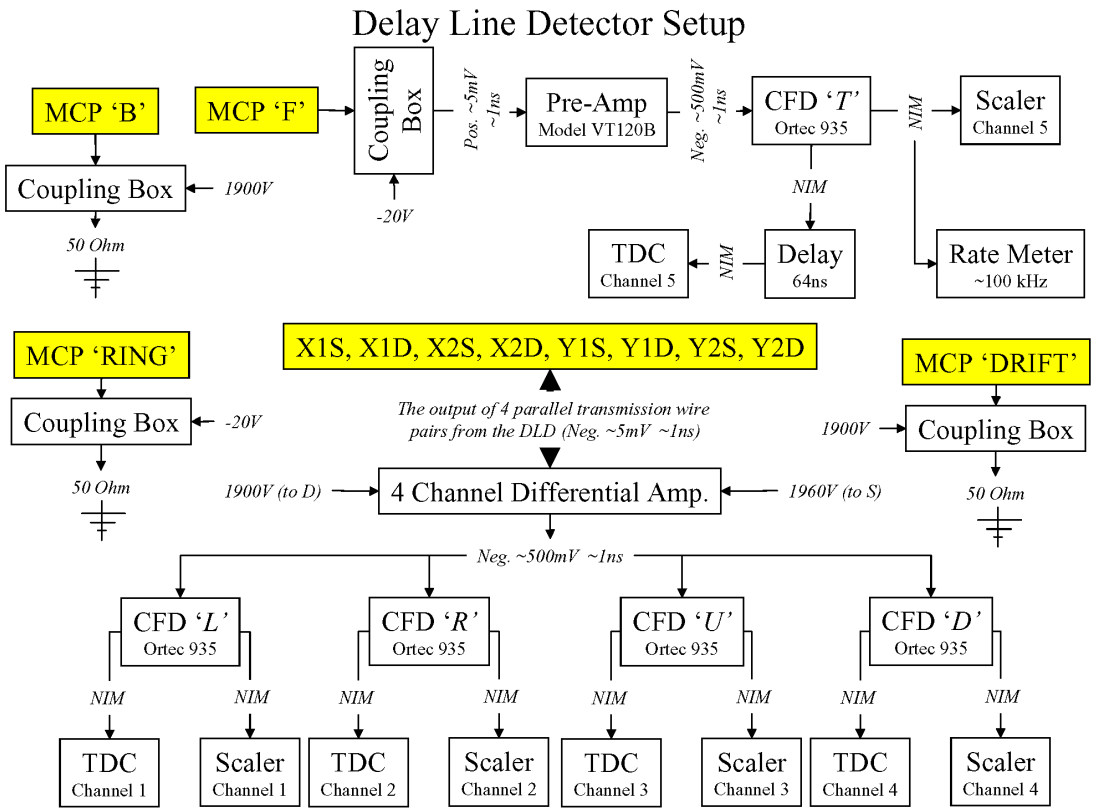

Figure C.5: Delay-line-detector electronics schematic.

(i.e. decoupling the signal), one can use the remaining pulses which result from a particle impact to determine the time of impact of a particle. This is done by sending the decoupled signal through a constant-fraction-discriminator (CFD) and recording the time of the pulse with a TDC. In our measurements, we use the front plate signal only because it is of higher quality that the back plate signal and the two contain redundant information. Furthermore, the timing signal is delayed by 64 ns so that the photon signal (discussed in appendix D.3.2) is within the TDC window. Second, let us consider the two-dimensional parallel transmission wire wrap of the DLD. Parallel transmission wires are used because the long wire wrap picks up a great deal of background noise, which would overwhelm the true signals. To eliminate this problem, each transmission wire pair has one wire at a slightly higher voltage (e.g. 60V) than the other so as to collect the electron cloud signal. The lower voltage wire of each pair is used to pick up the background noise of the system. Each end of

each pair is then sent to a differential amplifier so that the background noise can be subtracted and the true signal can be amplified. These signals are then sent through CFDs, which produce fast negative time signals that are stored in the time-to-digital converter (TDC) and referenced to the photodiode signal. This gives timing signals from each edge of the DLD, which can be converted into a position for each hit as discussed in appendix D.3.

C.3.5 Ion beam chopping

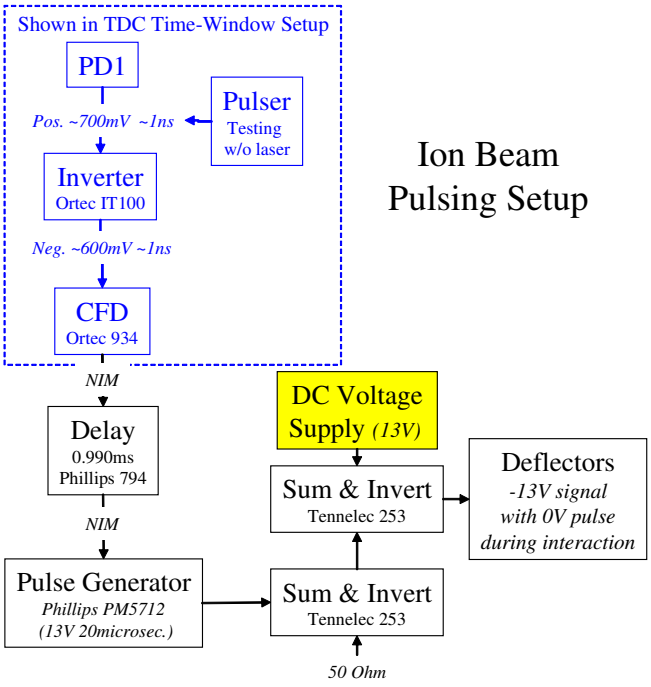

Figure C.6: Electronics schematic for chopping the molecular-ion beam.

Large current densities can damage the MCPs of the DLD detector and as the measurements discussed within this dissertation are performed with the molecular-ion beam directed straight towards our detector, it is important to limit damage as much as possible. This is done for the most part by tuning the ion beam as directly into the FC as possible using the method discussed above in the beam viewer section. However, to further limit the cumulative damage that can take place from the scattered beam that is incident upon the detector, we discard the temporal portion of the ion beam that is not needed, i.e. we chop out the portion of the ion beam that passes through

the interaction region when the laser is not present. To do this we need to synchronize the deflection of the beam to a safe position (i.e. a place where the beam is stopped from reaching the interaction region and detector) while the laser is off. For this reason, the signal from the timing photo diode (as described in the "time of laser-molecule interaction section") is used to trigger a voltage supply that in turn applies 13 V to a deflector before the interaction point, see figure C.6.

C.3.6 Front-end electronics

All the event mode signals are input into three standard VME modules — (i) a scaler, (ii) an ADC, and (iii) a TDC — and are in a VME crate connected to a Linux box via fiber optical link, as shown in figure C.7. This link allows the Linux box to directly communicate/control with the VME electronics using one of the processors in a dual processor setup.

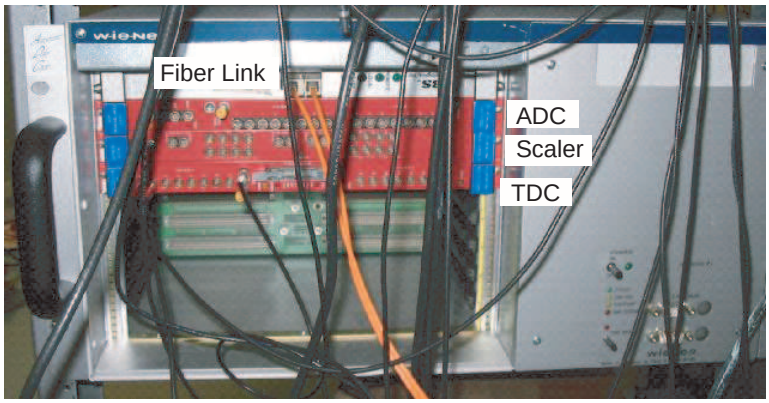

Figure C.7: VME crate with scaler, ADC, TDC, and fiber-optical link marked.

Appendix D

Two-Dimensional Delay-Line-Detector Signal Processing

D.1 Basic particle detection

D.1.1 Introduction

The Two-Dimensional delay-line-detector (DLD) used in the experiments described within this dissertation is a RoentDek delay-line-detector model DLD80, which has a 40.0 mm detection radius and a reported maximum resolution of 70μm.[239] A particle hitting the DLD creates an electron cascade from the two multi-channel plates (MCPs) in front of the DLD. This electron cloud is then accelerated toward the two-dimensional parallel transmission wire wrap comprising the DLD, which is shown in figure D.1. Each transmission wire pair has one wire at a slightly higher voltage (e.g. 60V) than the other so as to collect the electron cloud signal. The lower voltage wire of each pair is used to pick up the background noise of the system. Each end of each pair is then sent to a differential amplifier so that the background noise can be subtracted and the true signal can be amplified. These signals are then sent through constant-fraction discriminators (CFDs), which produce fast negative time signals that are stored in the time-to-digital converter (TDC) and referenced to the photodiode signal. This gives timing signals from each edge of the DLD, which will be denoted by L, R, U, and D for left, right, up, and down, respectively. In addition, the hit on the DLD MCP is also detected from the front and/or back plate and is denoted by T for

detection time. To relate these signals to desired quantities, namely the dissociation momentum vectors, is not important to this section and will be discussed in detail in appendix B.

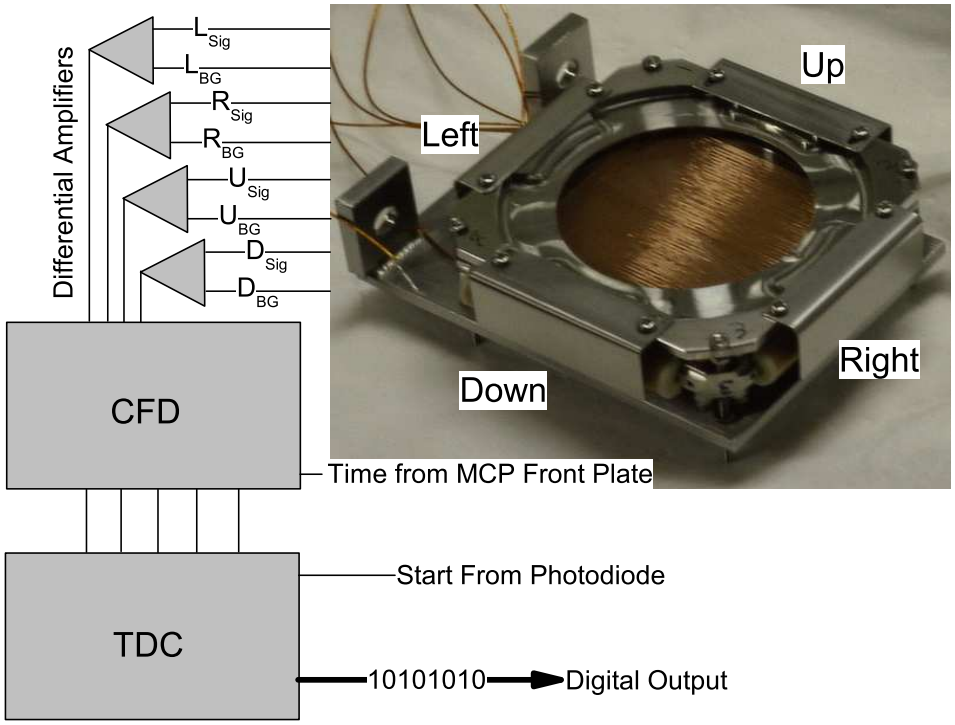

Figure D.1: Delay-Line-Detector without the MCPs attached and electronics schematic.

D.1.2 Finding signal groups

For each laser pulse, the TDC has a matrix of timing signals[107] in which each column corresponds to a particular signal wire (i.e. L, R, U, D, and T) and each row corresponds to another signal on that wire. So, for a particular pulse, the TDC matrix may look like the right side of equation D.1. The goal is to transform this input to an array consisting of grouped TDC signals which correspond

[107]Note, that there is a detection probability for detecting each signal which is dependant on many factors. This functionality is beyond the scope of this section and is discussed in detail in one of our recent publications.[93]

to a proper hit on the detector, i.e.

$$\text{Measured TDC Matrix} \Rightarrow \begin{bmatrix} \mathbf{L} & \mathbf{R} & \mathbf{U} & \mathbf{D} & \mathbf{T} \\ L_1^A & R_1^B & U_1^B & D_1^A & T_1^A \\ L_2 & R_2^A & U_2^A & D_2^B & T_2 \\ L_3^B & R_3 & U_3 & D_3 & T_3^B \\ L_4 & & U_4 & D_4 & \end{bmatrix} \Rightarrow \text{Properly Grouped TDC Matrix} \Rightarrow \begin{bmatrix} \mathbf{L} & \mathbf{R} & \mathbf{U} & \mathbf{D} & \mathbf{T} \\ L_1^A & R_2^A & U_2^A & D_1^A & T_1^A \\ L_3^B & R_1^B & U_1^B & D_2^B & T_3^B \end{bmatrix}, \tag{D.1}$$

where the subscripts correspond to the order in which the signal was detected and superscripts correspond to the real particles of interest A and B. So, for example, L_3^B is the third timing signal to be recorded from the left-signal wire and it was produced by the impact of particle B on the DLD. (Of course there is no way of knowing which signals correspond to which particles at this point and the superscripts are here to help illustrate the signal sorting process.) From the TDC matrix equation D.1 (left) one must find the group(s) of signals that correspond to the detection of particular atoms or ions D.1 (right). This procedure is complicated for two reasons. One, the TDC signals are in order of detection, which means that a particular row does not necessarily equate to a single particle impact on the detector. Two, there are signals produced by electronic noise or background particles.

D.1.2.1 Eliminating background

As described in appendix B, the time-of-flight (TOF) and position signal distributions correspond to the momentum distribution of the process under examination. Thus, most signals that do not correspond to process(es) under study (e.g. background gas ions or electronic noise) can be discarded as shown in figure D.2.

This is because the L, R, U, D, and T signals for true events of interest must fall within certain time gates determined by the axial TOF spectrometer geometry, the DLD orientation, and the process under examination. In the case shown in figure D.2, the events of interest are H or D fragments originating from the laser interaction. Thus, time gates can be used as an initial test to easily eliminate a great deal of background data. Note that only the T signal is shown since L, R, U, and D are very similar to T. This process typically eliminates $\gtrsim 85\%$ of the total signals

recorded by the TDC. This background elimination corresponds to a move from the example TDC

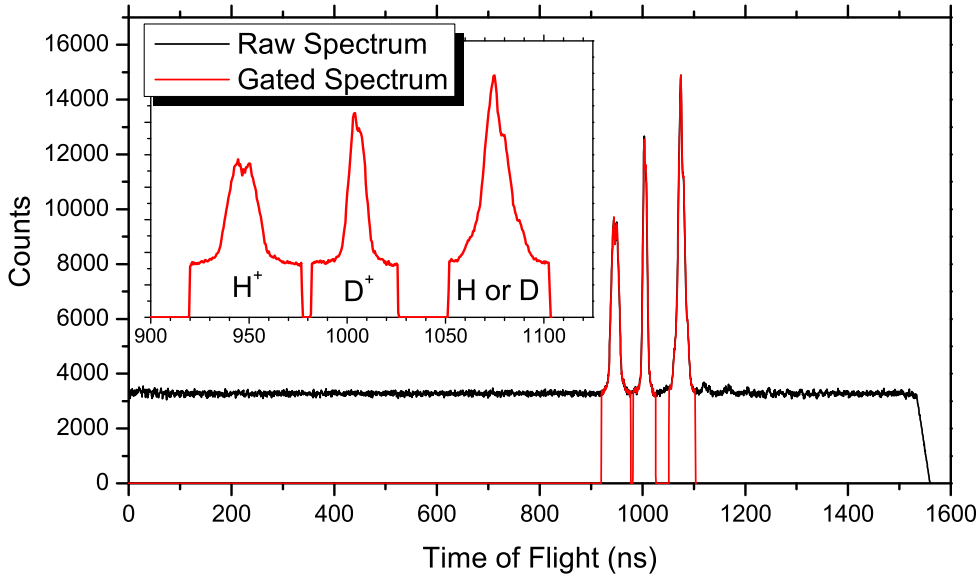

Figure D.2: Typical TOF gating to eliminate background signals in an HD^+ dissociation experiment.

matrix equation D.1 (left) to a reduced matrix, which may yet have background events and is still not sorted into event groups. In the current example this process results in equation D.2 (right).

$$\begin{matrix}\text{Measured}\\ \text{TDC}\\ \text{Matrix}\end{matrix} \Rightarrow \begin{bmatrix} \mathbf{L} & \mathbf{R} & \mathbf{U} & \mathbf{D} & \mathbf{T} \\ L_1^A & R_1^B & U_1^B & D_1^A & T_1^A \\ L_2 & R_2^A & U_2^A & D_2^B & T_2 \\ L_3^B & R_3 & U_3 & D_3 & T_3^B \\ L_4 & & U_4 & D_4 & \end{bmatrix} \Rightarrow \begin{matrix}\text{Background}\\ \text{Eliminated}\end{matrix} \Rightarrow \begin{bmatrix} \mathbf{L} & \mathbf{R} & \mathbf{U} & \mathbf{D} & \mathbf{T} \\ L_1^A & R_1^B & U_1^B & D_1^A & T_1^A \\ L_2 & R_2^A & U_2^A & D_2^B & T_3^B \\ L_3^B & & & D_3 & \end{bmatrix} \tag{D.2}$$

D.1.2.2 Detector conditions

To further reduce the TDC matrix and properly order the event groups, the functionality of the DLD needs to be considered in more depth. The DLD is well modeled by assuming the pulse propagation time in the position wires (from the point of initiation to a particular edge of the detector) is symmetric and linearly equivalent to the distance from the point of initiation to the edge of the DLD. There are deviations from this model, but they are small and will be discussed

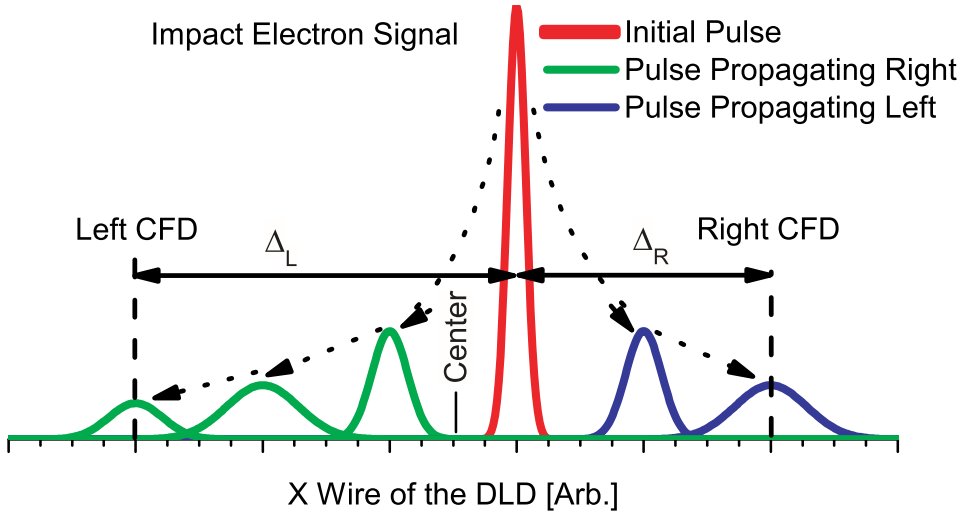

Figure D.3: Linear propagation in DLD. The initial electron pulse, caused by the output of the MCP, propagates both directions in the DLD wire towards the edge of the detector and the CFDs. In this approximation, the centroids of the propagating pulses reach each edge of the detector at a time after the initiation of the pulse corresponding linearly to the distance away from the respective edge. In this figure the particle hit just right of center and three successive snapshots of the pulse propagation in time are shown.

as a correction to the current algorithm in appendix D.2.

Focusing on the x-wire for a moment, the time recorded in the Left channel of the TDC, L, is the time it takes a signal to propagate to the left side of the detector and is proportional to the distance from the initiation point to the left edge of the detector Δ_L plus the time of the impact T and some constant delay C_2. The proportionality constant, C_1, simply corresponds to the signal propagation speed, v, thus

$$L = C_1\Delta_L + T + C_2 = \Delta_L/v + T + C_2 \tag{D.3}$$

as depicted in figure D.3 where v is the pulse propagation speed. Likewise, for the right side of the DLD,

$$R = \Delta_R/v + T + C_2\ . \tag{D.4}$$

Additionally, since the length of the position wires of the DLD, and similarly the distance from one

edge of the DLD to the other, are fixed,

$$\Delta_L + \Delta_R = C_3 \ , \tag{D.5}$$

where $C_3 \equiv$ the width of the detector. Thus,

$$L + R - 2T = C_3/v + 2C_2 = C_4 \equiv -X_{delay} \ , \tag{D.6}$$

where C_4 is a constant, which will now be called X_{delay}[108] since it can be thought of as twice the delay between the timing signal T and the corresponding x-signals, namely L and R. The same procedure can be done in the y-direction, yielding the conditions:

$$\boxed{L + R + X_{\text{delay}} = U + D + Y_{\text{delay}} = 2T} \ . \tag{D.7}$$

More explicitly, this means that

$$\begin{aligned} L + R + X_{\text{delay}} &\simeq U + D + Y_{\text{delay}} \\ L + R + X_{\text{delay}} &\simeq 2T \\ U + D + Y_{\text{delay}} &\simeq 2T \ . \end{aligned}$$

Furthermore, these equations can be written as the strict conditions

$$\begin{aligned} L + R + X_{\text{delay}} - 2T &\leq \text{Tol\_XT} \\ U + D + Y_{\text{delay}} - 2T &\leq \text{Tol\_YT} \\ L + R + X_{\text{delay}} - U + D + Y_{\text{delay}} &\leq \text{Tol\_XY} \ . \end{aligned}$$

where "Tol_XT", "Tol_YT", and "Tol_XY" are the acceptable deviations, or tolerances, for the relationships between the x-wire and T, the y-wire and T, and the x- and y-wires, respectively. It is also easily shown and obvious from figure D.3 that, given our model, the position, measured

[108] Note that a minus sign has been added to X_{delay} in equation D.6 to make the conditions that follow simpler.

from the center of the detector, adheres to the formulas:[109]

$$x \propto X = L - R \quad \text{and} \quad y \propto Y = D - U \ . \tag{D.8}$$

In this representation (x,y) denotes the (horizontal,vertical) position of the hit on the detector in mm.[110] Additionally, X and Y denote horizontal and vertical position of the hit on the detector in channels, which are integers and are determined by the detector and electronics[111]. The position of a hit from the center of the detector is given by

$$r^2 = x^2 + y^2 \propto R^2 = X^2 + Y^2 = (L - R)^2 + (D - U)^2 \ , \tag{D.9}$$

where r and R are the radius of the hit in some units and in channels respectively. Since hits can only be recorded if they hit the MCP of the DLD, which has a constant radius, Det_Rad in channels,

$$(L - R)^2 + (D - U)^2 \leq \text{Det\_Rad}^2 \ . \tag{D.10}$$

With the conditions given by D.7 and D.10, one can loop through all possible signal groups (i.e. combinations of L, R, U, D, and T) to determine which combinations constitute signal groups that could be produced by a single real hit on the DLD. This allows us to make the final step in the TDC matrix reduction and grouping set forth in equation D.1.

$$\begin{array}{c}\text{Background}\\ \text{Eliminated}\end{array} \Rightarrow \left[\begin{array}{ccccc} \mathbf{L} & \mathbf{R} & \mathbf{U} & \mathbf{D} & \mathbf{T} \\ L_1^A & R_1^B & U_1^B & D_1^A & T_1^A \\ L_2 & R_2^A & U_2^A & D_2^B & T_3^B \\ L_3^B & & & D_3 & \end{array}\right] \Rightarrow \begin{array}{c}\text{Properly}\\ \text{Grouped}\\ \text{TDC}\\ \text{Matrix}\end{array} \Rightarrow \left[\begin{array}{ccccc} \mathbf{L} & \mathbf{R} & \mathbf{U} & \mathbf{D} & \mathbf{T} \\ L_1^A & R_2^A & U_2^A & D_1^A & T_1^A \\ L_3^B & R_1^B & U_1^B & D_2^B & T_3^B \end{array}\right] \tag{D.11}$$

By looping through all possible signal groups, the proper signal groups are found and the extraneous

[109] Note that since the travel time through a position wire is assumed to be constant, any time gained at one end of a position wire (e.g. L) will be lost in the other end (e.g. R). Thus, it is more intuitive to insert a factor of 2 in equation D.8 (e.g. $X = (L - R)/2$). However, this factor is omitted here and absorbed into the proportionality constant so computation can still be done quickly with integers instead of with slower floating-point numbers.

[110] Note that any real units can be used here, but mm and ns will be used as the standard units here unless otherwise specified.

[111] The determination of the proportionality constants in these equations will be discussed in appendix D.3.

signals are eliminated. The following code outline illustrates the logic:[112]

```
for(iL=0;iL<Ldepth;iL++){
  for(iR=0;iR<Rdepth;iR++){
    for(iU=0;iU<Udepth;iU++){ \\loop through all possible combinations
      for(iD=0;iD<Ddepth;iD++){
        for(iT=0;iT<Tdepth;iT++){
          L = TDC[1][iL];
          R = TDC[2][iR];
          U = TDC[3][iU]; \\pull signals out of the TDC Matrix
          D = TDC[4][iD];
          T = TDC[5][iT];
          X = L - R; \\determine the x,y-position on the detector in channels
          Y = D - U;
          if(sqrt(X*X+Y*Y)<Det_Rad){\\ensures that the hit is on the detector
            \\ensures the x-delay condition is fulfilled
            if(abs((L + R + X_delay) - (T + T)) < Tol_XT){
              \\ensures the y-delay condition is fulfilled
              if(abs((U + D + Y_delay) - (T + T)) < Tol_YT){
                \\ensures the x-delay y-relationship is fulfilled
                if(abs((L + R + X_delay) - (U + D + Y_delay)) < Tol_XY){
                  \\ANY COMBINATION OF L,R,U,D,T MAKING IT HERE IS ACCEPTED
```

With this logic, a signal group, which either does not correspond to a real particle hit or corresponds to a background particle, has a probability to fulfill the conditions. These 'false' groups cannot be eliminated at this point because there is no way to distinguish them from real hits by particles of interest. However, the physical requirements of the system under study will allow further cleaning of false groups (as illustrated in appendix B).

D.1.3 Reconstructing signal groups

D.1.4 Lost position signal

Occasionally, one of the signals constituting a real signal group (L, R, U, D, or T) is lost due to electronic imperfections, e.g. the finite time required by a CFD between two signals to trigger on

[112] Note that the example code shown here has been arranged for ease of understanding the logic of the process and therefore will not have the optimal compilation or processing speed. The full c++ code is peripheral to this dissertation and too long to be presented here but can be provided upon request.

the second signal (i.e. pulse-pair resolution). In the case that only one of the signals is lost, the remaining four signals can be used to reconstruct the lost data. First, consider the case in which one of the position signals (L, R, U, or D) is lost and the remaining three position signals and the timing signal (T) remain. If the left, L, signal is lost, then using the conditions of equation D.7 one can reconstruct the signal with the following:

$$L = \frac{(2T - R - X_{\text{delay}}) + (U + D + Y_{\text{delay}} - R - X_{\text{delay}})}{2} \ . \tag{D.12}$$

This is derived by taking the average of the two reinvent conditions in equation D.7.[113] Of course, one must be careful not to double count signal groups or reconstruct an impossible signal (i.e. a hit that is physically impossible because it is outside of the detector or outside of the range of interest discussed in the subsection D.1.2.1. The following code outline shows the logic behind such a reconstruction[114]. Again, false groups may be found, but physical requirements of the system

[113] Note that in equation D.12 the inherent jitter in the tolerance conditions has been ignored for the time as it will be discussed in detail in appendix D.2.4.2.

[114] This exercise has only been done for the left signal, L, but the extension to the other position signals is obvious.

under study will eliminate the vast majority of these hits.

```
for(iR=0;iR<Rdepth;iR++){
  for(iU=0;iU<Udepth;iU++){ \\loop through all possible combinations
    for(iD=0;iD<Ddepth;iD++){
      for(iT=0;iT<Tdepth;iT++){
        R = TDC[2][iR];
        U = TDC[3][iU]; \\pull signals out of the TDC Matrix
        D = TDC[4][iD];
        T = TDC[5][iT];
        if(R, U, D, and T are not part of another hit){\\ensures no double counting
          L = ((2*T-R-X_delay)+(U+D+Y_delay-R-X_delay))/2; \\remake L
          X = L - R; \\determine the x,y-position on the detector in channels
          Y = D - U;
          if(sqrt(X*X+Y*Y)<Det_Rad){\\ensures that the hit is on the detector
            \\ensures the x-delay condition is fulfilled
            if(abs((L + R + X_delay) - (T + T)) < Tol_XT){
              \\ensures the y-delay condition is fulfilled
              if(abs((U + D + Y_delay) - (T + T)) < Tol_YT){
                \\ensures the x-delay y-relationship is fulfilled
                if(abs((L + R + X_delay) - (U + D + Y_delay)) < Tol_XY){
                  \\ANY COMBINATION OF L,R,U,D,T MAKING IT HERE IS ACCEPTED
```

Note that in this algorithm the conditional statement excluding previously used signals is important as one does not want to double count previously used signal groups.

D.1.4.1 Lost time signal

Now, the reconstruction of a lost timing signal, T, will be considered. If the time signal, T, is lost, then using the conditions of equation D.7 one can reconstruct the signal with the following:

$$T = \frac{(L + R + X_{delay}) + (U + D + Y_{delay})}{4} , \tag{D.13}$$

which is the average of the two reinvent conditions in equation D.7.

```
for(iL=0;iL<Ldepth;iL++){
  for(iR=0;iR<Rdepth;iR++){
    for(iU=0;iU<Udepth;iU++){ \\loop through all possible combinations
      for(iD=0;iD<Ddepth;iD++){
        L = TDC[1][iL];
        R = TDC[2][iR];
        U = TDC[3][iU]; \\pull signals out of the TDC Matrix
        D = TDC[4][iD];
        if(L, R, U, and D are not part of another hit){\\ensures no double counting
          X = L - R; \\determine the x,y-position on the detector in channels
          Y = D - U;
          if(sqrt(X*X+Y*Y)<Det_Rad){\\ensures that the hit is on the detector
            T = ((L + R + X_delay)+(U + D + Y_delay))/4; \\remake T
            \\ensures the x-delay condition is fulfilled
            if(abs((L + R + X_delay) - (T + T)) < Tol_XT){
              \\ensures the y-delay condition is fulfilled
              if(abs((U + D + Y_delay) - (T + T)) < Tol_YT){
                \\ensures the x-delay y-relationship is fulfilled
                if(abs((L + R + X_delay) - (U + D + Y_delay)) < Tol_XY){
                  \\ANY COMBINATION OF L,R,U,D,T MAKING IT HERE IS ACCEPTED
```

One can go even further and reconstruct hits that have lost two position signals (i.e. one of the x-signals (L or R) and one of the y-signals (U or D)) or hits that have lost a position signal and the timing signal with much the same method. However, each additional level of reconstruction will add additional random events, which must be accounted for and subtracted.

D.1.5 Experimental implementation

In this section, the way in which this logic has been implemented and how one can determine the necessary DLD parameters will be discussed. In particular, how one moves from the linear signal propagation model, signal group searching, and reconstruction techniques to practical data analysis is discussed. This should result in the ability to determine the position and time at which a particle hits the DLD in channels defined by the electronics in use.

D.1.5.1 Determining X_{delay} and Y_{delay}

Equation D.7 in the previous sections refers to constants that are essential to signal analysis, namely X_{delay} and Y_{delay}, which are determined by the DLD and electronics. Although these constants could be roughly determined by tracing back and estimating all the constants involved (e.g. the speed a signal travels in the wire, the DLD wire length, etc.), it is easier to examine real signals to determine these values.

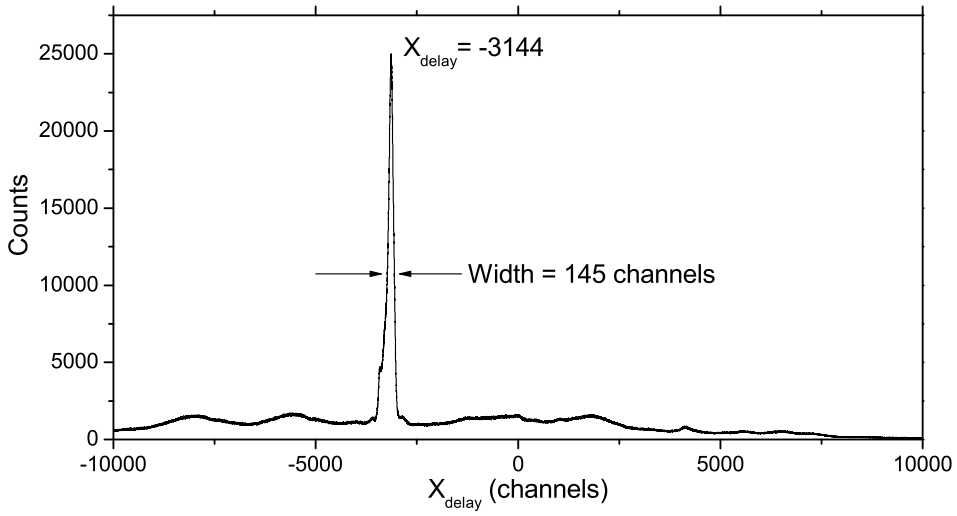

Figure D.4: Using all possible signal combinations from the raw TDC data, a histogram of X_{delay} is and plotted. The peak and width of this distribution can be used as the X_{delay} and X_{delay} tolerances, respectively. Note that a similar plot is generated for Y_{delay}.

One can see that equation D.7 can be manipulated into a form defining X_{delay} and Y_{delay} in terms of measurable (i.e. L, R, U, D, and T) as

$$X_{delay} = 2T - L - R \quad \text{and} \quad Y_{delay} = 2T - U - D. \tag{D.14}$$

Thus, if particles are incident upon the DLD, one can plot a histogram of the values of X_{delay} and Y_{delay}. As shown in figure D.4, this allows one to determine the values of X_{delay} and Y_{delay}. In addition, the widths of these peaks give a rough range of acceptable values for X_{delay} and Y_{delay}, which will be referred to as "Tol_XT" and "Tol_YT", respectively.

D.1.5.2 Determining the radius of the DLD in channels

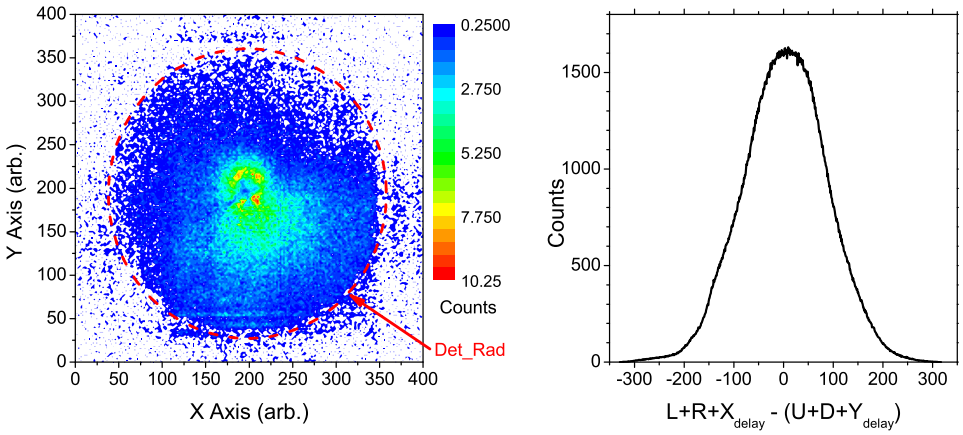

Figure D.5: (a) A 2D histogram of the x-y-position of hits on the DLD. In the case displayed, the radius of the DLD is obviously less than 200 channels. (b) A 1D histogram of Tol_XY.

With the acceptable ranges and mean values of X_{delay} and Y_{delay} now set, one can determine the other sorting parameters and begin to fine tune the signal finding process. To determine the values of the detector radius and the range of acceptable values of "Tol_XY", one can set the values to very large numbers and sort the data using the algorithm outlined in subsection D.1.2.2. This will output values for L, R, U, D, and T that can be converted into values corresponding to "Det_Rad" and "Tol_XY" using the relations

$$\text{Tol\_XY} = L + R + X_{delay} - (U + D + Y_{delay}) \quad \text{and} \quad \text{Det\_Rad} = \sqrt{(L-R)^2 + (D-U)^2}\ . \tag{D.15}$$

The histograms for Tol_XY and position, as shown in figure D.5, will allow one to set these input parameters properly. Note that one can also work back from the actual size of the DLD in mm to a maximum radius in channels by using the conversion method presented in appendix D.3.

D.1.5.3 More reconstruction produces more spurious events

At this point one should have all the parameters necessary to run the signal finding and reconstruction algorithms previously discussed in this appendix. However, one must be careful when implementing reconstruction algorithms because with each additional level of reconstruction, less

constraints are placed on signal groups before they are accepted as real. This means that as the amount of reconstruction allowed increases, so will the number of both real events (which correspond to actual particle impacts on the DLD) and the number of spurious events (which fulfill the signal conditions only by random coincidence).

Balancing Reconstruction Gain with Random Production One must strike an acceptable balance between the real and spurious signal gains so as to increase the particle detection efficiency as much as possible without compromising the validity of the measured distributions due to large amounts of unreal events. This will not be discussed in detail here because it depends heavily on the type of measurement being done and the additional constraints one can impose on the data due to the physical constraints of the system under study.

Tagging Reconstructed Events In general, however, it has been useful in all the measurements we have undertaken to make the level of reconstruction an input parameter and to "tag" each event with the type of reconstruction used in its creation. To tag each event one needs to attach an additional piece of information, which corresponds to the reconstruction method employed in finding the group, to each accepted signal group. Thus, each accepted signal group will have a value corresponding to signal quality, S, in addition to the values for L, R, U, D, and T discussed above. By permanently associating signal quality, S, with each signal group one can look at the distribution of signal qualities involved at any subsequent point in the data analysis to further help in determining the best level of reconstruction along with the error associated with the spurious recreations.

D.2 Nonlinear corrections to delay-line-detector signal processing

D.2.1 Introduction

Previously in appendix D.1, it was assumed that the quantities X_{delay} and Y_{delay} were constants depending on the electronic setup and independent of the position of the hit on the DLD. This is correct in the first order approximation. However, when the values of X_{delay} and Y_{delay} are examined

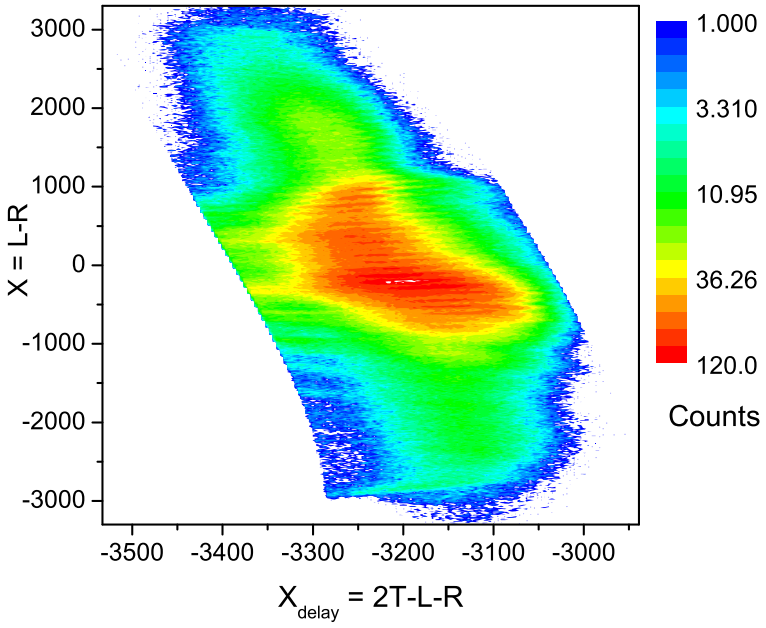

Figure D.6: A two dimensional histogram of $X_{delay}(X)$, which was obtained by calculating X_{delay} from equation D.14 for all possible signal groups. Note that unless otherwise mentioned, units will be in the ~ 25 ps channels of our TDC.

in fine detail as a function of X and Y, respectively, there is a weak dependence on position (see figure D.6). In other words, $X_{delay} = f(X)$ and $Y_{delay} = f(Y)$.[115] Regardless of the model use to describe these nonlinearities, one can better limit the background signals and reconstruct lost signals by accounting for this functionality.

D.2.2 Finding the functionality of X_{delay} and Y_{delay}

If one plots X_{delay} and Y_{delay} as a function of X and Y, respectively, the approximate functionality can be obtained. This is done by calculating the X_{delay} value and error[116] for every X position and fitting the data with a polynomial. In our experiment it was found that a third-order polynomial,

$$X_{delay}(X = L - R) = \alpha_0 + \alpha_1 \cdot X + \alpha_2 \cdot X^2 + \alpha_3 \cdot X^3 \tag{D.16}$$

$$Y_{delay}(Y = D - U) = \beta_0 + \beta_1 \cdot Y + \beta_2 \cdot Y^2 + \beta_3 \cdot Y^3 \ , \tag{D.17}$$

[115] Note that in our measurements X_{delay} and Y_{delay} were found to have a negligible dependance on the orthogonal position, i.e. Y and X, respectively.

[116] I will use the standard deviation, i.e. $\sqrt{\langle x^2 \rangle - \langle x \rangle^2}$ for my error.

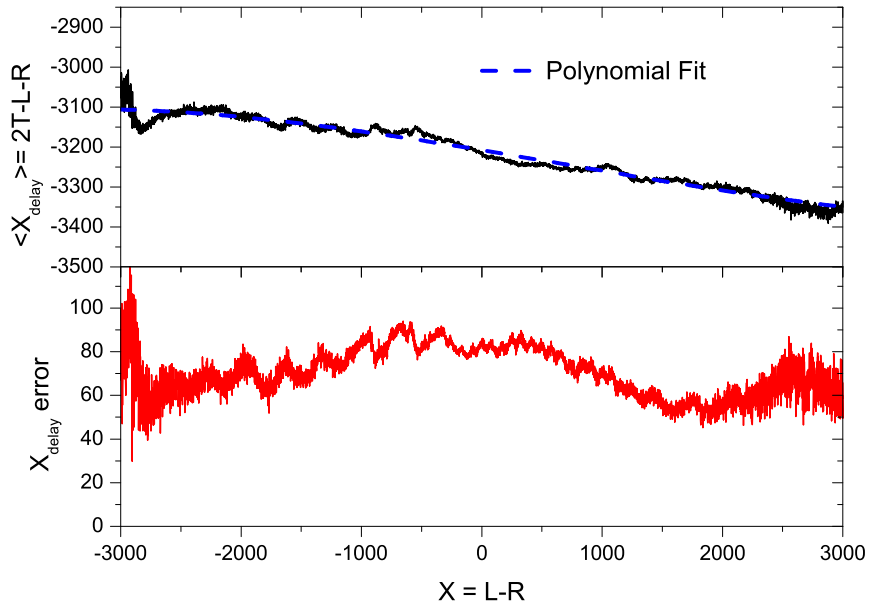

Figure D.7: Third order polynomial fit of the expectation value of $X_{delay}(X)$. The points and standard deviation at each point, denoted as X_{delay} error, are determined from the distributions shown in figure D.6. Note that the β coefficients can be determined in the same way using the $Y_{delay}(Y)$ data.

fit the measured distribution quite well. In the example shown in figure D.7, α_0, α_1, α_2, and α_3 were determined to be (-3207.8 ± 0.2), (-0.0502 ± 0.0002), $(-2.21 \times 10^{-6} \pm 6 \times 10^{-8})$, and $(1.07 \times 10^{-9} \pm 5 \times 10^{-11})$, respectively.

D.2.3 Improved gating conditions

Now that $X_{delay}(X)$ and $Y_{delay}(Y)$ have been determined, they can be used to improve background signal reduction. This is done with a slight modification to the delay gating algorithm following equation D.11 in appendix D.1, in which the constants X_{delay} and Y_{delay} are replaced by the functions $X_{delay}(X)$ and $Y_{delay}(Y)$ determined in equations D.16 and D.17, respectively. The improvement to gating gained with the third-order polynomial fit is shown in figure D.8. In this figure, the right panels (a-c) display results using a single value for X_{delay}, while the left panels (d-f) display results using a third-order polynomial fit for X_{delay}. In this case, the polynomial fit produces a much more Gaussian distribution and reduces the number of random coincidences

passing through the analysis. Additionally, the Gaussian distribution's width is reduced by $\sim 40\%$, which reduces the corresponding uncertainty in reconstructed signals by $\sim 40\%$.

D.2.4 Improved data reconstruction

D.2.4.1 Converging on reconstructed values

In addition to the improved noise reduction, determining $X_{delay}(X)$ and $Y_{delay}(Y)$ allows one to reconstruct more realistic data. To do this only small modifications to the algorithms shown in appendix D.1 are needed. When reconstructing the T signal one only needs to replace the constant X_{delay} and Y_{delay} with their functional forms. Reconstruction of one of the position signals is a bit more difficult as X_{delay} or Y_{delay} depend on the quantity which we are trying to reconstruct. For example, L cannot be directly reconstructed because it depends on X_{delay}, which in turn depends on L as seen in equations D.12 and D.16. Reconciling this cyclical relationship is possible assuming the higher order fit parameters, α_1, α_2, and α_3, are small. In this case, one can implement a convergence routine to find the missing signal. For example,

```
L = ((2*T-R-Alpha_0)+(U+D+Y_delay(Y)-R-Alpha_0))/2; \\initial guess at remaking L
L_Old = L+1000;
while(abs(L_Old-L) > Convergence_Limit){ \\loop until L converges
   L_Old = L;
   L = ((2*T-R-X_delay(L-R))+(U+D+Y_delay(Y)-R-X_delay(L-R)))/2;
}
```

where "Convergence_Limit" is the acceptable convergence range.

D.2.4.2 Incorporating uncertainty in reconstructed values

In the code above one sees that the signal that is reconstructed will fulfill the X_{delay} and/or Y_{delay} conditions exactly (e.g. in the code shown XT_Tol= 0). This is in contrast to the observed distribution shown in figure D.8(f). From this figure, one can see that X_{delay} has an approximately Gaussian distribution with a full width at half-maximum (FHWM) of 154 channels. Thus, proper

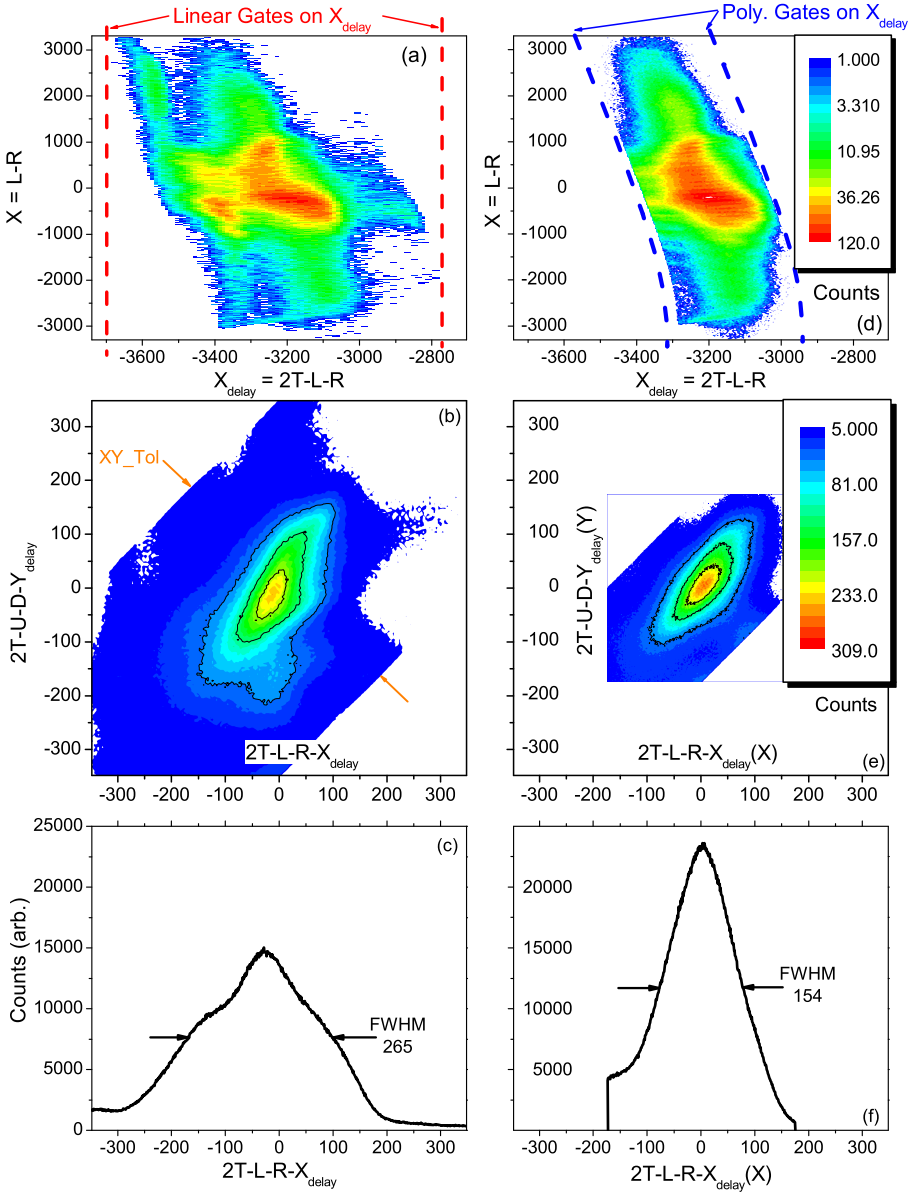

Figure D.8: A comparison of the results using a single value for X_{delay} (panels a-c) and using a third-order polynomial fit for X_{delay} (panels d-f). (a and d) Histograms of $X_{delay}(X)$ vs. X using a linear (a) and a third-order polynomial (d) gate, respectively. Note that the width of the polynomial gate can be and is set narrower than the linear gate because it closely matches the contours of the data. (b and e) Histograms of XT_Tol vs. YT_Tol using using a constant value (b) and a third-order polynomial (e) for X_{delay} and Y_{delay}. (c and f) Histograms of XT_Tol using a constant value for X_{delay} (c) and a third-order polynomial (f). Note that using the polynomial fit reduced the width and produces a much more Gaussian distribution.

reconstruction of signals should include random jitter such that the width of the X_{delay} and Y_{delay} distributions from the reconstructed data matches that of the directly measured data. This can be accomplished by implementing the following algorithm after the convergence algorithm displayed above.

```
JitterX = Random(XdelFWHM); \\Make jitter in distributions
JitterY = Random(YdelFWHM);
X_delay_new = X_delay(L-R)+JitterX; \\add jitter to delays
Y_delay_new = Y_delay(D-U)+JitterY;
L = ((2*T-R-X_delay_new)+(U+D+Y_delay_new-R-X_delay_new))/2;
```

---

where "Random" is a function that returns a random number weighted by the Gaussian distribution corresponding to the input FWHM. The effect of this addition is shown in figure D.9.

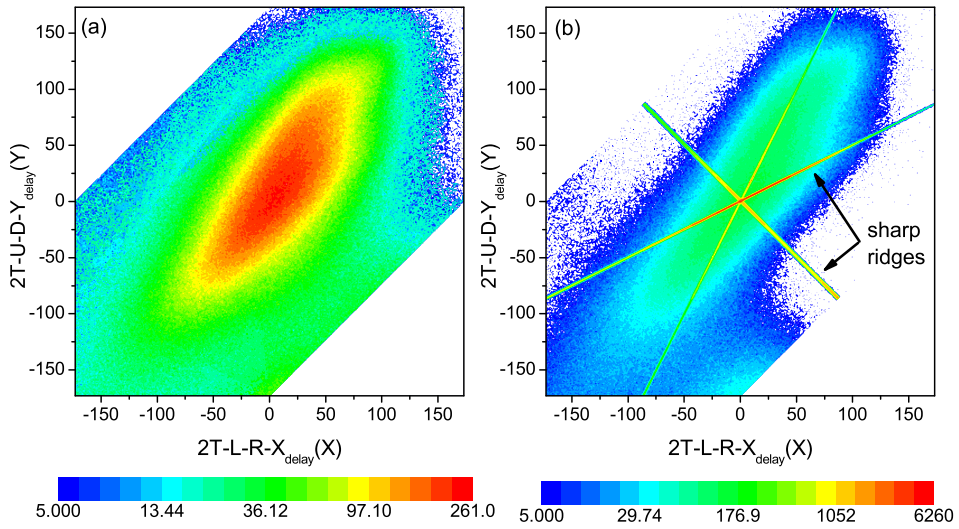

Figure D.9: Histograms of XT_Tol vs. YT_Tol with (a) and without (b) jitter. Note that the data produced without introducing a jitter has ridges that are artificially sharp, which can produce false structure in the momentum distributions.

D.3 Extracting lab positions and times from delay-line-detector signals

D.3.1 Introduction

Sections D.1 and D.2 focused on how to best distinguish and find a signal group resulting from a single particle impact on the delay-line-detector (DLD). This appendix will focus on how to determine the lab coordinates that correspond to a signal group. That is to say, the procedures that allow one to move from the recorded signals (i.e. L, R, U, D, and T) to the true time and position of a particle impact on the detector will be discussed.

D.3.2 Absolute time

To determine how the time recorded by the time-to-digital converter (TDC), T, is related to the time at which the laser and molecules interact in our measurements, t_0, a dual measurement of the photon pulse is employed. First, a small portion of the primary laser pulse, which travels into the interaction region, reflects off one of the spectrometer rings and is incident upon the DLD producing a timing signal, which will be referred to as T_{photon}. Second, a small fraction of the pulsed laser beam in our measurements is split off the main beam before the interaction region and detected by a photo diode attached to the same TDC producing timing signal T_{PD}. The values recorded by the TDC for these two times are

$$T_{photon} = \alpha(t_0 + \frac{l}{c} + \Delta_{DLD}) \tag{D.18}$$

$$T_{PD} = \alpha(t_0 + \Delta_{PD}) \ , \tag{D.19}$$

where α is the conversion for time in some real units to TDC channels, l is the distance from the reflecting spectrometer ring to the DLD, c is the speed of light, and Δ_{DLD} and Δ_{PD} are the response times of the DLD and photo diode electronics, respectively. Subtracting these two quantities yields

$$T_{photon} - T_{PD} = \alpha(\frac{l}{c} + \Delta_{DLD} - \Delta_{PD}) \Rightarrow \Delta_{DLD} - \Delta_{PD} = \frac{T_{photon} - T_{PD}}{\alpha} - \frac{l}{c} \ . \tag{D.20}$$

Furthermore, a hit on the DLD MCP will produce a TDC timing signal, T_{signal}, related to the true time of impact, t_{signal}, by

$$T_{signal} = \alpha(t_{signal} + \Delta_{DLD}) \ . \tag{D.21}$$

Now rearranging these equations yields

$$T_{signal} - T_{PD} = \alpha(t_{signal} - t_0 + \Delta_{DLD} - \Delta_{PD}) \tag{D.22}$$

$$T_{signal} - T_{PD} = \alpha(t_{signal} - t_0 + \frac{T_{photon} - T_{PD}}{\alpha} - \frac{l}{c}) \tag{D.23}$$

$$t_{signal} - t_0 = \frac{T_{signal} - T_{PD}}{\alpha} + \frac{T_{PD} - T_{photon}}{\alpha} + \frac{l}{c} \tag{D.24}$$

$$t_{signal} - t_0 = \frac{T_{signal} - T_{photon}}{\alpha} + \frac{l}{c} \ . \tag{D.25}$$

Thus, one can determine at what time relative to the interaction instant a given particle hits the DLD if T_{signal} and T_{photon} are recorded and α and l (which are inherent properties of the electronics and geometry used, respectively) are known.

D.3.3 Extracting the lab positions assuming linear signal propagation

In this section we will determine the lab position of a hit in useful units using a mask and make the same assumptions made in section D.1, namely that the signals propagate through the DLD wires at a constant speed. Using this model one can see that the lab position of a hit on the DLD, (x, y), can be written as

$$x = (L - R)C_x \propto X \tag{D.26}$$

$$y = (D - U)C_y \propto Y \ , \tag{D.27}$$

which matches the relations derived in equation D.8. To determine the scaling factors, C_x and C_y, a mask with a well known hole pattern, as seen in figure A.4, is placed in front of the DLD (figure D.10). Then the known hole positions (x_i^{mask}, y_i^{mask}) in millimeters are fit to the DLD data

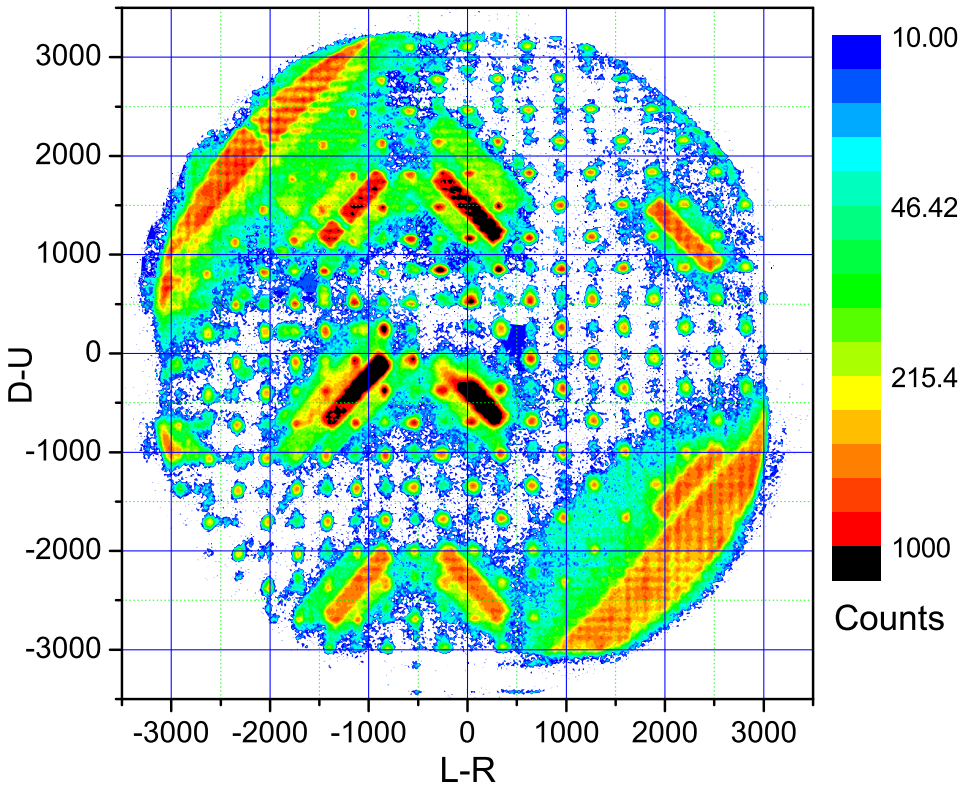

Figure D.10: Raw DLD image produced with a mask.

$(X_i^{DLD}, Y_i^{DLD}) = (L-R, D-U)$ to determine the scaling factors, C_x and C_y. In other words,

$$C_x = \frac{1}{N}\sum_i^N \frac{x_i^{mask}}{X_i^{DLD}} \quad \text{and} \quad C_y = \frac{1}{N}\sum_i^N \frac{y_i^{mask}}{Y_i^{DLD}} \ . \tag{D.28}$$

For the particular experimental setup used for the experiments described within this dissertation $(C_x, C_y) = (0.0124 \pm 0.0003, 0.0118 \pm 0.0005)\frac{\text{mm}}{\text{channel}}$.

D.3.4 Extracting improved lab positions assuming non-linear signal propagation

In the previous section, the signal propagation of the DLD was assumed to be linear. However, very close examination of figure D.10 along with a consideration of section D.2 reveals that the outputs of the detector are slightly non-linear. There are a number of papers discussing the cause of these non-linearities in the DLD in great detail [240–243] (e.g. the CFDs do not trigger exactly

at the center of the pulse, the CFDs may not be symmetric, the pulse travel time is not linearly proportional to the distance it travels, etc.). However, the physics underlying the operation of a DLD is not within the scope of the research presented in this dissertation. Thus, a more "brute force" method can be employed to associate the DLD signals with the proper lab positions and cleaning conditions.

Using the mask data shown in figure D.10 along with the real dimensions of the mask, one can create a translation matrix to move from L, R, U, and D in channels to x and y in mm. This is done by first associating the real position of the center of each hole with the appropriate L, R, U, and D values. Then, for values of L, R, U, and D between but not exactly at one of these points, a linear interpolation between the nearest four points is used. In our experiments we decided to forgo the additional computation required by this method in favor of the simpler linear-propagation model as the deviation between the two methods was small in comparison to other experimental sources of error (e.g. the spread in XT_Tol, YT_Tol, and XY_Tol as shown in figure D.8 and discussed in section D.2).